# Production of Dark Matter and Baryon Asymmetry in Non-standard Cosmologies

**Suruj Jyoti Das**

*A thesis submitted for the degree of*

**Doctor of Philosophy**

*Supervisor*

**Dr. Debasish Borah**

**Department of Physics**
**Indian Institute of Technology Guwahati**
**Guwahati- 781039, Assam, India**

# Production of Dark Matter and Baryon Asymmetry in Non-standard Cosmologies

*A thesis submitted by*

**Suruj Jyoti Das**

to

Indian Institute of Technology Guwahati
in partial fulfillment of the requirements
for the award of the degree of
Doctor of Philosophy in Physics

*Supervisor*

**Dr. Debasish Borah**


**Department of Physics**
**Indian Institute of Technology Guwahati**
**Guwahati- 781039, Assam, India**


*This thesis is dedicated to*
*my parents*
*and*
*my friend Tanu.*


*"The world is not magic — and that's the most magical thing about it"*

***-Sean Carroll.***

# Declaration

**Suruj Jyoti Das**,
Roll No. 186121031
Department of Physics
Indian Institute of Technology Guwahati
Guwahati, India
email: suruj@iitg.ac.in

I hereby declare that works presented in the thesis entitled "**Production of Dark Matter and Baryon Asymmetry in Non-standard Cosmologies**" have been carried out by me under the supervision of **Dr. Debasish Borah** at the Department of Physics, Indian Institute of Technology Guwahati, India. The thesis has not been submitted anywhere else for any degree. Works presented in the thesis are all my own unless referenced to the contrary in the thesis.

Date: 30/03/2023

Suruj Jyoti Das

Signature

# Certificate

**Dr. Debasish Borah,**
Associate Professor
Department of Physics
Indian Institute of Technology Guwahati
Guwahati, India
email: dborah@iitg.ac.in

It is certified that the work contained in the thesis entitled "**Production of Dark Matter and Baryon Asymmetry in Non-standard Cosmologies**" by Mr. Suruj Jyoti Das (Roll No. - 186121031), a Ph.D. student in the Department of Physics, Indian Institute of Technology Guwahati is carried out under my supervision and has not been submitted elsewhere for the award of any other degree.

Date: March 30, 2023

Signature

# Acknowledgements

*"A grateful heart is a magnet for miracles"*

*– Jane Fuller.*

It gives me immense pleasure to express my heartfelt gratitude to all those people whom I have been blessed with. First and foremost, I would like to express my deepest gratitude towards my supervisor Dr. Debasish Borah, without whom this journey would not have been possible. I am highly thankful to him for introducing me to this astounding research field, and for his constant support, guidance, encouragement and valuable advice which really helped me with fruitful results. I indeed feel extremely privileged to have him as my supervisor, who not only helped me to remain optimistic, ambitious, passionate and dedicated throughout my journey, but also assisted me in exploring many amazing and novel research topics and provided me the opportunity to work with some outstanding collaborators. I also truly appreciate his patience and tolerance regarding my lapses and limitations. I have truly learned a great deal from him, whether it be in terms of knowledge or work ethics in general. I will always treasure all the enlightening discussions we had in his office on scraps of paper or the board, and all the ideas and experiences we shared at times over coffee with our group.

I would like to thank my doctoral committee members: Dr. Debaprasad Maity, Dr. Bibhas Ranjan Majhi and Dr. Sayan Chakrabarti for their valuable comments and suggestions during the yearly assessments of my research work. I am also grateful to all the members of our weekly HEP and Gravity Journal clubs, for providing a platform to keep myself updated with the latest trends in high energy physics, gravity and cosmology. Apart from helping me in pursuing my curiousity and inculcating new ideas to look into, these meetings have also helped me in improving my presentation and speaking skills. I also acknowledge Hemanta Da and Basab Da for their cooperation with computational issues.

I would like to thank all of my collaborators and co-authors: Dr. Abhijit Kumar Saha, Devabrat Mahanta, Dr. Basabendu Barman, Dr. Rishav Roshan, Dr. Rome Samata, Dr. Federico R. Urban and Prof. Nobuchika Okada, from whom I had the opportunity to learn and explore different topics. Especially, I am obliged to Abhijit da, Devabrat da, Basabendu da and Rishav da with whom I could sit for hours, almost any day to fix issues in codes and brainstorm several doubts and problems. I would also like to thank Dr. Filippo Sala and Dr. Marek Lewicki for their hospitality and partial support during my visits to LPTHE and the University of Warsaw respectively, and for providing me the opportunity to deliver a talk in their seminars. It was indeed a great learning experience. I thank the organisers and participants of all the schools, conferences and workshops I have attended during my Ph.D., for the fabulous and fruitful times spent.

The list of acknowledgments would be incomplete without mentioning the wonderful seniors of my group: Dibyendu da, Devabrat da and Pritam da. Over all these years, we

have undoubtedly spent several fruitful hours discussing several concepts of physics, and also non-physics related topics. I could always approach them for any help, be it installing any package for work or any unacademic work. I would also like to gratefully acknowledge the support of other members of our group: Nayan, Indrajit and Disha. They have helped me in learning about several new and emerging topics. I would like to thank all the other members of high energy physics and gravity groups, with whom I have discussed time to time on several problems and ideas.

For being a part of my Ph.D. journey, I am thankful to Sumit, Sahabub, Prantik, Nikhil, Partha and all of my Ph.D. friends and batchmates, who made my life here in IITG enjoyable and a memorable one. I would like to thank Nikhil with whom I have spent numerous evenings in the basketball court, which helped me to relax after a long day of work at the lab. I would also like to express my gratitude to all those who help us with the food and maintenance in the hostel and overall in the campus, and make our life here easy and comfortable. Since this thesis is being completed during the COVID pandemic, I would like to offer my gratitude to all the frontline workers who have helped us through the tough times. You guys are the real heroes!

I would like to offer my sincerest gratitude to all those who have helped and supported me to reach this far in my life. Above all, I would like to convey a very special thanks to my family, starting with my parents, without whom all these would have been just a distant dream. I thank them for raising me with unconditional love, care and sacrifices, such that I could get good quality education and be at this position today. I am also eternally indebted to my siblings: my brother and my sister, for their constant support, sacrifices and important advice throughout many important stages of my life. I thank Mriganka da for his timeless encouragement. I would also like to express my gratitude towards my grandparents for their love and affection towards me.

I am highly obliged to my closest friend Tanushree, who had always been there for me right from my college days when I chose Physics as my career. She had been a constant pillar of strength and support for me, and perhaps the best person I have ever come across. I would like to thank her for inspiring and motivating me always, and bringing the best out of me. She had taught me to be fearless and confident in what I do and believed in me at times even when I doubted myself. I thank her for everything.

I thank the teachers and professors I had the privilege to learn from at different stages of my life, and especially those who have inspired me in pursuing my career in physics. I take this opportunity to thank my M.Sc. project supervisor: Dr. Shubho Roy, with whom I got my first exposure to research. Last but not the least, I would like to thank my close friends: Pranab, Navarun, Rituraj, Anand, Ananya, Tarik, Sangeeta, Jinti, Suvashis, Abhinandan, and many more. You all really have been a vital part of my life. Cheers to you all!

*– S. J. D.*

# Publications included in the thesis :

1. **"Thermal keV neutrino dark matter in minimal gauged B-L model with cosmic inflation"**,
   Debasish Borah, **Suruj Jyoti Das**, Abhijit Kumar Saha,
   *e*print: arXiv: 2110.13927 [hep-ph],
   Published in **Phys.Rev.D 106 (2022) 5, 055010**.

2. **"Probing WIMP Dark Matter via Gravitational Waves Spectral Shapes"**,
   Debasish Borah, **Suruj Jyoti Das**, Abhijit Kumar Saha, Rome Samanta,
   *e*print: arXiv: 2202.10474 [hep-ph],
   Published in **Phys.Rev.D 106 (2022) 1, L011701**.

3. **"Low scale leptogenesis and dark matter in the presence of primordial black holes"**,
   **Suruj Jyoti Das**, Devabrat Mahanta, Debasish Borah,
   *e*print: arXiv: 2104.14496 [hep-ph],
   Published in **JCAP 11 (2021) 019**.

4. **"Non-thermal Origin of Asymmetric Dark Matter from Inflaton and Primordial Black Holes**,
   Basabendu Barman, Debasish Borah, **Suruj Jyoti Das**, Rishav Roshan,
   *e*print: arXiv: 2111.08034 [hep-ph],
   Published in **JCAP 03 (2022) 03, 031**.

5. **"Cogenesis of Baryon Asymmetry and Gravitational Dark Matter from PBH"**,
   Basabendu Barman, Debasish Borah, **Suruj Jyoti Das**, Rishav Roshan,
   *e*print: arXiv: 2204.10339 [hep-ph],
   Published in **JCAP 08 (2022) 068**.

6. **"Gravitational wave signatures of PBH-generated baryon-dark matter coincidence"**,
   Basabendu Barman, Debasish Borah, **Suruj Jyoti Das**, Rishav Roshan,
   *e*print: arXiv: 2212.00052 [hep-ph],
   **Currently under review**.

# Other publications :

1. **"Cosmic Inflation in Minimal $U(1)_{B-L}$ Model: Implications for (Non) Thermal Dark Matter and Leptogenesis"**,
   Debasish Borah, **Suruj Jyoti Das**, Abhijit Kumar Saha,
   *e*print: arXiv: 2005.11328 [hep-ph],
   Published in **Eur.Phys.J.C 81 (2021) 2, 169**.

2. **"Gravitational origin of dark matter and Majorana neutrino mass with non-minimal quartic inflation"**,
   Debasish Borah, **Suruj Jyoti Das**, Abhijit Kumar Saha,
   *e*print: arXiv: 2011.02489 [hep-ph],
   Published in **Phys.Dark Univ. 33 (2021) 100858**.

3. **"Probing high scale seesaw and PBH generated dark matter via gravitational waves with multiple tilts"**,
   Debasish Borah, **Suruj Jyoti Das**, Rishav Roshan,
   *e*print: arXiv: 2208.04965 [hep-ph],
   **Currently under review**.

4. **"PBH-infused seesaw origin of matter and unique gravitational waves"**,
   Debasish Borah, **Suruj Jyoti Das**, Rome Samanta, Federico R. Urban,
   *e*print: arXiv: 2211.15726 [hep-ph],
   Published in **JHEP 03 (2023) 127**.

5. **"Affleck-Dine Cogenesis of Baryon and Dark Matter"**,
   Debasish Borah, **Suruj Jyoti Das**, Nobuchika Okada,
   *e*print: arXiv: 2212.04516 [hep-ph],
   **Currently under review**.

# Abstract

This thesis is devoted to the study of two long-standing problems of particle physics and cosmology: the origin of *dark matter* and the *baryon asymmetry* of our Universe, in the presence of a non-standard cosmological history in the first few seconds of the evolution of our Universe. We focus especially on early matter-dominated eras, considering two possible origins of them, one due to a *long-lived particle* (LLP), and the other from *primordial black holes* (PBH). Apart from investigating the standard dark matter (DM) and baryon asymmetry production mechanisms in the presence of these non-standard epochs, the thesis mostly touches upon dark matter scenarios beyond the conventional WIMP paradigm which has been searched for several years now in dark matter direct detection experiments like XENON, LUX etc. and also in collider search experiments like the large hadron collider (LHC), with no positive results so far. While the DM candidates we study are unlikely to show up in these conventional DM search experiments, we propose an alternative and novel probe to look for these DM candidates, which is through stochastic gravitational waves generated in the early Universe. The shape of such gravitational wave spectrum is determined by the non-standard cosmological background which in turn dictates the dark matter phenomenology. The setups we consider can also generate the baryon asymmetry of the Universe through leptogenesis (baryogenesis), which occurs at a very high scale that is out of direct reach from any current experiments, but can be probed indirectly through gravitational waves. The amplitudes and frequencies of these gravitational wave spectra are within reach of near-future gravitational wave detectors such as LISA, DECIGO, CE etc. In addition, the particle physics setups we have considered also have detection prospects on their own, which get modified in the presence of a non-standard cosmological epoch.

In the first two chapters of the thesis, we provide an introduction to dark matter and baryon asymmetry (chapter 1) followed by a discussion of non-standard cosmic epochs (chapter 2) arising from LLP and PBH domination, along with their effects on stochastic gravitational wave background from cosmic strings and PBH density fluctuations. The

objective of the thesis along with its outline is narrated towards the end of chapter 2. The main content of original work is presented in the next four chapters.

# Permissions and Attributions

- The content of chapter 3 is based on the following works
  (a) **Phys.Rev.D 106 (2022) 5, 055010** in collaboration with Debasish Borah and Abhijit Kumar Saha.
  (b) **Phys.Rev.D 106 (2022) 1, L011701** in collaboration with Debasish Borah, Abhijit Kumar Saha and Rome Samanta.
- The content of chapter 4 is based on the following works
  (a) **JCAP 11 (2021) 019** in collaboration with Devabrat Mahanta and Debasish Borah.
  (b) **JCAP 03 (2022) 03, 031** in collaboration with Basabendu Barman, Debasish Borah and Rishav Roshan.
- The content of chapter 5 is based on the following work
  (a) **JCAP 08 (2022) 068** in collaboration with Basabendu Barman, Debasish Borah and Rishav Roshan.
- The content of chapter 6 is based on the following work
  (a) **arXiv:2212.00052 [hep-ph]** in collaboration with Basabendu Barman, Debasish Borah and Rishav Roshan.

# Contents

# List of Figures

# List of Tables

# Chapter 1

# Introduction

The quest for the fundamental building blocks of our Universe has led us to the Standard Model (SM) of particle physics, which describes the elementary particles of the Universe and their fundamental interactions via the strong, weak and electromagnetic forces [1–5]. The SM is based on the principles of quantum field theory and gauge symmetries. Despite its great success and confirmation in different experiments with good precision, it still fails to provide a complete picture of our Universe. Out of the many problems that the SM fails to address, one of the most astonishing ones has been the existence of an unknown non-luminous, non-baryonic form of matter in our Universe, commonly known as dark matter, which dominates the energy budget of the Universe over the normal baryonic matter. None of the particles in the SM satisfies the criteria of being a DM candidate. In addition, the origin of the known baryonic content is also a mystery since it is found to be highly asymmetric between matter and antimatter, whereas the known laws of physics predict equal amounts of particles and antiparticles to be created in the early Universe after the Big Bang. The SM again fails to explain this observed matter-antimatter asymmetry.

Since this thesis is centered around these two problems, i.e. the existence of dark matter and the baryon asymmetry, in this introductory chapter we elaborate on these two topics. The chapter is organized as follows. In section 1.1, we discuss DM, beginning with its observational pieces of evidence in section 1.1.1, followed by some well-known particle DM candidates crucial for this thesis. The next section 1.2 discusses the baryon asymmetry of our Universe (BAU). The observational shreds of evidence in support of

BAU are discussed in Section 1.2.1. In the succeeding sections, we describe the conditions and a well-known mechanism for generating the baryon asymmetry, upon which this thesis is based.

## 1.1 Dark Matter

### 1.1.1 Observational evidences

The first strong hint towards the existence of dark matter dates back to the 1930s when the Swiss astronomer Fritz Zwicky was observing galaxies in the nearby Coma cluster [6]. By using the Doppler shifts of the galaxies to estimate their velocity dispersion, he was able to calculate the gravitational mass in the cluster by employing the Virial Theorem. The mass in the cluster can also be inferred by measuring the luminosity of the stars. He found the latter to be around 400 times smaller than the gravitational mass, indicating the presence of much more matter than we could see. He coined the term '*dunkle materie*' (in German) for the unseen matter, which means *dark matter*.

The next strong piece of evidence of DM came from the observation of *rotation curves* of galaxies, in the 1970s by Vera Rubin and Kent Ford [7]. Now, following the usual Newtonian mechanics, the velocity of objects orbiting around the center of the galaxies varies as

$$v_{\rm orb}(r) = \sqrt{\frac{GM(r)}{r}}, \tag{1.1}$$

where G is the gravitational constant and $M(r)$ corresponds to the mass enclosed within a radius '$r$'. For masses beyond the galactic disk, it is expected that $M(r)$ remains constant and $v_{\rm orb} \propto 1/\sqrt{r}$. However, surprisingly it was observed that even at large distances from the galactic centre, the velocity remains constant, indicating the presence of some extra, unseen mass much beyond the center, varying as $M(r) \propto r$. The rotation curves of 21 Sc galaxies, as observed by V. Rubin are shown in Fig. 1.1.

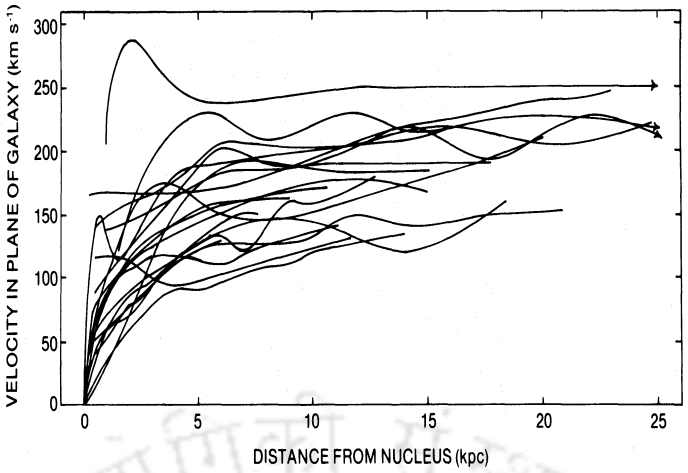


FIGURE 1.1: Variation of mean velocities of 21 Sc galaxies, with distance from the nucleus, as observed by V. Rubin [8].

Another evidence to support the existence of DM at even larger scales of galaxy clusters comes from the phenomena of bending of light due to the gravitational field of massive objects, as predicted by general relativity. Because of this *gravitational lensing* effect, light traveling from distant galaxies to reach an observer gets bent due to the presence of a massive cluster of galaxies in between the source and the observer. This may result in multiple images of the distant galaxy if the gravitational field is very strong (*strong lensing*), or in distorted or sheared images if the lensing is not strong enough (*weak lensing*). Thus, the lensed images carry information about the amount and distribution of matter in the clusters and can be used to infer the presence of dark matter. A schematic diagram of this gravitational lensing effect is shown in the upper panel of Fig. 1.2. The bottom panel of Fig. 1.2 shows the image of galaxy cluster Cl 0024+17 captured by the Hubble Space Telescope, with the blue shading on the right indicating the position of dark matter needed to explain the lensing effects seen.

The most direct evidence of DM comes from the *'Bullet Cluster'* 1E0657-558 [9, 10], which represents the collision of two galaxy clusters. Upon such a collision, the mismatch between the behavior of normal matter and dark matter is quite apparent. The ordinary baryonic matter, consisting of hot gas experience a drag force because of the electromagnetic interactions and are slowed down. This is shown by the pink clumps in Fig. 1.3, as seen by the Chandra X-ray observatory. On the other hand, the dark matter

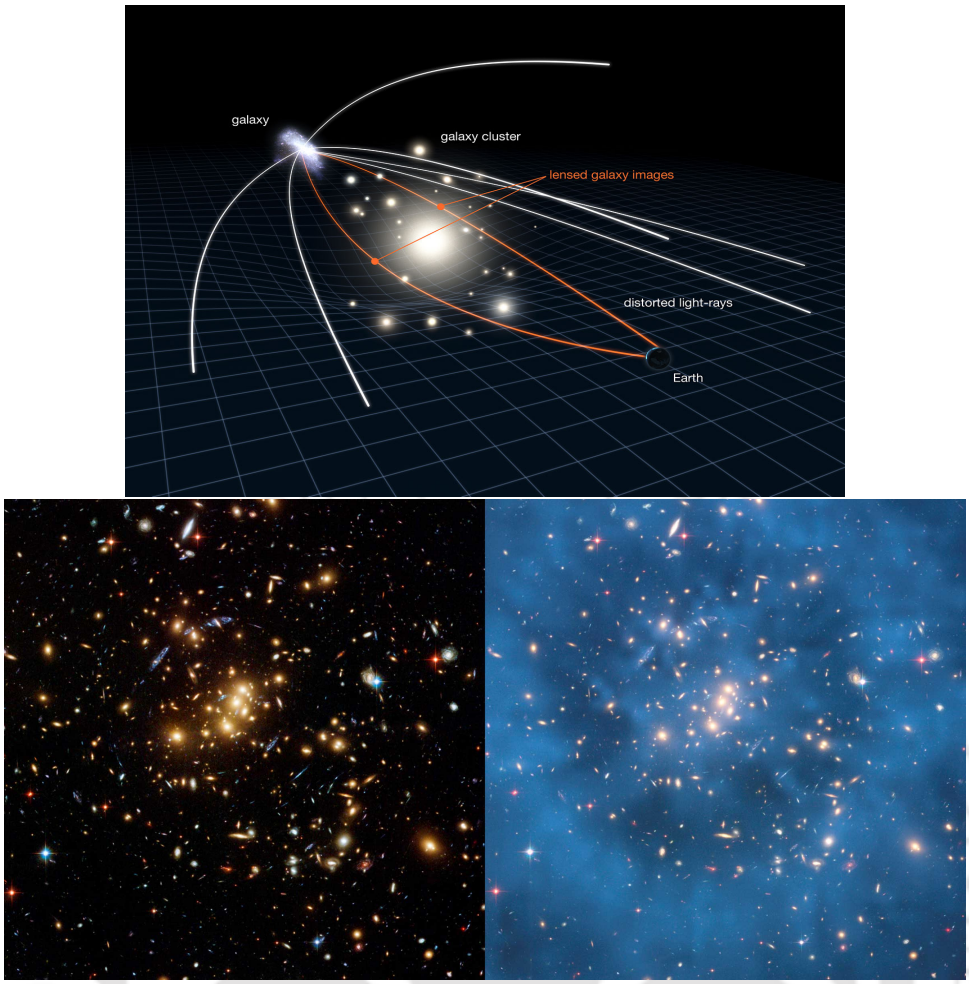


FIGURE 1.2: *Upper panel*: Schematic diagram illustrating the phenomena of gravitational lensing. Image credits: ESA/ NASA. *Bottom panel*: Hubble images of the massive galaxy cluster Cl 0024+17. The blue arcs on the left image are distorted images of galaxies behind the cluster. The blue shading has been added on the right image to indicate the location of dark matter. Image credits: NASA.

halos of the clusters pass straight through each other, shown by the blue regions in Fig. 1.3, which are mapped using gravitational lensing.

The existence of DM on cosmological scales is strongly evident from observations of the *Cosmic Microwave Background* (CMB) radiation, which are photons from the epoch of recombination when the first atoms were formed, at a temperature of around 0.3 eV. After recombination, photons decoupled from the thermal bath and have been traversing freely through the Universe, observed today as the CMB. Data from the Wilkinson Microwave Anisotropy Probe (WMAP) [12] and Planck 2018 [13] reveal the temperature of the CMB to be extraordinarily uniform, with a mean value $T \simeq 2.75$ K. However, there exist small

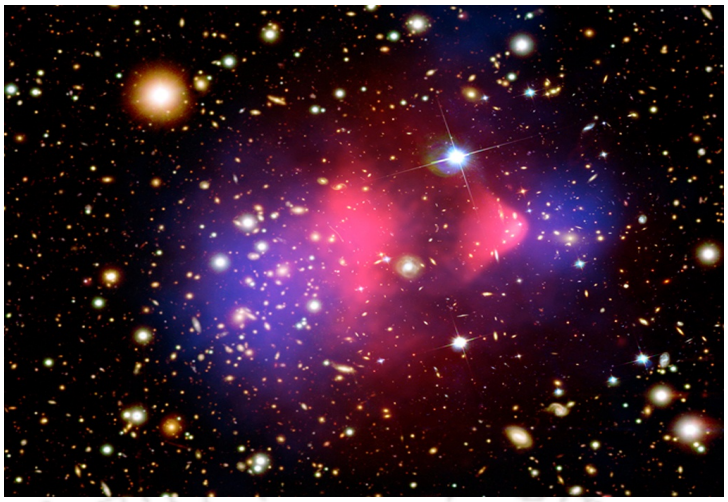

FIGURE 1.3: Image of the Bullet Cluster 1E0657-558, representing the collision of two galaxy clusters. The pink regions indicate the normal baryonic matter as observed by the Chandra X-ray observatory, whereas the blue regions indicate the dark matter inferred from gravitational lensing. The figure has been taken from Ref. [11].

temperature fluctuations in the CMB, which can be measured from the anisotropy power spectrum. The spectrum's shape depends on several cosmological parameters, one of them being the DM energy density. The current value of the DM energy density is conventionally denoted in terms of the quantity $\Omega_{\rm DM}h^2$, which is defined as

$$\Omega_{\rm DM}h^2 = \frac{\rho_{\rm DM,0}}{\rho_c}h^2\,, \tag{1.2}$$

where $\rho_{\rm DM,0}$ denotes the present DM energy density and $\rho_c$ is the critical energy density given by $\rho_c = 3M_P^2H_0^2$, Here, $H_0$ and $M_P$ represent the current Hubble parameter and the reduced Planck mass respectively, whereas $h = H_0/100$ km s$^{-1}$Mpc$^{-1}$. The left panel of Fig. 1.4 shows the CMB anisotropy spectrum with data from the Planck 2018 Collaboration (blue points). The different curves indicate the predictions with different values of the DM energy density defined in Eqn. (1.2). The present value of the DM relic density is reported as [14]

$$\Omega_{\rm DM}h^2 = 0.12 \pm 0.001\,, \tag{1.3}$$

at 68 % C.L. CMB thus predicts that DM contributes to $\sim$ 26 % of the total energy budget of the Universe, indicated by the pie chart in the right panel of Fig. 1.4. This is also supported by the Sloan Digital Sky Survey (SDSS) [15, 16]. Besides these, it is also established from N-body simulations [17] that DM is necessary for the formation of *large scale structures* from an initial homogeneous Universe.

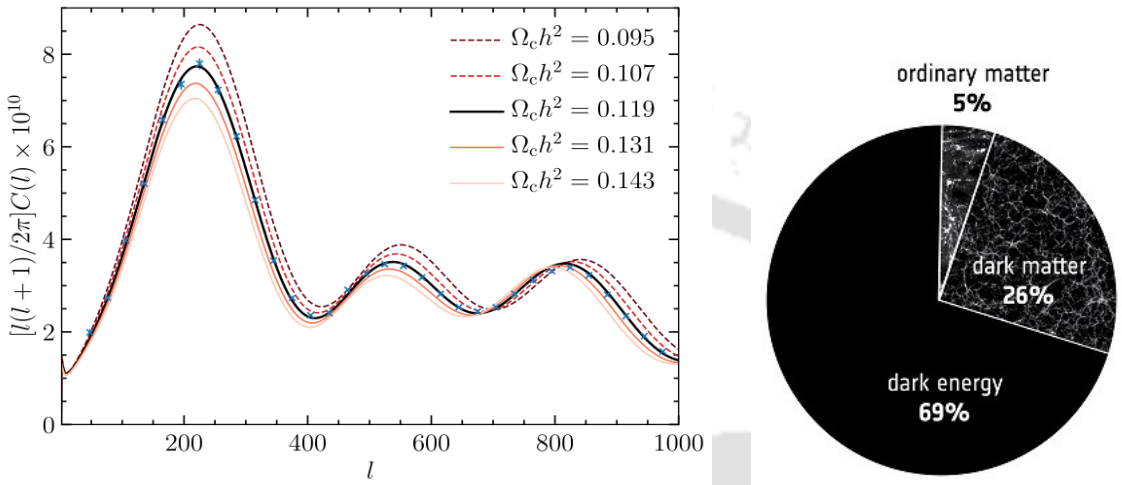


FIGURE 1.4: *Left panel*: CMB anisotropy spectrum for different values of the cold DM energy density (Eqn. (1.2)), indicated by $\Omega_c h^2$. The blue points are the data from Planck 2018. The figure has been taken from Ref. [18]. *Right panel*: A pie chart showing the cosmic energy budget, taken from ESA.

### 1.1.2 The DM landscape

The plethora of evidence discussed above clearly establishes the fact that our Universe contains dark matter at different scales. However, the identity of the particle nature of dark matter still remains an open question. Nevertheless, we can rule out many possibilities by the known properties of DM. First of all, the DM particle should be electrically neutral since it does not interact via electromagnetic interactions. It should be massive and stable on cosmological scales to be present in the current Universe with the observed abundance. These criteria rule out all the particles in the SM as potential candidates for DM except neutrinos which are electrically neutral and weakly interacting. However, being relativistic they have a large free streaming length and hence would be relativistic at the time of galaxy formation, which would hinder structure formation. In addition, the

neutrinos are also not abundant enough to produce the observed DM abundance. We can thus conclude that we need some particle beyond the SM (BSM) as a DM candidate.

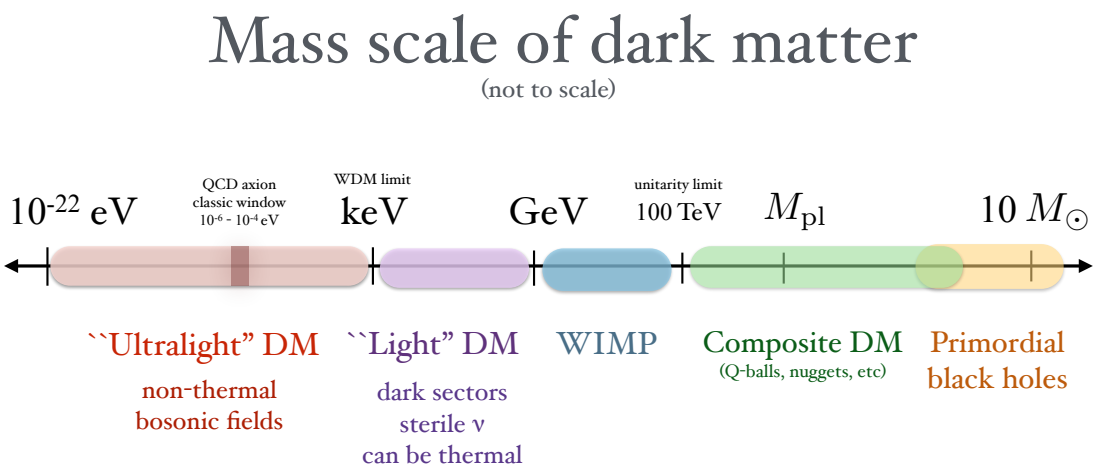


FIGURE 1.5: Landscape of possible DM candidates, along with their mass range. The figure is taken from Ref. [19].

Over the past few decades, physicists have proposed several ideas for potential DM candidates, which could be elementary particles, composite objects or Primordial Black Holes. Fig. 1.5 shows a landscape of the mass range of some of the DM candidates, which can be as light as $10^{-22}$ eV for ultralight bosonic DM or as heavy as a few solar masses for black holes. In this section, we discuss a few popular DM candidates which are motivating from a particle physics perspective and have been considered in this thesis.

#### 1.1.2.1 Thermal DM (WIMP)

The Weakly Interacting Massive Particle (WIMP) has been one of the most popular and leading candidates to explain dark matter. A recent review of WIMP can be found in Ref. [20]. Here, the interaction strength of the DM particle with the SM sector is considered such that DM can be in thermal equilibrium in the early Universe. As the Universe expands, the interaction rate of DM becomes less than the expansion rate of the Universe at some epoch, after which the DM particles decouple from the thermal bath of SM particles. The number of DM particles then reaches an asymptotically constant value. This phenomenon is commonly known as the *'freeze-out'* mechanism. In order to track the

number density of the DM particles and find their freeze-out abundance, one needs to solve the Boltzmann equation for the DM number density $n_{\rm DM}$. Considering the process $\mathrm{DM(p)} + \mathrm{DM(p')} \leftrightarrow \mathrm{SM(q)} + \mathrm{SM(q')}$, where $p$, $p'$, $q$, $q'$ denote the corresponding momenta, the Boltzmann equation is given by [18, 21]

$$\dot{n}_{\rm DM} + 3Hn_{\rm DM} = -\int \frac{g_{\rm DM}d^3p}{(2\pi)^3 2E_p}\frac{g_{\rm DM}d^3p'}{(2\pi)^3 2E_{p'}}\frac{g_{\rm SM}d^3q}{(2\pi)^3 2E_q}\frac{g_{\rm SM}d^3q'}{(2\pi)^3 2E_{q'}} \times (2\pi)^4\delta^4(p+p'-q-q') \times \mid \mathcal{M}_{\rm DM\,DM\to SM\,SM} \mid^2 (f_{\rm DM}f_{\rm DM} - f^{\rm eq}_{\rm DM}f^{\rm eq}_{\rm DM}), \tag{1.4}$$

where dot denotes derivative w.r.t. time. $g_i, E_i$ represents the internal degrees of freedom and energy respectively of the species '$i$'. $\mathcal{M}_{\rm DM\,DM\to SM\,SM}$ is the amplitude for the process DM + DM $\to$ SM + SM. The phase space density $f_{\rm DM}$ and the number density $n_{\rm DM}$ are related as

$$n_{\rm DM} = \int \frac{g_{\rm DM}d^3p}{(2\pi)^3} f_{\rm DM}. \tag{1.5}$$

The equilibrium phase space density can be assumed to follow the Boltzmann distribution, $f^{\rm eq}_{\rm DM} = e^{-E_{\rm DM}/T}$. Eqn. (1.4) can be simplified and written in terms of the thermally averaged cross-section $\langle\sigma v\rangle$ as

$$\dot{n}_{\rm DM} = -3Hn_{\rm DM} - \langle\sigma v\rangle(n^2_{\rm DM} - {n^{\rm eq}_{\rm DM}}^2), \tag{1.6}$$

where [22]

$$\langle\sigma v\rangle = \frac{g^2_{\rm DM}}{8m^4_{\rm DM}TK^2_2(\frac{m_{\rm DM}}{T})}\int_{s_0}^{\infty}\sigma\sqrt{s}(s-4m^2_{\rm DM})K_1(\frac{\sqrt{s}}{T})ds\,. \tag{1.7}$$

The above integration is over the square of the center of mass energy '$s$' of the system, with $s_0 = 4m^2_{\rm DM}$ being the threshold energy for the process. $K_i$'s represent the modified Bessel functions of order $i$ and $\sigma$ is the annihilation cross-section of the process

$\mathrm{DM} + \mathrm{DM} \rightarrow \mathrm{SM} + \mathrm{SM}$. The equilibrium number density $n_{\mathrm{DM}}$ is found to be

$$n_{\mathrm{DM}}^{\mathrm{eq}} = \frac{g_{\mathrm{DM}} T^3}{2\pi^2} \left(\frac{m_{\mathrm{DM}}}{T}\right)^2 K_2(m_{\mathrm{DM}}/T). \tag{1.8}$$

Now, the first term on the R.H.S. of Eqn. (1.6) implies the dilution of the DM number density because of the expansion of the Universe, whereas the second term represents the collision term which indicates the interaction rate of DM with the SM bath. It is convenient to rewrite the Boltzmann equation for the DM number density in terms of comoving coordinates such that the dilution due to the Universe expansion cancels out. Such coordinates can be $Y_{\mathrm{DM}} = n_{\mathrm{DM}}/s$, $N_{\mathrm{DM}} = n_{\mathrm{DM}} a^3$ etc. Here, '$a$' denotes the scale factor and '$s$' represents the entropy density which can be written as

$$s = \frac{2\pi^2}{45} g_{*s}(T) T^3. \tag{1.9}$$

$g_{*s}(T)$ represents the total entropy degrees of freedom at temperature T and is given by

$$g_{*s}(T) = \sum a_i g_i \left(\frac{T_i}{T}\right)^3, \tag{1.10}$$

where the summation is over all the species of particles in the thermal bath. $g_i$ denotes the number of internal degrees of freedom of the species having temperature $T_i$, whereas $a_i = 1$ and $7/8$ for bosons and fermions respectively. In terms of $Y_{\mathrm{DM}}$, Eqn. (1.6) simplifies into[1]

$$\frac{dY_{\mathrm{DM}}}{dx} = -\frac{xs\langle\sigma v\rangle}{H(m_{\mathrm{DM}})}(Y_{\mathrm{DM}}^2 - {Y_{\mathrm{DM}}^{\mathrm{eq}}}^2), \tag{1.11}$$

where $x = m_{\mathrm{DM}}/T$ and

$$H(m_{\mathrm{DM}}) = 1.66\sqrt{g_\star(T)}\frac{m_{\mathrm{DM}}^2}{M_P}. \tag{1.12}$$

[1]Here, the variation of $g_{*s}$ with temperature is assumed to be small, considering which slightly changes Eqn. (1.11) (see Ref. [23]).

$g_\star(T)$ represents the total relativistic degrees of freedom at temperature T and is given by

$$g_\star(T) = \sum a_i g_i \left(\frac{T_i}{T}\right)^4. \tag{1.13}$$

In Fig. 1.6, the evolution of the comoving number density of DM is shown, along with the equilibrium density, for different values of interaction cross sections $\langle\sigma v\rangle$. As anticipated above, the DM number density initially follows the equilibrium distribution until an epoch after $T \sim m_{\rm DM}$, when it decouples from the equilibrium bath producing a freeze-out abundance. Increasing $\langle\sigma v\rangle$ keeps the DM in equilibrium longer, thus decreasing the final abundance as shown.

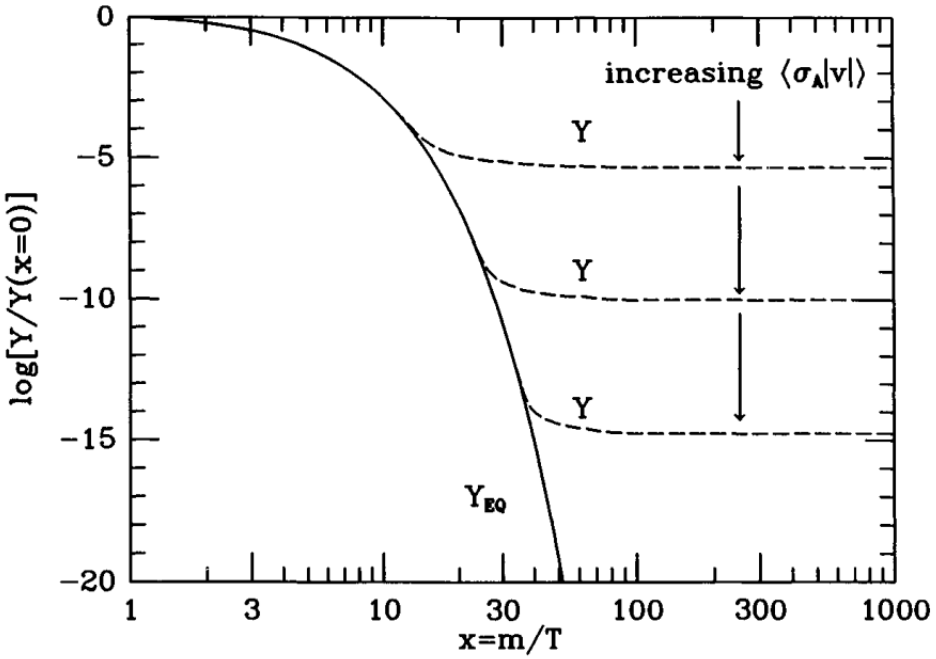


FIGURE 1.6: Evolution of the comoving number density of DM (dashed lines) for different values of $\langle\sigma v\rangle$, along with the equilibrium number density (solid line). The figure has been taken from Ref. [21].

In order to find an analytical estimate of the freeze-out abundance, we can recast Eqn. (1.11) in terms of the quantity $\lambda$ defined as [18, 21, 24]

$$\lambda = \frac{2\pi^2}{45} g_{*s} \frac{m_{\rm DM}^3 \langle\sigma v\rangle}{H(m_{\rm DM})}. \tag{1.14}$$

This gives

$$\frac{dY_{\rm DM}}{dx} = -\frac{\lambda}{x^2}(Y_{\rm DM}^2 - Y_{\rm DM}^{\rm eq\ 2}). \tag{1.15}$$

Now, at late times $Y_{\rm DM}$ is much larger than $Y_{\rm DM}^{\rm eq}$, the latter being Boltzmann-suppressed. Thus, below the temperature $T_f$ when the DM energy density starts to freeze-out, we have

$$\frac{dY_{\rm DM}}{dx} = -\frac{\lambda}{x^2}Y_{\rm DM}^2\,, \text{ for } x > x_f = m_{\rm DM}/T_f. \tag{1.16}$$

Integrating from $x = x_f$ to $x = \infty$ gives us the DM freeze-out abundance as

$$Y_{\rm DM}(x=\infty) = Y_{DM}^{\infty} \simeq \frac{x_f}{\lambda}, \tag{1.17}$$

where we have assumed $Y_{\rm DM}(x = x_f) \gg Y_{\rm DM}^{\infty}$.

This freeze-out abundance can be related to the dark matter relic density today. We have

$$\Omega_{\rm DM} = \frac{\rho_{\rm DM,0}}{\rho_{\rm c,0}} = \frac{m_{\rm DM}Y_{\rm DM,0}s_0}{3M_P^2H_0^2} = \frac{m_{\rm DM}Y_{\rm DM}^{\infty}s_0}{3M_P^2H_0^2}\,, \tag{1.18}$$

where '0' indicates the present values of the quantities. Using Eqn. (1.17), (1.14) and substituting the measured values of $T_0$ and $H_0$ finally gives us

$$\Omega_{\rm DM}h^2 \sim 0.1\left(\frac{x_f}{\sqrt{g_\star(m_{\rm DM})}}\right)\frac{10^{-8}\ {\rm GeV}^{-2}}{\langle\sigma v\rangle}. \tag{1.19}$$

'$x_f$' usually lies around 10 to 30. Thus, we see that the observed DM relic density can be produced with cross-sections around $10^{-8}$ GeV$^{-2}$, which are characteristics of weak interactions. This is known popularly as the *WIMP miracle*, which is a very positive aspect from a particle physics viewpoint since there are several theories/models that consist of particles with cross-sections in such a ballpark.

**Relativistic freeze-out:** Depending on the mass and interaction strength of the DM

particle, it might also decouple while it is still relativistic, i.e. $x \ll 1$. Such thermal DM candidates are known as *warm dark matter*. In such a scenario, the freeze-out abundance is simple to calculate and is given by just the equilibrium abundance at the time of decoupling.

$$Y_{\rm DM}^{\infty} = Y_{\rm DM}^{\rm eq} = 0.278 \frac{g_{\rm DM}}{g_{*s}(x_f)}. \tag{1.20}$$

The DM relic density then comes out to be [21]

$$\Omega_{\rm DM} h^2 = 7.83 \times 10^{-2} \frac{g_{\rm DM}}{g_{*s}(x_f)} \left(\frac{m_{\rm DM}}{\rm eV}\right). \tag{1.21}$$

Now, thermal DM masses below $\mathcal{O}(\text{keV})$ lead to damping of the matter power spectrum at small scales and are constrained from the Lyman-$\alpha$ forest [25–27]. Hence, we can see from Eqn. (1.21) that even with very high decoupling temperature, or with large extra relativistic degrees of freedom beyond SM, one would have an overabundance of DM relic density.

#### 1.1.2.2 Non-thermal DM (FIMP)

If the interaction strength of DM with the SM sector is very weak, then DM cannot be in thermal equilibrium in the early Universe. This happens if the couplings between DM and SM, parametrized in terms of a dimensionless parameter, are typically less than around $10^{-7}$ [28]. In such a scenario, DM cannot be produced by the freeze-out mechanism discussed above, and hence should have been formed through some non-thermal route. One such possibility is the production from particles in the thermal bath through decays or scatterings. This happens until the number density of the SM particles becomes Boltzmann-supressed, thus ending the yield. The comoving number density then reaches a constant value and the dark matter abundance is said to *freeze in* [28, 29]. Such types of DM are known as Feebly Interacting Massive Particle (FIMP). In order to track the evolution of the DM number density, we need to solve its Boltzmann equation, which can be

written, in terms of the comoving coordinate as [29]

$$\frac{dY_{\rm DM}}{dx} = 2\frac{\Gamma_{\rm SM\to DM\,DM}}{Hx}\frac{K_1(x)}{K_2(x)}Y^{\rm eq}_{\rm SM}, \tag{1.22}$$

where we have considered DM to be produced from the decay of SM particle in the bath with decay rate denoted by $\Gamma_{\rm SM\to DM\,DM}$. The evolution of the comoving DM number density is shown in Fig. 1.7, for different values of the decay rate. Here, in contrast to the freeze-out scenario, increasing the interaction strength, which is determined by $\Gamma$, increases the DM freeze-in abundance.

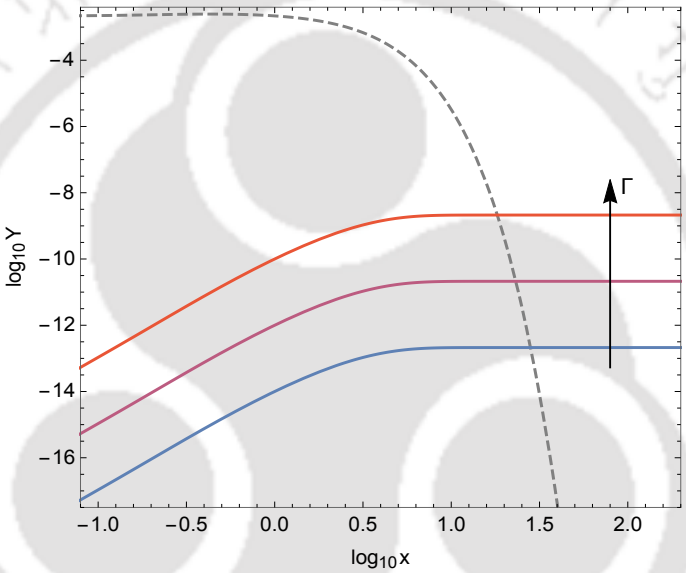


FIGURE 1.7: Evolution of the comoving number density of DM for different values of the interaction rate $\Gamma$. The figure has been taken from Ref. [29].

## 1.2 Baryon Asymmetry

### 1.2.1 Observational evidences

If we look around us, it's clear that we are surrounded by matter and anti-matter is very rare. We see anti-matter mostly in cosmic rays in the form of anti-protons with an abundance of $\mathcal{O}(10^{-4})$ times less than that of protons [30]. It can also be produced on earth

at various laboratories such as CERN and Fermilab. Even on larger scales, there are indications of matter-antimatter asymmetry. This is from the fact that in nearby clusters, galaxies containing matter would annihilate with ones containing anti-matter producing $\gamma$-rays. The absence of such $\gamma$-ray flux suggests that the cluster consists entirely of baryons. A review regarding the absence of large amounts of antimatter in our Universe can be found in Ref. [31]. In a baryon symmetric Universe, annihilations of nucleons and anti-nucleons would remain in thermal equilibrium upto a temperature of around 22 MeV, when $n_B/s = n_{\bar{B}}/s \simeq 7 \times 10^{-20}$ [21], where $n_B$ ($n_{\bar{B}}$) denotes the baryon (anti-baryon) number density and $s$ is the entropy density. In order to produce the correct observed abundance of baryons, some contrived mechanisms must have existed at higher temperatures ($T \gtrsim 38$ MeV [21]), separating nucleons and anti-nucleons far apart. Thus, the most natural conclusion is that the early Universe started with an asymmetry between baryons and anti-baryons, with the excess baryons surviving the 'annihilation catastrophe'. The baryon asymmetry is conventionally denoted in terms of the baryon-to-photon ratio $\eta_B$ defined as

$$\eta_B = \frac{n_B - n_{\bar{B}}}{n_\gamma}, \tag{1.23}$$

where $n_\gamma$ is the number density of photons given by $n_\gamma = \frac{2\zeta(3)}{\pi^2} T^3$. It is related to the baryonic yield

$$Y_B = \frac{n_B - n_{\bar{B}}}{s} \tag{1.24}$$

as $\eta_B = 7.05\, Y_B$, in the present Universe.

Now, the measurement of the quantity $\eta_B$ is based on two independent indirect probes of the early Universe. One of them is related to the epoch of Big Bang Nucleosynthesis (BBN) when protons and neutrons first combined to form the light elements like $D, {}^3H, {}^3\mathrm{He}, {}^4\mathrm{He}, {}^7\mathrm{Li}$, a few minutes after the Big Bang singularity. This happens through a chain of nuclear reactions, starting with $n + p \leftrightarrow D\gamma$. The main reactions are shown in the left panel of Fig. 1.8. The primordial abundances of these light elements calculated

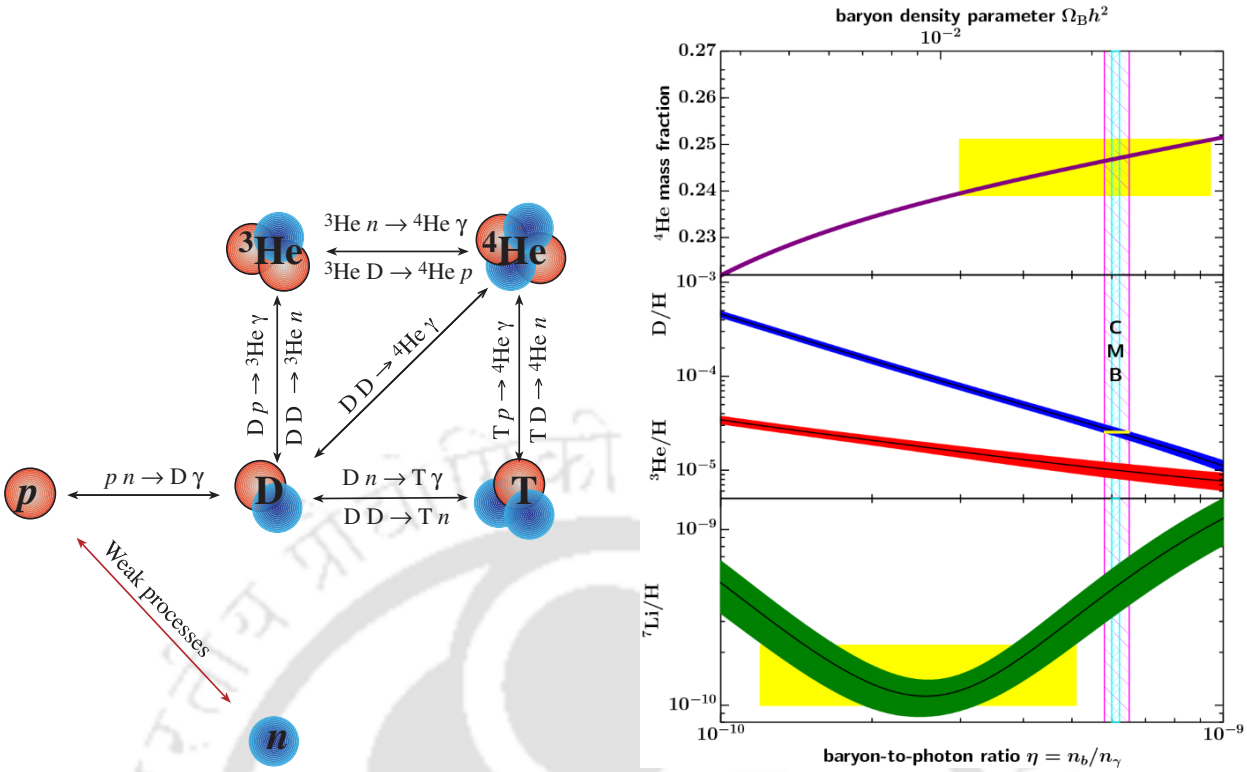


FIGURE 1.8: *Left panel*: A schematic diagram from Ref. [32], showing the major nuclear reactions taking place during BBN. *Right panel*: Contours showing the BBN predictions for abundances of light elements as a function of $\eta_B$. The yellow boxes indicate the astrophysical observations. The vertical narrow band represents the predicted value from CMB at 95 % CL, while the wider band denotes the BBN concordance range at 95 % CL. The figure has been taken from Ref. [33].

from the BBN theory depend crucially on the parameter $\eta_B$. For example, the presence of excess photons over baryons keeps the reaction $n + p \leftrightarrow D\gamma$ in thermal equilibrium up to a much later temperature of $T \approx B/|ln(\eta_B)|$ than the Deuterium binding energy $B \sim 2$ MeV [32]. In the right panel of Fig. 1.8, the predictions of BBN calculations for the primordial abundances of the light elements are shown as a function of $\eta_B$. Observationally, the abundances of these light elements are from astrophysical sites with lower contents of other heavier “metal" elements such as C, N, O, Fe. These observed abundances are indicated by the yellow boxes.

The other measurement of the quantity $\eta_B$ is from the anisotropy power spectrum of the CMB [14], discussed in Section 1.1.1. The shape of the spectrum depends on the amount of baryonic content of the Universe. The blue-shaded vertical band in the right

panel of Fig. 1.8 denotes the value of $\eta_B$ measured from CMB, which is in excellent agreement with the prediction of BBN. The current best-fit value of $\eta_B$ is reported as [14]

$$\eta_B = 6.1 \times 10^{-10}\,. \tag{1.25}$$

### 1.2.2 Sakharov's conditions

An initial baryon asymmetry would get diluted because of cosmic inflation, when the Universe underwent a rapid accelerated expansion [34–36]. Considering an initial baryon symmetric Universe after inflation, the observed asymmetry needs to be generated dynamically through some mechanism. In 1967, A. Sakharov realized that three conditions need to be satisfied in order to dynamically generate the asymmetry [37]. These are discussed below:

(1) **Baryon Number violation**: Baryon Number (B) violation is obvious for the generation of an asymmetry since if all interactions conserve B, no net asymmetry in the number of baryons could have been generated.

(2) **C and CP violation**: Let us consider a baryon number violating process $X \to A + B$, where $B$ carries some baryon number, whereas X and A do not. If charge-conjugation (C) is a symmetry, then the rate of this process is the same as its C-conjugate process $\bar{X} \to \bar{A} + \bar{B}$. Thus, there is no net baryon number production, unless there exists C violation.

In addition to C, charge conjugation-parity (CP) must also be violated. To understand this, let us consider a B-violating process like $X \to q_L + q_L$ and $X \to q_R + q_R$, where $q_L$, $q_R$ are the left-handed and right-handed quarks respectively and X does not carry baryon number. Now, even if C violation would imply the rate $\Gamma(X \to q_{L,R} + q_{L,R}) \neq \Gamma(\bar{X} \to \bar{q}_{L,R} + \bar{q}_{L,R})$, if CP is conserved, we would have $\Gamma(X \to q_{L,R} + q_{L,R}) = \Gamma(\bar{X} \to \bar{q}_{R,L} + \bar{q}_{R,L})$. Thus,

$$\Gamma(X \to q_L + q_L) + \Gamma(X \to q_R + q_R) = \Gamma(\bar{X} \to \bar{q}_R + \bar{q}_R) + \Gamma(\bar{X} \to \bar{q}_L + \bar{q}_L)\,, \tag{1.26}$$

giving rise to no net baryon asymmetry.

(3) **Departure from thermal equilibrium**: Considering again the process $X \to A + B$, if it is in thermal equilibrium, then the rate of the inverse process $A + B \to X$ would also be the same. Thus, B created would be destroyed at the same rate, leading to no net baryon asymmetry.

In SM, baryon and lepton number ($L$) are violated by non-perturbative processes known as sphalerons [38, 39], which however conserve the linear combination $B - L$. The out-of-equilibrium condition can be satisfied in the SM if the electroweak phase transition is of first order which requires the Higgs mass $M_H \lesssim 50$ GeV [40–42], which is experimentally ruled out. CP violation is provided in the SM by the CKM phase of the quark sector. However, being suppressed by the small quark masses, it is too small to generate the observed baryon asymmetry [43, 44]. In essence, SM fails to produce the observed baryon asymmetry.

There have been many extensions of the SM, trying to explain the observed baryon asymmetry, some of the popular ones being GUT baryogenesis, electroweak baryogenesis, Affleck-dine mechanism and leptogenesis. GUT theories are an attempt to unify the strong, electromagnetic and weak interactions under a single gauge group such as $SU(5)$ [45], $SO(10)$ [46]. Such theories naturally lead to heavy particles which can decay in the early Universe satisfying Sakharov's conditions, and producing the observed baryon asymmetry. However, GUT theories of baryogenesis suffer from many drawbacks, which have ruled out most of them. First of all, they typically predict the masses of the decaying scalar or gauge bosons to be very heavy ($\gtrsim 10^{15}$ GeV) in order to avoid proton decay. Measurements from CMB put an upper bound on the inflationary scale [47], which in turn predicts a lower reheating temperature $\lesssim 10^{13}$ GeV, below the GUT scale. Hence, the thermal production of baryon number is suppressed. Another significant challenge is the role of the sphaleron processes which tend to wash out the net $B + L$ number [48], so unless there exists some $B - L$ violating interactions, absent in many GUT models, the asymmetry almost vanishes. On the other hand, typical models of electroweak baryogenesis require light particles, which have tight constraints from colliders [49–51]. In view

of these drawbacks, generating the baryon asymmetry through the Affleck-dine mechanism or through leptogenesis has gained more popularity over the last few years. In the Affleck-dine mechanism [52], the coherent motion of a scalar field typically plays the role in generating the baryon asymmetry. In this thesis, we mostly focus on baryogenesis through leptogenesis, which we elaborate upon below.

### 1.2.3 Leptogenesis

Leptogenesis [53] has been one of the most popular mechanisms to generate the baryon asymmetry of the Universe. Here, as the name suggests, the asymmetry is first created in the lepton sector, which later gets converted into baryon asymmetry through non-perturbative sphaleron processes at the electroweak scale. The added advantage of the leptogenesis setup is that it can be closely connected to the origin of tiny neutrino mass, which the SM of particle physics fails to explain. The mechanism can be embedded in the Type-I seesaw framework [54–58], where the SM is extended by three right-handed neutrinos (RHN) $N_R$, with the following gauge-invariant Lagrangian:

$$-\mathcal{L}_\nu = Y_\nu \overline{l_L}\tilde{\mathbf{H}} N_R + \frac{1}{2} M_R \overline{N_R^c} N_R + h.c.\,, \tag{1.27}$$

where $l_L$, $\mathbf{H}$ denotes the SM lepton doublet and Higgs field respectively, and $\tilde{\mathbf{H}} = i\sigma_2 \mathbf{H}^*$, $\sigma_2$ being the Pauli matrix. The second term in the above Lagrangian is the Majorana mass term, which is the source of lepton-number violation. After the electroweak symmetry breaking, the Dirac mass matrix can be written as $m_D = Y_\nu v/\sqrt{2}$, where $v \approx 246$ GeV. Assuming $m_D \ll M_R$, the Majorana mass matrix for the three light SM neutrinos is given by $m_\nu \simeq -m_D^T\, M_R^{-1}\, m_D$. To obtain sub-eV SM neutrino mass, one requires $M_R \sim \mathcal{O}(10^{14})$ GeV, with $Y_\nu \sim \mathcal{O}(1)$.

The RHNs can be in thermal equilibrium at a higher temperature. Now, because of the Majorana condition $N_i = N_i^c$, the lepton number violating out-of-equilibrium decays $N_i \to l_\alpha + \mathbf{H}$ and $N_i \to \overline{l_\alpha} + \overline{\mathbf{H}}$ would take place when $T \lesssim M_i$, where $N_i$ represents the mass eigenstates with mass $M_i$ (i=1,2,3) and $\alpha = e, \mu, \tau$. The CP-asymmetry parameter is

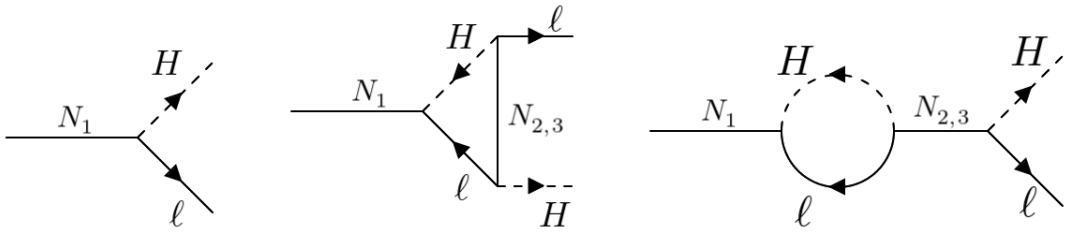


FIGURE 1.9: Feynman diagrams for RHN ($N_1$) decay to Higgs ($H$) and leptons ($l$), which contribute to the CP asymmetry given by Eqn. (1.29), which has contribution from the interference of the tree-level diagram with the vertex diagram (middle) and the self-energy diagram (right) at one-loop level.

defined as

$$\epsilon_{i\alpha} = \frac{\Gamma(N_i \to l_\alpha + \mathbf{H}) - \Gamma(N_i \to \overline{l_\alpha} + \overline{\mathbf{H}})}{\Gamma(N_i \to l_\alpha + \mathbf{H}) + \Gamma(N_i \to \overline{l_\alpha} + \overline{\mathbf{H}})}, \tag{1.28}$$

where $\Gamma$ represents the decay rate. Considering only the tree-level decay rate, $\epsilon_{i\alpha} = 0$. However, taking the interference of the tree-level and the loop-level decay rate leads to non-zero values of CP asymmetry, in the presence of complex Yukawa couplings $Y_\nu$. The relevant diagrams contributing to the CP-violating decay rate are shown in Fig. 1.9, which produces the CP asymmetry value to be [53, 59–64]

$$\epsilon_{i\alpha} = \frac{1}{8\pi (Y_\nu^\dagger Y_\nu)_{ii}} \sum_{j \neq i} \left[ \mathcal{F}\left(\frac{M_j^2}{M_i^2}\right) \mathrm{Im}[(Y_\nu^*)_{\alpha i} (Y_\nu)_{\alpha j} (Y_\nu^\dagger Y_\nu)_{ij}] + \mathcal{G}\left(\frac{M_j^2}{M_i^2}\right) \mathrm{Im}[(Y_\nu^*)_{\alpha i} (Y_\nu)_{\alpha j} (Y_\nu^\dagger Y_\nu)^*_{ij}] \right], \tag{1.29}$$

where $\mathcal{F}(x)$ and $\mathcal{G}(x)$ are the loop functions defined as

$$\mathcal{F}(x) = \sqrt{x}\left[1 + \frac{1}{1-x} + (1+x)\ln\left(\frac{x}{1+x}\right)\right], \tag{1.30}$$

$$\mathcal{G}(x) = \frac{1}{1-x}. \tag{1.31}$$

Ignoring the effect of lepton flavors [65–68], Eqn. (1.29) simplifies into

$$\epsilon_i = \sum_\alpha \epsilon_{i\alpha} = \frac{1}{8\pi (Y_\nu^\dagger Y_\nu)_{ii}} \sum_{j\neq i} \mathcal{F}\left(\frac{M_j^2}{M_i^2}\right) \mathrm{Im}[(Y_\nu^\dagger Y_\nu)_{ij}^2]. \tag{1.32}$$

These CP-violating out-of-equilibrium decays of the RHNs generate a net lepton asymmetry, with number density $n_L = n_l - n_{\bar{l}}$, which is proportional to the CP-asymmetry parameter $\epsilon_{i\alpha}$. The number density of leptons can also get modified due to other *washout* processes which tend to decrease the asymmetry. These include [64, 69, 70] (a) inverse decays; (b) $\Delta L = 1$ scatterings: $N_i + l_\alpha(\bar{l}_\alpha) \leftrightarrow q(\bar{q}) + \bar{u}(u)$, $N_i + u(\bar{u}) \leftrightarrow \bar{l}_\alpha(l_\alpha) + q(\bar{q})$, $N_i + l_\alpha \leftrightarrow \overline{\mathbf{H}} + V_\mu, N_i + V_\mu \leftrightarrow l_\alpha + \overline{\mathbf{H}}, N_i + \overline{\mathbf{H}} \leftrightarrow l_\alpha + V_\mu$, where $q, u, V_\mu$ denotes quarks, up-type quarks and vector bosons respectively; (c) $\Delta L = 2$ scatterings: $l_\alpha + \mathbf{H} \leftrightarrow \bar{l}_\beta + \overline{\mathbf{H}}, l_\alpha(\bar{l}_\alpha) + l_\beta(\bar{l}_\beta) \leftrightarrow \overline{\mathbf{H}} + \overline{\mathbf{H}}$.

For a hierarchical RHN mass spectrum $M_3 \gg M_2 \gg M_1$, the asymmetry generated by the heavier RHNs $M_{2,3}$ are usually washed out. Hence, we consider only the lightest RHN $N_1$ for our analysis. Now, in order to calculate the net lepton asymmetry, one needs to solve the Boltzmann equations for the number density of RHNs and the lepton/ $B-L$ asymmetry. In terms of the comoving coordinates $N_i = n_i/n_\gamma$, where $n_\gamma$ denotes the number density of photons, the relevant equations are given by [70]

$$\frac{dN_{N_1}}{dz} = -(D+S)\left(N_{N_1} - N_{N_1}^{\mathrm{eq}}\right), \tag{1.33}$$

$$\frac{dN_{B-L}}{dz} = -\epsilon_1 D\left(N_{N_1} - N_{N_1}^{\mathrm{eq}}\right) - W N_{B-L}, \tag{1.34}$$

where $z = M_1/T$. Here, $(D, S, W) = (\Gamma_D, \Gamma_S, \Gamma_W)/Hz$. $\Gamma_D$ corresponds to the decay rate given by

$$\Gamma_D(z) = \frac{1}{8\pi}\left(Y_\nu^\dagger Y_\nu\right)_{11} M_1 \frac{K_1(z)}{K_2(z)}, \tag{1.35}$$

where the ratio of the Bessel functions accounts for the thermally-averaged dilation factor. The scattering rate of $N_1$ denoted by $\Gamma_S$ is mediated by Higgs field $\mathbf{H}$ in s and t

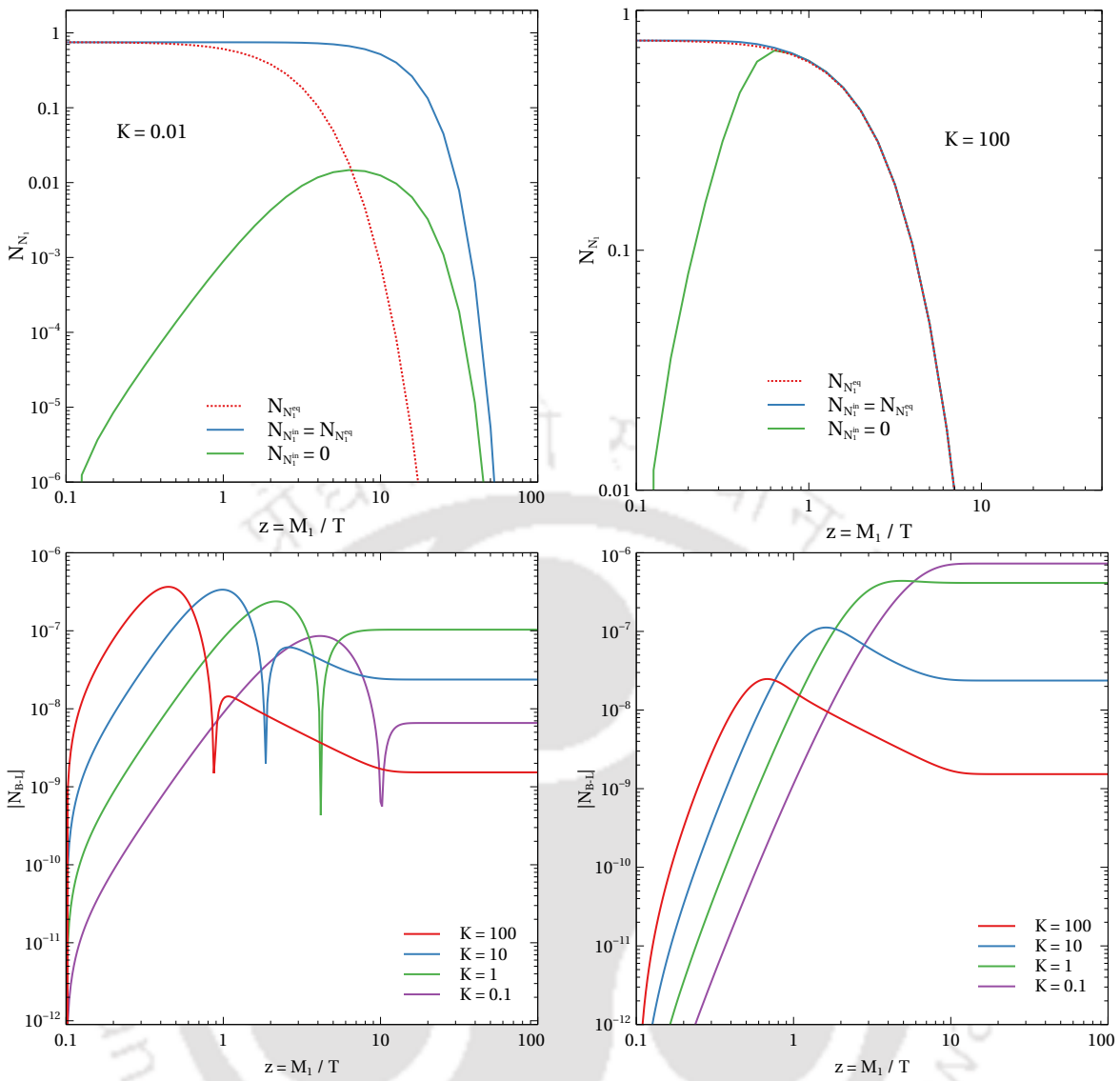


FIGURE 1.10: *Upper panel*: Evolution of the comoving number density of $N_1$, for weak washout with $K = 0.01$ (left) and strong washout with $K = 100$ (right). *Lower panel*: Evolution of the $B - L$ asymmetry for different values of decay parameters $K$, considering $N_{N_1}^{\text{in}} = 0$ (left) and $N_{N_1}^{\text{in}} = N_{N_1}^{\text{eq}}$ (right).

channels. The washout rate $\Gamma_W$ has contributions from the inverse decays and scatterings discussed above. The inverse decay rate can be written in terms of the decay rate as $\Gamma_{\text{ID}} = \Gamma_D(z)\frac{N_{N_1}^{\text{eq}}(z)}{N_1^{\text{eq}}(z)}$, which gives the washout term due to inverse decay $W_{\text{ID}}$ as

$$W_{\text{ID}}(z) = \frac{1}{4}Kz^3K_1(z). \tag{1.36}$$

$K$ denotes the decay parameter defined as

$$K = \frac{\Gamma_D(z=\infty)}{H(z=1)}. \tag{1.37}$$

The washout term due to inverse decay can be approximately written as [70]

$$W_{\rm ID}(z) \simeq \frac{1}{4} K z^2 \sqrt{1+\frac{\pi}{2}z}\, e^{-z} \tag{1.38}$$

which is in equilibrium when $W_{\rm ID}(z) \geq 1$. It can be easily seen from Eqn. (1.38) that $W_{\rm ID}(z)$ reaches a maximum value $\simeq 0.3$ K. Therefore, for $K > 3$, there exists an interval where the inverse decays can be in equilibrium. On the other hand, for $K < 3$, the inverse decays are always out of equilibrium. $K$ is thus a measure of the strength of the washout. $K \ll 1$ corresponds to the weak washout regime whereas $K \gg 1$ denotes strong washout. Considering only the decays and inverse decays for simplicity, the Boltzmann equations (1.33), (1.34) are solved numerically, and the evolution of $N_1$ and $N_{B-L}$ is shown in Fig. 1.10. The upper panel shows the evolution of $N_1$ considering weak washout with $K = 0.01$ (left) and strong washout with $K = 100$ (right). For weak washout, the decay of the RHNs occurs at a lower temperature, with smaller washout effects. The two solid curves correspond to two different initial conditions for $N_1$, one with an equilibrium initial abundance ($N_{N_1}^{\rm in} = N_{N_1}^{\rm eq}$), and the other with a vanishing initial abundance ($N_{N_1}^{\rm in} = 0$). For the latter case, the RHNs are produced from the inverse decays. For the case of $K \ll 1$, $N_1$ reaches the equilibrium abundance much later than the case of a strong washout where the $N_1$ abundance rises rapidly to reach equilibrium. The lower panel shows the evolution of the asymmetry $N_{\rm B-L}$ for different values of the decay parameter $K$, considering vanishing initial abundance (left panel) and equilibrium initial abundance (right panel). The final asymmetry decreases in the case of strong washouts, as expected. The kink in the left panel corresponds to the epoch when $N_1$ reaches equilibrium and the value of $N_{B-L}$ changes sign. It is important to note here that the inverse decays serve a dual purpose. Apart from leading to washout of the asymmetry, they are also important

to produce $N_1$ from a vanishing abundance. This explains the decrease in the final asymmetry in the bottom left panel of Fig. 1.10, for $K = 0.1$. Here, although we are in the weak washout regime, the initial production of $N_1$ itself is small, leading to lower value of the final $B - L$ asymmetry. This behavior is absent in the bottom right panel where $N_1$ is assumed to be in equilibrium from the start.

The $B - L$ conserving sphaleron processes convert the $B - L$ asymmetry into baryon asymmetry with a conversion factor which is given by [48] (see Appendix A)

$$N_{\rm B} = \frac{8N_f + 4N_{\mathbf{H}}}{22N_f + 13N_{\mathbf{H}}} N_{\rm B-L} = C_{\rm sph} N_{\rm B-L}\,, \tag{1.39}$$

which for the SM with $N_f = 3$ and $N_{\mathbf{H}} = 1$, gives $C_{\rm sph} = \frac{28}{79}$. The final baryon asymmetry $\eta_B$ can be analytically estimated to be [70]

$$\eta_B = \frac{C_{\rm sph}}{f} \epsilon_1 \kappa\,, \tag{1.40}$$

where the factor $f$ accounts for the change in the relativistic degrees of freedom from the scale of leptogenesis until recombination and comes out to be $f = \frac{106.75}{3.91} \simeq 27.3$. $\kappa$ is known as the efficiency factor which incorporates the effects of washout processes.

**Davidson-Ibarra bound:** The Dirac Yukawa matrix $Y_\nu$ can be parametrized using the Casas-Ibarra (CI) parametrisation [71] as,

$$Y_\nu = \frac{\sqrt{2}}{v} \sqrt{M_R}\, \mathbb{R}\, \sqrt{m_\nu^d}\, \mathcal{U}^\dagger\,, \tag{1.41}$$

where $\mathcal{U}$ represents the Pontecorvo-Maki-Nakagawa-Sakata (PMNS) leptonic mixing matrix [72], which in the diagonal charged lepton basis, can diagonalize the light neutrino mass matrix as

$$m_\nu = \mathcal{U}^* m_\nu^d \mathcal{U}^\dagger\,. \tag{1.42}$$

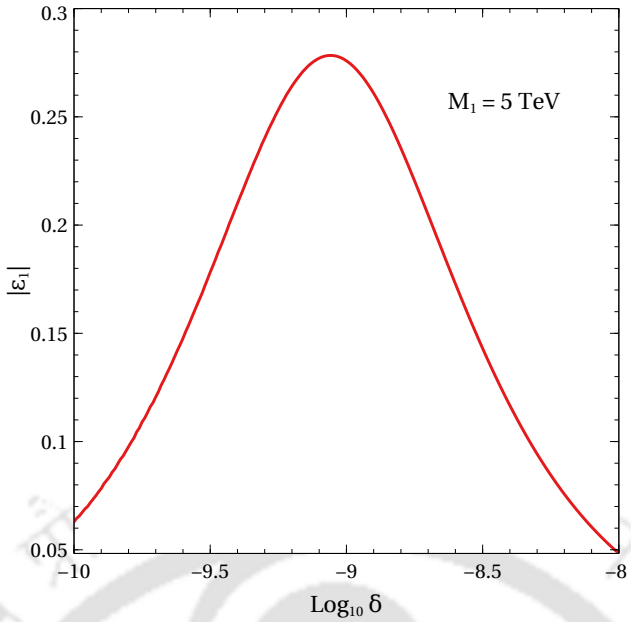


FIGURE 1.11: The CP asymmetry parameter $\epsilon_1$ (Eqn. (1.46)) as a function of the mass difference $\delta = |M_1 - M_2|$, for RHN mass $M_1 = 5$ TeV.

$m_\nu^d = \text{diag}(m_1, m_2, m_3)$ consists of the mass eigenvalues, where the $m_i$ are the light neutrino masses. $\mathbb{R}$ is a complex orthogonal matrix satisfying $\mathbb{R}^T\mathbb{R} = I$. Using this parameterization, the CP-asymmetry parameter $\epsilon_1$ (Eqn. (1.32)) can be written as [73]

$$|\epsilon_1| \simeq \frac{3}{8\pi}\frac{M_1}{v^2}\frac{\sum_i m_i^2 \text{Im}(\mathbb{R}_{1i}^2)}{\sum_i m_i |\mathbb{R}_{1i}|^2} \tag{1.43}$$

which using the orthogonality condition of $\mathbb{R}$ gives us

$$|\epsilon_1| \lesssim \frac{3}{8\pi}\frac{M_1}{v^2}(m_3 - m_1). \tag{1.44}$$

For hierarchical RHN mass spectra, we have

$$|\epsilon_1| \lesssim \frac{3}{8\pi}\frac{M_1}{v^2}m_3. \tag{1.45}$$

Using Eqn. (1.25) for the observed value of baryon asymmetry, and the upper bound on $m_3 \sim 0.05$ eV [33], the above upper bound on the CP asymmetry gives us a lower bound on the RHN mass scale as $M_1 \gtrsim 10^9$ GeV [73]. This bound can be relaxed by around $1-2$ orders if we include the effect of different lepton flavors [65–68]. In addition, if the RHNs

have degenerate mass, i.e. $M_1 \sim M_2$, the leptogenesis scale can be lowered upto the TeV scale, which we discuss below.

**Resonant leptogenesis:** In the case of degenerate RHN masses, the CP asymmetry parameter is calculated to be [62]

$$\epsilon_i = \frac{\mathrm{Im}[(Y_\nu^\dagger Y_\nu)^2_{ij}]}{(Y_\nu^\dagger Y_\nu)_{ii}(Y_\nu^\dagger Y_\nu)_{jj}} \frac{\Delta M^2_{ij} M_i \Gamma_j}{\left(\Delta M^2_{ij}\right)^2 + M_i^2 \Gamma_j^2}\,, \tag{1.46}$$

where $\Delta M^2_{ij} = M_i^2 - M_j^2$ and $\Gamma_j$ is the decay width given by

$$\Gamma_j = \frac{1}{8\pi}\left(Y_\nu^\dagger Y_\nu\right)_{jj} M_j\,. \tag{1.47}$$

The CP asymmetry parameter is significantly enhanced for $|M_i - M_j| = \Gamma_j/2$ and can reach upto $\mathcal{O}(1)$. In Fig. 1.11, we show $\epsilon_1$ as a function of $\delta = |M_1 - M_2|$, for RHN mass $M_1 = 5$ TeV. Considering $\mathcal{O}(1)$ Yukawa couplings, the decay rate $\Gamma_2 \simeq 10^{-9}$ GeV$^{-1}$. It is clear from the plot that $\epsilon_1$ maximizes at $\delta \simeq \Gamma_2/2$.

To summarize, in this chapter we have discussed some well-known mechanisms for producing dark matter and the baryon asymmetry of our Universe, focusing particularly on the ones relevant to this thesis. All these analyses are carried out assuming a standard cosmology, where the Universe begins with radiation domination after inflation. Since this thesis considers these mechanisms in the presence of a non-standard cosmological background, in the following chapter we provide an introduction to the non-standard cosmologies which have been considered for this thesis.

# Chapter 2

# Non-standard cosmologies

The Standard Cosmological Model of our Universe, based on the principles of general relativity, predicts a cosmic history, as shown in Fig. 2.1. It is evident from observations of redshift of distant galaxies that the Universe has been expanding starting from an initial hot, dense state. The energy components of the Universe (matter, radiation etc.) decide its expansion dynamics, as given by the Einstein's equation of general relativity. The Universe should be radiation-dominated at the epoch of BBN, in order to produce the light elements in the required amounts, at a temperature of $\mathcal{O}$(MeV). As the Universe keeps on expanding, the radiation energy density dilutes faster than that of matter, as a result of which matter starts to dominate the energy density of the Universe, at a temperature $\sim 0.75$ eV. Matter keeps on dominating leading to the formation of stars and galaxies, until the very recent dark energy domination. Although this standard cosmological picture has been quite transparent, the cosmic history before BBN is unknown and the Universe at such an early stage may be dominated by some other components with any equation of state. It is usually assumed that after reheating [74, 75], the Universe is always radiation-dominated up to the era of BBN. However, there are no experimental evidences to verify this. In fact, the reheating period itself could be prolonged leading to some non-standard cosmic eras before BBN [76–78].

There are various possible cosmic eras that could exist before BBN, which have been explored in the literature. These include early matter domination ($w = 0$), kination domination ($w = 1$), early dark energy domination ($w = -1$). '$w$' is the equation of state parameter which is defined as the ratio of pressure to the energy density of the background

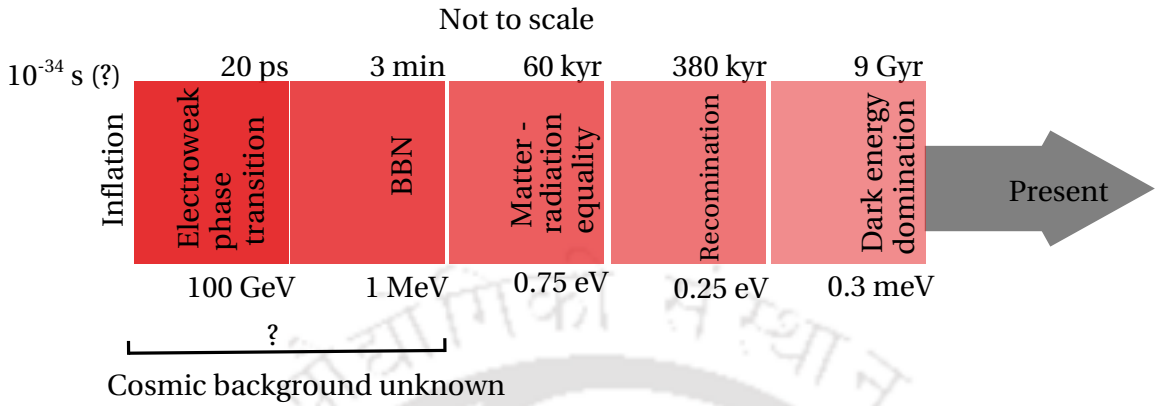


FIGURE 2.1: A schematic diagram showing the important phases in the evolution of our Universe.

component of the Universe. These possibilities can be motivated by different aspects and theories. A recent review of such non-standard cosmic epochs can be found in Ref. [79]. In this thesis, we focus on early matter domination (EMD) before BBN, since it can have close connections with well-motivated particle physics scenarios and is easier to realize in the early Universe. Now, such EMD eras can arise from different sources. We focus on two possible sources: (a) a long-lived non-relativistic particle, (b) Primordial Black Holes produced in the early Universe.

This chapter is organized as follows. In section 2.1, we discuss EMD arising from a long-lived particle. Section 2.2 discusses EMD due to PBH. After briefly describing some of the key concepts of PBH, we elaborate briefly on the phenomena of Hawking radiation in section 2.2.1. Next, in section 2.3 we dicuss about the impacts of EMD on gravitational waves generated in the early Universe, with some details of GW produced from cosmic strings in section 2.3.1 and PBH density fluctuations in section 2.3.2. Finally, in section 2.4, we describe the objective of this thesis.

## 2.1 Early matter-domination due to a long-lived particle

A non-relativistic particle (say $\phi$) in the early Universe behaves as matter with its energy density scaling as $\rho_\phi \propto a^{-3}$. In order for $\phi$ to dominate the energy density of the Universe over radiation, its initial energy density should be large enough. Also, it should have a lifetime large enough such that it does not decay before it could start dominating. This can be realized through tiny couplings of $\phi$ with SM particles. However, one should also ensure that the lifetime of $\phi$ is not very large, as it needs to decay before BBN to produce a radiation-dominated Universe. There could be many origins of the field $\phi$. It might be due to the oscillating inflaton field during reheating, or some decay products of the inflaton. It could be some scalar moduli field based on typical string theory models [80]. Another possibility is that $\phi$ freezes out from the thermal bath with some initial abundance set by its interactions with the thermal bath. It can then become long-lived and behave as non-relativistic matter, before it decays prior to BBN. We consider this last scenario for our purpose.

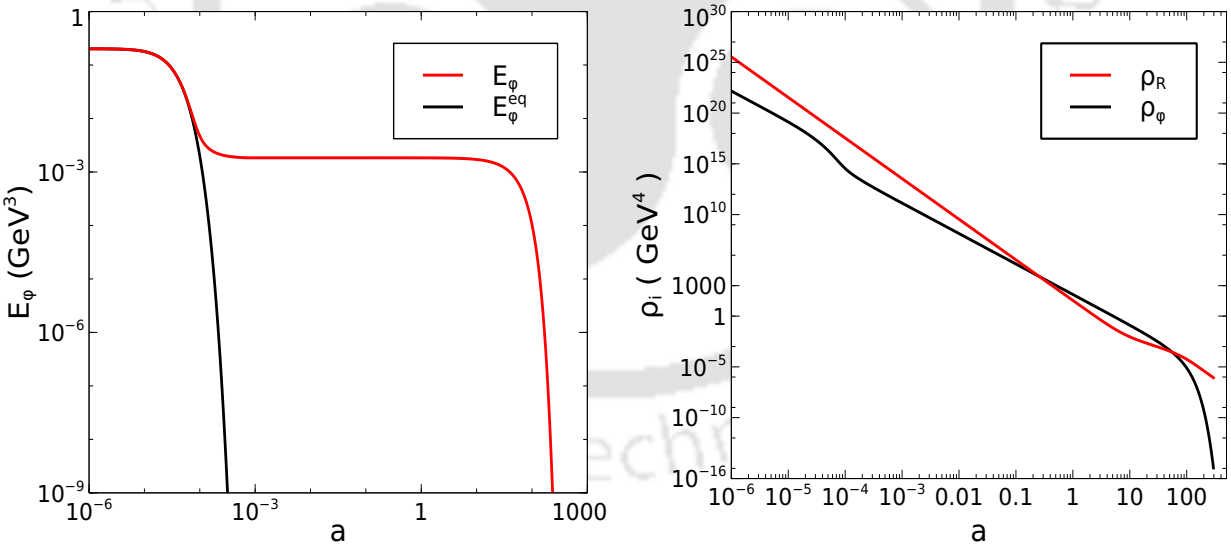


FIGURE 2.2: *Left panel*: Evolution of the comoving number density of $\phi$ along with the equilibrium number density. *Right panel*: Evolution of the energy density of SM radiation along with that of the long-lived $\phi$ field. The figure has been taken from Ref. [81].

Let us assume that $\phi$ has some interactions with the SM radiation bath characterized by the thermally averaged cross-section $\langle \sigma v \rangle$, which ensures that it is thermalised in the

early Universe. It then freezes out, after it becomes non-relativistic. $\phi$ decays later with a decay width given by $\Gamma_\phi$. The whole scenario can be tracked by solving the coupled Boltzmann equations for $n_\phi$ and entropy density $s$ (or equivalently the thermal bath temperature $T$). It is convenient to define the comoving coordinate $E_\phi = n_\phi a^3$, in terms of which the Boltzmann equation for the comoving number density of $\phi$ and the temperature evolution equation can be written as [82]

$$\frac{dE_\phi}{da} = \frac{\langle\sigma v\rangle}{Ha^4}\left((E_\phi^{\rm eq})^2 - E_\phi^2\right) - \frac{\Gamma_\phi}{Ha}E_\phi\,, \tag{2.1}$$

$$\frac{dT}{da} = \left(1 + \frac{T}{3g_{*s}}\frac{dg_{*s}}{dT}\right)^{-1}\left[-\frac{T}{a} + \frac{\Gamma_\phi M_\phi}{3H\,s\,a^4}E_\phi\right]. \tag{2.2}$$

Here, H denotes the Hubble parameter which at late times when $\phi$ acts as matter is given by $H = \sqrt{\frac{\frac{M_\phi E_\phi}{a^3} + \rho_R}{3M_P^2}}$.

In Fig. 2.2 , we show the evolution of comoving energy density of $\phi$ with the scale factor. As seen, $\phi$ was initially a part of the thermal bath and in thermal equilibrium. It then freezes out after becoming non-relativistic, behaving as matter until it finally decays. The right panel shows the evolution of the energy density of $\phi$, along with SM radiation. Initially, the Universe is radiation-dominated until $\phi$ starts to dominate from $a \sim 1$. We recover the radiation-dominated Universe when $\phi$ finally decays.

## 2.2 Early matter-domination due to Primordial Black Holes

Primordial Black Holes are black holes that could have formed in the early Universe through some non-stellar routes. Initially proposed by Hawking [83], they differ in many ways from the usual astrophysical black holes, which are formed through the gravitational collapse of a star with mass larger than the Chandrasekhar limit $\approx 1.4\ M_\odot$(solar mass). The masses of PBH can span a wide range from being as light as a few grams to as heavy as some orders of solar mass.

PBH can be formed through several mechanisms in the early Universe. The high energy density of the early Universe is well-suited for the formation of PBH, which can have

a wide range of masses. Within the framework of such mechanisms, PBH are typically formed through the gravitational collapse of highly overdense region of inhomogeneities in the early Universe [84]. The source of these inhomogeneities could be from quantum fluctuations during inflation, which collapse upon re-entering the horizon. Since CMB observations of the power spectrum [13] related to the perturbations generated from inflation tightly constrain the large scales, an enhancement to the power spectrum is required at the smaller scales. Several ideas have been proposed to realize this, which include inflation models with running spectral index [85], and inflection point inflation models [86] leading to an ultra slow-roll phase. On the other hand, non-inflationary routes of forming PBH include collapse of loops formed by cosmic strings [87] and collisions of bubbles formed after a symmetry breaking [88]. A review of PBH formation mechanisms can be found in Ref. [89, 90]. For the purpose of this thesis, we remain agnostic about the formation mechanism of PBH and rather focus on its phenomenological consequences. We also consider PBH with a monochromatic mass function, i.e. all black holes are assumed to be of the same mass.

Considering PBH to be formed during the early radiation dominated Universe, when the thermal plasma has a temperature, say $T_{\rm in}$, the initial mass of PBH can be related to the mass enclosed in the particle horizon $M_H$ as

$$M_{\rm BH}(T_{\rm in}) = \gamma M_H = \gamma \frac{4\pi}{3} \frac{\rho_R(T_{\rm in})}{H^3(T_{\rm in})}. \tag{2.3}$$

Here, $\gamma \approx 0.2$ [90] is a dimensionless parameter connected to the gravitational collapse, whereas $\rho_R$ denotes the radiation energy density at the temperature $T_{\rm in}$. Thus, PBH formed around the Planck scale, would have mass as low as around $10^{-5}$ g, whereas those formed around MeV scale, would be as massive as around $10^5\ M_\odot$. A lower bound on the PBH mass can be inferred from the upper bound on the inflationary scale [47]

$$H_I \leq 2.5 \times 10^{-5} M_{\rm Pl} \implies M_{\rm BH}(T_{\rm in}) \gtrsim 0.1\ g. \tag{2.4}$$

From Eqn. (2.3), we get the PBH formation temperature as

$$T_{\rm in} = \left(\frac{45\,\gamma^2}{16\,\pi^3\,g_\star\,(T_{\rm in})}\right)^{1/4} \sqrt{\frac{M_{\rm pl}}{M_{\rm BH}(T_{\rm in})}}\,M_{\rm pl}\,. \tag{2.5}$$

Here, $M_{\rm pl}$ is the Planck mass. PBH evaporate away through Hawking radiation, which is discussed in the next subsection. If they are heavier than $\sim 10^{15}$ g, they are stable now and can be potential candidates for dark matter. PBH in the asteroid mass range of $10^{17} - 10^{23}$ g, can contribute to 100% of the DM relic density. The fraction of DM as PBH is usually defined in terms of the parameter $f_{\rm PBH} = \Omega_{\rm PBH}/\Omega_{\rm DM}$, where $\Omega$'s denote the relative energy densities defined similarly to that in Eqn. (1.18). PBH with mass less than $\sim 10^{15}$ g would have evaporated away by today and the evaporation products have considerable effects on BBN, CMB, galactic and extragalactic $\gamma$-rays, and $e^\pm$ observed by Voyager-1. These constrain the PBH mass vs $f_{\rm PBH}$ plane, which is shown in the left panel of Fig. 2.3. On the other hand, heavier PBH with $M_{\rm BH}(T_{\rm in}) \gtrsim 10^{15}$ g have constraints from gravitational lensing, gravitational waves, accretion and dynamical effects, which are shown in the right panel of Fig. 2.3. A nice comprehensive summary of these constraints can be found in Ref. [90].

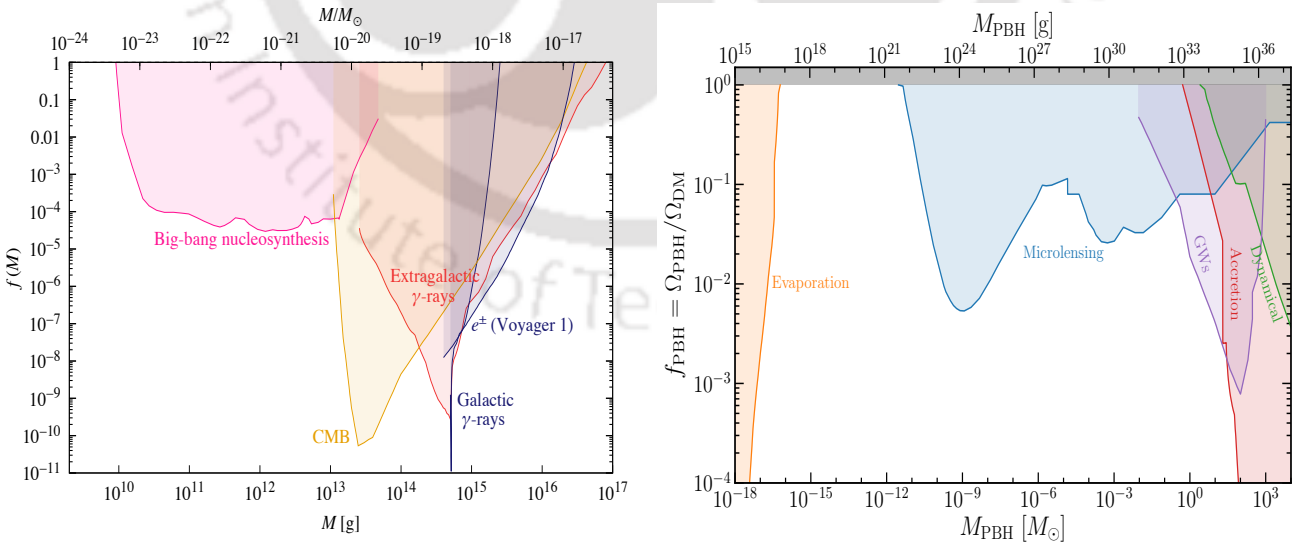


FIGURE 2.3: Contraints in the PBH mass vs PBH fraction plane from several experiments (see text) for PBH mass range which have evaporated by today (left panel) and which are stable now (right panel). The figures have been taken from Ref. [90, 91].

In this thesis, we do not consider PBH as DM, rather we focus on the effect of PBH evaporation on the phenomenology of DM and baryon asymmetry[1]. For this, we take into account PBH with initial mass $M_{\rm BH}(T_{\rm in}) \lesssim 10^8$ g, which evaporate before the epoch of BBN as we will see, and hence can evade all the constraints mentioned above. PBH can lead to a matter domination in the early Universe if their initial energy density is large enough. This initial energy density is generally compared with that of radiation at the time of PBH formation by defining the parameter $\beta$ as

$$\beta = \frac{\rho_{\rm BH}(T_{\rm in})}{\rho_R(T_{\rm in})}. \tag{2.6}$$

Thus, if the lifetime of PBH is large enough such that they do not evaporate earlier, they

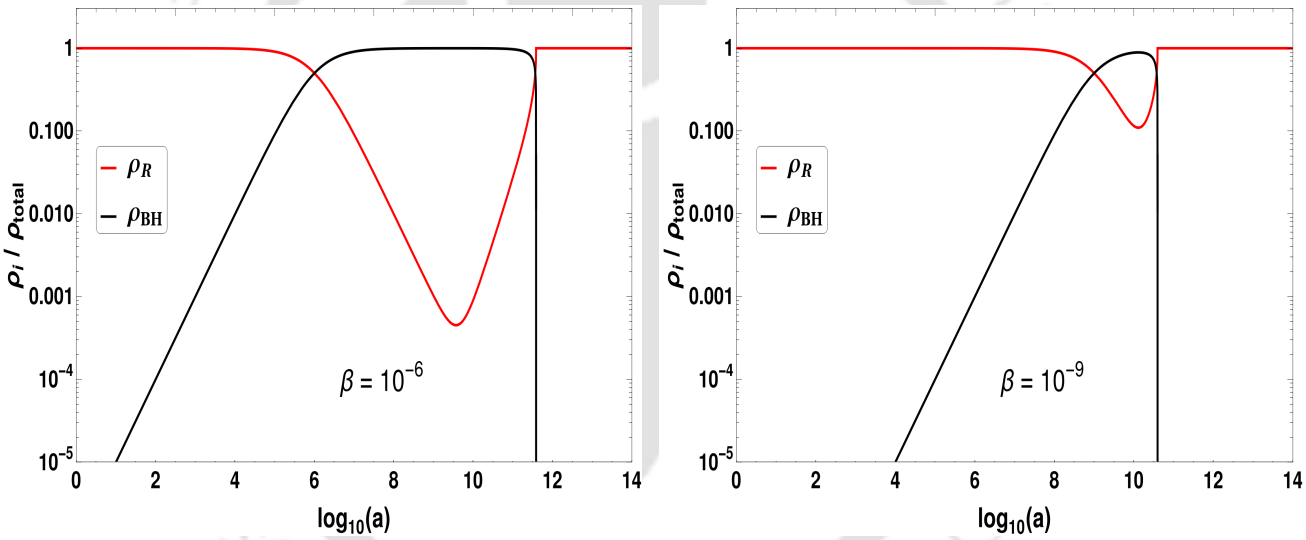


FIGURE 2.4: Evolution of the energy densities of PBH and radiation with the scale factor, for $\beta = 10^{-6}$ (left panel) and $\beta = 10^{-9}$ (right panel), considering $m_{\rm in} = 10^5$ g.

can dominate the energy density, behaving as a matter component. This, as we will see, will put a lower bound on $\beta$ depending on the initial PBH mass. In Fig. 2.4, considering $m_{\rm in} = 10^5$ g, we show the evolution of the ratio of the PBH and radiation energy densities to the total energy density of the Universe, for $\beta = 10^{-6}$ (left panel) and $\beta = 10^{-9}$ (right panel), from which one can clearly see that lowering the initial energy density of PBH

[1]The role of evaporating PBH in generating the baryon asymmetry and dark matter relic abundance has been studied in different contexts in Ref. [92–105].

namely, $\beta$ shortens the epoch of PBH domination before they evaporate away. Below we discuss the evaporation of PBH in some detail.

### 2.2.1 PBH evaporation through Hawking radiation

In his famous paper entitled "Black hole explosions?" [92], considering the effect of quantum mechanics Hawking demonstrated that a black hole emits a thermal spectrum of particles, as if it were a black body with a temperature

$$T_{\rm BH} = \frac{1}{8\pi G M_{\rm BH}} \approx 1.06 \left(\frac{10^{13}\ {\rm g}}{M_{\rm BH}}\right)\ {\rm GeV}. \tag{2.7}$$

This Hawking temperature is related to the black hole's surface gravity [106]. The instantaneous rate of emission of a particle species $i$, with momentum between $p$ and $p+dp$, and within a time interval $dt$ is given by [100, 104]

$$\frac{d^2\mathcal{N}_i}{dp\,dt} = \frac{g_i}{2\pi^2} \frac{\sigma_{s_i}(M_{\rm BH}, m_i, p)}{\exp\left[E_i(p)/T_{\rm BH}\right] - (-1)^{2s_i}} \frac{p^3}{E_i(p)}. \tag{2.8}$$

Here, $g_i$, $s_i$ represent the internal degrees of freedom and spin respectively of the emitted particle, and $E_i(p) = \sqrt{m_i^2 + p^2}$, $m_i$ being the particle's rest mass. The quantity $\sigma_{s_i}$ is known as the absorption cross-section (with the associated greybody factor $\Gamma_{s_i} = \sigma_{s_i} p^2/\pi$) which accounts for the back-scattering of the emitted particles because of gravitational potentials [92, 106–108]. In the limit $GM_{\rm BH}p \gg 1$, the cross-section can be given by the *geometrical optics* limit, $\sigma_{s_i} = 27\pi G^2 M_{\rm BH}^2$ [107–110]. Now, because of the emission of particles, black holes would start evaporating away losing their mass. This would increase the Hawking temperature (cf. Eqn. (2.7)). The emission of a particle with rest mass $m_i$ is suppressed for $m_i < T_{\rm BH}$. However, as $T_{\rm BH}$ keeps on increasing, the emission of other massive particles would also occur. The rate of mass loss can be obtained as

$$\begin{aligned} \frac{dM_{\rm BH}}{dt} &= -\sum_i \int_0^\infty E_i \frac{d^2\mathcal{N}_i}{dpdt} dp\,, \\ &= -\kappa\varepsilon(M_{\rm BH}) \left(\frac{1\ {\rm g}}{M_{\rm BH}}\right)^2, \end{aligned} \tag{2.9}$$

where the sum is over all particle species and $\kappa = 5.34 \times 10^{25}$ gs$^{-1}$ [109, 110]. Since the emission depends only on gravitational interactions, all particles independent of their SM or other BSM interactions are emitted. $\varepsilon(M_{\rm BH})$, known as the evaporation function, carries information about the spectra of the emitted particles [109, 111]. Integrating Eqn. (2.9), we can find the lifetime of PBH as [101, 112]

$$\tau = \frac{10240\,\pi\, m_{\rm in}^3}{\mathcal{G}\, g_{\star,H}(T_{\rm BH})\, M_{\rm pl}^4}\,, \tag{2.10}$$

where $m_{\rm in} = M_{\rm BH}(T_{\rm in})$ is the initial PBH mass and $\mathcal{G} \sim 3.8$ is the greybody factor [110, 112]. $g_{\star,H}(T_{\rm BH})$ accounts for all the particles with mass below $T_{\rm BH}$ and can be written as [110, 112]

$$g_{\star,H}(T_{\rm BH}) \equiv \sum_i \omega_i\, g_{i,H}\,;\, g_{i,H} = \begin{cases} 1.82 & \text{for } s = 0\,, \\ 1.0 & \text{for } s = 1/2\,, \\ 0.41 & \text{for } s = 1\,, \\ 0.05 & \text{for } s = 2\,, \end{cases} \tag{2.11}$$

with $\omega_i = 2\,s_i + 1$ for massive particles of spin $s_i$, $\omega_i = 2$ for massless species with $s_i > 0$ and $\omega_i = 1$ for $s_i = 0$.

The associated temperature of the Universe at the time of evaporation, i.e. the evaporation temperature comes out to be

$$T_{\rm evap} \equiv \left(\frac{45\, M_{\rm pl}^2}{16\,\pi^3\, g_\star\,(T_{\rm evap})\,\tau^2}\right)^{1/4}. \tag{2.12}$$

In the left panel of Fig. 2.5, we show the three important temperatures associated with PBH: the initial Hawking temperature $T_{\rm BH}^{\rm in}$ (Eqn. (2.7) with $M_{\rm BH} = m_{\rm in}$), the PBH formation temperature $T_{\rm in}$ (Eqn. (2.5)) and the evaporation temperature $T_{\rm evap}$ (Eqn. (2.12)) as a function of the initial PBH mass $m_{\rm in}$. As we can see, PBH with a smaller initial mass are formed at a higher temperature with a higher Hawking temperature and also evaporates earlier. We consider PBH to evaporate before BBN, such that the radiation produced from PBH does not disrupt the successful BBN predictions and evades the constraints shown

in Fig. 2.3. This puts an upper bound on the initial PBH mass as

$$m_{\rm in} \lesssim 3.4 \times 10^8 \text{ g}. \tag{2.13}$$

This upper bound from BBN on the initial PBH mass, along with the lower bound from CMB (Eqn. (2.4)) are shown by the dashed vertical lines in Fig. 2.5.

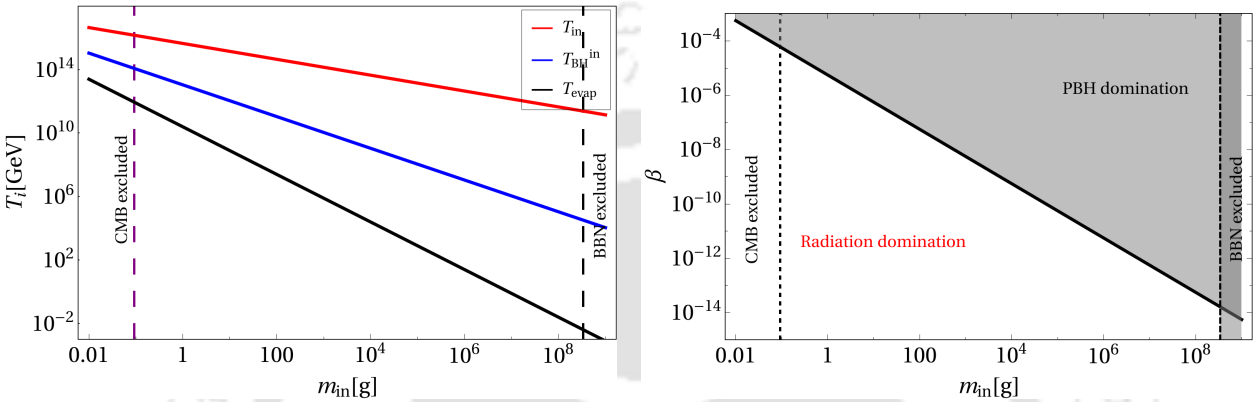


FIGURE 2.5: *Left panel*: Variation of the PBH formation (red), evaporation (black) and the Hawking temperature (blue) with the initial PBH mass. The purple and black dashed vertical lines correspond to the lower and upper bounds from CMB and BBN (see text). *Right panel*: $\beta_c$ as a function of the initial PBH mass shown by the black thick diagonal line which segregates radiation domination and PBH domination. The figures have been taken from Ref. [113].

In order for PBH to dominate the energy density of the Universe before they evaporate, one should have $\rho_{\rm BH}(t) > \rho_R(t)$ atleast at $t = t_{\rm evap}$. We have [112]

$$\frac{\rho_{\rm BH}(t_{\rm evap})}{\beta\rho_R(t_{\rm evap})} = \frac{\rho_{\rm BH}(t_{\rm evap})}{\rho_{\rm BH}(t_{\rm in})}\frac{\rho_R(t_{\rm in})}{\rho_R(t_{\rm evap})} = \frac{a(t_{\rm evap})}{a(t_{\rm in})} = \left(\frac{g_\star(T_{\rm in})}{g_\star(T_{\rm evap})}\right)^{1/4}\frac{T_{\rm in}}{T_{\rm evap}}, \tag{2.14}$$

which gives the following condition on $\beta$ for PBH-domination

$$\beta > \beta_c = \gamma^{-1/2}\sqrt{\frac{\mathcal{G}\, g_{\star,H}(T_{\rm BH})}{10240\,\pi}}\,\frac{M_{\rm pl}}{m_{\rm in}}, \tag{2.15}$$

The right panel of Fig. 2.5 shows the region of PBH-domination (shaded in grey) in the $m_{\rm in} - \beta$ plane.

Now, the number of particles $\mathcal{N}$ emitted from PBH can be estimated by considering the differential mass decrease as [94]

$$dM_{\rm BH} = -M_P^2 \frac{dT_{\rm BH}}{T_{\rm BH}^2} = -dE\,, \tag{2.16}$$

where $dE$ is the corresponding energy emitted by PBH. Considering the mean energy of the emitted particles as $3T_{\rm BH}$, the differential number of emitted particles can be written as

$$d\mathcal{N} = \frac{dE}{3T_{\rm BH}} = M_P^2 \frac{dT_{\rm BH}}{3T_{\rm BH}^3} \tag{2.17}$$

which after integration leads to

$$\mathcal{N} = \frac{g_{X,H}}{g_{\star,H}} \begin{cases} \frac{4\pi}{3}\left(\frac{m_{\rm in}}{M_{\rm pl}}\right)^2 & \text{for } M_X < T_{\rm BH}^{\rm in}\,, \\ \frac{1}{48\pi}\left(\frac{M_{\rm pl}}{M_X}\right)^2 & \text{for } M_X > T_{\rm BH}^{\rm in}\,, \end{cases} \tag{2.18}$$

where $X$ indicates the emitted particle with degrees of freedom $g_{X,H}$ (cf. Eqn. (2.11)) and mass $M_X$. Note that for $M_X < T_{\rm BH}^{\rm in}$, the emission of particles take place from the beginning of PBH formation, hence the lower limit of integration on $T_{\rm BH}$ is $T_{\rm BH}^{\rm in}$. In this case, $\mathcal{N}$ depends only on $m_{\rm in}$. On the other hand, for heavy particles such that $M_X > T_{\rm BH}^{\rm in}$, the emission occurs only when $T_{\rm BH}$ reaches $M_X$, hence changing the integration lower limit to $M_X$. Here, $\mathcal{N}$ depends only on $M_X$.

## 2.3 Effect of early matter domination on gravitational wave spectra

Testing the cosmological history before BBN has been a challenging task in our pursuit of understanding the early Universe. In this regard, gravitational waves (GW) from primordial sources related to physics before BBN may provide a new window to look into the very early Universe. Observation of GW by the LIGO/VIRGO collaboration has been a

revolutionary discovery [114] and although the source of this GW was from the relatively late Universe, this discovery has motivated us to look for other GW signals from the early Universe. Such primordial sources of GW are typically stochastic in nature and can have several origins including inflation, reheating/preheating, phase transitions, topological defects etc. A review of these mechanisms generating a stochastic GW signal can be found in [115]. In this thesis, we focus on two such sources of gravitational waves: (a) cosmic strings [116], (b) PBH density fluctuations [117–119]. Such GW have unique spectral shapes, which depend on the background cosmic history. Hence, probing these GW signals may provide a hint towards the pre-BBN cosmic history.

### 2.3.1 Cosmic Strings

Cosmic Strings [120, 121] are one-dimensional topological defects, which can be formed after the spontaneous symmetry breaking of a continuous symmetry, if the vacuum manifold is not simply connected. The simplest realization can be through a $U(1)$ symmetry group, with a complex scalar field $\phi$. The field develops a 'Mexican-hat' potential in the early Universe, with a degenerate circle of minima, as shown in Fig. 2.6. The field value at the minima can be written as $\phi = \Phi e^{i\theta}$. In regions of space where the phase angle $\theta$ could not vary continuously, the field is forced to take the original high energy value at $\phi = 0$, forming a vortex [122] as shown in Fig. 2.6. In three dimensions, these defects manifest as a linear structure and are known as Cosmic Strings. The strings are characterized by their energy per unit length, known as the string tension $\mu$, which is proportional to the square of the symmetry-breaking scale $\Lambda_{\rm CS}$. The tension is generally denoted by the dimensionless quantity $G\mu$, where $G$ is the gravitational constant. Thus, we have $G\mu \sim G\Lambda_{\rm CS}^2$.

The strings form a network after they are formed and are stretched by the expansion of the Universe. Long strings may intercommute with themselves or with other strings, forming loops and chopping themselves. The loops oscillate and can lose their energy in the form of particle emission or through gravitational wave radiation. Numerical simulations [123, 124] based on Nambu-Goto action have found that for gauged symmetry,

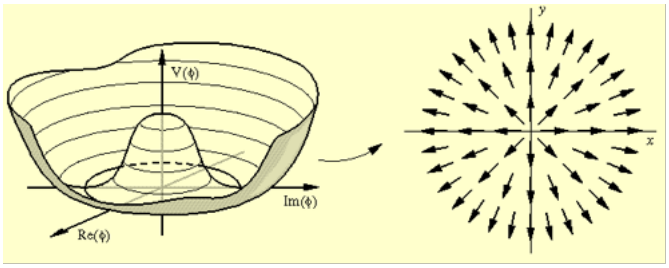


FIGURE 2.6: Diagram illustrating the formation of cosmic strings after a spontaneous symmetry breaking leading to a 'Mexican-hat' potential (left). Regions of space where cosmic string is formed at the core of a vortex (right). The figure has been taken from www.ctc.cam.ac.uk.

the dominant channel of energy loss from cosmic strings is through GW radiation from oscillating loops. The rate of energy loss or the power of GW emission is given by the quadrupole formula [125]

$$P_{\rm GW} = \frac{G}{5}(Q''')^2\,, \tag{2.19}$$

where $Q$ is the quadrupole moment of the oscillating loop and the triple time derivative comes out to be $Q''' \propto \mu$. Thus, the rate of energy loss can be written as

$$\frac{dE}{dt} = -\Gamma G\mu^2\,, \tag{2.20}$$

where $\Gamma \approx 50$ [126]. Because of the GW emission, the loop starts to shrink from its initial length $l_i = \alpha t_i$ at the time of formation $t_i$, as

$$l(t) = \alpha t_i - \Gamma G\mu(t - t_i). \tag{2.21}$$

$\alpha$ is known as the loop size parameter and simulations suggest $\alpha = 0.1$ [127, 128]. The total energy loss from a loop constitutes a set of normal mode oscillations with frequencies $f_k = 2k/l$, where $k$ represents the mode numbers $k = 1, 2, 3....\infty$. The GW density parameter is defined as

$$\Omega_{\rm GW}(t_0, f) = \frac{f}{\rho_c}\frac{d\rho_{\rm GW}(t_0, f)}{df} = \sum_k \Omega^{(k)}_{\rm GW}(t_0, f)\,, \tag{2.22}$$

where $f$ represents the current frequency and $t_0$ is the present time. Since the GW energy density redshifts as $a^{-4}$, we have [101, 127]

$$\frac{d\rho_{GW}^{(k)}}{df} = \int_{t_F}^{t_0} \left[\frac{a(t_E)}{a(t_0)}\right]^4 P_{GW}(t_E, f_k) \frac{dF}{df} dt_E \,, \tag{2.23}$$

where $f_k = f_E$ denotes the emitted frequency at the time $t_E$, whereas $t_F$ is the loop formation time. $\frac{dF}{df} = f\left[\frac{a(t_0)}{a(t_E)}\right]$ accounts for the redshift of the frequency. $P_{GW}(t_E, f_k)$ is the power emitted by the loops, which is given by the following integration over the length of the loops

$$\begin{aligned} P_{GW}(t_E, f_k) &= G\mu^2\Gamma_k \int n(l, t_E)\delta\left(f_k - \frac{2k}{l}\right) dl \\ &= \frac{2kG\mu^2\Gamma_k}{f_k^2} n(t_E, f_k) = \frac{2kG\mu^2\Gamma_k}{f^2\left[\frac{a(t_0)}{a(t_E)}\right]^2} n\left(t_E, \frac{2k}{f}\left[\frac{a(t_E)}{a(t_0)}\right]\right). \end{aligned} \tag{2.24}$$

The GW spectrum depends on the nature of small-scale structure in the loops which can be in the form of cusps or kinks [129, 130]. For our study, we consider cusp-like structures to dominate the GW spectra. In this case, we have $\Gamma_k = \frac{\Gamma k^{-4/3}}{\sum_{m=1}^{\infty} m^{-4/3}}$, with $\sum_k \Gamma_k = \Gamma$. $n$ denotes the number density of loops, which in a cosmological background with $a \propto t^\beta$ is found from the Velocity dependent One Scale (VOS) model [131–133] and numerical simulations to be [127]

$$n(t_E, l_k(t_E)) = \frac{A_\beta}{\alpha} \frac{(\alpha + \Gamma G\mu)^{3(1-\beta)}}{[l_k(t_E) + \Gamma G\mu t_E]^{4-3\beta}\, t_E^{3\beta}} \,. \tag{2.25}$$

where $A_\beta$ is a constant depending on the cosmological background. Using Eqns. (2.22)-(2.25), we finally have the current GW energy density for the mode $k$ as

$$\Omega_{\rm GW}^{(k)}(t_0, f) = \frac{2kG\mu^2\Gamma_k}{f\rho_c} \int_{t_{osc}}^{t_0} dt \left[\frac{a(t)}{a(t_0)}\right]^5 n\left(t, l_k\right) , \tag{2.26}$$

where the integration over time is from the moment $t_{\rm osc}$ when the loops start oscillating after the damping because of thermal friction [134] becomes sub-dominant. For the case of loops formed and radiated during radiation domination, the GW spectrum have a

typical flat plateau, with the amplitude given by [101]

$$\Omega_{\rm GW}^{(k=1),\rm plateau}(f) = \frac{128\pi G\mu}{9\zeta(4/3)}\frac{A_r}{\epsilon_r}\Omega_r\left[(1+\epsilon_r)^{3/2}-1\right], \tag{2.27}$$

where $\epsilon_r = \alpha/\Gamma G\mu$, and $A_r = 5.4$ [133] for radiation domination. CMB measurements require $G\mu \lesssim 10^{-7}$ [135] and hence we have $\alpha \gg \Gamma G\mu$. This gives $\Omega_{\rm GW}^{(k=1)}(f) \propto \Lambda_{\rm CS}$, and hence a higher symmetry breaking scale is more likely to be probed in the GW detectors. In the left panel of Fig. 2.7, the GW spectrum is shown for different values of $G\mu$, along with the sensitivities of current and planned near-future GW detectors which include EPTA [136], SKA [137], A.LIGO/VIRGO [138–140], LISA [141], DECIGO [142], BBO [143], ET [144], CE [139].

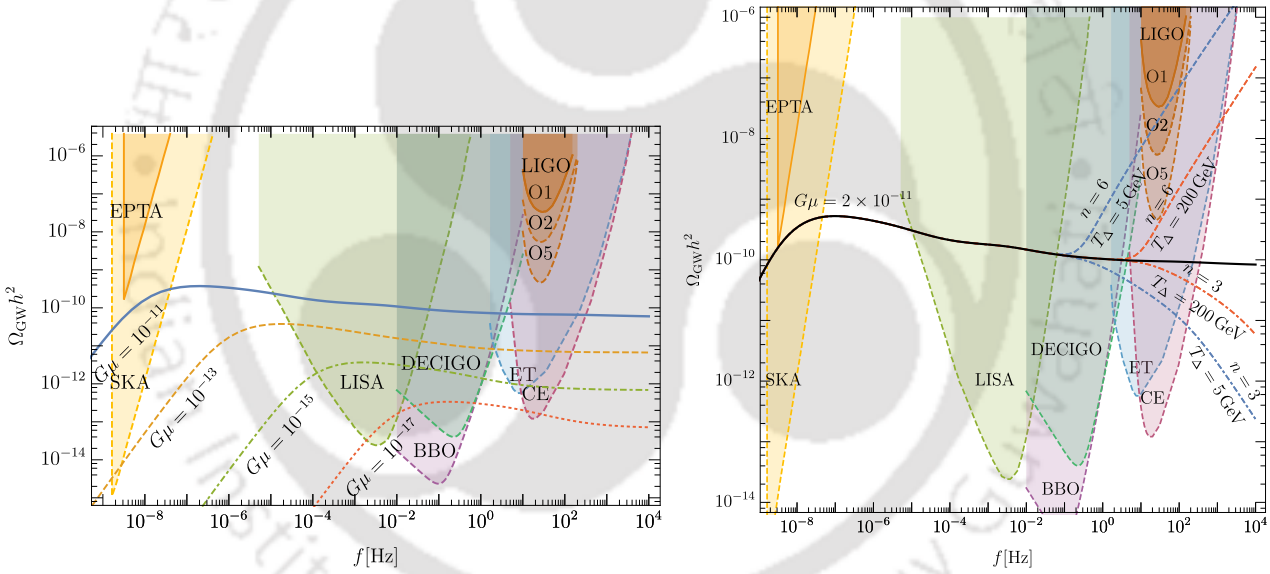


FIGURE 2.7: *Left panel*: GW spectrum for different values of $G\mu$ along with the sensitivities of different GW detectors (see text). *Right panel*: GW spectrum considering an early matter and kination dominated era, ending at two different temperatures. The figures have been taken from Ref. [145].

**Frequency-temperature relation**: The observed frequency today of the GW spectrum is related to the temperature at which the loops responsible for that particular frequency

have been formed. For loops created at a time $t_i$, the major contribution to the GW emission is much later, at a time when the loop reaches its half-life, given by[2] [130]

$$t_E = t_H \simeq \frac{\alpha t_i}{2\Gamma G\mu}. \tag{2.28}$$

The frequency emitted at the time $t_E$ is related to the length of the loop as $(f(t_E) = 2k/l(t_E))$. Considering $k = 1$, this gives us

$$\begin{aligned} \alpha t_i &\simeq \frac{4}{f}\frac{a(t_E)}{a(t_0)} \\ &\simeq \frac{4}{f}\left(\frac{t_E}{t_{\rm eq}}\right)^{1/2}\left(\frac{t_{\rm eq}}{t_0}\right)^{2/3}, \end{aligned} \tag{2.29}$$

where $t_{\rm eq}$, $t_0$ correspond to the standard matter-radiation equality time and the present time respectively. From Eqn. (2.28) and (2.29), the required relation between the frequency observed today and the time (or temperature $T$) is obtained to be [130, 145]

$$f = \sqrt{\frac{8}{\alpha\Gamma G\mu}}\left(\frac{t_{\rm eq}}{t_i}\right)^{1/2} t_0^{-1} = \sqrt{\frac{8}{z_{\rm eq}\alpha\Gamma G\mu}}\left(\frac{g_\star(T)}{g_\star(T_0)}\right)^{1/4}\frac{T}{T_0}t_0^{-1}, \tag{2.30}$$

where $z_{\rm eq} \simeq 3400$ is the redshift at matter-radiation equality.

**Testing non-standard cosmological backgrounds**: The dependence of the GW amplitude on the frequency can be qualitatively understood as follows. Basically, the frequency dependence receives contribution from two factors. One is the dilution of the GW energy density as $a^{-4}$ because of the Universe's expansion. Hence, the GW amplitude corresponding to higher frequencies which are emitted by loops formed at a higher temperature as explained above, encounters more suppression until the present time. However, at earlier times the loop production rate, which varies as $\propto t_i^{-4}$ [127, 146] also increases. An increase in the number of loops leads to enhanced GW amplitude. Thus, the total dependence on frequency is the effect of these two factors. For radiation domination, these two factors exactly cancel each other, leading to a flat spectrum. As seen in Fig. 2.7 (left

[2]This has the added advantage that the GW frequencies are exempted from the redshift factor $a(t_E)/a(t_i)$, which most other GW sources at the same energy scale undergo.

panel), the typical GW spectrum from cosmic strings is a flat plateau that falls down at lower frequencies because of contribution from loops from the recent matter domination. There might also be a deviation from flatness at higher frequencies if cosmological epochs other than radiation exist at higher temperatures before BBN. This deviation from flatness would first start to appear because of the contribution of those loops which have been formed at a time say $t_\Delta$ (with corresponding temperature $T_\Delta$), when the standard radiation era began or the non-standard era ended. Thus, the frequency at which the spectral break occurs or the turning point frequency $f_\Delta$ is given by Eqn. (2.30), with $t_i = t_\Delta$ and $T = T_\Delta$. The frequency dependency of the GW amplitude can be analytically estimated to be [130]

$$\Omega_{\rm GW} \propto f^{4\left(1-\frac{3}{n}-\frac{1}{m}\right)}. \tag{2.31}$$

Here, $a(t_i) \propto t_i^{2/n}$ and $a(t_E) \propto t_E^{2/m}$ represents the evolution of the cosmological background during loop formation time and GW emission time respectively. For instance, for loops formed during an early matter (kination) domination, and GW emission during radiation domination, we have $n = 3(6)$ and $m = 4$, which gives $\Omega_{\rm GW} \propto f^{-1}(f^1)$ [3]. In the right panel of Fig. 2.7, the GW spectrum is shown in the presence of two non-standard cosmic epochs: matter and kination, ending at a temperature $T_\Delta = 5$ GeV (blue dashed contour) and $T_\Delta = 200$ GeV (red dashed contour). Clearly, for higher temperatures, the spectral break occurs at a higher frequency, as discussed above (cf. Eqn. (2.30)).

[3] From Eqn. (2.26) one can see that the spectra for the $k^{\rm th}$ mode is related to the fundamental $k = 1$ mode through [130]

$$\Omega_{GW}^{(k)}(f) = k^{-4/3}\Omega_{GW}^{(1)}(f/k). \tag{2.32}$$

For the part of GW spectra varying as $\Omega_{GW}^{(1)} \propto f^{-1}$, summing over all modes changes this slope to $f^{-1/3}$ [130] for EMD.

### 2.3.2 PBH density fluctuations

Primordial black holes can play a role in generating GW in several ways: (a) PBH can emit gravitons through Hawking radiation (cf. section 2.2.1), which can lead to ultra-high frequency GW [147]; (b) PBH can lead to the formation of mergers, which can also emit GW [148, 149]; (c) the primordial scalar fluctuations generated from inflation which led to the formation of PBH, can induce GW at second order in perturbation theory [150]; (d) the distribution of PBH after they are formed is inhomogeneous leading to scalar density fluctuations, which can also induce GW at the second order [117–119]. We focus on this last possibility. This is because the GW frequency spectrum formed through such a mechanism is within the reach of near-future GW detectors, as we will see. In addition, they are independent of the formation mechanism of PBH. Moreover, such GW can be produced only when PBH dominate the energy density of the Universe and hence it is a distinct feature of early matter domination because of PBH. We briefly discuss here the basic idea behind such GW, closely following Ref. [117, 118].

Once PBH are formed, they are randomly distributed in space, with the distribution following Poissonian statistics. This approximation is restricted only to length scales which are larger than the Schwarzschild radius of the black hole. In addition, at distances smaller than the mean separation between PBH, the granularity of PBH becomes important and we can no longer treat them as a continuous fluid. The mean separation at the time of formation can be written as

$$d_{\rm in} \equiv \left(\frac{3M_{\rm BH}(T_{\rm in})}{4\pi\rho_{\rm BH}(T_{\rm in})}\right)^{1/3} = \gamma^{1/3}\beta^{-1/3}H(T_{\rm in})^{-1}\,. \tag{2.33}$$

Following the Poissonian statistics, the two-point correlation function of the density contrast comes out to be

$$\left\langle \frac{\delta\rho_{\rm BH}(\mathbf{r})}{\rho_{\rm tot}}\frac{\delta\rho_{\rm BH}(\mathbf{r}')}{\rho_{\rm tot}}\right\rangle = \frac{4}{3}\pi\left(\frac{d}{a}\right)^3\Omega_{\rm BH}^2\delta(\mathbf{r}-\mathbf{r}')\,, \tag{2.34}$$

where $\rho_{\rm tot}$ denotes the total energy density and '**r**' is the comoving distance coordinate. Taking the Fourier transform gives the PBH density perturbation spectrum as

$$\langle \delta\rho_{\rm BH}(k)\delta\rho_{\rm BH}(k')\rangle = \frac{4\pi}{3}\left(\frac{d}{a}\right)^3 \rho_{\rm BH}^2\,\delta(k-k')\,, \tag{2.35}$$

with $k$ representing the comoving wavenumber. '$d$' is the redshifted mean separation distance between PBH given by $d = d_{\rm in}(a_{\rm in}/a)$. The condition of distance scales being larger than the mean separation as discussed above puts an ultraviolet cutoff on the comoving wavenumber as

$$k_{\rm UV} = a_{\rm in}H_{\rm in}\beta^{1/3}\gamma^{-1/3}\,. \tag{2.36}$$

Now, since the initial energy density of PBH is negligible compared to that of radiation, the PBH density fluctuations are isocurvature in nature, with the dimensionless initial isocurvature power spectrum given by

$$\mathcal{P}_S(k) = \frac{2}{3\pi}\left(\frac{k}{k_{\rm UV}}\right)^3\,, \tag{2.37}$$

where $S$ in the 'subscript' represents the PBH isocurvature perturbation given by

$$S = \frac{\delta\rho_{\rm BH}}{\rho_{\rm BH}} - \frac{3}{4}\frac{\delta\rho_R}{\rho_R}. \tag{2.38}$$

Once PBH dominates the energy density of the Universe, these isocurvature perturbations can source a curvature perturbation $\Phi$, which follows the following equation at first order in perturbation theory[4]

$$\Phi'' + 3\mathcal{H}(1+c_s^2)\Phi' + (\mathcal{H}^2(1+3c_s^2) + 2\mathcal{H}')\Phi - c_s^2\Delta\Phi = \frac{a^2\rho_{\rm PBH}}{2M_{\rm pl}^2}c_s^2 S\,, \tag{2.39}$$

[4]The perturbed metric is considered in the Newton gauge and is given by

$$ds^2 = a^2(\tau)\left[-(1+2\Psi)d\tau^2 + (\delta_{ij}+2\Phi\delta_{ij}+h_{ij})dx^i dx^j\right]\,,$$

where $\tau$ denotes the conformal time, and $\Psi$, $\Phi$, $h_{ij}$ are the lapse, curvature and tensor perturbations respectively.

where 'prime' denotes derivative w.r.t. conformal time, $\mathcal{H} = a'/a$ and $c_s^2 \equiv \frac{4}{9}\frac{\rho_R}{\rho_{\rm BH}+\frac{4}{3}\rho_R}$ .

The tensor perturbations, on the other hand, obey the following equation of motion

$$h_k^{s\,\prime\prime} + 2\mathcal{H}h_k^{s\,\prime} + k^2 h_k^s = 4S_k^s\,, \tag{2.40}$$

where '$s$' denotes the polarisation $(+), (\times)$. The source function $S_k^s$ appearing on the R.H.S. is proportional to the factor $(\mathcal{H}^{-1}\Phi_q' + \Phi_q)(\mathcal{H}^{-1}\Phi_{k-q}' + \Phi_{k-q})$. Now, the amplitude of $\Phi$ is constant during PBH domination and is enhanced by a factor of $\mathcal{O}(k\tau_{\rm evap})$ during transition to radiation domination after PBH evaporation. This changes the time derivative $\mathcal{H}^{-1}\Phi'$ from zero to a large value $\sim (k\tau_{\rm evap})\Phi_{\rm PBH}$, where $\Phi_{\rm PBH}$ denotes the $\Phi$ value during PBH domination. Thus, an immense amount of GW is induced as the source term in Eqn. (2.40) is proportional to $\mathcal{H}^{-2}\Phi'^2$. The two-point correlation function for the tensor perturbation is given by

$$\langle h_{k_1}^r(\eta)(h_{k_2}^s)^*(\eta)\rangle \equiv \delta^{(3)}(k_1-k_2)\delta^{rs}\frac{2\pi^2}{k_1^3}\mathcal{P}_h(\eta,k_1), \tag{2.41}$$

where '$r$', '$s$' denotes the polarisation. The amplitude of the GW energy density observed today can be expressed as

$$\Omega_{\rm GW,0}(k)h^2 = 0.39\left(\frac{g_*(T_c)}{106.75}\right)^{-1/3}\Omega_{r,0}h^2\Omega_{\rm GW,c}(k)\,. \tag{2.42}$$

Here, $\Omega_{\rm GW,c}(k)$ represents the energy density of GW in the radiation-dominated era after evaporation, when it becomes constant at a temperature $T_c$. It then dilutes away similar to radiation. $\Omega_{r,0}h^2 \sim 4.18\times10^{-5}$ is the present energy density of radiation [151].

It can be shown that the dominant contribution to the GW amplitude $\Omega_{\rm GW,c}(k)$ is from modes $k$ satisfying $k \gg k_{\rm eq}$, where $k_{\rm eq}$ corresponds to the modes entering the horizon when the PBH energy density becomes equal to that of radiation, i.e. when the PBH start dominating the total energy density. This is mainly because the GW amplitude is directly proportional to the factor $k\tau_{\rm evap} \simeq k/k_{\rm evap}$. Hence, the small scales are largely enhanced.

For the cut-off scale $k_{\rm UV}$, this factor is found to be

$$\frac{k_{\rm UV}}{k_{\rm evap}} \approx 2.3 \times 10^6 \left(\frac{g_{\star,H}(T_{\rm BH})}{108}\right)^{-1/3} \left(\frac{m_{\rm in}}{10^4 {\rm g}}\right)^{2/3} . \tag{2.43}$$

Even, for PBH mass as low as 1 g, this factor comes to be $\sim 5000$. The amplitude near this resonance is calculated to be

$$\Omega_{\rm GW,c,res}(k \sim k_{\rm UV}) \approx \frac{1}{24576\pi\, 2^{1/3}\sqrt{3}} \left(\frac{k_{\rm UV}}{k_{\rm evap}}\right)^{17/3} \left(\frac{k_{\rm eq}}{k_{\rm UV}}\right)^{8} ,$$

which can be written in terms of the PBH parameters $\beta$ and $m_{\rm in}$ as

$$\Omega_{\rm GW,c,res}(k \sim k_{\rm UV}) \approx 10^{30} \beta^{16/3} \left(\frac{\gamma}{0.2}\right)^{8/3} \left(\frac{g_{\star,H}(T_{\rm BH})}{108}\right)^{-17/9} \left(\frac{m_{\rm in}}{10^4 {\rm g}}\right)^{34/9} . \tag{2.44}$$

Thus, the amplitude is quite large unless $\beta$ is very small. The dominant contribution to the total GW energy density can be written in terms of observed frequency as [152]

$$\Omega_{\rm GW}(t_0, f) \simeq \Omega_{\rm GW}^{\rm peak} \left(\frac{f}{f^{\rm peak}}\right)^{11/3} \Theta\left(f^{\rm peak} - f\right) , \tag{2.45}$$

where $\Omega_{\rm GW}^{\rm peak}$ is found from Eqn. (2.42) and (2.44) to be

$$\Omega_{\rm GW}^{\rm peak} \simeq 2 \times 10^{-6} \left(\frac{\beta}{10^{-8}}\right)^{16/3} \left(\frac{m_{\rm in}}{10^7 {\rm g}}\right)^{34/9} . \tag{2.46}$$

$f_{\rm peak}$ is the frequency corresponding to the UV cutoff scale $k_{\rm UV}$, and is given by

$$f^{\rm peak} \simeq 1.7 \times 10^3 {\rm Hz} \left(\frac{g_{\star,H}(T_{\rm BH})}{108}\right)^{1/6} \left(\frac{g_{\star}(T_{\rm evap})}{106.75}\right)^{1/4} \left(\frac{g_{*s}(T_{\rm evap})}{106.75}\right)^{-1/3} \left(\frac{m_{\rm in}}{10^4 {\rm g}}\right)^{-5/6} . \tag{2.47}$$

For PBH mass $m_{\rm in} \gtrsim 10^4$ g, the frequency can be within reach of near future GW detectors such as ET [144], A.LIGO [138], DECIGO [142] and LISA [141]. In Fig. 2.8, the total GW spectrum arising from PBH density fluctuations is shown for two benchmark values of initial PBH mass and $\beta$, along with the sensitivity curves of different GW detectors. As

expected, the peak frequency shifts to the left for higher values of PBH mass (cf. Eqn. (2.47)).

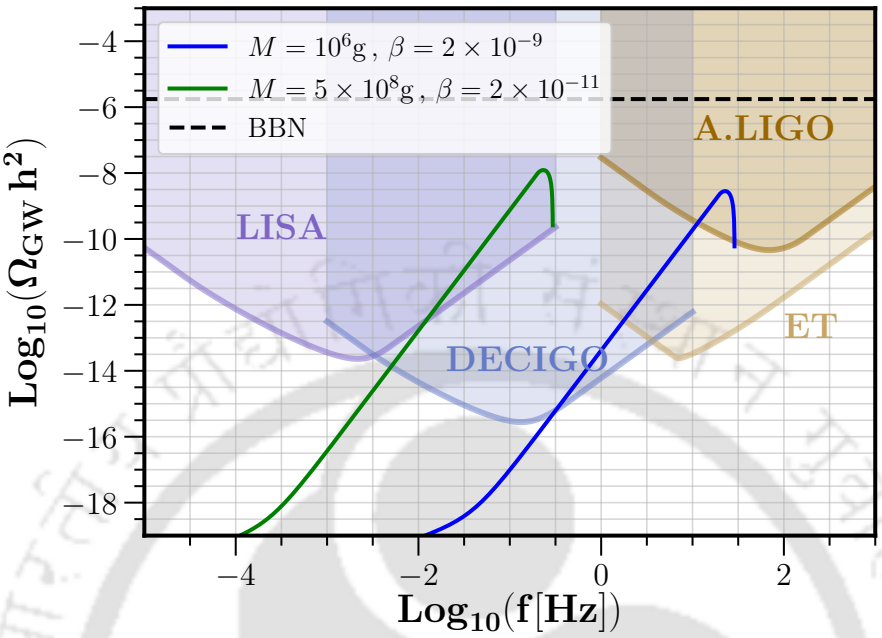


FIGURE 2.8: GW spectrum from PBH density fluctuations for two benchmark values of initial PBH mass (denoted by $M$ here) and $\beta$, along with the sensitivities of several GW detectors. The black dashed horizontal line represents the bound from BBN (cf. Eqn. (2.50)). The figure has been taken from Ref. [118].

**Upper bound on the PBH fraction $\beta$:** Since GW behave as radiation, they can contribute to the relativistic energy degrees of freedom during BBN. Now, the radiation energy density during BBN can be written in terms of the well-known parameter $N_{\rm eff}$, which represents the effective number of neutrino species in the Universe as

$$\rho_R = \frac{\pi^2}{30}\left(2 + \frac{7}{8} \times 2N_{\rm eff}\left(\frac{4}{11}\right)^{4/3}\right) T^4. \tag{2.48}$$

The extra relativistic energy can be written in terms of the parameter $\Delta N_{\rm eff}$ as

$$\rho_R - \rho_R^{\rm SM} = \Delta\rho_R = \frac{\pi^2}{30}\left(\frac{7}{8} \times \Delta N_{\rm eff}\left(\frac{4}{11}\right)^{4/3}\right) 2T^4. \tag{2.49}$$

Thus, if GW exist during BBN, then we should have

$$\begin{aligned} \rho_{\rm GW} &\leq \Delta\rho_R \\ \implies \Omega_{\rm GW,BBN} &\leq \frac{7}{8} \times \Delta N_{\rm eff} \left(\frac{4}{11}\right)^{4/3} . \end{aligned} \tag{2.50}$$

Using $\Delta N_{\rm eff} \lesssim 0.28$ from the latest Planck 2018 results [14], we get $\Omega_{\rm GW,BBN} \approx 0.39\,\Omega_{\rm GW,c,res} < 0.05$. Using Eqn. (2.44) for the GW energy density, we get an upper bound on $\beta$ as

$$\beta < 1.1 \times 10^{-6} \left(\frac{\gamma}{0.2}\right)^{-1/2} \left(\frac{g_{\star,H}(T_{\rm BH})}{108}\right)^{17/48} \left(\frac{g_\star(T_{\rm evap})}{106.75}\right)^{1/16} \left(\frac{m_{\rm in}}{10^4 {\rm g}}\right)^{-17/24} , \tag{2.51}$$

depending on the PBH mass $m_{\rm in}$.

## 2.4 Objective of the thesis

The purpose of this thesis is to investigate dark matter phenomenology and the generation of baryon asymmetry in the presence of non-standard cosmologies. This is motivated from several aspects. First of all, the search for the very popular WIMP dark matter in several DM direct detection [153, 154] and colliders experiments, considering the standard cosmology has not led us to any positive results so far. The bounds from these experiments on the DM mass and its interaction cross-section have already ruled out several DM models and pushed many others into a very tight corner. A deviation from the standard cosmology where the Universe is assumed to be radiation dominated during the time of DM production in the early Universe can alter the DM dynamics. Moreover, the cosmological history before BBN is also experimentally unknown. Hence, it is motivating to consider the possibility of non-standard epochs before BBN, which not only changes the DM phenomenology but also provides insights into interesting early Universe phases such as PBH or LLP domination. On the other hand, the phenomenology of usual baryogenesis mechanisms is also affected in the presence of such non-standard cosmic epochs. In addition to the detection challenges of DM, baryogenesis or leptogenesis typically being a high scale phenomena is out of reach of any terrestrial experiments.

Hence, it is important to consider an alternate search strategy of DM and baryogenesis. This can be realized through stochastic gravitational waves generated in the early Universe. The shape of these GW spectra depends on the details of the non-standard cosmic epochs, and can have interesting connections with DM and baryo(lepto)genesis. We look into such possible connections, which could help in probing DM and baryogenesis with the help of GW signals within the sensitivities of near-future GW detectors.

Keeping these motives in mind, we first consider DM and leptogenesis scenarios with an early matter domination due to a long-lived particle in Chapter 3. We consider two kinds of DM candidates: thermal keV warm DM and Miracle-less WIMP DM. The latter can be probed through GW produced from cosmic strings which are possible to be formed in the setup we consider. Baryon asymmetry can be generated in both cases through leptogenesis, requiring a resonant enhancement. In chapter 4, we explore DM and leptogenesis scenarios with an early matter domination arising because of primordial black holes. Here, we first consider a low-scale leptogenesis setup along with DM and study how the presence of PBH can alter the phenomenology. Next, we consider the production of non-thermal asymmetric dark matter along with baryon asymmetry through leptogenesis, both sourced by PBH. Moving on, in chapter 5, we consider a DM and leptogenesis scenario, in the presence of multiple early matter dominated eras, one caused by PBH and another appearing because of a long-lived particle. Here, we take into account the case of purely gravitational DM which can be produced directly from PBH evaporation. Leptogenesis can also be realized in such a setup through resonance. In chapter 6, we consider a scenario of direct baryogenesis without the leptogenesis route and superheavy DM with only gravitational interactions, both sourced by PBH. The scenario can be probed through GW produced from PBH density fluctuations. Finally, we conclude in chapter 7, along with some of the future directions I wish to work upon.

# Chapter 3

# DM and Leptogenesis with LLP domination

## 3.1 Introduction

In this chapter, we explore the phenomenology of dark matter and leptogenesis in the presence of early matter domination arising from a long-lived particle. We investigate particle physics setups motivated from solving the dark matter and baryon asymmetry puzzles, where the need for an extra matter-dominated era before BBN naturally arises. In particular, we consider the phenomenologically motivating gauged $B - L$ model, which contains three right-handed neutrinos required to cancel the gauge anomalies. The model also contains a complex singlet scalar to spontaneously break the $B - L$ gauge symmetry while simultaneously generating RHN masses. The presence of RHN naturally assists in accommodating active neutrino masses (which SM by itself can not explain) via type-I seesaw. In addition, we consider a vector like fermion, which can be a candidate for dark matter. The decays of RHNs can assist in generating the baryon asymmetry through leptogenesis.

We consider two possibilities regarding the nature of dark matter. In the first scenario, we consider the vector like fermion as a warm dark matter (WDM) candidate. As discussed in chapter 1 in the context of SM neutrinos, the hot dark matter (HDM) paradigm is disfavoured due to its relativistic nature giving rise to a large free streaming length (FSL) [155, 156] which can erase small-scale structures. In the case of WDM, the dark

matter can remain semi-relativistic during the epoch of matter radiation equality. The FSL of WDM falls in the intermediate regime between those of cold dark matter (CDM) and HDM. Typically, WDM candidates have masses in the keV regime which once again stays intermediate between sub-eV scale masses of typical HDM and GeV-TeV scale masses of typical CDM. A popular choice of WDM candidate is a right-handed sterile neutrino, singlet under the SM gauge symmetry. A comprehensive review of keV sterile neutrino DM can be found in [157]. To assure the stability of DM, the sterile neutrino should have tiny or zero mixing with the SM neutrinos leading to a lifetime larger than the age of the Universe. The lower bound on WDM mass arises from observations of the Dwarf spheroidal galaxies and Lyman-$\alpha$ forest which is around 2 keV [1] [155, 159–161]. Although WDM may not be traced at typical direct search experiments or the LHC, it can have interesting signatures at indirect search experiments. For example, a sterile neutrino WDM candidate having mass 7.1 keV can decay on cosmological scales to a photon and a SM neutrino, indicating an origin to the unidentified 3.55 keV X-ray line reported by analyses of Ref. [162] and [163] using the data collected by the XMM-Newton X-ray telescope. On the other hand, WDM can have interesting astrophysical signatures as it has the potential to solve some of the small-scale structure problems of the CDM paradigm [164]. For example, due to small FSL, the CDM paradigm gives rise to formation of structures at a scale as low as that of the solar system, giving rise to tensions with astrophysical observations. The WDM paradigm, due to its intermediate FSL can bring the predictions closer to observations. Now, the thermally produced keV scale warm dark matter in a gauged $U(1)_{B-L}$ model turns overabundant (cf. Eqn. (1.21)). As a remedy, the relic can be brought down to the observed limit by late time entropy production due to decay of a long lived RHN, which leads to an early matter-dominated era as discussed in chapter 2. We assume $N_3$ (the heaviest RHN) to be in thermal equilibrium in the early Universe and its late decay depletes the thermally overproduced keV scale DM by entropy dilution.

In the second scenario, we consider a case where DM-SM interaction rates fall short of

[1] Similar order of bounds on fermionic dark matter can be obtained in order to obey the Pauli exclusion principle in dense systems containing dark matter such as dwarf galaxies, which is commonly known as the Tremaine-Gunn bound [158].

the required WIMP DM criteria, but large enough to produce it in thermal equilibrium. While typical WIMP DM mass is restricted to be within a few GeV [165] to few hundred TeV [166], the class of DM we study here, dubbed as *Miracle-less WIMP*, can have a much wider range of masses. The DM stability and interactions are taken care of by an Abelian gauge symmetry, which for our study we take to be the gauged $B - L$. A high scale symmetry breaking, leading to a superheavy $Z'$ gauge boson ensures that DM-SM interactions remain in the Miracle-less WIMP ballpark. Alternative search strategies need to be adopted for such DM which may not show up in conventional DM searches looking for WIMP DM. We propose a novel way of testing this special class of DM at future gravitational wave experiments. The spontaneous breaking of the gauge symmetry can lead to the formation of cosmic strings (CS), as discussed in chapter 2. These CS can generate stochastic GW with a characteristic spectrum that can be within the reach of near-future GW detectors if the scale of symmetry breaking is sufficiently high. In our setup, due to intermediate annihilation rates, such DM in Miracle-less WIMP ballpark gets thermally overproduced and additional mechanism should be in place to bring it within observed limits. In particular, entropy production from a heavy long-lived particle (which can again be provided by one of the RHNs) leading to an early matter-dominated era can bring down the relic of thermally overproduced DM within observed limits. Interestingly, such late entropy dilution also leads to unique spectral breaks in the GW spectrum generated by CS network, which can be connected to the DM phenomenology.

This chapter is organized as follows. We start with a description of the gauged $B - L$ model in section 3.2. In section 3.3, we discuss the first scenario of thermal keV DM and leptogenesis. The second scenario of Miracle-less WIMP DM and leptogenesis is discussed in section 3.4. We conclude in section 3.5.

## 3.2 Gauged B-L model

A gauged $B - L$ extension of the SM [167–172] is one of the most popular BSM frameworks. Realizing a stable DM candidate in the model requires non-minimal field content

or additional discrete symmetries. Also, a gauged $B-L$ model with just SM fermion content, is not anomaly free due to the non-vanishing triangle anomalies for both $U(1)^3_{B-L}$ and mixed $U(1)_{B-L}-(\text{gravity})^2$ anomalies. These triangle anomalies for the SM fermion content are given as

$$\begin{aligned} \mathcal{A}_1\left[U(1)^3_{B-L}\right] &= \mathcal{A}_1^{\text{SM}}\left[U(1)^3_{B-L}\right] = -3\,, \\ \mathcal{A}_2\left[(\text{gravity})^2\times U(1)_{B-L}\right] &= \mathcal{A}_2^{\text{SM}}\left[(\text{gravity})^2\times U(1)_{B-L}\right] = -3\,. \end{aligned} \tag{3.1}$$

Remarkably, if three right handed neutrinos with $B-L$ charge -1 each are added to the model, they contribute $\mathcal{A}_1^{\text{New}}\left[U(1)^3_{B-L}\right] = 3, \mathcal{A}_2^{\text{New}}\left[(\text{gravity})^2\times U(1)_{B-L}\right] = 3$ leading to vanishing amount of triangle anomalies. This is one of the most economical setup for anomaly cancellation and hence we adopt it for our purpose.

The complex singlet scalar having $B-L$ charge 2 not only leads to spontaneous breaking of gauge symmetry but also generates RHN masses dynamically. In this work, we simply add one vector like fermion $\chi$ to the minimal gauged $B-L$ model having $B-L$ charge $q_\chi \neq 0$, which acts as a DM candidate[2]. In order to ensure its stability we choose $q_\chi \neq 1$ and fix it at an order one value of $4/3$ for numerical calculations in our analysis. The gauge invariant Lagrangian of the model can be written as

$$\mathcal{L} \;=\; \mathcal{L}_{\text{SM}} - \frac{1}{4}B'_{\alpha\beta}\,B'^{\alpha\beta} + \mathcal{L}_{\text{scalar}} + \mathcal{L}_{\text{fermion}}\,, \tag{3.2}$$

where $\mathcal{L}_{\text{SM}}$ represents the SM Lagrangian involving quarks, gluons, charged leptons, left handed neutrinos and electroweak gauge bosons. The second term in the $\mathcal{L}$ indicates the kinetic term of $B-L$ gauge boson ($Z_{BL}$), expressed in terms of field strength tensor $B'^{\alpha\beta} = \partial^\alpha Z^\beta_{BL} - \partial^\beta Z^\alpha_{BL}$. The gauge invariant scalar Lagrangian of the model (involving

[2]It is important to note that the lightest RHN $N_1$ can also act as a DM candidate by imposing a $Z_2$ symmetry under which it is $Z_2$ odd, whereas the SM particles are $Z_2$ even. However, if we also want to incorporate cosmic inflation, it is not possible to realise thermal WIMP DM in such a setup, mainly because of constraints from inflation on the $B-L$ gauge coupling, as shown in details in Ref. [173]. While $N_1$ could still be a warm DM candidate, if we demand one of the other RHNs to act as a LLP, then we cannot explain neutrino mass in this minimal setup.

SM Higgs $H_S$ and singlet scalar $\Phi$) is given by,

$$\mathcal{L}_{\text{scalar}} = (D_\mu H_S)^\dagger (D^\mu H_S) + (D_\mu \Phi)^\dagger (D^\mu \Phi) - V(H_S, \Phi)\,, \tag{3.3}$$

where,

$$\begin{aligned} V(H_S, \Phi) = &-\mu_1^2 |H_S|^2 - \mu_2^2 |\Phi|^2 + \lambda_1 |H_S|^4 \\ &+\lambda_2 |\Phi|^4 + \lambda_3 |H_S|^2 |\Phi|^2. \end{aligned} \tag{3.4}$$

The covariant derivatives of scalar fields are written as,

$$D_\mu H_S = \left(\partial_\mu + i\frac{g_1}{2}\sigma_a W_\mu^a + i\frac{g_2}{2} B_\mu\right) H_S, \tag{3.5}$$

$$D_\mu \Phi = \left(\partial_\mu + i2 g_{\text{BL}} Z_{BL\mu}\right) \Phi, \tag{3.6}$$

with $g_1$ and $g_2$ being the gauge couplings of $SU(2)_L$ and $U(1)_Y$ respectively and $W_\mu^a$ ($a$ = 1, 2, 3), $B_\mu$ are the corresponding gauge fields. On the other hand $Z_{BL}$, $g_{BL}$ are the gauge boson and gauge coupling respectively for $U(1)_{B-L}$ gauge group. The gauge invariant Lagrangian involving RHNs and DM $\chi$ can be written as

$$\begin{aligned} \mathcal{L}_{\text{fermion}} = &\, i \sum_{\kappa=1}^{3} \overline{N_{R_\kappa}} D(Q_\kappa^R) N_{R_\kappa} - \sum_{\substack{j=1 \\ \alpha=e,\mu,\tau}}^{3} Y_D^{\alpha j}\, \overline{l_L^\alpha} \tilde{H}_S N_R^j \\ &- \sum_{i,j=1}^{3} Y_{N_{ij}} \Phi\, \overline{N_{R_i}^C} N_{R_j} + \overline{\chi} \gamma^\mu (\partial_\mu + i g_{BL} q_\chi Z_{BL_\mu}) \chi \\ &- m_\chi \overline{\chi} \chi. + \text{h.c.} \end{aligned} \tag{3.7}$$

The covariant derivative for $N_{R\kappa}$ is defined as

$$D(Q_\kappa^R)\, N_{R_\kappa} = \gamma^\mu \left(\partial_\mu + i g_{BL}\, Q_\kappa^{(R)}\, Z_{BL\mu}\right) N_{R_\kappa}\,, \tag{3.8}$$

with $Q_\kappa^R = -1$ is the $B - L$ charge of right handed neutrino $N_{R_\kappa}$. Hereafter, we denote the RHNs by $N_i, i = 1, 2, 3$ only without explicitly specifying their chirality.

After spontaneous breaking of both $B-L$ symmetry and electroweak symmetry, the SM Higgs doublet and singlet scalar fields are expressed as,

$$H_S = \begin{pmatrix} H_S^+ \\ \frac{h+v+iA}{\sqrt{2}} \end{pmatrix}, \quad \Phi = \frac{\phi + v_{BL} + iA'}{\sqrt{2}} \tag{3.9}$$

where $v$ and $v_{BL}$ are vacuum expectation values (VEVs) of $H_S$ and $\Phi$ respectively. The right handed neutrinos and $Z_{BL}$ acquire masses after the $U(1)_{B-L}$ breaking as,

$$M_{Z_{BL}} = 2g_{BL}v_{BL}, \tag{3.10}$$

$$M_{N_i} = \sqrt{2}Y_{N_i}v_{BL}. \tag{3.11}$$

We have considered diagonal Yukawa matrix $Y_N$ in the $(N_1, N_2, N_3)$ basis. Using Eqn.(3.10) and Eqn.(3.11), it is possible to relate $M_{Z_{BL}}$ and $M_{N_i}$ by,

$$M_{N_i} = \frac{1}{\sqrt{2}g_{BL}} Y_{N_i} M_{Z_{BL}}. \tag{3.12}$$

After the spontaneous breaking of $SU(2)_L \times U(1)_Y \times U(1)_{B-L}$ gauge symmetry, the mixing between scalar fields $h$ and $\phi$ appears and can be related to the physical mass eigenstates $H_1$ and $H_2$ by a rotation matrix as,

$$\begin{pmatrix} H_1 \\ H_2 \end{pmatrix} = \begin{pmatrix} \cos\theta & -\sin\theta \\ \sin\theta & \cos\theta \end{pmatrix} \begin{pmatrix} h \\ \phi \end{pmatrix}, \tag{3.13}$$

where the scalar mixing angle $\theta$ is found to be

$$\tan 2\theta = -\frac{\lambda_3 v v_{BL}}{(\lambda_1 v^2 - \lambda_2 v_{BL}^2)}. \tag{3.14}$$

The mass eigenvalues of the physical scalars are given by,

$$M_{H_1}^2 = 2\lambda_1 v^2 \cos^2\theta + 2\lambda_2 v_{BL}^2 \sin^2\theta - 2\lambda_3 v v_{BL} \sin\theta\cos\theta, \tag{3.15}$$

$$M_{H_2}^2 = 2\lambda_1 v^2 \sin^2\theta + 2\lambda_2 v_{BL}^2 \cos^2\theta + 2\lambda_3 v v_{BL} \sin\theta\cos\theta. \tag{3.16}$$

Here $M_{H_1}$ is identified as the SM Higgs mass whereas $M_{H_2}$ is the singlet scalar mass.

One of the strong motivations of the minimal $U(1)_{B-L}$ model is the presence of heavy RHNs which can yield correct light neutrino mass via type I seesaw mechanism. The analytical expression for the light neutrino mass matrix is

$$m_\nu = m_D M_N^{-1} m_D^T, \tag{3.17}$$

where $m_D = Y_D v/\sqrt{2}$. We consider the right handed neutrino mass matrix $M_N$ to be diagonal. Since in our case one of the RHNs (say $N_3$) is long lived, it interacts with SM leptons very feebly, the lightest active neutrino would be very tiny.

There are several theoretical and experimental constraints that restrict the model parameters of the minimal $U(1)_{B-L}$ model. To begin with, the criteria to ensure the scalar potential bounded from below yields following conditions involving the quartic couplings,

$$\lambda_{1,2,3} \geq 0,\ \lambda_3 + \sqrt{\lambda_1\lambda_2} \geq 0 \tag{3.18}$$

On the other hand, to avoid perturbative breakdown of the model, all dimensionless couplings must obey the following limits at any energy scale,

$$|\lambda_{1,2,3}| < 4\pi,\ |Y_D, Y_N| < \sqrt{4\pi},\ |g_1, g_2, g_{BL}| < \sqrt{4\pi}. \tag{3.19}$$

The non-observation of the extra neutral gauge boson in the LEP experiment [174, 175] imposes the following constraint on the ratio of $M_{Z_{BL}}$ and $g_{BL}$ :

$$\frac{M_{Z_{BL}}}{g_{BL}} \geq 7 \text{ TeV}. \tag{3.20}$$

The recent bounds from the ATLAS experiment [176, 177] and the CMS experiment [178] at the LHC rule out additional gauge boson masses below 4-5 TeV from analysis of 13 TeV centre of mass energy data. However, such limits are derived by considering the corresponding gauge coupling $g_{BL}$ to be similar to the ones in electroweak theory and hence the bounds become less stringent for smaller gauge couplings.

Additionally, the parameters associated with the singlet scalar of the model are also constrained [179, 180] due to the non-zero scalar-SM Higgs mixing. The bounds on scalar singlet-SM Higgs mixing angle arise from several factors namely $W$ boson mass correction [181] at NLO, requirement of perturbativity and unitarity of the theory, the LHC and LEP direct search [182, 183] and Higgs signal strength measurement [183]. If the singlet scalar turns lighter than SM Higgs mass, SM Higgs can decay into a pair of singlet scalars. Latest measurements by the ATLAS collaboration restrict such SM Higgs decay branching ratio into invisible particles to be below 13% [184] at 95% CL.

In our case, we work with very small singlet scalar-SM Higgs mixing and considered all the scalar quartic couplings to be positive. These help in evading the bounds on scalar singlet mixing angle and the boundedness of the scalar potential from below. We choose the magnitude of the relevant couplings below their respective pertubativity limits.

## 3.3 Thermal keV DM and leptogenesis

As mentioned before, keV scale dark matter $\chi$ gets thermally overproduced requiring late entropy injection from heavier RHNs (we consider late decay of $N_3$). In order to fully track the evolution of the system we solve the Boltzmann equations for $N_3$ and the SM temperature, given by Eqns. (2.1), (2.2) (with $\phi \to N_3$) along with the Boltzmann equation

for DM given by

$$\frac{dE_\chi}{da} = \frac{\langle\sigma v\rangle_\chi}{Ha^4}\left((E_\chi^{\rm eq})^2 - E_\chi^2\right) . \tag{3.21}$$

$N_3$ is considered to freeze out while being non-relativistic in a way similar to WIMP type DM belonging to CDM category. This can be ensured if $N_3$ is heavy enough $M_{N_3} \sim \mathcal{O}(M_{Z_{BL}})$. The interaction cross-sections for the light dark matter $\chi$ (denoted by $\langle\sigma v\rangle_\chi$) is dominated by the $Z_{BL}$ mediated annihilations into SM fermions [185]. On the other hand, the heaviest RHN $N_3$ can annihilate to SM particles as well as $\{Z_{BL}Z_{BL}, Z_{BL}H_2, Z_{BL}H_2, H_2H_2, N_{1,2}N_{1,2}, \chi\chi\}$ final states. We incorporate all the relevant processes in thermally averaged annihilation cross sections for both $\chi$ and $N_3$. Here we do not include other RHNs $N_{1,2}$ considering them to decay promptly into SM leptons having negligible impact on DM phenomenology. In the left panel of Fig. 3.1, we show the evolution of the DM interaction rate ($\Gamma$) and the expansion rate of a radiation dominated Universe (Hubble parameter) for different $g_{BL}$ values keeping $M_{Z_{BL}}$ fixed at 10 TeV. The right panel shows the same for varying $M_{Z_{BL}}$ values, with $g_{BL}$ being fixed at 0.05. It is clear from these plots that for lower $g_{BL}$ and higher $M_{Z_{BL}}$ values, $\chi$ decoupling occurs earlier with dark matter being relativistic, due to smaller interaction rate. Note that, lowering $g_{BL}$ also makes DM enter into equilibrium at late epochs and decreasing it beyond a particular value may not lead to its thermalisation at all.

We solve the system of Boltzmann equations (Eqns. (2.1), (2.2), (3.21)) in the post-reheating era, assuming the initial value of the scale factor and temperature satisfying $T_i a_i = 1$. The relevant independent parameters which are crucial for DM phenomenology are given by,

$$\left\{g_{BL}, M_{Z_{BL}}, M_{N_3}, \Gamma_{N_3}\right\}. \tag{3.22}$$

The mass scale $M_{N_3}$ and $M_{Z_{BL}}$ are connected through the stability condition $\Delta \sim 0$ at inflationary energy scale (see Appendix B). The scalar sector couplings are considered to be small and have little impact on the DM phenomenology except the $\lambda_2$ which fixes $M_{H_2}$.

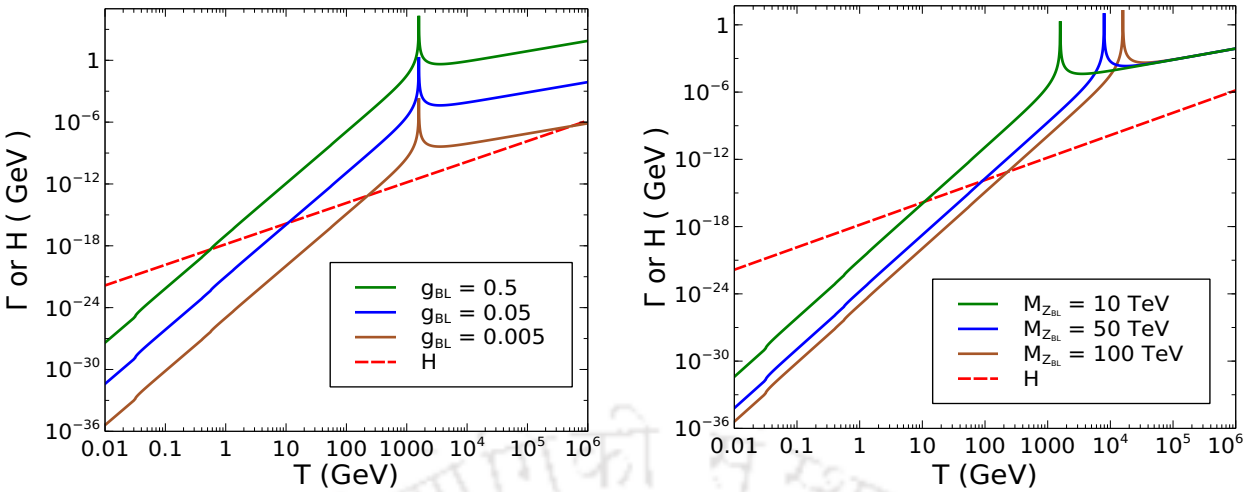


FIGURE 3.1: DM interaction rate and Hubble parameter in a radiation dominated Universe as function of temperature for different $g_{BL}$ values (left panel) and different $M_{Z_{BL}}$ values (right panel).

The decay of $N_3$ can occur dominantly at tree level to SM Higgs and leptons in the final states. The decay width of the $N_3$ is proportional to $|Y_D^{\alpha 3}|^2 M_{N_3}$ where we have always considered $M_{N_3} > M_{H_1} \simeq 125$ GeV.

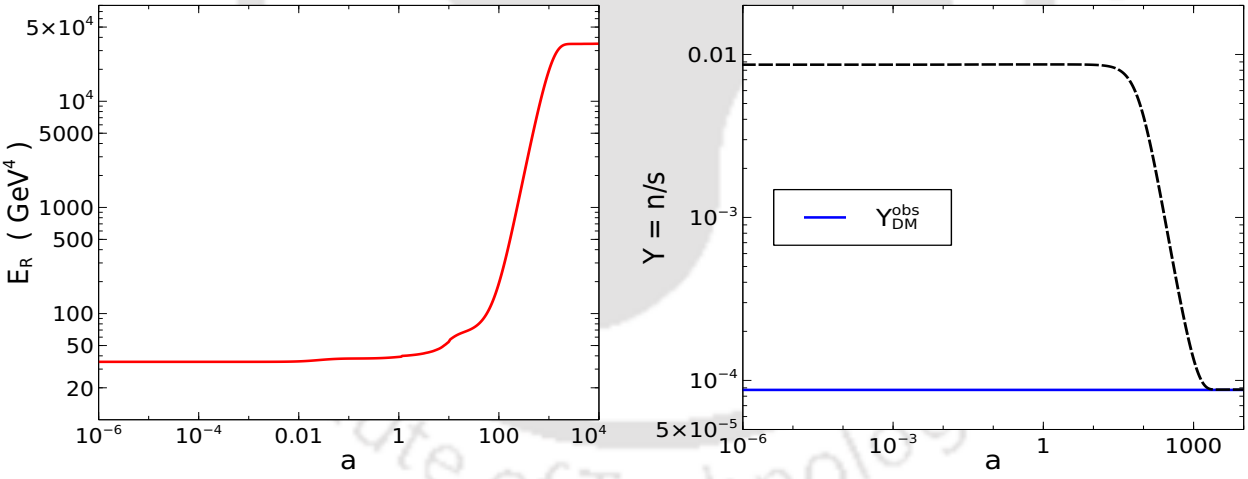


FIGURE 3.2: *Left panel*: Enhancement of radiation energy density is shown due to $N_3$ decay at late time. *Right panel*: The evolution of comoving DM density (dashed line) as function of scale factor where the effect of late time entropy dilution can be clearly observed. The blue solid line corresponds to the required comoving DM number density at present epoch from observations.

We first stick to a benchmark scenario (as given in Table 3.1) to explain the dynamics of the DM phenomenology. The solution of the coupled Boltzmann equations for the benchmark point in Table 3.1 are shown in Figs. 3.2, 3.3. The left panel of Fig. 3.2 shows

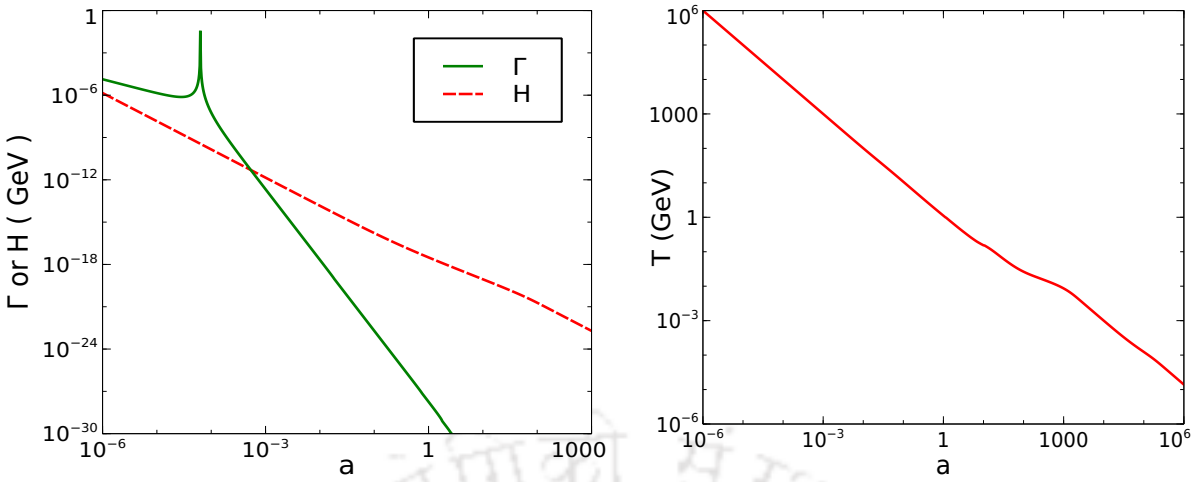


FIGURE 3.3: *Left panel*: The interaction rate of DM $\chi$ in comparison to Hubble expansion rate of the Universe with an intermediate $N_3$ dominated phase. It is seen that the DM decouples before $N_3$ dominates (see Fig. 3.2) the energy density of the Universe for the benchmark point as listed in Table 3.1. *Right panel*: The temperature evolution of the Universe with an intermediate $N_3$ dominated phase.

| Parameters | Values |
|---|---|
| $g_{BL}$ | 0.01 |
| $M_{Z_{BL}}$ | 100 TeV |
| $M_{DM}$ | 5 keV |
| $\Gamma_{N_3}$ | $10^{-22}$ GeV |

TABLE 3.1: Benchmark point used for Figs. 3.2, 3.3

the enhancement of radiation energy density ($E_R = \rho_R a^4$) from out-of-equilibrium decay of $N_3$ at late epoch. In the right panel of Fig. 3.2, the evolution of comoving DM density (dashed line) is shown as a function of the scale factor which goes through late time dilution due to sizeable entropy production from $N_3$ decay. For the chosen benchmark point, the final relic abundance exactly matches the measured one by Planck 2018, shown by the solid blue line. In the left panel of Fig. 3.3, we draw a comparison between the interaction rate of $\chi$ and the Hubble parameter by considering an intermediate $N_3$ dominated era. We find that DM reaches thermal equilibrium at early epochs, prior to $N_3$ domination, and decouples before the $N_3$ domination in the Hubble parameter sets in. The right panel of Fig. 3.3 shows the temperature evolution with the scale factor. The temperature varies as $\sim \frac{1}{a}$ before the start of $N_3$ domination as well as after the completion of $N_3$ decay with a small kink when $N_3$ decays indicating the entropy injection. In between for a brief period,

different pattern of the temperature evolution is observed which is due to $N_3$ domination and the entropy injection into the radiation bath.

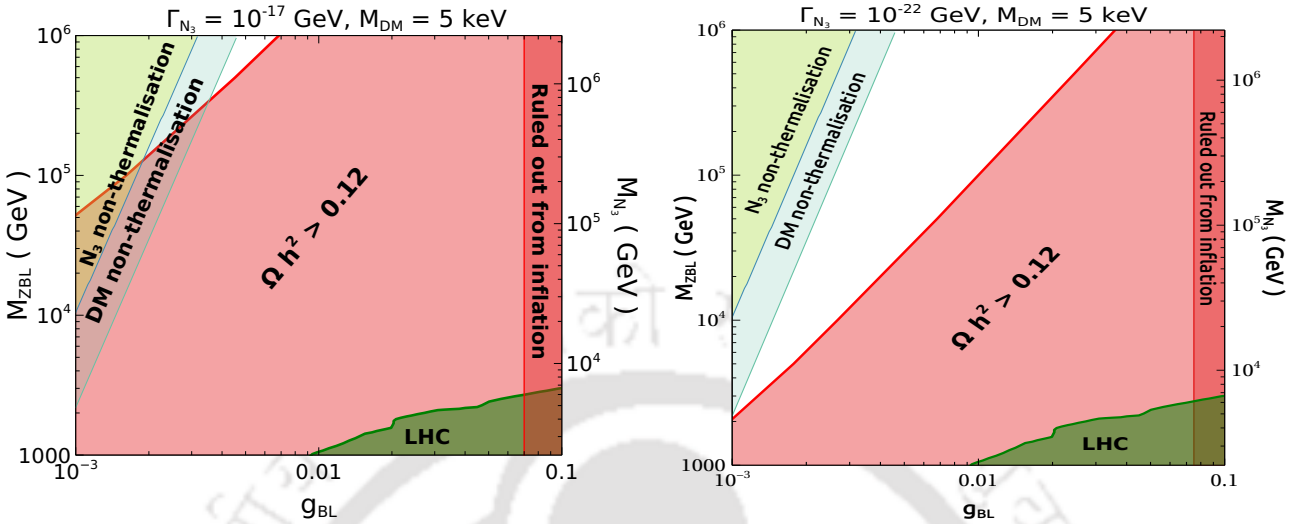


FIGURE 3.4: Parameter space in $g_{BL} - M_{Z_{BL}}$ plane after imposing all relevant constraints. Only the white region is allowed leading to observed DM relic $\Omega_\chi h^2 \lesssim 0.12$. Decay width of $N_3$ is fixed at $\Gamma_{N_3} = 10^{-17}$ GeV (left panel), $\Gamma_{N_3} = 10^{-22}$ GeV (right panel).

We then perform a numerical scan by fixing $\Gamma_{N_3}$ at two different benchmark values to constrain the $g_{BL} - M_{Z_{BL}}$ plane from the condition of satisfying the five requirements namely, (i) $N_3$ thermalisation at early epochs, (ii) $\chi$ thermalisation at early epochs, (iii) bound on $g_{BL}$ from inflationary dynamics (see Appendix B), (iv) LHC bounds and (v) correct final relic of DM. The resulting parameter space after applying all relevant bounds is shown in Fig. 3.4. The left panel is for $\Gamma_{N_3} = 10^{-17}$ GeV while in the right panel we have $\Gamma_{N_3} = 10^{-22}$ GeV. The mass of $N_3$ is varied in the range of $10^3 - 10^6$ GeV as shown in the figure. The light blue and light green regions in the upper left corners are ruled out due to non-thermalisation of $\chi$ and $N_3$ respectively. The region corresponding to larger values of $g_{BL}$ are disfavoured by inflationary criteria mentioned earlier. The pink shaded region corresponds to DM overabundance or equivalently, insufficient entropy dilution from $N_3$ decay. The disfavored region from the LHC in the same plane is also highlighted by the brown shaded region. The relatively weaker bound from the LHC results from the search for high mass dilepton resonances. Note that the expression for $\Gamma_{N_3}$ contains $M_{N_3}$ which varies for each point (satisfying the condition $\Delta = 0$) in the $g_{BL} - M_{Z_{BL}}$ plane, however

a constant $\Gamma_{N_3}$ can always be obtained by tuning the neutrino Yukawa coupling $Y_D^{\alpha 3}$. We identify the allowed region (white) where the first four constraints mentioned above are satisfied and also DM relic corresponds $\Omega h^2 \lesssim 0.12$. Along the boundary line between pink and white coloured regions corresponding to correct DM relic $\Omega_\chi h^2 \sim 0.12$, larger $g_{BL}$ requires heavier $Z_{BL}$. This attributes to the fact that, for a fixed $M_{Z_{BL}}$ a larger value of $g_{BL}$ makes the $N_3$ to decouple later from the radiation bath. This leads to suppressed freeze-out abundance of $N_3$ and eventually reduced amount of entropy production from its decay. To obviate that, one needs to raise $M_{Z_{BL}}$ accordingly in order to decrease the interaction cross section for $N_3$ and successively obtaining the correct relic abundance. In the same context, a larger $\Gamma_{N_3}$ (early decay of $N_3$) for constant $g_{BL}$ and $M_{Z_{BL}}$ means lower impact on dilution of DM abundance. Hence we see less amount of allowed region (white) in the left panel of Fig. 3.4 compared to the right panel with lower $\Gamma_{N_3}$.

To show the dependence on $N_3$ decay width further, in Fig. 3.5, we obtain the relic satisfied region ($\Omega h^2 \lesssim 0.12$) in $M_{\rm DM} - \Gamma_{N_3}$ plane considering two different sets of $(g_{BL}, M_{Z_{BL}})$. The allowed space shrinks significantly for larger $g_{BL}$ since the freeze-out of $N_3$ is delayed compared to the scenario with smaller $g_{BL}$ value leading to less entropy dilution. Also, for larger DM mass, the required order of $\Gamma_{N_3}$ is smaller to bring the DM abundance within the desired limit. This is due to the fact that larger DM mass yields enhanced relic and hence needs larger amount of entropy injection to the SM bath at late epochs for sufficient dilution of overproduced thermal DM relic. It is pertinent to comment here that the decay width of $N_3$ cannot be arbitrary small. Decay of $N_3$ around or after the epoch of big bang nucleosynthesis (BBN) may raise the neutrino temperature [186] which is strictly restricted by the number of relativistic degrees of freedom during BBN as measured by Planck [14]. In view of this, it is safe to keep lifetime ($\tau_{N_3}$) of $N_3$ typically below few seconds. We have highlighted the corresponding bound on $\Gamma_{N_3}$ (red) in Fig. 3.5.

**Neutrino mass and leptogenesis**: It is clear from the above discussion that one requires very small decay width of the $N_3$ for adequate entropy production which dilutes

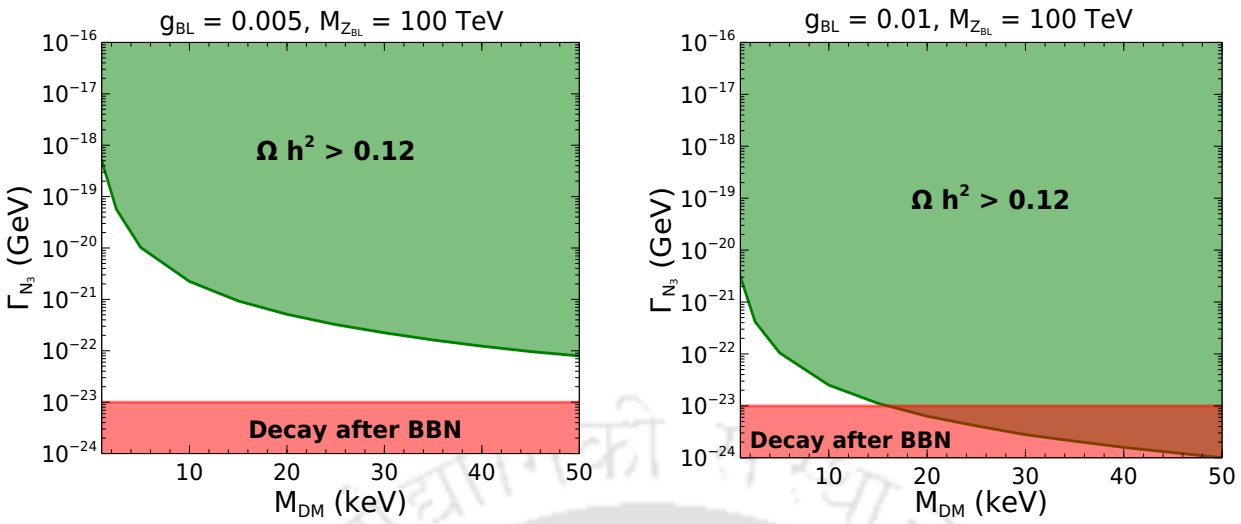


FIGURE 3.5: Parameter space in $M_{\rm DM} - \Gamma_{N_3}$ plane for two sets of $(g_{BL}, M_{Z_{BL}})$ values. A lower bound on $\Gamma_{N_3}$ is also shown such that $N_3$ decays completely before the BBN.

the thermally overproduced DM relic. This, in turn, will require tiny Dirac Yukawa coupling of $N_3$ ($Y_D^{\alpha 3}$) with SM leptons. We anticipate that such smallness of $Y_D^{\alpha 3}$ can be associated with unique prediction of lightest active neutrino mass. The other entries of Dirac Yukawa matrix can satisfy the neutrino oscillation data since dynamics or interaction pattern of $N_1$ and $N_2$ are not relevant for DM phenomenology within our setup.

We can write the Dirac Yukawa couplings in terms of neutrino parameters using the Casas Ibarra parameterization (cf. Eqn. (1.41)). We make the following choice of $\mathbb{R}$ [187]

$$\mathbb{R} = \begin{pmatrix} 0 & \cos\gamma & \sin\gamma \\ 0 & -\sin\gamma & \cos\gamma \\ 1 & 0 & 0 \end{pmatrix}, \tag{3.23}$$

in order to be consistent with feebly coupled $N_3$. In the DM phenomenology, we have worked in the limit: $Y_D^{\alpha 1}, Y_D^{\alpha 2} \ll Y_D^{\alpha 3}$. Note that $\Gamma_{N_3} \simeq \frac{1}{16\pi}\sum_\alpha \left|Y_D^{\alpha 3}\right|^2$ [3]. We express the diagonal SM neutrino mass matrix $m_\nu^d$ as $\{m_{\nu_l}, \sqrt{m_{\nu_1}^2 + \Delta m_{21}^2}, \sqrt{m_{\nu_1}^2 + \Delta m_{31}^2}\}$ considering normal hierarchy and the lightest active neutrino mass $m_{\nu_l}$ as a free parameter. We have also used the best fit values for $\Delta m_{21}^2$ and $\Delta m_{21}^2$ and neutrino mixing angles [33] with

[3] $N_3$ has two decay modes at tree level: (i) $N_3 \to h\nu_\alpha$ with $\Gamma_{N_3 \to h\nu_\alpha} \propto |Y_D^{\alpha 3}|^2 M_{N_3}$ and (ii) $N_3 \to Z_{BL}\nu_\alpha$ with $\Gamma_{N_3 \to Z_{BL}\nu_\alpha} \propto \frac{|Y_D^{\alpha 3}|^2 v^2}{M_{N_3}} g_{BL}^2$. When $M_{N_3} > v = 246$ GeV and $g_{BL} \ll 1$ the later decay process of $N_3$ is always subdominant.

| | $m_{\rm DM}$ | $g_{BL}$ | $M_{Z_{BL}}$ (GeV) | $M_{N_3}$ (GeV) | $\Gamma_{N_3}$ (GeV) | $m_{\nu_l}$ (eV) |
|---|---|---|---|---|---|---|
| BP I | 5 keV | 0.0025 | $7.7 \times 10^4$ | $1.7 \times 10^5$ | $4 \times 10^{-19}$ | $\mathcal{O}(10^{-14})$ |
| BP II | | 0.005 | $8.2 \times 10^4$ | $1.8 \times 10^5$ | $4.7 \times 10^{-21}$ | $\mathcal{O}(10^{-16})$ |

TABLE 3.2: Two representative benchmark points of our proposed set up that simultaneously provide correct DM relic and also uniquely predict the order of lightest active neutrino mass.

Dirac CP violating parameter $\delta_{CP} = \frac{5\pi}{2}$. Note that the eigenvalues of the neutrino mass matrix is independent of elements of $\mathbb{R}$ matrix.

In Fig. 3.6, we show different contours (dashed) for $m_{\nu_l} = \{10^{-14}, 10^{-15}, 10^{-16}, 10^{-17}\}$ eV in the $\Gamma_{N_3} - M_{Z_{BL}}(M_{N_3})$ plane. We also show the relic density satisfied lines (solid) in the same plane for three different values of $g_{BL}$ considering $M_{\rm DM} = 5$ keV. The requirement of DM thermalisation in the early Universe which rules out grey shaded region in Fig. 3.6, restricts the lightest neutrino mass to be $m_{\nu_l} \lesssim \mathcal{O}(10^{-14})$ eV. We infer from this figure that the $B - L$ gauge coupling is correlated with the lightest active neutrino mass for a fixed set of $\Gamma_{N_3}$ and $M_{\rm DM}$. Any intersecting point between constant $g_{BL}$ and constant $m_{\nu_l}$ contours in Fig. 3.6 provides us suitable choices of the model parameters that simultaneously can yield correct DM relic with required entropy dilution and satisfy the neutrino oscillation data with definite prediction of lightest active neutrino mass. As an example, in Table 3.2 we tabulate two benchmark points that illustrate such interesting correlations.

Next, we check whether the proposed framework can accommodate successful baryogenesis via leptogenesis [53] in the presence of same amount of late time entropy production that dilutes the thermally overproduced DM relic. For this purpose we utilise the first benchmark point, tabulated in Table 3.2. The free parameters that remain unconstrained from the dynamics of inflation, phenomenology of dark matter and prediction of lightest neutrino mass are the mass scales $M_{N_1}, M_{N_2}$ and the rotation angle $\gamma$. The dependence of neutrino parameters data on $M_{N_1}, M_{N_2}$ can be absorbed in the respective Dirac Yukawa couplings. Note that, $N_3$ being feebly coupled to SM leptons, contributes negligibly to the production of lepton asymmetry, as compared to $N_1$ and $N_2$. The Boltzmann equations that govern the dynamics for $N_1$, $N_2$ decay and the yield of $B - L$ asymmetry are given

by [188],

$$aH\frac{dn_1}{da}+3Hn_1=-\gamma_{D_1}\left(\frac{n_1}{n_1^{\rm eq}}-1\right)-\left\{\left(\frac{n_1}{n_1^{\rm eq}}\right)^2-1\right\}\gamma_{Z^1_{BL}}, \tag{3.24}$$

$$aH\frac{dn_2}{da}+3Hn_2=-\gamma_{D_2}\left(\frac{n_2}{n_2^{\rm eq}}-1\right)-\left\{\left(\frac{n_2}{n_2^{\rm eq}}\right)^2-1\right\}\gamma_{Z^2_{BL}}, \tag{3.25}$$

$$aH\frac{dn_{B-L}}{da}+3Hn_{B-L}=-\sum_{j=1}^{2}\left\{\frac{1}{2}\frac{n_{B-L}}{n_L^{\rm eq}}+\varepsilon_j\left(\frac{n_{N_j}}{n_{N_j}^{\rm eq}}-1\right)\right\}\gamma_{D_j}, \tag{3.26}$$

where $n_i(n_{B-L})$ are the number densities for $N_i$ ($B-L$ asymmetry) and $\varepsilon_i$ represents the lepton asymmetry parameter. The standard convention to express the comoving abundance of $B-L$ asymmetry is given by $\frac{n_{B-L}}{s}$, with the entropy density defined as $s=\frac{2\pi^2}{45}g_{*s}T(a)^3$. The $\gamma_{D_i}$ includes the effects of decays and inverse decays while $\gamma_{Z^i_{BL}}$ takes into account the contribution from the $Z_{BL}$ mediated scatterings $ff\leftrightarrow N_iN_i$ (see [188] for the analytical expressions). We do not include the other $2\to 2$ processes since their effects turn out to be sub-dominant in the present analysis [188, 189]. The temperature and the entropy density of the Universe as function of scale factor are evaluated using Eqn. (2.2). Recall that earlier we have considered $Y_{N_{1,2}}\ll Y_{N_3}$. The value of $M_{N_3}$ is $\mathcal{O}(10^5)$ GeV in the first benchmark of Table 3.2. For illustrative purpose, we consider a low scale leptogenesis and fix $M_{N_1}$ at 2 TeV and write $M_{N_2}=M_{N_1}+\Delta$. In that case the amount of lepton asymmetry essentially depends on $\Delta$ and $\gamma$ only, once the other parameters are fixed according to BP I in Table 3.2 with $M_{N_1}=2$ TeV. As discussed in chapter 2, production of sufficient lepton asymmetry from such TeV scale RH neutrinos (violating the Davidson Ibara bound [73]) is possible only in the resonant scenario.

Next, we look for a particular set of $\{\Delta,\gamma\}$ such that we obtain required order of baryon asymmetry (consistent with the observation), surviving the combined effect of washouts and late time entropy dilution. We have made the choice $\Delta=9\times10^{-14}$ GeV and $\gamma=0.7+0.5i$ for the BP I in Table 3.2. Below we note down the numerical estimate

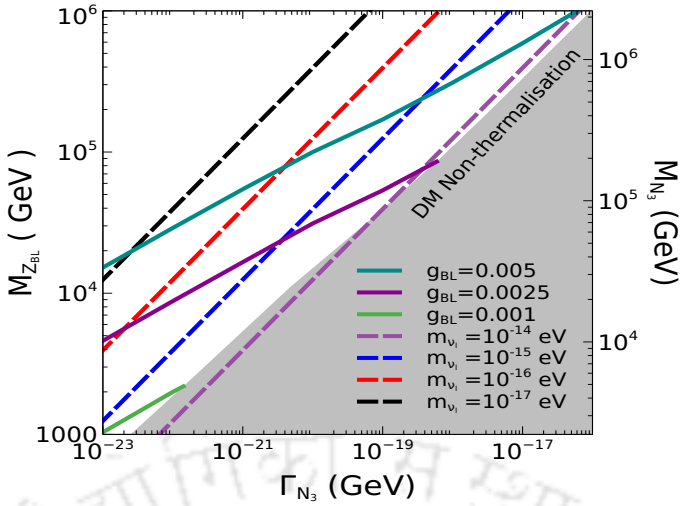


FIGURE 3.6: Contours of lightest neutrino mass in $\Gamma_{N_3} - M_{Z_{BL}}(M_{N_3})$ plane. The DM relic satisfied contours are also shown for different $g_{BL}$ values considering $M_{\rm DM} = 5$ keV.

the neutrino Yuwkawa matrix as obtained by implementing the Casas Ibarra parametrisation following Eqn. (1.41). The Yukawa structure for $N_1$ and $N_2$ turns out to be (considering the mass of the lightest active neutrino vanishing),

$$Y_D^{3\times 2} = \begin{pmatrix} 1.67\times 10^{-7} + 5.52\times 10^{-7}\, i & 9\times 10^{-7} + 1.48\times 10^{-9}\, i \\ -3.42\times 10^{-7} - 4.32\times 10^{-7}\, i & -1.13\times 10^{-6} + 2.12\times 10^{-7}\, i \\ 1.42\times 10^{-6} + 3.78\times 10^{-7}\, i & 8.19\times 10^{-7} - 6.54\times 10^{-7}\, i \end{pmatrix}. \tag{3.27}$$

This particular Yukawa structure yields following outputs

$$\Gamma_{N_1} = 2.2\times 10^{-10}, \quad \Gamma_{N_2} = 2.6\times 10^{-10} \tag{3.28}$$

$$\varepsilon_1 = 0.00048, \quad \varepsilon_2 = 0.00056. \tag{3.29}$$

We also find $\Delta = 0.0004\times\Gamma_{N_1} = 0.00034\times\Gamma_{N_2}$. It is pertinent to affirm that the neutrino oscillation data is automatically satisfied since we have used the best fit values for $\Delta m^2_{21}$, $\Delta m^2_{31}$ and neutrino mixing angles in the Casas Ibara parametrisation as earlier mentioned considering vanishing lightest active neutrino mass. We have solved Eqns. (3.24)-(3.26) assuming $N_1$ and $N_2$ to follow the equilibrium distribution initially with the temperature same as the one of SM thermal bath. The generated lepton asymmetry gets converted

to baryon asymmetry of the Universe via standard sphaleron process till $T \sim 100$ GeV which is quantified by Eqn. (1.39). In left of Fig. 3.8, we show the evolution of $\frac{|n_{B-L}|}{s}$ as function of scale factor considering the set $\{\Delta = 9 \times 10^{-14}\,\text{GeV}, \gamma = 0.7 + 0.5i\}$ till $a \sim 0.01$ which approximately implies $T \sim 100$ GeV. At this temperature, the conversion of lepton asymmetry to baryon asymmetry ends since the $SU(2)_L$ sphaleron processes get switched off. In right of left of Fig. 3.8, we have shown the evolution pattern for baryon asymmetry from $T \sim 100$ GeV till the present epoch.

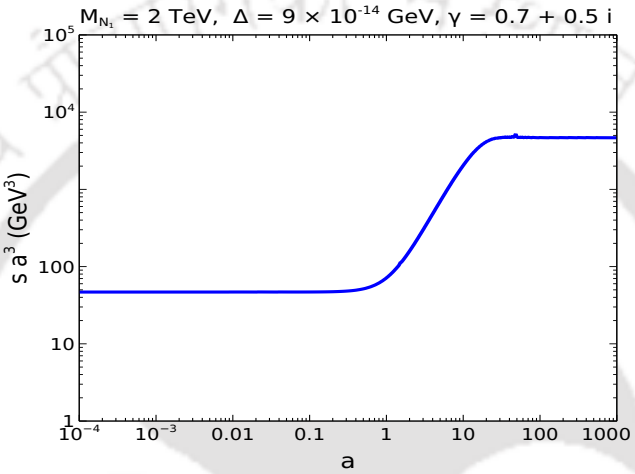


FIGURE 3.7: Evolution of entropy density as function of scale factor is shown for the BP I as tabulated in Table 3.2.

We see that initially $\frac{|n_{B-L}|}{s}$ gets produced from the out of equilibrium decay of $N_1$ and $N_2$. Once the production ends, $\frac{|n_{B-L}|}{s}$ decreases to some extent due to the wash-out effects like inverse decay and then freezes to a particular amount, resulting in the plateau region till $a \sim 0.01$. At this point with $T \sim 100$ GeV, we use Eqn.(1.39) to obtain the $\frac{n_B}{s}$ and then find out its evolution as function of scale factor till present epoch. From Fig. 3.7, we see a late time enhancement of the entropy density ($s$) due to long lived $N_3$ decay. This results into dilution of the $\frac{n_B}{s}$ from its value at $a \sim 0.01$ and we finally obtain the remnant amount of $\frac{n_B}{s} \sim (9 \times 10^{-11})$ which overlaps with the observed baryon asymmetry of the Universe [14]. Thus the present framework indeed offers the possibility to realise successful baryogenesis via leptogenesis satisfying inflationary bounds on model parameters and WDM relic abundance with significant late time entropy dilution.

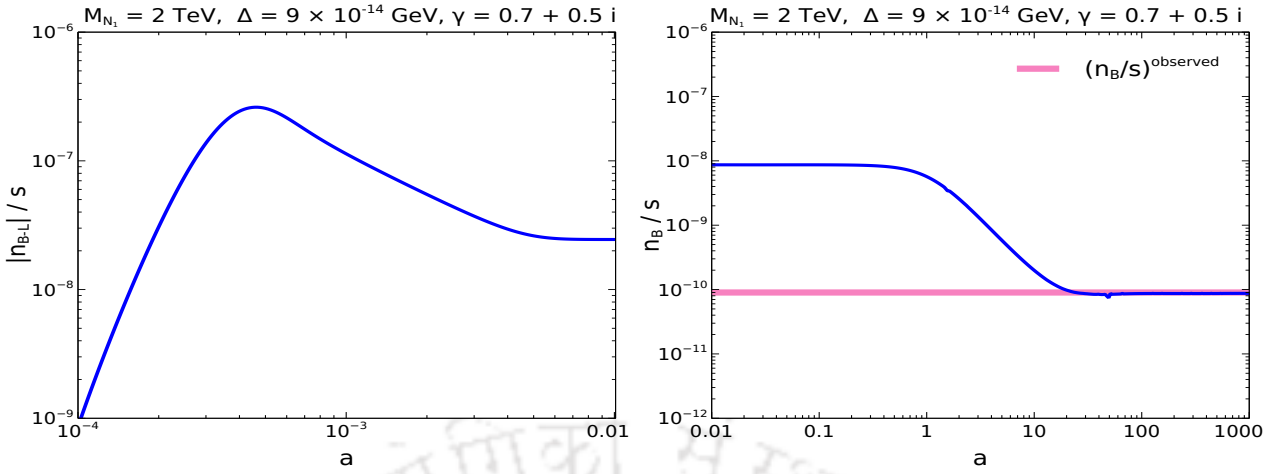


FIGURE 3.8: [Left] Evolution of $B-L$ asymmetry as function of scale factor for the benchmark point I as tabulated in Table 3.2 till $T \sim 100$ GeV. [Right] The evolution of baryon asymmetry from $T \sim 100$ GeV till the present epoch is shown. The choice of $\Delta$ and $\gamma$ have been made such that we attain observed value of baryon asymmetry $\sim 9 \times 10^{-11}$[14] (as indicated by the horizontal red line) of the Universe considering a TeV scale $N_1$.

As mentioned earlier, keV scale warm dark matter can alleviate some of the small scale structure issues of cold dark matter paradigm. Due to larger free-streaming length, such WDM scenarios can give rise to different structure formation rates which can be probed by several galaxy survey experiments. For example, the authors of [190] constrained thermal WDM mass around keV scale by comparing the predictions of DM sub-structures in Milky Way with the estimates of total satellite galaxy population. Similar bounds on thermal WDM mass were also derived in [191] by using constraints from stellar streams. It should be noted that the free streaming length of WDM can get slightly modified due to the late time entropy dilution in our setup but expected to keep the lower bound on WDM mass in the order of $\mathcal{O}(1)$ keV.

## 3.4 Miracle-less WIMP DM and leptogenesis

For $B-L$ gauge symmetry breaking around the TeV corner and $g_{\rm BL} \sim \mathcal{O}(1)$, DM can freeze-out non-relativistically, falling into the standard WIMP paradigm, as long as DM mass remains below a few hundred TeV [166]. We consider high scale symmetry breaking namely, large $v_{\rm BL}(M_{Z_{\rm BL}})$ to ensure that DM freezes out at an early epoch while it is still

relativistic. Now, a large $M_{Z_{BL}}$ implies weaker annihilation rate of the DM to visible sector particles and hence generally leads to overabundance provided the DM is thermalised in early Universe. This overabundance can be brought down by the late decay of one of the RHNs (which we take to be $N_1$ here) after the DM freeze-out, which injects entropy into the thermal bath [192]. In order to realize this possibility of sizeable entropy production, it is necessary for the long-lived $N_1$ to dominate the energy density of the Universe at late epochs. The key phases in the Universe relevant for our discussion are summarised in Fig. 3.9 showing the intermediate matter domination phase MD1 due to long-lived $N_1$ [193]. A precise description of such non-standard Universe is possible by considering a system of coupled Boltzmann equations which govern the evolutions for the temperature of the Universe ($T$) and comoving number densities of both DM and the diluter $N_1$, similar to Eqns. (2.1), (2.2), (3.21). Fig. 3.10 shows the evolution of radiation and $N_1$ densities for benchmark parameters where we observe an intermediate phase of $N_1$ domination. The standard radiation-dominated phase RD2 with the Hubble parameter $H \propto \frac{T^2}{M_P}$ is recovered after $N_1$ decays.

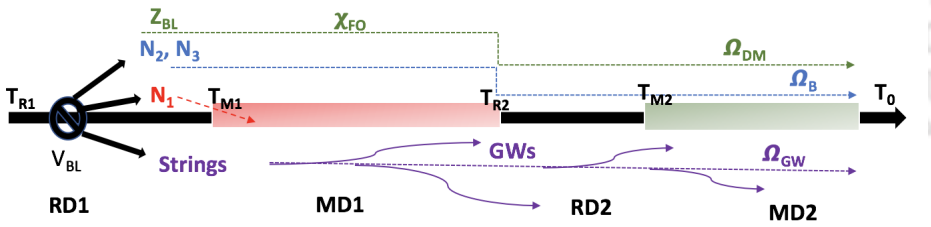


FIGURE 3.9: Schematic of the important phases in the evolution of the Universe from $T_{R_1}$ to $T_0$.

The DM relic density, for relativistic freeze-out, is given by Eqn. (1.21). If $\chi$ leads to overabundance, the required entropy dilution factor $S = \Omega_\chi h^2/0.12$ can be approximated as [192],

$$S \simeq \left[2.95 \times \left(\frac{2\pi^2 g_\star(T_{N_1})}{45}\right)^{1/3} \frac{(rM_{N_1})^{4/3}}{(\Gamma_{N_1} M_P)^{2/3}}\right]^{3/4}, \tag{3.30}$$

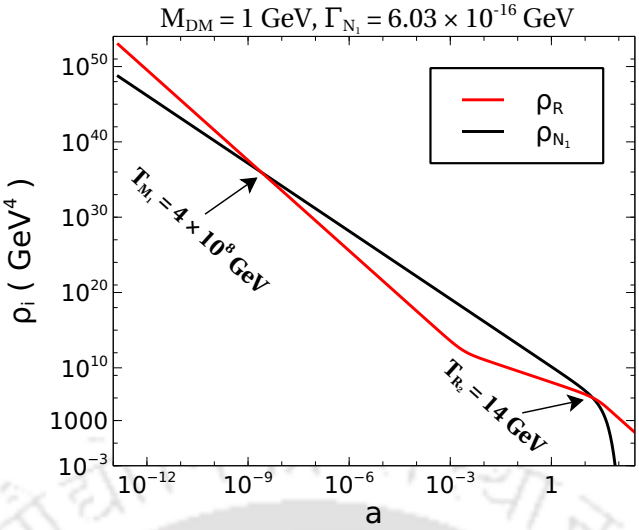


FIGURE 3.10: The evolution of radiation (red) and $N_1$ (black) densities for $M_{\rm DM} = 1$ GeV, $M_{N_1} = 7 \times 10^{10}$ GeV, $v_{\rm BL} = 2.5 \times 10^{12}$ GeV, $g_{\rm BL} = 0.2$, $\Gamma_{N_1} = 6.03 \times 10^{-16}$ GeV such that $\Omega_{\rm DM}h^2 \sim 0.12$. Here, the scale factor is normalised such that $a_{\rm initial} = \left(\frac{1\ \text{GeV}}{T_{\rm initial}}\right)$ with $T_{\rm initial}(\simeq v_{\rm BL})$ is considered to be the initial temperature of the initial radiation dominated Universe.

where $g_\star(T_{N_1})$ is the number of relativistic dof during $N_1$ decay at $T = T_{N_1}$. The parameter $r$ is the freeze-out number density of $N_1$. Assuming instantaneous decay of $N_1$ and considering relativistic freeze-out for $N_1$ we find,

$$T_{N_1} \simeq 3.104 \times 10^{-10} \left(\frac{M_{N_1}}{m_\chi}\right) \text{GeV}. \tag{3.31}$$

The temperature $T_{N_1}$ is inversely proportional to DM mass and approximately marks the end of early matter domination in the assumption of instantaneous $N_1$ decay. In principle, $T_{N_1}$ should be nearly equal to $T_{R_2}$. The obtained $T_{N_1}$ can be easily translated to $\Gamma_{N_1}$ using $H(T_{N_1}) = \Gamma_{N_1}$ which is the required decay width to bring down the relic within observed limit. For the benchmark point in Fig. 3.10, we found $T_{N_1} = 21.72$ GeV from Eqn. (3.31). In the numerical analysis for the same benchmark point we earlier obtained $T_{R_2} = 14$ GeV. The small discrepancy between numerical and analytical estimate emerges due to the approximation of instantaneous decay of $N_1$ in the analytical computation.

**Gravitational Wave Spectral Shape with Miracle-less WIMP**: As discussed in chapter 2, cosmic strings are one of the potential sources of primordial GW, which have gained

a great deal of attention after the recent finding of a stochastic common spectrum process across many pulsars[194–198]. The resulting GW background is detectable when the symmetry breaking scale $\Lambda_{CS} \gtrsim 10^9$ GeV, a fact that makes CS an outstanding probe of super-high scale physics[199–206]. This includes the present scenario of Miracle-less WIMP featuring a high-scale ($\Lambda_{\rm CS} \equiv v_{\rm BL}$) breaking of a gauged $U(1)_{B-L}$. Present day GW energy density corresponding to the mode $k$ is computed with the integral given by Eqn. (2.26), with the flat plateau because of standard radiation domination given by Eqn. (2.27). Interestingly, if there is a matter domination which in our case is provided by the

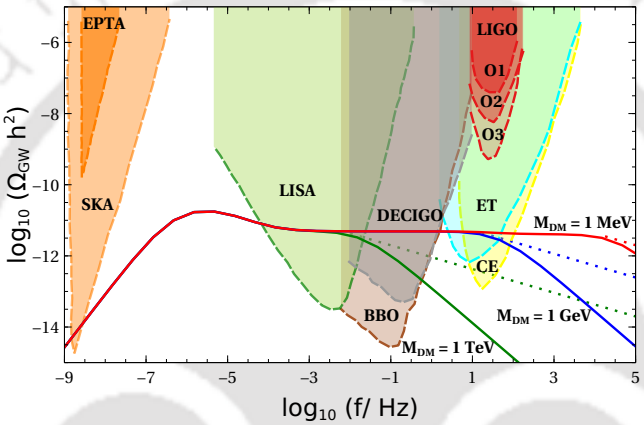


FIGURE 3.11: Fundamental mode ($k = 1$) GW spectra for the benchmark point in Fig. 3.10 with different combinations of $M_{\rm DM}, \Gamma_{N_1}$ to satisfy correct relic. The dotted lines indicate the spectral behaviour beyond the turning point frequency when all the modes are summed.

long-lived $N_1$, the plateau breaks[130, 145, 146] at a turning point frequency given by Eqn. (2.30), with the temperature $T$ given by $T_\Delta \equiv T_{N_1} \simeq T_{R_2}$ and at standard matter radiation equality at a temperature $T_{M_2}$ respectively. Beyond $f_\Delta$, the spectrum goes as $\Omega_{\rm GW} \sim f^{-1}$ for $k = 1$ mode (when infinite modes are summed, $\Omega_{\rm GW} \sim f^{-1/3}$[101, 130, 207, 208]). This spectral behavior therefore, serves as a probe of early matter domination which in our case is a natural requirement to obtain correct relic density of Miracle-less WIMPs.

Similar turning points ($f_c$) can be obtained from the lower bound on $t_i > t_c$ that corresponds to $\alpha t_i > l_c$ [130], where $l_c$ is a critical length below which particle production becomes dominant. Therefore, to claim the spectral break to be a consequence of the end of a matter era, we should have $f_\Delta < f_c$. For cusps like structures, $l_c = \frac{\mu^{-1/2}}{(\Gamma G \mu)^2}$ [209] which

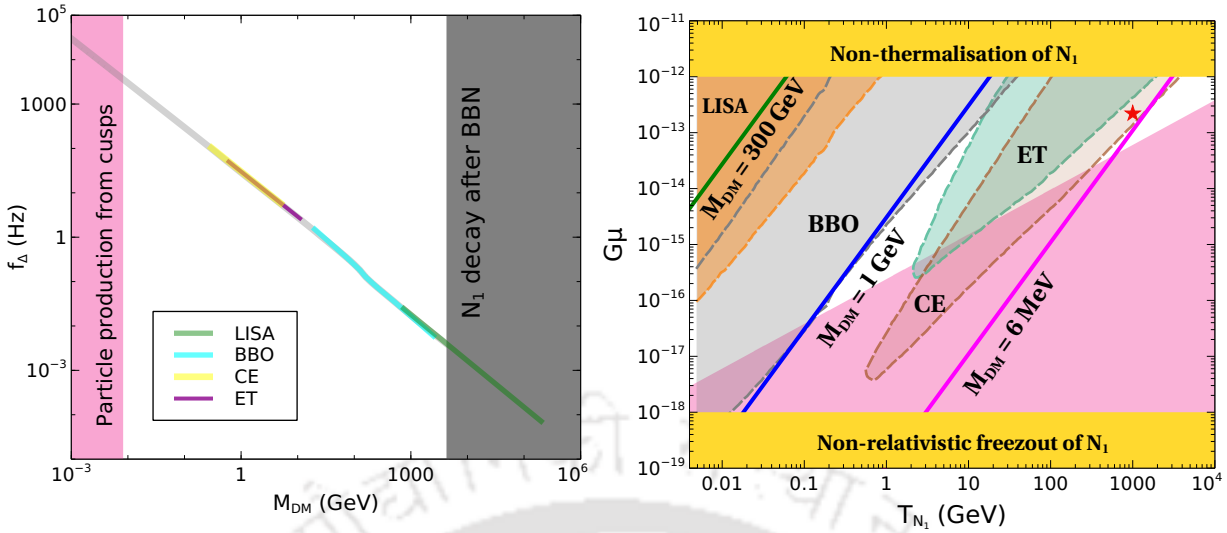


FIGURE 3.12: Left: Contour representing DM relic $\Omega_\chi h^2 = 0.12$ in the $f_\Delta - M_{\rm DM}$ plane for fixed $v_{\rm BL}, g_{\rm BL}$ and $M_{N_1}$ values (as in Fig. 3.10) along with the future sensitivities of different GW detectors. Right: Contours in the $T_{N_1} - G\mu$ plane for three different DM masses satisfying correct relic, along with future GW detector sensitivities for a chosen benchmark point $g_{\rm BL} = 0.2$ and $Y_{N_1} = 0.03 g_{\rm BL}$. The symbol '$\star$' indicates a benchmark point satisfying leptogenesis requirements. In the pink region of both the figures, the particle production dominates over the GW emission and hence discarded.

translates to a lower bound on $G\mu$ as

$$G\mu \gtrsim 2.4 \times 10^{-16} T_\Delta^{4/5}. \tag{3.32}$$

Let us also mention that the temperature $T_c$ corresponding to $l_c \equiv \alpha t_c$ always lies between $T_{M_1}$ and $T_{R_2}$. This means the loops which effectively contribute to the GWs, are formed in the $N_1$ dominated epoch, making the very first radiation domination (RD1) irrelevant to the computation.

We compute the $\Omega_{\rm GW}$ for the three DM masses, differing by order of magnitudes, as shown in Fig. 3.11. We tune $\Gamma_{N_1}$ appropriately for each of the DM masses such that $\Omega_\chi h^2 = 0.12$. The relevant model parameters other than $M_{\rm DM}$ and $\Gamma_{N_1}$ are considered to be the same as in Fig. 3.10 which precisely determine the $G\mu$=1.32 $\times 10^{-13}$. Since $M_{N_1}$ and $g_{\rm BL}$ are fixed, the MD1 phase starts at the same temperature for all the three DM masses in Fig. 3.11. Within such non-standard framework, the GW spectra is expected to show spectral break ($f_\Delta$) at higher frequency depending on the value of $T_{N_1}$. In general,

a lower $T_{N_1}$ implies a longer period of MD1 phase and further leads to a smaller spectral break frequency $f_\Delta$. Previously in Eqn. (3.31) we have derived an unique relationship between $T_{N_1}$ and DM mass where $T_{N_1} \propto \frac{1}{M_{\rm DM}}$. This leads to a one-to-one correlation between $f_\Delta$ and DM mass $M_{\rm DM}$ with a larger DM mass resulting in smaller $f_\Delta$ as observed in Fig. 3.11. This feature is also prominent in left panel of Fig. 3.12, where we have determined the $f_\Delta$ for different order of DM mass ranging from 1 MeV to 1 PeV. We also mark different parts of the $M_{\rm DM} - f_\Delta$ line following various planned experimental sensitivities. The region which escapes the detection sensitivities is highlighted in light grey, corresponding to lighter DM. The success of the big bang nucleosynthesis (BBN) restricts the DM mass to remain below 8 TeV while for $M_{\rm DM} \lesssim 10$ MeV, particle production from cusps dominates and hence disfavored. We find that a substantial range of the DM mass (100 MeV-8 TeV), allowed by relevant constraints, is within the reach of GW detectors like LISA [141], BBO [143], ET [144], CE [139] keeping the Miracle-less WIMP verifiable or falsifiable in near future.

In the right panel of Fig. 3.12, we obtain the predictions for three different DM masses in the $T_{N_1}$-$G\mu$ plane such that the relic bound is satisfied. We have used Eqn. (3.31) with the assumption $T_{R_2} \simeq T_{N_1}$ and expressed $M_{N_1}$ as function of $G\mu$ by fixing $g_{\rm BL} = 0.2$ and $Y_{N_1} = 0.03 g_{\rm BL}$. The future sensitivities of different experiments namely LISA [141], BBO [143], ET [144] and CE [139] are also assembled in the same plane. For any particular point with specific $(T_{N_1}, G\mu)$ coordinates along a fixed $m_{\rm DM}$ line, one can compute the turning frequency $f_\Delta$. This figure illustrates whether any of the above-mentioned future GW experiments has the ability to probe that particular $f_\Delta$. For DM mass of 300 GeV, the corresponding $f_\Delta$ falls within the LISA sensitivity [141]. On the other hand, the proposed sensitivity of CE [139] experiment can probe DM mass as light as 6 MeV in the present framework. We also point out the region in $T_{N_1} - G\mu$ plane where thermalisation of $N_1$ can not be achieved in early Universe (yellow shaded region on top). The yellow shaded bottom region favors non-relativistic freeze-out for $N_1$ and hence our analytical derivation of $T_{N_1}$ in Eqn. (3.31) does not remain valid.

**Leptogenesis with Miracle-less WIMP:** Here again, the presence of the RHNs $N_2$, $N_3$

can help in generating the baryon asymmetry of the Universe via leptogenesis. Due to significant entropy dilution at late epoch, the resonant leptogenesis mechanism appears to be the suitable one to achieve the observed $\eta_B$. The present day baryon to photon ratio can be conventionally parameterized as a function of lepton asymmetry parameter ($\varepsilon$) and efficiency factor ($\kappa_f$) through the analytical expression given by Eqn. (1.40). Following the Casas-Ibarra (CI) parametrization (cf. Eqn. (1.41)), we consider the rotation matrix $\mathbb{R}$ as

$$\mathbb{R} = \begin{pmatrix} \cos\delta' & 0 & \sin\delta' \\ -\sin\delta\sin\delta' & \cos\delta & \sin\delta\cos\delta' \\ -\cos\delta\sin\delta' & -\sin\delta & \cos\delta\cos\delta' \end{pmatrix} \tag{3.33}$$

Since $N_1$ is long-lived with very small decay width in our set-up making it effectively decoupled from seesaw mechanism, we can approximately set $\delta' \sim 0$. In this limit, effectively the Dirac Yukawa coupling $Y_D$ represents a $2 \times 3$ matrix in flavour basis. The lepton asymmetry can be generated from the decays $N_2$ and $N_3$. In order to obtain resonant enhancement to the lepton asymmetry parameter, $N_2$ and $N_3$ need to be nearly degenerate with their mass splitting expressed as $\frac{M_{N_3}-M_{N_2}}{M_{N_2}} = \Delta$. As a benchmark point, we make the following choices of the relevant parameters,

$$M_{N_2} = 10^{11}\,\text{GeV},\ \Delta = 2.6 \times 10^{-6},\ \delta = 0.71 + 0.42i.$$

The mass scale of $N_2$ is chosen to be high such that it decays completely during the very first radiation dominated epoch. Considering the lightest neutrino mass to be vanishing, we have used the best fit values of experimentally observed neutrino oscillation parameters. Correspondingly we obtain $\varepsilon_{2,3} = 0.33$ and $\kappa_f^2 \sim 7.8 \times 10^{-3}$, $\kappa_f^3 \sim 6.7 \times 10^{-3}$ using the standard expressions as noted in Ref. [62]. These choices lead to $\eta_B \simeq 4.58 \times 10^{-5}$ in the standard scenario which is clearly overproduced. Therefore, to match with the present day observed value for $\eta_B$, the required amount of entropy dilution factor is $7.5 \times 10^4$ which corresponds to the DM mass $\sim 8.5$ MeV. For $T_{N_1} \sim 1$ TeV, the 8.5 MeV DM mass implies $G\mu \simeq 2 \times 10^{-13}$ with $Y_{N_1} = 0.03 g_{\rm BL}$ and $g_{\rm BL} = 0.2$ (from Eqn.(3.31)) as marked

by red colored '$\star$' symbol in right panel plot of Fig. 3.12. This particular point in the $T_{N_1} - G\mu$ plane which represents the simultaneous satisfaction of DM relic abundance and baryon asymmetry of the Universe is verifiable by CE experiment. A more rigorous analysis including lepton flavour effects [65–68] is left for future studies.

## 3.5 Conclusion

To conclude, in the first scenario we have proposed a simple extension of the minimal gauged $B - L$ model in order to realise the possibility of realising cosmic inflation, keV scale warm dark matter and light neutrino mass and mixing simultaneously. A thermal DM candidate of keV scale (an SM gauge singlet vector-like fermion) leads to overproduction as it freezes out while being relativistic like active neutrinos. We invoke the late entropy dilution mechanism from a long-lived heavier RHN ($N_3$, to be specific) in order to bring the overproduced keV scale DM abundance within Planck 2018 limits. The requirement of sufficient entropy dilution demands $N_3$ to freeze-out in the early Universe leading to an intermediate matter-dominated epoch. The thermalisation temperature of DM and the decaying particle in the early Universe as well as the efficiency of the entropy dilution purely depend on their interactions regulated by the $B - L$ model parameters. Due to the minimal nature of the model and the involvement of cosmic inflation, we indeed find a small parameter space in agreement with all these requirements. In particular, we have observed that to achieve correct relic abundance of dark matter, it is preferable to have heavier $Z_{\rm BL}$ ($\gtrsim \mathcal{O}(1)$ TeV ) with a larger lifetime of $N_3$. Additionally, we also predict the lightest active neutrino mass to be $m_{\nu_l} \lesssim 10^{-14}$ eV considering a keV order WDM mass while satisfying the neutrino oscillation data. This prediction is also dependent on the $B - L$ model parameters with higher $g_{\rm BL}$ leading to lowering of $m_{\nu_l}$ further for a constant lifetime of $N_3$. Such tiny values of the lightest active neutrino mass, as predicted by the model, will keep the effective neutrino mass much out of reach from ongoing tritium beta decay experiments like KATRIN [210]. Additionally, near future observation of neutrinoless double beta decay (NDBD) [211] can also falsify our scenario, particularly for normal

ordering of light neutrinos. This is due to the fact that future NDBD experiments can probe normal ordering only for lightest active neutrino mass, $m_{\text{lightest}} > 10^{-2}$ eV which lies much above the tiny value predicted in our scenario. Thermal leptogenesis is possible from the out-of-equilibrium decay of other two RHNs namely, $N_1$ and $N_2$ in the presence of long lived $N_3$. We have found that a sufficient amount of lepton asymmetry can be obtained in the resonant regime which can survive the late-time injection of large entropy, and can get converted into the observed baryon asymmetry via electroweak sphalerons. In addition to the predictive nature as far as model parameters are concerned, warm dark matter of keV scale also has interesting astrophysical implications in terms of small scale structure formation. By allowing a tiny mixing of such WDM with active neutrinos will also give rise to the the possibility of monochromatic photon from its radiative decay leading to tantalizing indirect detection prospects.

In the second scenario, we have proposed a novel way of probing DM having a wide range of masses by observations of spectral breaks in GW spectrum generated by cosmic strings, with complementary predictions which distinguish it from a general non-standard cosmological scenario with similar impacts on GW spectrum. Presence of a high scale Abelian gauge symmetry breaking results in generation of cosmic strings with observable GW spectrum while also causing insufficient DM annihilations mediated by superheavy gauge boson. Thermally generated DM with such insufficient annihilation rates, dubbed as Miracle-less WIMP, leads to overproduced relic abundance, requiring late entropy dilution. Adopting the minimal gauged B-L framework with several other motivations, we ensure such entropy dilution due to late decay of one of the RHNs. Depending upon DM mass, one requires different decay time of such diluter, leading to unique turning frequencies in the usually flat GW spectrum generated by cosmic strings. For a wide range of DM mass, such turning frequencies remain within reach of next generation GW experiments like LISA, BBO, CE, ET. The heavier two RHNs generate light neutrino masses as well as the baryon asymmetry of the Universe via leptogenesis. We have observed that simultaneous realisation of successful leptogenesis and DM relic is possible in the present framework with the turning frequency falling within reach of the

above GW experiments. Because of the presence of the long-lived diluter, this scenario also predicts vanishingly small lightest active neutrino mass $m_{\text{lightest}} \leq 10^{-20}$ eV, which provides a complementary probe in neutrino experiments like KATRIN [210] and neutrinoless double beta decay (NDBD) [211] as discussed above.

# Chapter 4

# DM and Leptogenesis with PBH domination

## 4.1 Introduction

This chapter explores the phenomenology of dark matter and leptogenesis in the presence of early matter domination arising because of primordial black holes. As mentioned in chapter 2, we consider ultralight PBH which evaporate through Hawking radiation before the epoch of BBN. PBH differ from other forms of early matter domination, since they do not rely on other new interactions either for their formation or their evanescence after the emission of particles. PBH can produce heavy particles which can then decay in a CP-violating way to give rise to lepto/baryogenesis [94, 96]. The final baryon asymmetry produced is thus dependent on the PBH parameters, especially the initial mass of PBH. Apart from this pure non-thermal contribution, if the mother particle leading to the CP-violating decay is produced thermally and hence contributing to thermal leptogenesis through out-of-equilibrium decays (see section 1.2.3), PBH can also play a significant role in diluting the thermally generated asymmetry. This depends on the evaporation temperature of PBH relative to the scale of leptogenesis. On the other hand, PBH can also affect the production of DM in several ways [102, 103]. They can directly produce DM through Hawking evaporation. In addition, they can also have an impact on thermal freeze-out DM production and non-thermal freeze-in production of DM, depending on when the PBH evaporate relative to the freeze-out/ freeze-in temperature. We consider

two scenarios to investigate the effect of PBH on the production of the baryon asymmetry and dark mattter.

In the first scenario, we consider a low scale leptogenesis scenario along with WIMP and FIMP type DM in the presence of PBH. Unlike in earlier works where high scale thermal or non-thermal leptogenesis were studied in the presence of PBH [96, 98–100], here we adopt a radiative seesaw scenario where scale of leptogenesis can be as low as a few TeV even with hierarchical right handed neutrinos. We consider the scenario where PBH evaporate before the electroweak phase transition while focusing on three specific cases where evaporation occurs before, during or after the scale of leptogenesis. We find the PBH parameter space which can give rise to the observed asymmetry in the model, assuming PBH domination in the early Universe. Although the dependency of the generated asymmetry on the relevant parameters of the particle physics model is already well studied, we demonstrate the asymmetry in the PBH parameter space, and find some interesting deviation from the usual thermal leptogenesis scenario, in the presence of PBH. We also investigate the possible scenarios of DM genesis in the same setup and reach at some interesting conclusions.

In the second scenario, we explore the case of *Asymmetric Dark Matter*, motivated from the 'Cosmic Coincidence problem', which is the intriguing observation of the similarity in the abundances of dark matter and baryonic matter, $\Omega_{\rm DM} \approx 5\,\Omega_{\rm Baryon}$, within the same order of magnitude. Although several popular BSM frameworks can certainly explain the origin of DM and BAU independently, the above coincidence is hard to ignore and one has to provide a dynamical origin behind such a serendipity. There have been several works in pursuit of finding a common origin for DM and baryon asymmetry, a brief review of which can be found in [212]. This broadly falls into two categories. In the first one, the usual mechanism for baryogenesis is extended to the dark sector assuming the dark sector to be asymmetric [213–216]. In typical asymmetric dark matter (ADM) scenario, the same out-of-equilibrium decay of a heavy particle into baryon and dark sector can give rise to asymmetries in the two sectors of similar order of magnitudes $n_B - n_{\overline{B}} \sim |n_{\rm DM} - n_{\overline{\rm DM}}|$. The second approach is to produce such asymmetries through

annihilations [217–219], where one or more particles involved in the process eventually go out of thermal equilibrium to generate a net asymmetry. The so-called WIMPy baryogenesis [220–222] belongs to this category, where a DM particle freezes out to generate its own relic abundance while simultaneously producing an asymmetry in the baryon sector. The idea extended to leptogenesis is called WIMPy leptogenesis [223–228]. Motivated by these, we consider a simple realisation of the asymmetric dark matter scenario where out-of-equilibrium decay of heavy right handed neutrinos can play the role in generating both dark and visible sector asymmetries simultaneously [229, 230]. The same RHNs can also give rise to light neutrino masses via Type-I seesaw mechanism [55, 56, 231, 232]. We consider a non-thermal source of these asymmetries, which is realised through the presence of PBH, producing RHNs via Hawking radiation.

This chapter is organized as follows. The first scenario is presented in section 4.2, starting with the details of the particle physics set-up, followed by its standard predictions without PBH in section 4.2.1. In section 4.2.2, we discuss leptogenesis in this set-up in the presence of PBH followed by discussion of scalar doublet DM in section 4.2.3. In section 4.2.4, we discuss the possibility of fermion singlet DM with leptogenesis due to heavier right handed neutrino decay. We summarise our results and conclude in section 4.2.5. The second scenario of Asymmetric DM from PBH is presented in 4.3, starting with the details of the setup in section 4.3.1, 4.3.2. In section 4.3.3, an analytical estimate of the asymmetry generated from PBH is given, followed by a full numerical analysis in section 4.3.4. We end with the conclusion in section 4.3.5.

## 4.2 Low scale leptogenesis and DM in the presence of PBH

As mentioned before, we consider a specific particle physics model which allows the possibility of TeV scale leptogenesis, DM and non-zero neutrino mass. This is the minimal scotogenic model [233] where the SM is extended by three gauge singlet right handed neutrinos $N_i$ (with $i = 1, 2, 3$), one additional scalar doublet $\eta$. An additional $Z_2$ symmetry is imposed under which these newly added particles are odd while all SM particles are

even. The leptonic Yukawa Lagrangian relevant for light neutrino mass is

$$\mathcal{L} \supset \frac{1}{2}(M_N)_{ij}N_iN_j + Y_{ij}\,\bar{L}_i\tilde{\eta}N_j + \text{h.c.}\,. \tag{4.1}$$

Clearly, there is no coupling of neutrinos to the SM Higgs doublet $\Phi_1$ due to the unbroken $Z_2$ symmetry. However, light neutrino masses arise at radiative level with $Z_2$ odd particles taking part in the loop.

The scalar potential of the model can be written as

$$\begin{aligned} V(\Phi_1,\eta) &= \mu_1^2|\Phi_1|^2 + \mu_2^2|\eta|^2 + \frac{\lambda_1}{2}|\Phi_1|^4 + \frac{\lambda_2}{2}|\eta|^4 + \lambda_3|\Phi_1|^2|\eta|^2 \\ &\quad + \lambda_4|\Phi_1^\dagger\eta|^2 + \left[\frac{\lambda_5}{2}(\Phi_1^\dagger\eta)^2 + \text{h.c.}\right]. \end{aligned} \tag{4.2}$$

where $\Phi_1$ is the SM Higgs doublet. Light neutrino masses which arise at one loop level can be evaluated as [233, 234]

$$\begin{aligned} (m_\nu)_{ij} &= \sum_k \frac{Y_{ik}Y_{jk}M_k}{32\pi^2}\left(\frac{m^2_{H^0}}{m^2_{H^0}-M_k^2}\ln\frac{m^2_{H^0}}{M_k^2} - \frac{m^2_{A^0}}{m^2_{A^0}-M_k^2}\ln\frac{m^2_{A^0}}{M_k^2}\right) \\ &\equiv \sum_k \frac{Y_{ik}Y_{jk}M_k}{32\pi^2}\left[L_k(m^2_{H^0}) - L_k(m^2_{A^0})\right], \end{aligned} \tag{4.3}$$

where $M_k$ is the mass eigenvalue of the mass eigenstate $N_k$ in the internal line and the indices $i,j = 1,2,3$ run over the three neutrino generations as well as three copies of $N_i$. Also, $A^0, H^0$ are the neutral pseudoscalar and scalar respectively contained in $\eta$. The function $L_k(m^2)$ is defined as

$$L_k(m^2) = \frac{m^2}{m^2-M_k^2}\ln\frac{m^2}{M_k^2}\,. \tag{4.4}$$

Using the physical scalar mass expressions [235], one can write $m^2_{H^0} - m^2_{A^0} = \lambda_5 v^2$. Thus, light neutrino mass is directly proportional to the parameter $\lambda_5$. In upcoming discussions, we will discuss the effects of $\lambda_5$ in details.

### 4.2.1 Standard TeV scale thermal leptogenesis in the scotogenic model

Similar to the vanilla leptogenesis scenario, here also non-zero CP asymmetry is generated by out-of-equilibrium decay of the lightest right handed neutrino $N_1$. Successful leptogenesis is possible at a scale as low as 10 TeV, even with hierarchical right handed neutrinos. Such low scale leptogenesis with hierarchical right handed neutrinos has been discussed by several authors [235–242] while quasi-degenerate right handed neutrino scenario was discussed in earlier works [243, 244]. For hierarchical right handed neutrinos, such a low scale leptogenesis is a significant improvement over the usual Davidson-Ibarra bound $M_1 > 10^9$ GeV for vanilla leptogenesis in Type-I seesaw framework [73], discussed in chapter 1. For details of the corresponding Davidson-Ibarra bound in this model, please refer to Appendix C.

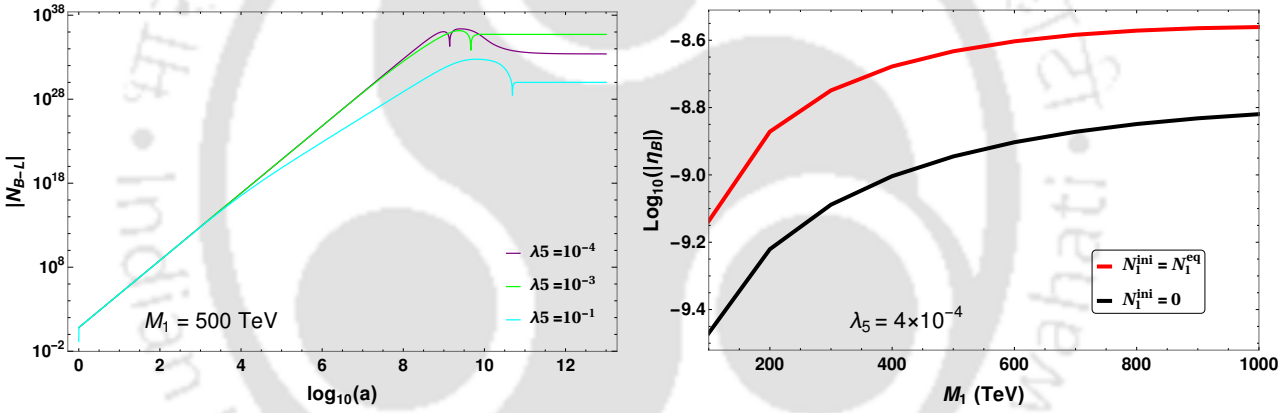


FIGURE 4.1: *Left panel*: Evolution plot of the comoving number density of B-L for different $\lambda_5$ values in radiation dominated Universe, taking $M_1 = 500$ TeV. The effect of the washout terms is clearly evident for $\lambda_5 = 10^{-4}$. *Right panel*: Baryon asymmetry as a function of leptogenesis scale for two different initial $N_1$ abundance and $\lambda_5 = 4 \times 10^{-4}$. The lightest neutrino mass has been fixed at $10^{-11}$ eV for both the plots.

Now, the CP asymmetry parameter ( cf. Eqn. (1.29) with $H \to \eta$), neglecting the flavour effects (summing over final state flavours $\alpha$) is found to be [239]

$$\epsilon_i = \frac{1}{8\pi(Y^\dagger Y)_{ii}} \sum_{j\neq i} \mathrm{Im}[((Y^\dagger Y)_{ij})^2] \frac{1}{\sqrt{r_{ji}}} F(r_{ji}, \eta_i) \tag{4.5}$$

where the function $F(r_{ji}, \eta)$ is defined as

$$F(r_{ji}, \eta_i) = \sqrt{r_{ji}} \left[ f(r_{ji}, \eta_i) - \frac{\sqrt{r_{ji}}}{r_{ji} - 1} (1 - \eta_i)^2 \right]. \tag{4.6}$$

While the details of leptogenesis in standard cosmology has already been worked out, we briefly comment on the differences arising due to initial number densities of $N_1$. In earlier works [235, 239–241], the right handed neutrino was assumed to be in thermal equilibrium initially. While it is possible to produce TeV scale right handed neutrinos in equilibrium in the presence of additional interactions, it is not guaranteed in the minimal scotogenic model. This is due to the fact that $N_1$ couples to the SM bath only through Dirac Yukawa coupling, which can be small if $N_1$ is kept in the TeV regime. First, we consider $N_1$ to be initially in equilibrium, i.e., $n_{N_1^{\rm ini}} = n_{N_1^{\rm eq}}$ and next we consider the case of vanishing initial abundance of $N_1$ that is, $n_{N_1^{\rm ini}} \approx 0$. As we will see, the latter case will be more realistic for us because of the small Yukawas and we continue with this assumption in subsequent analysis. Even if Yukawas are sizeable, at the epoch of PBH formation, the abundance of $N_1$ can be negligible as it is yet to enter thermal equilibrium with the bath particles. While the initial abundance is vanishingly small, $N_1$ gets produced at later epochs from the inverse decays and scatterings. The same terms, later act as washout terms which tend to erase the asymmetry during the scale of leptogenesis. This can be seen in Fig. 4.1 (left), where we have shown the evolution of comoving number density of $B - L$ with scale factor from a high temperature upto the sphaleron scale. In the right panel of Fig. 4.1, we show the final baryon asymmetry as a function of leptogenesis scale, for both the cases mentioned above. It can be clearly seen that a vanishing initial abundance of $N_1$ decreases the asymmetry. We have considered a mass hierarchy: $M_2 = 10\, M_1$ and $M_3 = 100\, M_1$, which is also used in our subsequent analysis.

### 4.2.2 Scotogenic leptogenesis in the presence of PBH

For the discussion of leptogenesis in the presence of PBH, we closely follow the notations of Ref. [100]. Since we consider thermal leptogenesis in the presence of PBH, we solve the required Boltzmann equations for the PBH energy density, radiation energy density, right handed neutrinos and lepton asymmetry, which in terms of the scale factor $a$, can be written as

$$\frac{d\varrho_{\rm BH}}{da} = \frac{1}{M_{\rm BH}}\frac{dM_{\rm BH}}{da}\varrho_{\rm BH}\,, \tag{4.7}$$

$$\frac{d\varrho_{\rm Rad}}{da} = -\frac{\epsilon_{\rm SM}(M_{\rm BH})}{\epsilon(M_{\rm BH})}\frac{1}{M_{\rm BH}}\frac{dM_{\rm BH}}{da}a\varrho_{\rm BH}\,, \tag{4.8}$$

$$aH\frac{dn^T_{N_1}}{da} = -\left(n^T_{N_1}-n^{\rm eq}_{N_1}\right)\Gamma^T_1\,, \tag{4.9}$$

$$aH\frac{dn^{\rm BH}_{N_1}}{da} = -\left(n^{\rm BH}_{N_1}\right)\Gamma^{\rm BH}_1 + n_{\rm BH}\Gamma_{{\rm BH}\to N_1}\,, \tag{4.10}$$

$$aH\frac{dn_{B-L}}{da} = \epsilon_1\left[\left(n^T_{N_1}-n^{\rm eq}_{N_1}\right)\Gamma^T_1 + n^{\rm BH}_{N_1}\Gamma^{\rm BH}_1\right] - Wn_{B-L} - \Delta W\frac{M_1}{T}Hn_{B-L}. \tag{4.11}$$

Here, $\varrho_{\rm BH} = a^3\rho_{\rm BH}$ and $\varrho_{\rm Rad} = a^4\rho_{\rm Rad}$ are the comoving energy densities of PBH and radiation respectively. The mass loss rate is given by Eqn. (2.9). In presence of the PBH, the Hubble parameter $H$ entering in the Boltzmann equations is given by[1] $H = \sqrt{\frac{\varrho_{\rm BH}a^{-3}+\varrho_{\rm Rad}a^{-4}}{3M_{\rm P}^2}}$. In the above Boltzmann equations, $n^T_{N_1}$ and $n^{\rm BH}_{N_1}$ are comoving $N_1$ densities generated from thermal bath and PBH (non-thermal source) respectively. $\Gamma_{{\rm BH}\to N_1}$ is the non-thermal production term for $N_1$ (originating from PBH evaporation) and can be written as [100]

$$\Gamma_{{\rm BH}\to N_1} = \int_0^\infty \frac{d^2\mathcal{N}}{dp\,dt}\,dp \simeq \frac{27T_{\rm BH}}{32\pi^2}\left(-z_{\rm BH}{\rm Li}_2(-e^{-z_{\rm BH}}) - {\rm Li}_3(-e^{-z_{\rm BH}})\right), \tag{4.12}$$

where ${\rm Li}_s(z)$ are the poly-logarithm functions of order $s$ and $z_{\rm BH} = M_1/T_{\rm BH}$. The thermal average decay widths are defined as $\Gamma^T_1 = \frac{K_1(M_1/T)}{K_2(M_1/T)}\Gamma_1$ and $\Gamma^{\rm BH}_1 = \frac{K_1(M_1/T_{\rm BH})}{K_2(M_1/T_{BH})}\Gamma_1$.

In the asymmetry equation (4.11), $W = \frac{1}{4}\Gamma^T_{N_1}K_2(z)z^2$ is the washout term from the inverse decays. $\Delta W$ is the washout term because of $\Delta L = 2$ scatterings of the type $l\eta \to$

[1]The contribution of $N_1$ in Hubble is found to be negligible.

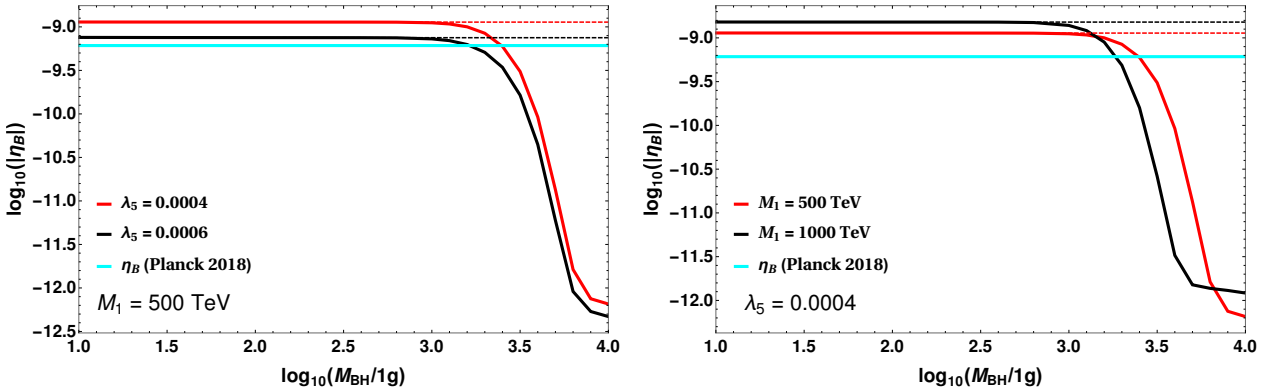


FIGURE 4.2: Final baryon asymmetry as a function of the initial PBH mass (denoted as $M_{\rm BH}$ here), for two values of $\lambda_5$ keeping $M_1$ fixed at 500 TeV (left panel), and for two values of $M_1$ keeping $\lambda_5$ fixed at 0.0004 (right panel). Lightest neutrino mass is fixed at $m_\nu^1 = 10^{-11}$ eV for both.

$\bar{l}\eta^*$ and can be written as [239]

$$\Delta W = \frac{36\sqrt{5}M_P M_1 \bar{m}_{\tilde{\zeta}}^2}{2\sqrt{\pi}\sqrt{g_*}v^4 z^2 \lambda_5^2}, \tag{4.13}$$

where $z = M_1/T$, v is the electroweak symmetry breaking scale and $\bar{m}_{\tilde{\zeta}}^2$ is the effective mass parameter [239]. The $\Delta L = 1$ scatterings are usually suppressed due to the presence of heavy right handed neutrinos in external legs.

Now, since the entropy of the Universe is not conserved because of PBH evaporation, we need to follow the evolution of the temperature of the thermal plasma separately through the equation

$$\frac{dT}{da} = -\frac{T}{\Delta}\left(\frac{1}{a} + \frac{\epsilon_{SM}(M_{\rm BH})}{\epsilon(M_{\rm BH})}\frac{1}{M_{BH}}\frac{dM_{BH}}{da}\frac{a\varrho_{\rm BH}}{4\varrho_{\rm Rad}}\right), \tag{4.14}$$

where

$$\Delta = 1 + \frac{T}{3\,g_{*s}(T)}\frac{dg_{*s}(T)}{dT}, \tag{4.15}$$

takes care of the variation of the total number of DOFs with temperature. We solve the above coupled Boltzmann equations from the time of PBH formation upto the sphaleron scale, with a vanishing initial abundance of $N_1$. The initial PBH mass $m_{\rm in}$ and the initial temperature are related through Eqn. (2.3). Depending on the initial mass of PBH it can evaporate at different epochs. PBH with a larger mass evaporate lately (cf. Eqn. (2.12)).

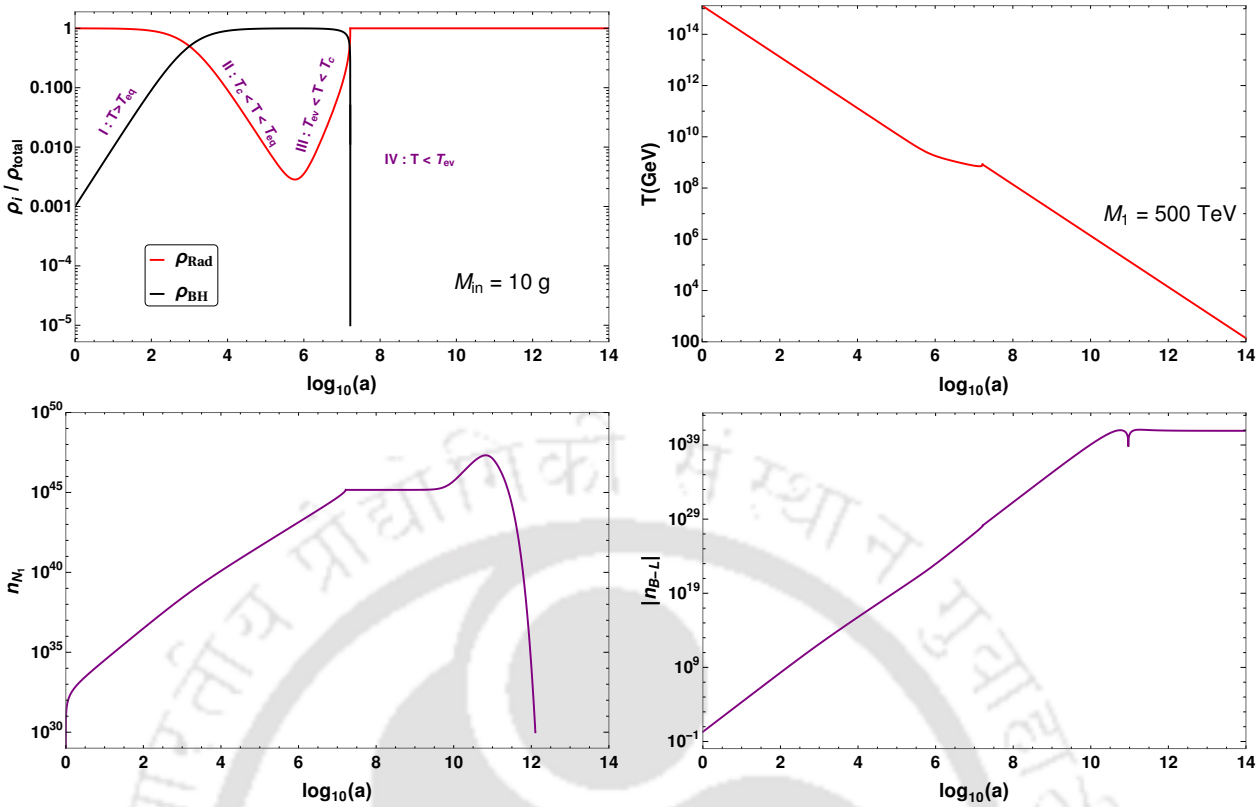


FIGURE 4.3: *Top panel*: Evolution of the energy densities (left) and temperature of the thermal plasma (right), taking $M_{\rm in} = 10$ g, $M_1 = 500$ TeV, $\lambda_5 = 4 \times 10^{-4}$, $m_\nu^1 = 10^{-11}$ eV. *Bottom panel*: Evolution of the comoving number densities of $N_1$ (left) and $B - L$ (right) for the same parameters. The different temperature regions shown in the top left panel are explained in Section 4.2.3.

From the leptogenesis point of view, we want PBH to evaporate before the sphaleron scale, $T_{\rm sph} \simeq 100\ GeV$, which gives a tighter upper bound on the initial PBH mass compared to that from BBN (cf. Eqn. (2.13)), as[2]

$$M_{\rm in} \lesssim 2 \times 10^5 \text{ g}. \tag{4.16}$$

Note that PBH evaporation after sphaleron temperature will lead to overall dilution of baryon asymmetry only as the non-thermally produced $N_1$ from late PBH evaporation cannot contribute to baryon asymmetry.

As we will see, a very small $\beta$ or sub-dominant PBH energy density in the early Universe does not change the predictions of thermal leptogenesis in scotogenic model significantly. Therefore, we will consider sizeable values of $\beta$ so that PBH can affect the results

[2]In this section, we denote the initial PBH mass as $M_{\rm in}$.

of thermal leptogenesis. On the other hand, such large values of $\beta$ often lead to over-production of dark matter as we will discuss in upcoming section. This actually forces us to have DM mass in a ballpark where PBH has no effect on its relic abundance. On the other hand, if PBH effect on DM relic is substantial, the corresponding values of $\beta$ will not have any significant effect on thermal leptogenesis. This complementary behaviour noticed in leptogenesis and DM with respect to fractional energy density of PBH is the main content of upcoming discussions.

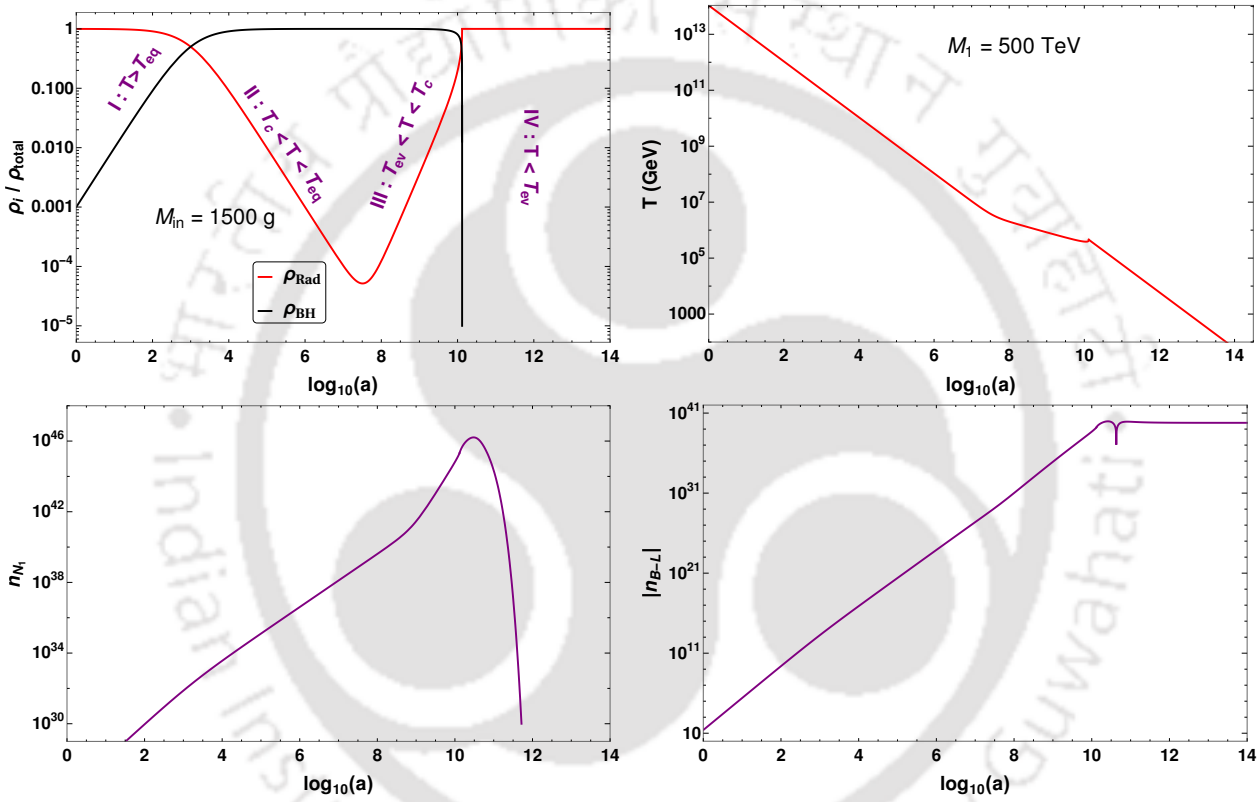


FIGURE 4.4: *Top panel*: Evolution of the energy densities (left) and temperature of the thermal plasma (right), taking $M_{\rm in} = 1500$ g, $M_1 = 500$ TeV, $\lambda_5 = 4 \times 10^{-4}$, $m_\nu^1 = 10^{-11}$ eV. *Bottom panel*: Evolution of the comoving number densities of $N_1$ (left) and $B - L$ (right) for the same parameters.

Now, depending on the PBH evaporation time relative to the scale of leptogenesis, we can have three different scenarios, also applicable in Type-I seesaw leptogenesis discussed in [100]. To be more specific, we can have scenarios where PBH evaporation takes place before, during and after the generation of lepton asymmetry. If we consider low scale leptogenesis at a scale of few hundreds of TeV, which is naturally possible in the scotogenic model, for most of the range of allowed initial PBH masses, they evaporate by the time

thermal leptogenesis occurs. For instance, for leptogenesis scale around $300 - 800$ TeV, PBH with mass less than around $600 - 1200$ g, evaporate before the scale of thermal leptogenesis. In this case, the right handed neutrinos produced by PBH evaporation only act as an initial condition for thermal leptogenesis. Thus, the asymmetry produced is almost the same as the thermal case. As PBH masses start increasing, they evaporate during or after the scale of leptogenesis. The evaporation injects entropy in the form of radiation and decreases the final baryon asymmetry. Although such evaporation can also generate additional sources of lepton asymmetry in terms of $N_1$, but entropy dilution effects dominate. This behaviour can be seen in Fig. 4.2, where we have shown the observed baryon asymmetry as a function of initial PBH mass, varying the relevant parameters in the scotogenic model. In the left panel plot, we keep the scale of leptogenesis fixed at 500 TeV, while showing the variation in baryon asymmetry for two different values of $\lambda_5$. In the right panel plot, we keep $\lambda_5$ fixed at 0.0004 and show the variation in baryon asymmetry for two different scales of leptogenesis. In Fig. 4.2, $\beta$ is kept fixed at $10^{-3}$. The effect of changing $\beta$ will be discussed later.

In Figs. 4.3, 4.4 and 4.5, we show the evolution plots of the energy densities, temperature of the thermal plasma and the comoving number densities of $N_1$ and $B - L$, for the cases of PBH evaporation before, during and after the scale of leptogenesis respectively. The value of $\beta$ is chosen to be $10^{-3}$ such that a PBH domination is guaranteed. The PBH domination for a finite epoch can be clearly seen from upper left panel plots in these figures. In Fig. 4.3, the initial PBH mass is taken to be 10 g, and hence it evaporates around $\log(a) \sim 7$, before the scale of thermal leptogenesis, which happens around $\log(a) \sim 11$. A kink in the temperature plot can be seen because of the entropy injection from PBH evaporation. The comoving number density of $N_1$ is increased initially from two contributions: the non-thermal PBH evaporation $n_{N_1}^{\rm BH}$ and from the inverse decays and scatterings $n_{N_1}^{T}$ of SM bath particles. $N_1$ can finally reach equilibrium, depending upon its Yukawa couplings, and its out of equilibrium decays produces a net asymmetry. Fig. 4.4 corresponds to an initial PBH mass of 1500 g, which evaporates during the scale of thermal leptogenesis, around $\log(a) \sim 10$. In Fig. 4.5, the initial PBH mass is taken to

be 70000 g such that it evaporates after thermal leptogenesis, around $\log(a) \sim 12$.

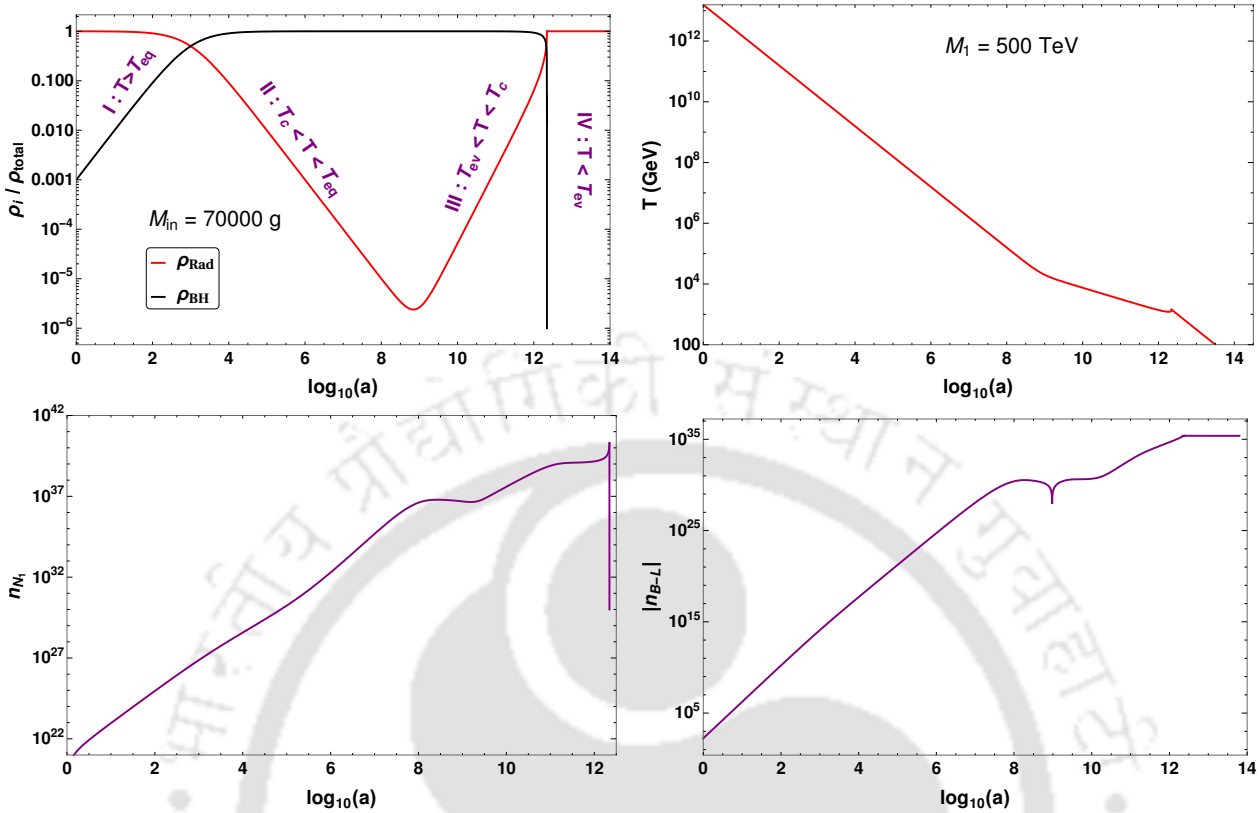


FIGURE 4.5: *Top panel*: Evolution of the energy densities (left) and temperature of the thermal plasma (right), taking $M_{\rm in} = 70000$ g, $M_1 = 500$ TeV, $\lambda_5 = 4 \times 10^{-4}$, $m_\nu^1 = 10^{-11}$ eV. *Bottom panel*: Evolution of the comoving number densities of $N_1$ (left) and $B - L$ (right) for the same parameters.

Finally, in Fig. 4.6 , we illustrate the effect of varying our model parameters $M_1, \lambda_5$ and the lightest neutrino mass $m_\nu^1$ (assuming normal ordering). We show the contours giving the correct observed asymmetry in the $M_{\rm in} - M_1$ plane, for different values of $\lambda_5$ (left) and for different $m_\nu^1$ (right). While we focus on the possibility of low scale leptogenesis from a few hundreds of TeV to 2000 TeV or so, it is also possible to discuss high scale leptogenesis. Since high scale leptogenesis within Type-I seesaw has already been discussed in the context of PBH in earlier works including [100], we outline this complementary window and study the effects of PBH domination in the early Universe. Now, in this regime, the decreasing behavior of $M_{in}$ with leptogenesis scale $M_1$ in order to give the correct asymmetry in Fig. 4.6 can be well understood from the right panel of Fig. 4.2. There, it can be noticed that for a higher leptogenesis scale, the intersection of $\eta_B$ with the observed asymmetry contour (cyan colour) occurs earlier. This is primarily because for a

higher leptogenesis scale, the during case discussed above (PBH evaporation during the scale of leptogenesis) occurs earlier and hence for a lower PBH mass. Thus, the departure from the thermal leptogenesis behavior starts occurring earlier. However, this trend of $M_{in}$ with $M_1$ is not always guaranteed, as can be seen in the orange contours at a lower value of $M_1$.

The changing behavior with $\lambda_5$ in the left panel can be understood as follows : For a higher value of $\lambda_5$, the asymmetry produced is lower (see left of Fig. 4.1). Hence, the dilution by PBH required in order to give the correct asymmetry should be minimal. This explains the lower value of PBH mass required for giving the correct asymmetry. The departure from this behavior seen in the figure can be attributed to the washout effects, which starts becoming important for a lower $\lambda_5$ and also for a higher value of $M_1$ (see Eqn. (4.13)). Similar conclusion can be drawn from the right panel of Fig. 4.6, since asymmetry for a higher neutrino mass $m_\nu^1$ is lower.

Note that in Fig. 4.6 (left panel), for $\lambda_5 = 0.0006$, the asymmetry produced for $M_1 \lesssim 400$ TeV is already below the observed value and hence additional dilution due to PBH evaporation will not help in generating the correct asymmetry. Similar pattern can be observed for light neutrino mass $m_\nu^1 = 10^{-8}$ eV in the right panel plot of Fig. 4.6. Moreover, in the left panel, for $\lambda_5 = 0.0003$ eV, the washout effects become dominant for $M_1 \gtrsim 1800$ TeV, and fails to give the observed asymmetry.

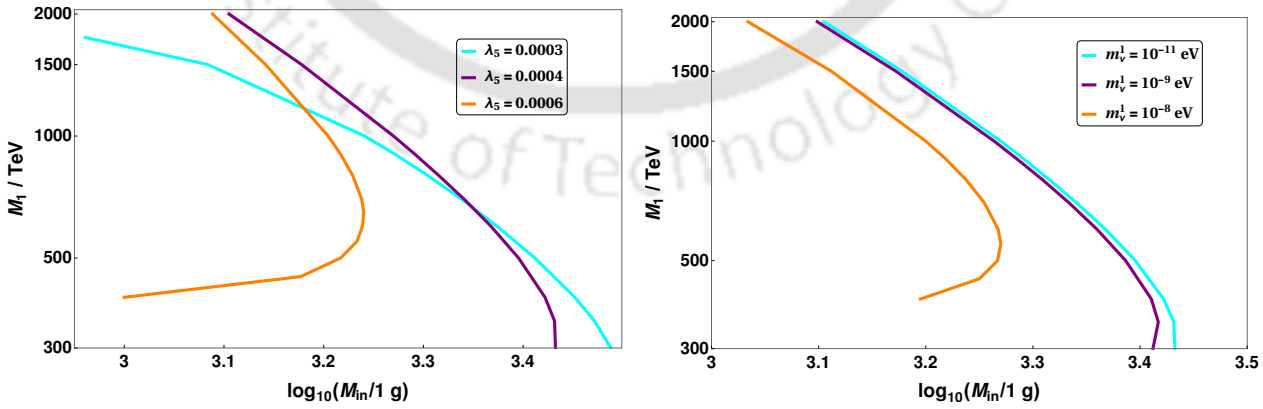


FIGURE 4.6: Contours giving the observed baryon asymmetry of the Universe, in the $M_{\rm in} - M_1$ plane for different $\lambda_5$ values(left) and for different values of $m_\nu^1$ (right), taking a PBH dominated Universe, $\beta = 10^{-3}$. In the left panel, $m_\nu^1$ is fixed at $10^{-11}$ eV and $\lambda_5$ is taken to be 0.0004 in the right panel.

### 4.2.3 Dark Matter in the presence of PBH

PBH evaporation can play an important role in generating DM relic density, for both thermal as well as non-thermal DM. For earlier works studying such effects in different contexts, see [98, 102, 103, 112, 245–255]. In our scenario, the lightest scalar of the inert doublet is the dark matter candidate. It can be in thermal equilibrium in the early Universe by virtue of its electroweak gauge interactions. As usual, when the interaction rate of dark matter becomes less than the Hubble, $\Gamma_{\rm DM} < H$, the DM goes out of equilibrium and eventually freezes out to give a relic abundance.

Now, in the presence of PBH, this typical WIMP phenomena can be modified. There can be different scenarios [102, 103] depending on the interplay between the freeze-out temperature of WIMP DM $T_{\rm fo}$ and the PBH evaporation temperature $T_{\rm ev}$. Two other important energy scales are given by $T_{\rm eq}$ and $T_c$ (see Fig. 4.5). Here, $T_{\rm eq}$ corresponds to the temperature, such that for $T > T_{\rm eq}$, PBH cannot dominate the energy density of the Universe. This is shown by the region marked as I in the top left panel of Fig. 4.3-4.5. If freeze-out happens during this epoch, we would have the usual WIMP case in a radiation dominated Universe, with a subsequent dilution of the relic due to PBH evaporation. Now, for $T_c < T < T_{\rm eq}$ (marked as II in the top left panel of Fig. 4.3-4.5), PBH can dominate the energy density of the Universe, if $\beta > \beta_c$. However, in this region SM radiation is still found to behave as free radiation, i.e., $\rho_{\rm Rad} \propto a^{-4}$ or equivalently $T \propto a^{-1}$. If freeze-out takes place during this epoch, one has to solve the WIMP dynamics assuming a matter-dominated background. Next, in the region III, PBH affect both the Hubble and the SM radiation evolution, which now scales as $\rho_{\rm Rad} \propto a^{-3/2}$ and the temperature of the plasma goes like $T \propto a^{-3/8}$ [82]. If DM freezes out during this epoch, one has to solve the WIMP dynamics in a matter dominated background as in the earlier case, but using the new temperature-scale factor relation mentioned above. Finally, region IV corresponds to the case when DM freezes out after PBH evaporation, $T_{\rm fo} < T_{\rm ev}$. In this region, the Universe is radiation dominated again, since the PBH have faded away completely, and the WIMP dynamics take place in a radiation dominated Universe, with no entropy dilution present like the earlier cases. Also, since DM can still be in equilibrium after PBH

evaporation, the DM produced from PBH evaporation enters into the thermal bath and gives no extra contribution to the relic.

Now, in order to investigate the effect of PBH on the WIMP dynamics, we first study the cases of PBH evaporation happening after DM freeze-out, i.e., $T_{\rm fo} > T_{\rm ev}$, which corresponds to the first three cases discussed above. Here, the contribution to the DM relic can be divided into two parts [102]: one produced by Hawking radiation, $\Omega^{\rm BH}_{\rm DM}h^2$ and the other from the WIMP freeze-out $\Omega^{\rm fo}_{\rm DM}h^2$, with a subsequent entropy dilution because of the PBH evaporation. Thus, $\Omega^{\rm total}_{\rm DM}h^2 = \Omega^{\rm BH}_{\rm DM}h^2 + \Omega^{\rm fo}_{\rm DM}h^2$. Now, since PBH have to evaporate before the BBN scale, one should have $T_{\rm fo} \gtrsim 0.1$ MeV. Assuming a typical freeze-out around $z_{\rm fo} = M_{\rm DM}/T_{\rm fo} \sim 30$, we can get an approximate lower bound on the DM mass for the case of $T_{\rm fo} > T_{\rm ev}$ as

$$M_{\rm DM} \gtrsim 3 \text{ MeV}. \tag{4.17}$$

This is trivially satisfied for scalar doublet DM as constraints from direct search restrict its mass to be much heavier [256, 257]. Moreover, to be consistent with leptogenesis, note that the mass of DM should be less than the right handed neutrino, i.e. $M_{\rm DM} < M_1$, so that the right handed neutrino can decay to produce lepton asymmetry and scalar DM remains stable.

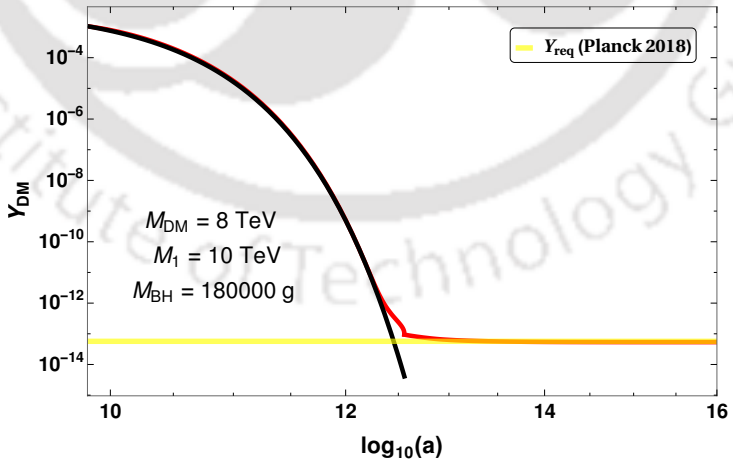


FIGURE 4.7: Evolution of $Y_{\rm DM}$ with scale factor for the benchmark values shown and considering $\beta > \beta_c$. The black line corresponds to the evolution of the equilibrium number density and the yellow line represents the value of $Y_{\rm DM}$ required to give the observed relic abundance of DM. Here, $\lambda_5 = 0.00008$ and mass of the charged scalar, $M_{\eta^+} = 8010$ TeV.

We first analyse the thermal DM production. We solve the Boltzmann equation for dark matter around the freeze-out time, considering DM mass to be 8 TeV. The relevant equation for its comoving number density $Y_{\rm DM}$ in terms $z = M_{\rm DM}/T$ can be written as

$$k\frac{d\,Y_{\rm DM}}{dz} = -\frac{<\sigma v> s}{Hz}\left(Y_{\rm DM}^2 - Y_{\rm eq}^2\right), \tag{4.18}$$

where $k = 1$ or $3/8$, depending on whether we are in region $I/II$ or region $III$ respectively. In Fig. 4.7, we show the evolution of $Y_{\rm DM}$ with the scale factor $a$. It can be seen that for the chosen benchmark values, DM production is thermally overabundant. However, entropy dilution from PBH evaporation around $\log(a) \sim 12.6$ can eventually lead to the correct relic abundance. Thus, small values of $<\sigma v>$, which otherwise give a large relic, can now be allowed. However, as will see in a while, PBH not only lead to entropy dilution but also overproduction of DM specially for large $\beta$.

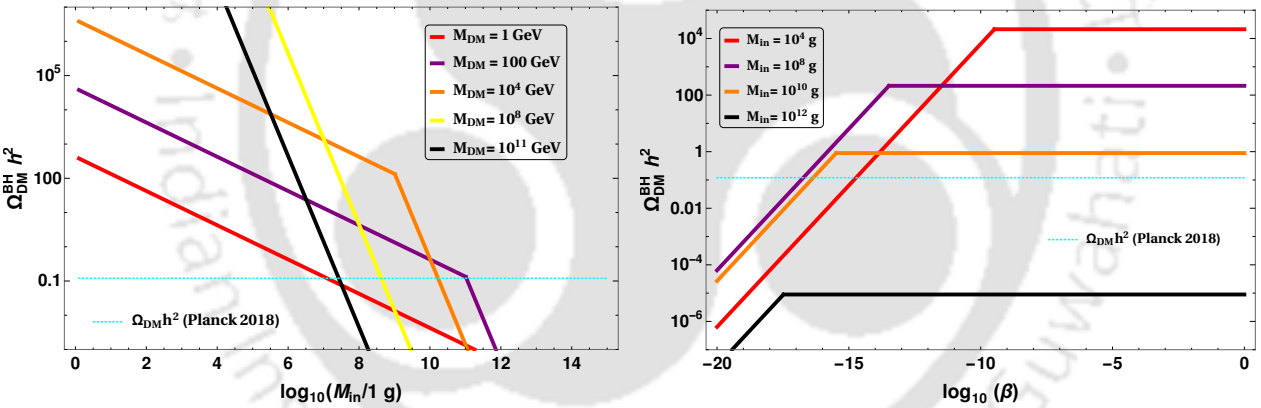


FIGURE 4.8: Variation of Dark Matter relic abundance $\Omega^{\rm BH}_{\rm DM}h^2$ coming from PBH evaporation with initial PBH mass $M_{\rm in}$ (left) and with initial PBH abundance $\beta$ (right). The dotted line represents the observed relic abundance. In the left panel, $\beta = 10^{-4}$, such that we have a PBH dominated Universe. The DM mass is taken to be 5 TeV in the right panel.

For the non-thermal contribution to the DM relic coming from PBH evaporation, the present DM relic can be estimated as [102, 103]

$$Y_{\rm DM} = \frac{n_{\rm DM}(T_0)}{s(T_0)} \simeq \frac{3}{4}N_{\rm DM} \times \begin{cases} \beta\frac{T_{\rm in}}{M_{\rm in}} & \text{for radiation domination, } \beta \leq \beta_c, \\ \frac{\bar{T}_{\rm evap}}{M_{\rm in}} & \text{for matter domination, } \beta \geq \beta_c, \end{cases} \tag{4.19}$$

where $n_{\rm DM}$ and $s$ corresponds to the number density and entropy density respectively, $T_0$ is the present temperature and $\bar{T}_{\rm evap} = \frac{2}{\sqrt{3}} T_{\rm evap}$ [103]. The number of DM particles emitted, $N_{\rm DM}$ can be estimated using Eqn. (2.18). In the left panel of figure 4.8, we show the DM relic abundance generated from PBH evaporation as a function of initial PBH mass $M_{\rm in}$ for different DM mass. The right panel of the figure shows the same as a function of $\beta$ for different values of $M_{\rm in}$. It can be seen that for DM masses between 4 GeV $\lesssim M_{\rm DM} \lesssim 10^9$ GeV, DM is overproduced, unless we are in a radiation dominated Universe (small $\beta$). This was also illustrated in [103, 258]. Note that in this regime, higher PBH masses which can give rise to the correct relic fall outside the BBN bound (cf. Eqn. (2.13)).

### 4.2.4 $N_2$ leptogenesis and fermion dark matter

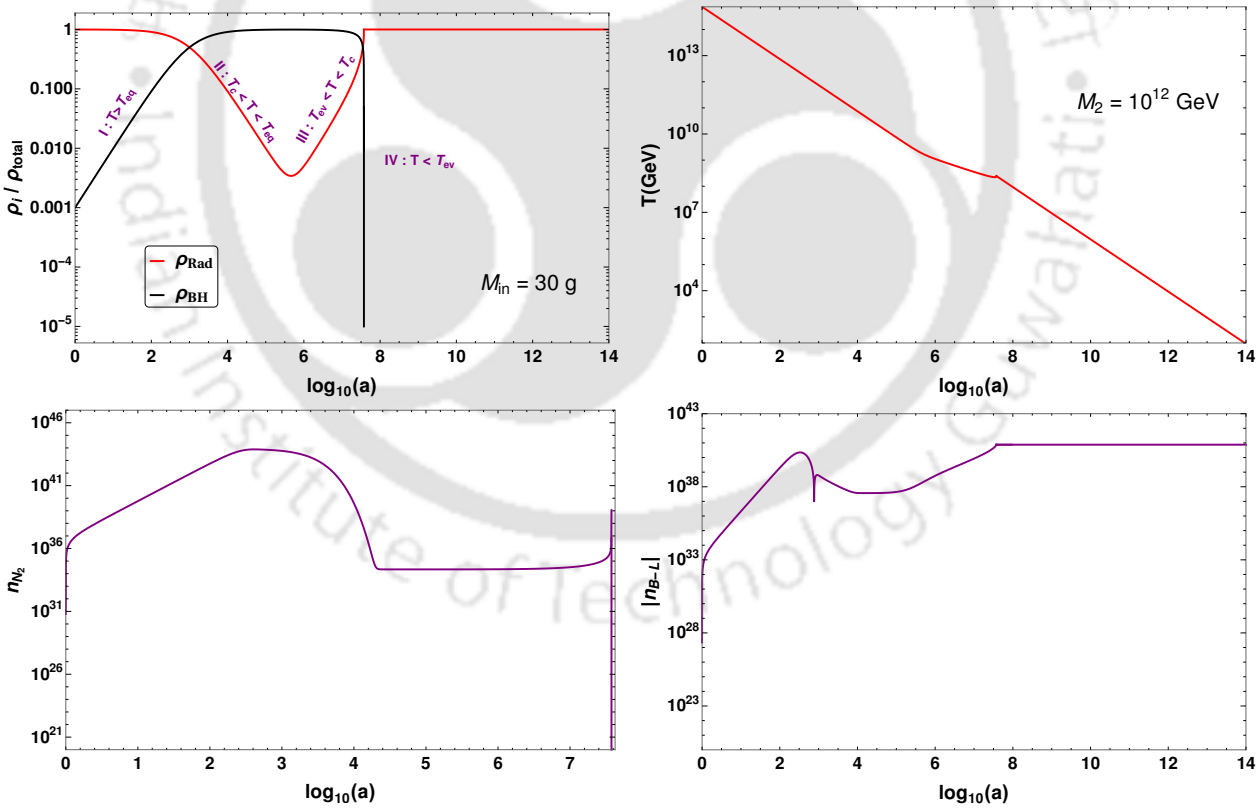


FIGURE 4.9: Upper panel : Evolution of the energy densities (left) and temperature of the thermal plasma (right), taking $M_{\rm in} = 30\ g$, $M_2 = 10^{12}$ GeV, $\lambda_5 = 0.5$, $m_\nu^1 = 10^{-18}$ eV. Lower plot : Evolution of the comoving number densities of $N_1$ (left) and $B - L$ (right) for the same parameters.

In this section, we explore the possibility of having leptogensis from $N_2$ decays while considering the lightest RHN $N_1$ as a dark matter candidate. Although $N_3$ decay can also generate lepton asymmetry in principle, we consider the asymmetry generated from $N_3$ decay or any pre-existing asymmetry to be washed out due to strong washout effects mediated either by $N_2$ or $N_3$ themselves. Such a scenario of $N_2$ leptogenesis in scotogenic model was studied in details recently in [241], and we follow the same prescription here, considering a mass hierarchy: $M_3 = 10^3\ M_2$. While the evolution of different quantities remain similar as before, the scale of leptogenesis gets pushed up for $N_2$ leptogenesis. Therefore, the typical PBH masses for "before", "during" and "after" scenarios described earlier can be much smaller. Additionally, since $N_1$ is much lighter compared to the scale of leptogenesis, apart from the $\Delta L = 2$ washout introduced by $l\eta \longrightarrow \bar{l}\eta^*$ scattering we can have $\Delta L = 1$ washout processes : $lW^{\pm}(Z) \longrightarrow N_1\eta$ and $l\eta \longrightarrow W^{\pm}(Z)N_1$ as well, which can affect leptogenesis. In our numerical analysis we take all these processes and solve the same Boltzmann equations as discussed in section 4.2.2. Therefore, in the $N_2$ leptogenesis scenario we are in a strong washout region which pushes the leptogenesis scale above $\mathcal{O} \geq 10^{10}$ GeV. The produced asymmetry gets further diluted if PBH evaporation takes place after the generation of asymmetry. For illustrative purposes, we show the evolution of different physical quantities for $N_2$ leptogenesis in figure 4.9 considering a scenario where PBH of 30 g initial mass evaporates after the scale of leptogenesis. Since the overall pattern is similar to $N_1$ leptogenesis discussed before except the change in scale of leptogenesis and PBH mass, we skip the detailed discussion of the other two possibilities in $N_2$ leptogenesis.

In Fig. 4.10, we show the variation of the final baryon asymmetry with initial PBH mass $M_{\rm in}$ for different leptogenesis scales, namely $M_2$, keeping $\beta$ fixed at $10^{-3}$. Here, in contrast to the behavior seen in our earlier case (refer to figure 4.2) of leptogenesis from $N_1$ decay, there is an increase in the asymmetry compared to the purely thermal contribution (dashed lines) for a certain region of initial PBH mass. This is because, here, in addition to the entropy injection by PBH, the RHNs emitted by PBH also contribute significantly to the asymmetry. This effect is more dominant when leptogenesis is over and the strong

washout effects had also decreased by the time PBH starts evaporating. For instance, with $M_2 = 10^{12}$ GeV, there is an increase in the asymmetry between 0.5 g $\lesssim M_{\rm in} \lesssim$ 1 g. At higher values of $M_{\rm in}$, the effect of dilution by PBH starts dominating over the enhancement by RHNs from PBH, which explains the decreasing behavior of the asymmetry. As we keep on decreasing the leptogenesis scale, this enhancement effect is shifted to the right, since now PBH with a higher initial mass evaporate after the leptogenesis scale as well as after the dominance of strong washout is over. For instance, with $M_2 = 10^{10}$ GeV, the contribution from RHNs emitted by PBHs is more dominant after $M_{\rm in} \gtrsim 10$ g, which leads to an increase in the asymmetry.

While both thermal and non-thermal $N_1$ DM with masses around the TeV corner were studied in [241], here $N_1$ is constrained to be in the light mass regime, since $M_1 \gtrsim 4$ GeV is overproduced in a PBH dominated Universe, as discussed in section 1.1. Now, depending on the lightest active neutrino mass which determines the Yukawas, $N_1$ can either be a thermal or a non-thermal dark matter candidate. Realising such light thermal dark matter is often challenging due to the Lee-Weinberg bound [165]. Unless there exists additional new particles in such low mass regime to assist in DM annihilation or coannihilation, such light thermal DM is typically overproduced due to small cross section. Hence, we consider the case of non-thermal dark matter, by taking the $N_1$ Yukawas small. Such DM, with negligible initial abundance gets frozen in at later epochs from the particles present in the thermal bath, either via decay or scattering. A recent review of such DM, also known as the feebly interacting (or freeze-in) massive particle (FIMP) paradigm, can be found in [29].

The DM candidate $N_1$ can be as light as a few keV (typical lower bound for fermion DM [157]) and as shown in earlier work [241], only normal ordering (NO) of light neutrinos is consistent with FIMP type $N_1$. On the other hand, inverted ordering (IO) cannot give rise to the required Yukawa coupling of $N_1$ DM. Thus, we stick to NO and consider tiny Yukawa coupling of $N_1$ via Casas-Ibarra (CI) parametrisation [71].

Now, for small $N_1$ Yukawas, $N_1$ cannot reach thermal equilibrium and hence we are in the ballpark of FIMP dark matter as mentioned above. Hence, $N_1$ needs to be produced

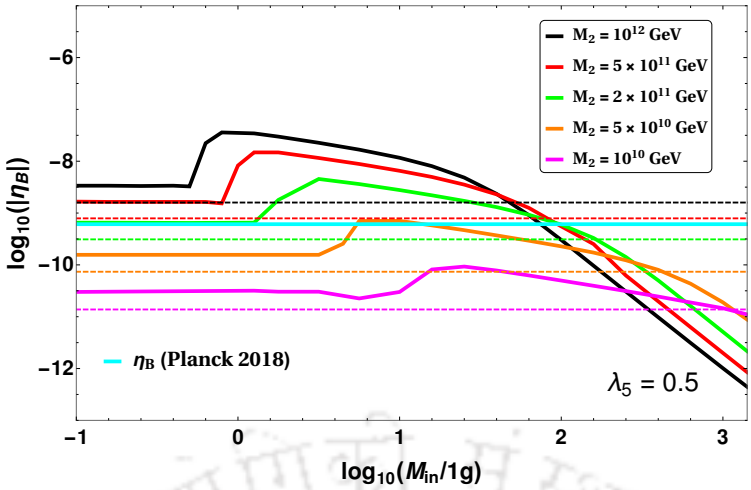


FIGURE 4.10: Final baryon asymmetry as a function of the PBH mass, for different leptogenesis scales $M_2$, taking $\lambda_5 = 0.5$ and lightest neutrino mass $m_\nu^1 = 10^{-18}$ eV. The Cyan line indicates the observed asymmetry and the dashed lines represent the asymmetry produced in the absence of PBH.

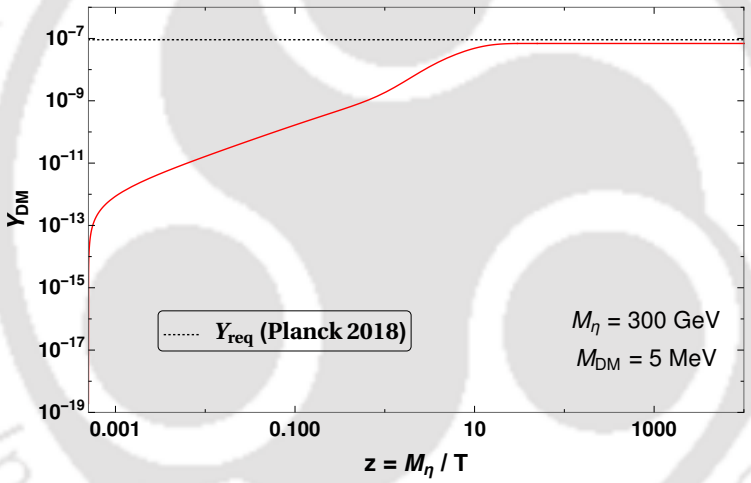


FIGURE 4.11: Evolution of comoving number density of DM considering $M_{\rm DM} = 5$ MeV, $M_\eta = 300$ GeV, $\lambda_5 = 0.5$ and $m_\nu^1 = 10^{-18}$ eV.

from the decays or scatterings of particles in the thermal bath. The dominant scattering processes are $lW^\pm(Z) \longrightarrow N_1\eta$ and $l\eta \longrightarrow W^\pm(Z)N_1$ whereas the dominant decay mode is $\eta \to N_1 l$. While the production from decay continues till $\eta$ gets Boltzmann suppressed, the contribution from scattering to DM yield gets saturated when the equilibrium abundance of $W^\pm/Z$ is Boltzmann-suppressed. For the chosen mass range of PBH so as to affect leptogenesis, light FIMP DM production from the bath particles happens after the evaporation of PBH. Thus, the total contribution to the DM relic will be the sum of DM density produced from the PBH (which now cannot enter into thermal equilibrium unlike

the WIMP case discussed in section 1.1) and the freeze-in production which would happen after PBH evaporation in a radiation dominated Universe. We solve the following Boltzmann equations for $\eta$ and $N_1$ to find the relic abundance from freeze-in.

$$\frac{dY_\eta}{dz} = -\frac{4\pi^2}{45}\frac{M_{\rm Pl} m_\eta}{1.66}\frac{\sqrt{g_\star(z)}}{z^2}\left[\sum_{p\equiv \text{SM particles}} \langle\sigma v\rangle_{\eta\eta\to pp}\left(Y_\eta^2 - (Y_\eta^{\rm eq})^2\right)\right] \tag{4.20}$$
$$- \frac{M_{\rm Pl}}{1.66}\frac{z}{m_\eta^2}\frac{\sqrt{g_\star(z)}}{g_s(z)}\Gamma_{\eta\to N_1 l} Y_\eta$$
$$\frac{dY_{N_1}}{dz} = \frac{M_{\rm Pl}}{1.66}\frac{z}{m_\eta^2}\frac{\sqrt{g_\star(z)}}{g_s(z)}\Gamma_{\eta\to N_1 l} Y_\eta$$
$$+ \frac{4\pi^2}{45}\frac{M_{\rm Pl} M_\eta}{1.66}\frac{\sqrt{g'_\star(z)}}{z^2} \times \left(\sum_{x=W^\pm,Z,\eta} \langle\sigma {\rm v}_{lx\to N_1 x}\rangle \ (Y_x^{eq} Y_l^{eq} - Y_{N_1} Y_x)\right) \tag{4.21}$$

where $z = M_\eta/T$ and $g_\star(z)$ is given by:

$$\sqrt{g'_\star(z)} = \frac{g_{*s}(z)}{\sqrt{g_\star(z)}}\left(1 - \frac{1}{3}\frac{d\ln g_{*s}(z)}{d\ln z}\right).$$

The evolution plot of the comoving number density of DM is shown in figure 4.11.

### 4.2.5 Summary and Conclusion

In the previous sections, we have highlighted the key features of the minimal scotogenic model in terms of leptogenesis and dark matter in the presence of primordial black holes. We now perform a numerical scan over the two key parameters of PBH, the initial PBH mass $M_{\rm in}$ and the initial PBH fraction $\beta$. The relevant parameter space along with different bounds is shown in Fig. 4.12 for low-scale leptogenesis scenario.

The pink shaded region is ruled out from the upper bound on the inflation scale (Eqn. (2.4)). The green and blue shaded regions are ruled out due to the criteria of PBH evaporation before BBN (Eqn. (2.13)) and the sphaleron scale (Eqn. (4.16)) respectively. The red dotted line marks the boundary between PBH domination and radiation domination (Eqn. (2.15)). In the orange shaded region, gravitational waves (GW) are overproduced

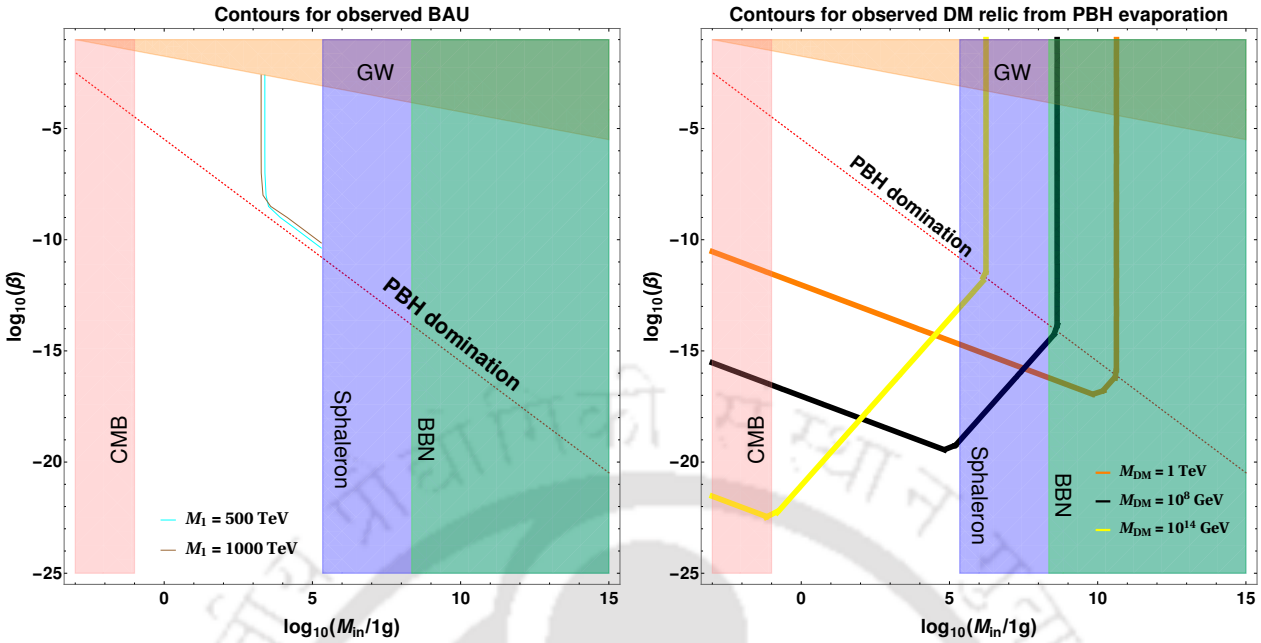


FIGURE 4.12: Parameter space in the $M_{\rm in} - \beta$ plane giving the observed baryon asymmetry of the Universe (left panel) from leptogenesis due to $N_1$ decay and observed DM relic from PBH evaporation $\Omega^{\rm BH}_{\rm DM}h^2$ (right). Here, $\lambda_5 = 0.0004$ and $m^1_\nu = 10^{-11}$ eV. The shaded regions are excluded from different observable as described in the text.

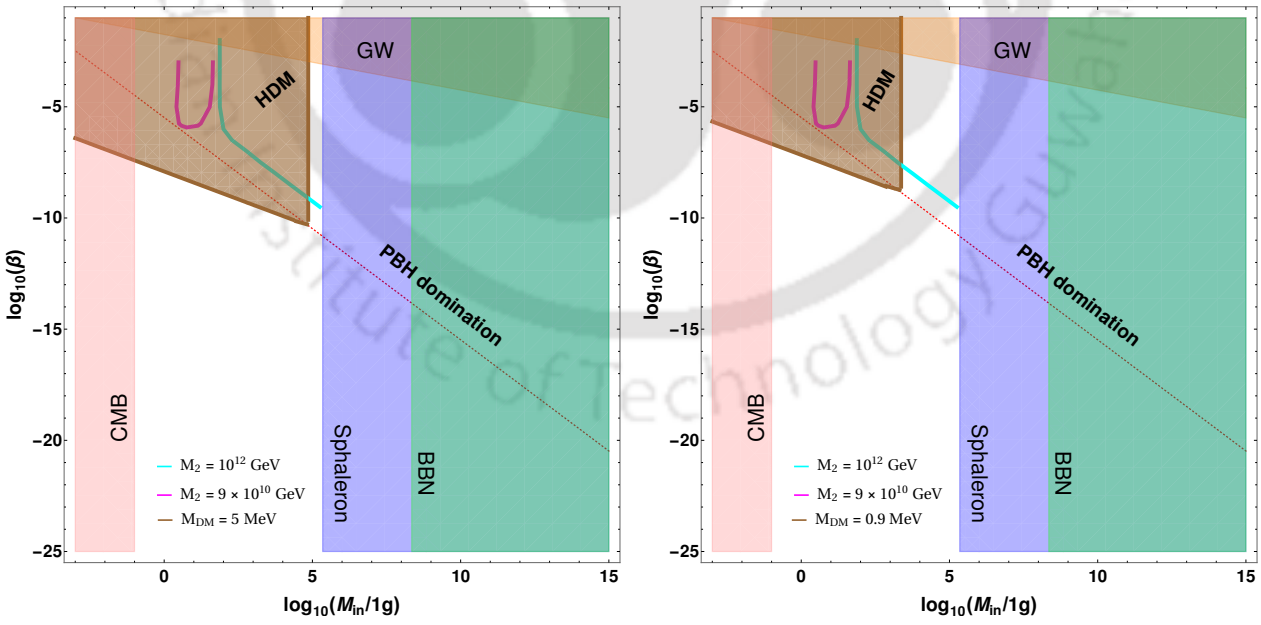


FIGURE 4.13: Parameter space in the $M_{\rm in} - \beta$ plane giving the observed baryon asymmetry of the Universe BAU (Cyan) and observed DM relic. The shaded regions are excluded from different observable as described in the text. Here, $M_{\rm DM} = 5$ MeV (left panel) and 0.9 MeV (right panel), $M_\eta = 300$ GeV, $\lambda_5 = 0.5$ and $m^1_\nu = 10^{-18}$ eV.

leading to a backreaction problem, as discussed in [117]. To avoid this, we require[3] [117]

$$\beta < 10^{-4} \left( \frac{10^9\ g}{M_{\rm in}} \right)^{1/4} . \tag{4.22}$$

The contours giving rise to the correct baryon asymmetry for two different leptogenesis scales are shown in the left panel plot of figure 4.12. The key model parameter $\lambda_5$ is fixed at 0.0004 and the lightest neutrino mass is taken to be $10^{-11}$ eV. For such choice of parameters, thermal leptogenesis leads to overproduction of baryon asymmetry. PBH with a sufficiently high mass can give rise to the correct asymmetry through entropy dilution. To understand the behavior with $\beta$, let us first concentrate on the leptogenesis scale of 500 TeV. As evident from the cyan coloured contour, the asymmetry is almost independent of $\beta$ (the vertical region). However, as we keep on decreasing $\beta$, the effect of PBH starts to diminish, which increases the asymmetry. Hence, to produce the correct asymmetry a higher value of PBH mass is required. This explains the departure of the cyan coloured contour from the vertical pattern. Similar behavior can be seen for the other leptogenesis scale as well.

Now, as discussed in section 4.2.3, DM relic is overproduced because of Hawking radiation from PBH for large $\beta$. In the right panel plot of Fig. 4.12, we show the contours giving the correct DM relic abundance with contribution only from PBH evaporation (assuming that thermal abundance is negligible either due to large DM annihilation or entropy dilution from PBH evaporation). The lower values of $\beta$, say less than around $\mathcal{O}(-10)$, can give the correct non-thermal DM relic abundance. However, for such tiny values of $\beta$, the leptogenesis setup will merge with the thermal leptogenesis, with no significant effect due to the presence of PBH. Note that non-thermally generated relic for DM with lower mass can be consistent with larger values of $\beta$ as well. It turns out that, if DM mass is below the GeV regime, non-thermal DM relic can be consistent with observed abundance even with large values of $\beta$. However, DM being part of a scalar doublet, such tiny masses are ruled out by direct search constraints. If the lightest $Z_2$ odd particle were

[3]The more recent analysis in Ref. [118] puts a slightly stronger bound on $\beta$ (cf. Eqn. (2.51)). However, our conclusions remain unaffected by this.

one of the neutral singlet fermions, then this possibility could have been realistic. Thus, for scalar doublet DM, the only realistic possibility is to have its mass around a TeV or lower so that it freezes-out below the sphaleron decoupling temperature. Since PBH of chosen mass evaporates before sphaleron decoupling, the DM produced from such evaporation enter the thermal bath without affecting final DM relic.

Next, in Fig. 4.13, we show the parameter space in the $M_{\rm in} - \beta$ plane, which gives the correct observed asymmetry along with the observed DM relic for $N_2$ leptogenesis scenario. Here since the leptogenesis scale is pushed high, PBH with a smaller mass can also start affecting the asymmetry. Hence, the contour for the correct observed asymmetry shifts towards left compared to that of figure 4.12 (left panel). The behavior of the observed asymmetry contour for the leptogenesis scale of $10^{12}$ GeV (shown in cyan color) is the same as that of $N_1$ leptogenesis discussed before, since it is thermally overproduced (refer to figure 4.10) and entropy dilution by PBH can give rise to the correct observed asymmetry. However, for a lower leptogenesis scale of $9 \times 10^{10}$ GeV (shown in magenta color), the asymmetry is thermally underproduced and contribution from RHNs emitted by PBH can increase the asymmetry as discussed in section 4.2.4. Now, as can be seen from Fig. 4.10, such asymmetry contours will intersect the observed asymmetry contour at two points. Thus, two values of initial PBH mass $M_{\rm in}$ can give rise to the correct asymmetry for a fixed value of $\beta$. Moreover, if we keep on decreasing $\beta$ further, the enhancement effect induced by PBH keeps on decreasing and at some point, we will not be able to get the observed asymmetry. This explains the U-shaped pattern obtained in Fig. 4.13 for $N_2$ leptogenesis scale of $9 \times 10^{10}$ GeV.

Now, our scenario corresponds to a case of mixed dark matter, where along with the cold or warm DM component from freeze-in, we have a potential hot component produced by PBH evaporation. Data from observations related to the CMB and baryon acoustic oscillation (BAO) allow us to put an upper bound on the fraction of this hot component with respect to the total DM, depending on the value of DM mass [259]. Here, we apply a conservative 10 % upper bound on such hot dark matter (HDM) component [103]. Considering DM mass as 5 MeV, the region which gives more than 10 % of the

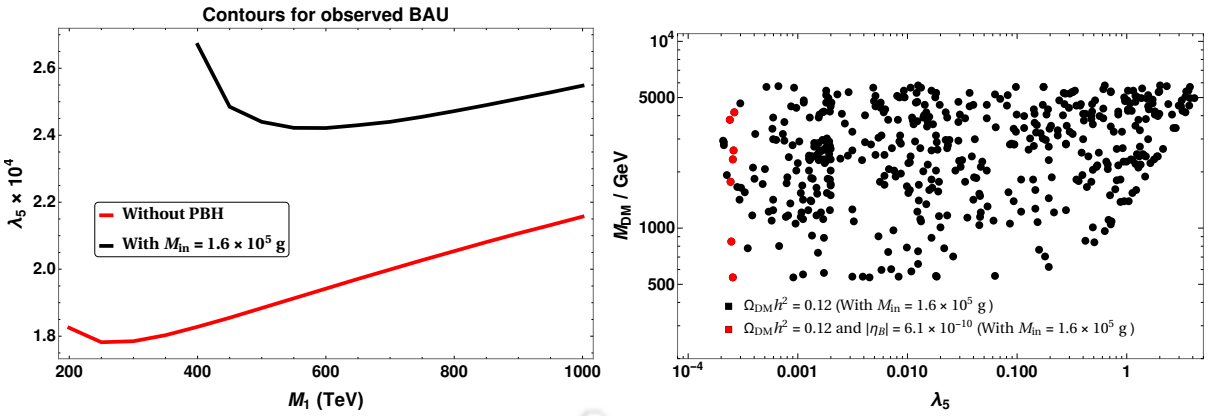


FIGURE 4.14: Left panel: Parameter space in the $\lambda_5 - M_1$ plane giving the observed BAU with and without the presence of PBH for $N_1$ leptogenesis with $\beta = 4 \times 10^{-11}$, $m_\nu^1 = 10^{-11}$ eV. Right panel: Scalar DM parameter space consistent with the requirement that its freeze-out occurs after PBH evaporation.

total DM from PBH evaporation is shown by the brown region (labelled as HDM) in the left panel plot of figure 4.13. The remaining contribution is given by the freeze-in component, which is independent of the PBH parameters. Thus, the white regions represent the region allowed by the observed DM relic. For example, the brown contour gives $\Omega_{\rm DM}^{\rm BH}h^2 = 0.1 \times 0.12$. The remaining 90% can be obtained from freeze-in by suitably choosing the other parameters of the model. For instance, figure 4.11 shows the evolution plot for the parameters which gives freeze-in contribution $\Omega_{\rm DM}^{\rm FIMP}h^2 = 0.9 \times 0.12$. While for DM mass of 5 MeV, the brown shaded region disfavours most parts of the cyan colored line, for lower DM mass say 0.9 MeV, the brown shaded region shrinks allowing more of the cyan colored line showing leptogenesis favoured parameter space, as shown in the right panel plot of figure 4.13. Decreasing DM mass further can also allow the other leptogenesis scale of $9 \times 10^{10}$ GeV.

Hence, we conclude that in our setup, considering leptogenesis from $N_1$ decay with scalar doublet dark matter, it is not possible to find a region of PBH parameters which can simultaneously affect DM genesis as well as leptogenesis. For PBH to affect leptogenesis, one requires large PBH fraction $\beta$. Typically, for the region of parameter space leading to overproduction of baryon or lepton asymmetry in the scotogenic model, presence of PBH with sufficient fraction $\beta$ can lead to entropy dilution bringing the prediction to agreement with observations. However, such large $\beta$ values lead to overproduction of DM

from PBH evaporation, for heavy DM mass regime where DM freeze-out occurs before PBH evaporation. Therefore, in order to have non-trivial effects of PBH on leptogenesis, we need to have DM in low mass regime so that its freeze-out occurs after PBH evaporation and relic is generated purely by thermal freeze-out. While successful DM genesis and leptogenesis in the presence of PBH can occur independently in this setup with above-mentioned choices of parameters, scenarios where such cogenesis occurs in a dependent manner can have interesting constraints on PBH properties. To explore this direction, we have also considered the scenario where leptogenesis occurs due to $N_2$ decay while the lightest right handed neutrino $N_1$ is the DM candidate. While the scale of leptogenesis is pushed to high scale regime in this case, the gauge singlet nature of $N_1$ allows us to consider it in the light mass window (few GeV or below) where it is not overproduced from PBH even with $\beta$ values leading to PBH domination. However, such light DM originating from PBH can lead to a hot DM component, tightly constrained from astrophysical bounds. While considering a conservative upper bound on such hot DM fraction of 10%, we found the PBH model parameters consistent with successful $N_2$ leptogenesis and non-thermal $N_1$ DM with mixed contribution from PBH as well as SM bath.

Finally, for illustrating more specific estimates of the model parameters in the presence of PBH, we show the parameter space for $N_1$ leptogenesis and scalar DM in figure 4.14. From the left panel plot it is clear that the asymmetry contour gets modified in the presence of PBH, with the behavior determined by the interplay of entropy dilution, enhancement from PBH evaporation and washout effects discussed in section 4.2.2. The PBH initial mass and initial fraction are chosen to be $1.6 \times 10^5$ g and $\beta = 4 \times 10^{-11}$ respectively, such that they evaporate long after the scale of leptogenesis and at the same time do not dilute the asymmetry much, because of a small value of $\beta$ (see left panel of figure 4.12). Such a high value of PBH mass can also constrain the scalar DM parameter space, from the condition that they evaporate before the DM freeze-out, to prevent the overproduction of DM relic discussed above. This is illustrated in the right panel of figure 4.14, where, by running a scan over the relevant parameters, we show the parameter space in the $M_{\rm DM} - \lambda_5$ plane giving the correct DM relic in the presence of PBH, having

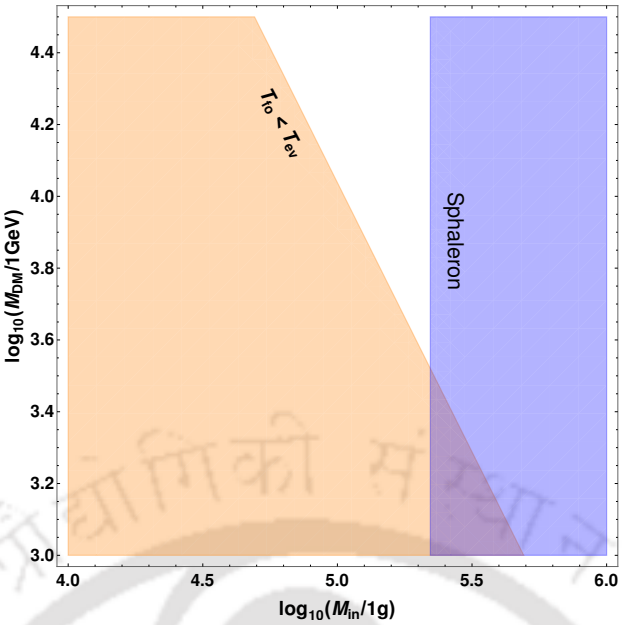


FIGURE 4.15: Region showing $T_{\rm fo} < T_{\rm ev}$ (orange shaded) in the $M_{\rm in} - M_{\rm DM}$ plane, taking $z_{\rm fo} = M_{\rm DM}/T \approx 25$, typical for thermal freeze-out.

the same mass of $1.6 \times 10^5$ $g$. Clearly, DM with high masses are ruled out because they freeze-out at a higher temperature before PBH evaporation, leading to overproduction. On the other hand lower DM mass below around 500 GeV are disallowed due to large annihilation rates into electroweak gauge bosons, keeping thermal relic density suppressed. The slope in large $\lambda_5$ region is observed as DM annihilation mediated by components of the inert doublet is enhanced in this regime for larger mass splitting within inert doublet components (where splitting is proportional to $\lambda_5$), requiring larger DM mass to keep the annihilation rates within required rate for generating correct thermal relic. The points shown in red color in the right panel plot are also consistent with correct baryon asymmetry (compare with left panel). Note that for a lower PBH mass, the condition of $T_{\rm fo} < T_{\rm ev}$ will be trivially satisfied. Hence, in general, PBH and DM with higher masses are more constrained. This is further demonstrated in figure 4.15, where in the $M_{\rm in} - M_{\rm DM}$ plane, we show the region of $T_{\rm fo} < T_{\rm ev}$ (orange shaded), which excluding the sphaleron bound, prohibits an extra small range of high PBH mass (white region) due to DM overproduction.

Similarly, we show the parameter space for $N_2$ leptogenesis and fermion DM in the

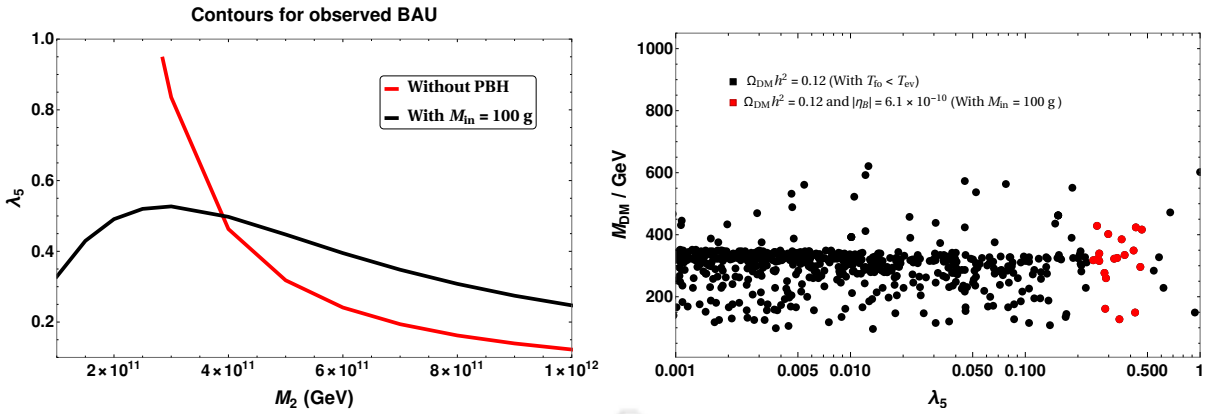


FIGURE 4.16: Left panel: Parameter space in the $\lambda_5 - M_2$ plane giving the observed BAU with and without the presence of PBH for $N_2$ leptogenesis with $\beta = 10^{-3}$, $m_\nu^1 = 10^{-18}$ eV. Right panel: Parameter space in the $\lambda_5 - M_{\rm DM}$ plane giving the observed fermion DM relic of the Universe with the condition $T_{\rm fo} < T_{\rm ev}$.

presence of PBH in figure 4.16. While non-thermal fermion DM has been discussed already, the $N_2$ leptogenesis favoured parameter space can be more tightly correlated with thermal fermion DM scenario [260], while also showing the crucial differences arising due to the presence of PBH. While the contours for successful leptogenesis are different with and without PBH, the fermion DM mass range gets shifted to smaller values from the requirement $T_{\rm fo} < T_{\rm ev}$. Since fermion DM Yukawa couplings remain small due to large $\lambda_5$ required for high scale $N_2$ leptogenesis, its relic is governed primarily due to coannihilation with inert doublet scalars, requiring them to be light and hence within discovery reach of ongoing experiments like the large hadron collider (LHC).

To summarize, we have performed a detailed analysis of leptogenesis and dark matter production in the presence of PBH considering the well-known scotogenic model as a working example which naturally allows a low scale seesaw and leptogenesis possibility. The important parameters of this particle physics set up are the leptogenesis scale $M_{1,2}$, DM mass $M_\eta$ (or $M_1$), $\lambda_5$ and the lightest neutrino mass $m_\nu^1$, which also determine the Yukawa couplings. Our main motivation was to investigate how the presence of PBH can affect the otherwise allowed (disallowed) parameter space of this model in a radiation dominated Universe, specially focusing on low scale leptogenesis which has not been discussed in earlier works. We indeed obtained some dependency on the PBH parameters: the initial PBH mass $M_{\rm in}$ and the initial PBH fraction $\beta$. These dependencies have been

illustrated in figures 4.2, 4.6 and 4.10, and further summarized in figures 4.12 and 4.13 along with the different bounds discussed above. Clearly, different values of parameters namely $M_{1,2}$, $M_\eta$, $\lambda_5$ and $m_\nu^1$ than that in the purely radiation dominated case is required now in the presence of PBH to generate the same baryon asymmetry. This is primarily due to the production of RHNs and DM by PBH and entropy injection by PBH. Although such a similar scenario was also considered in some earlier works, for example in [100] in the framework of high scale Type-I seesaw leptogenesis, here we explore the possibility of low scale seesaw in radiative neutrino mass model with the added bonus of a stable dark matter candidate. Since typical PBH initial mass and fraction affecting leptogenesis also lead to overproduction of DM, we are either forced to consider light thermal DM which freezes out after PBH evaporation or light non-thermal DM. We have constrained the PBH parameter space with both the observed baryon asymmetry and DM relic of the Universe, specially in our second case of fermionic DM, where the interplay between the three entities (leptogenesis, DM and PBH) is more involved as explained earlier. We also found the contribution to leptogenesis from RHN produced by PBH to dominate compared to the entropy dilution effect in the second case, for a region of PBH masses (see figure 4.10). This can relax the lower bound on the leptogenesis scale by an order or so compared to the thermal $N_2$ leptogenesis case in a purely radiation dominated Universe. The scalar DM scenario with $N_1$ leptogenesis is also predictive in the sense that large $\beta$ values for PBH affecting leptogenesis pushes DM mass into low mass regime. In such cases, DM can freeze-out after PBH evaporation without getting overproduced. Since scalar DM is part of an $SU(2)$ doublet, such light mass range can have interesting implications for discovery at collider or direct search experiments [261–264]. The comparison of leptogenesis and DM favoured parameter space for specific choices of PBH mass and initial fraction are shown in figure 4.14 and figure 4.16 for scalar DM ($N_1$ leptogenesis) and fermion DM ($N_2$ leptogenesis) respectively.

Apart from predicting different model parameters consistent with DM, BAU compared to the standard scenario (which can be looked up at particle physics based experiments), the PBHs can lead to observational consequences themselves. The different regions of PBH masses relevant for different leptogenesis scales and scenarios discussed in this work can give rise to a stochastic background of gravitational waves (GW) produced from PBH evaporation [147]. Such GW are in the high frequency regime (above THz), beyond the reach of presently functioning GW experiments. There have been several experimental proposals to detect such high frequency GW in future [265–269]. Morever, PBH could also emit GW through other mechanisms as discussed in section 2.3.2. In particular, for the PBH mass range considered here, the GW emitted from PBH density fluctuations could be within the reach of near future GW detectors. We leave such GW analysis for a future work. Moreover, if evidence of a PBH-dominated Universe with the above mass range is found, it would put tight constraints on purely thermal leptogenesis and dark matter models. In particular, future observations of PBH with mass around $10^3 - 10^4$ g can tightly constrain intermediate scale Type-I seesaw leptogenesis as found by [100] while scotogenic leptogenesis can still survive at low scale (or intermediate scale for $N_2$ case) as discussed earlier.

## 4.3 Asymmetric DM from PBH

### 4.3.1 The Minimal Setup

We provide a toy model to motivate our scenario. The minimum ingredients to generate the dark and visible sector asymmetries are adopted from [229]. The SM particle content is extended by two RHNs sufficient to fit light neutrino data via Type-I seesaw mechanism along with two dark sector particles namely a singlet scalar $\mathcal{S}$, a singlet Dirac fermion $\chi$ both odd under an in-built $\mathbb{Z}_2$ symmetry. The out-of-equilibrium CP-violating decay of these RHNs to the visible as well as to the dark sector produce asymmetry in both the sectors simultaneously. The interaction Lagrangian for such a scenario can be expressed as

$$-\mathcal{L} \supset \frac{1}{2} M_N \overline{N^c} N + y_N \overline{N}\, \tilde{H}^\dagger\, \ell + m_\chi \overline{\chi}\, \chi + y_\chi \overline{N}\, \mathcal{S}\, \chi + \text{h.c.}\,, \tag{4.23}$$

where we extend the SM particle spectrum by adding two generations of RHN $N_i$, singlet under the SM gauge symmetry. The SM leptons are denoted by $\ell$. A lepton number is assigned to the RHN such that its Majorana mass term is lepton number violating. Although three copies of RHNs are considered in typical Type-I seesaw model, two are sufficient to fit light neutrino data. We use the Casas-Ibara parametrisation (cf. Eqn. (1.41)) with the following choice of the R matrix

$$\mathbb{R} = \begin{pmatrix} 0 & \cos z & \sin z \\ 0 & -\sin z & \cos z \end{pmatrix}, \tag{4.24}$$

where $z = a + ib$ is a complex angle. The above structure of $\mathbb{R}$ can be justified by considering two RHNs or considering the third RHN $N_3$ to be very heavy and effectively decoupled from the bath. In such a scenario our neutrino Yukawa matrix becomes of dimension $2 \times 3$. Such a scenario also predicts the lightest active neutrino to be exactly massless.

The singlet fermion $\chi$ plays the role of viable DM candidate and carries a lepton number same as that of $N$. We consider this fermion to be vector like such that a bare mass term $m_\chi$ can be assigned to it without violating any $U(1)$ symmetry like global lepton number. To ensure the stability of the DM we impose an ad-hoc $\mathbb{Z}_2$ symmetry under which both the singlet scalar $\mathcal{S}$ and the single fermion $\chi$ are odd, while all other particles are even. This also implies, $m_\chi < m_\mathcal{S} < M_i$ such that the singlet fermion is the only DM in the present particle spectrum[4]. Note that, the scalar $\mathcal{S}$ is devoid of any vacuum expectation value (VEV) such that there is no mixing between the DM and the RHN that may lead to DM decay[5]. The detailed phenomenology of this minimal setup has been discussed in

[4]Possibility of either of them to be DM, depending on the mass hierarchy, has been addressed in [229].

[5]Non-zero VEV can result in DM decay into SM states that can have observational consequences [229, 270].

[229] by considering thermal RHNs. For thermal RHNs, the subsequent phenomenology is insensitive to early Universe histories. In this work, we consider non-thermal RHNs to be the dominant source of asymmetries.

### 4.3.2 The CP asymmetry

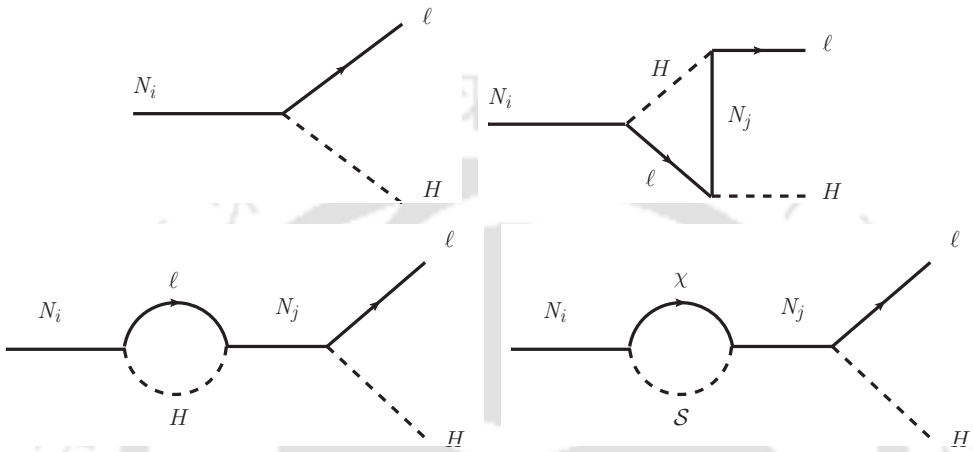


FIGURE 4.17: Tree level, vertex and the self-energy diagrams required for the generation of the asymmetry in the lepton sector.

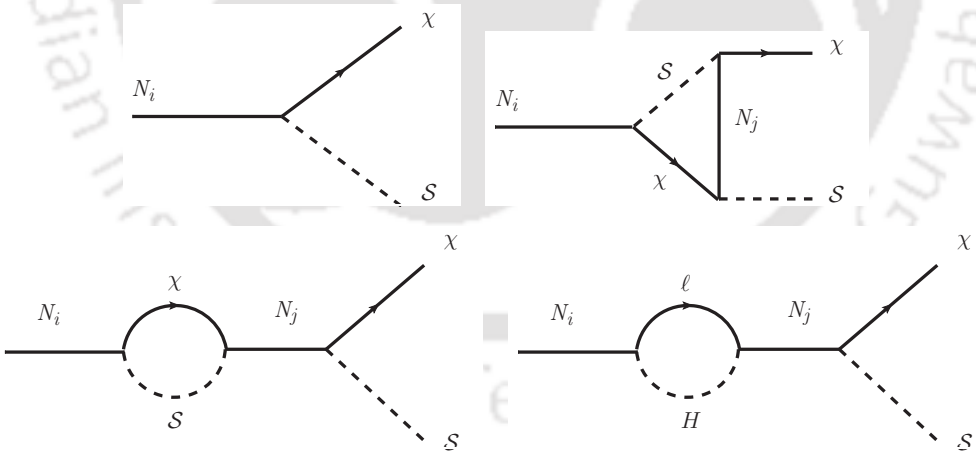


FIGURE 4.18: Same as Fig. 4.17 but for the generation of the asymmetry in the dark sector.

As advocated in the beginning, we are interested in the scenario where the asymmetry in the visible and in the DM sector are simultaneously generated from the non-thermal decay of RHNs where the latter originate solely from the evaporation of PBH. Assuming the symmetric component of the DM being washed out, it is the asymmetry $n_\chi - n_{\bar{\chi}}$

in number densities of DM particles that determines the DM abundance in late Universe. Since the DM $\chi$ carries a lepton number, hence lepton number asymmetries are generated in both the sector. We also assume $M_1 \ll M_2$ i.e, we can integrate out $N_2$ and consider contribution only from $N_1$ decay. The decay of $N_1$ to the SM final states also generate the thermal bath in this process. In Fig. 4.17 and Fig. 4.18 we depict the relevant Feynman diagrams that generate these asymmetries. Below we express the CP asymmetries produced in the two sectors from the decay of the lightest RHN $N_1$ [229]:

$$\epsilon_{\Delta L} = \frac{\sum_\alpha [\Gamma(N_1 \to l_\alpha + H) - \Gamma(N_1 \to \overline{l_\alpha} + H^*)]}{\Gamma_1} \tag{4.25}$$

$$\simeq \frac{M_1}{8\,\pi} \frac{\mathrm{Im}[(3\,y_N^*\,y_N^T + y_\chi^*\,y_\chi^T)\,M^{-1} y_N\,y_N^\dagger]_{11}}{[2\,y_N\,y_N^\dagger + y_\chi\,y_\chi^\dagger]_{11}}, \tag{4.26}$$

and

$$\epsilon_{\Delta\chi} = \frac{\Gamma(N_1 \to \chi + S) - \Gamma(N_1 \to \bar{\chi} + S^*)}{\Gamma_1} \tag{4.27}$$

$$\simeq \frac{M_1}{8\,\pi} \frac{\mathrm{Im}[(y_N^*\,y_N^T + y_\chi^*\,y_\chi^T) M^{-1} y_\chi\,y_\chi^\dagger]_{11}}{[2\,y_N\,y_N^\dagger + y_\chi\,y_\chi^\dagger]_{11}}, \tag{4.28}$$

where

$$\Gamma_1 = \frac{M_1}{16\,\pi}\,(2\,y_N\,y_N^\dagger + y_\chi\,y_\chi^\dagger)_{11}\,, \tag{4.29}$$

is the total decay width of $N_1$ and $M = \mathrm{diag}(M_1\,, M_2)$ is the diagonal RHN mass matrix considering two RHNs. We choose a hierarchical RHN mass spectrum with $M_2 = 50\,M_1$. Since we have a single generation of $\chi$, the $y_\chi$ matrix can be taken, in general, to be of the form

$$y_\chi = \begin{pmatrix} y_{\chi 1} \\ y_{\chi 2} \end{pmatrix}. \tag{4.30}$$

For the analysis purpose, we assume $y_{\chi i}$ to be real and identical, denoted by $y_\chi$. It is noteworthy that even with real $y_\chi$ we are being able to generate adequate CP-violation thanks to the complex Yukawa couplings in the visible sector. Moreover, relative difference in the two asymmetries depend upon the branching ratio of $N_1$ decay.

### 4.3.3 RHN from PBH: Baryogenesis and DM

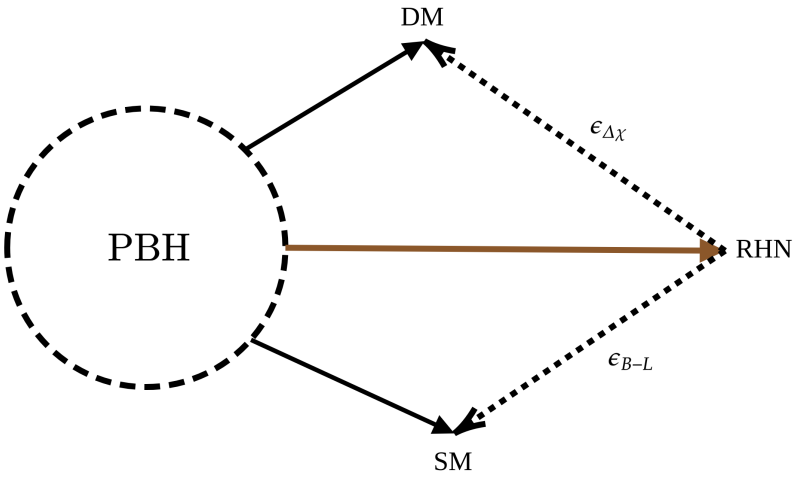


FIGURE 4.19: Schematic diagram of asymmetry production in the dark and in the visible sector in presence of primordial black holes.

PBH evaporation can lead to the generation of both RHNs and DM, depending on the PBH mass. However, in the present framework, we are not interested in DM generation from direct PBH evaporation, rather we are interested in the scenario of DM production from the asymmetry generated in the dark sector via RHN decay. While we can not prevent DM generation from PBH evaporation, eventually DM abundance is dictated by its asymmetric component only, which is generated by the RHN decay only. PBH emit RHNs (along with all the SM particles and DM), and the CP-violating decays of such non-thermal RHNs produce the asymmetry in the visible and dark sector. The scenario is schematically shown in Fig. 5.1. The lepton asymmetry is then further converted into the observed baryon asymmetry via sphaleron transition like in standard leptogenesis scenario. If $\mathcal{N}$ is the number of RHNs emitted from a single PBH then the present baryon number yield can be written as [94, 96, 101]

$$\frac{n_B}{s}(T_0) = \frac{\mathcal{N}}{\zeta}\,\epsilon_1\, a_{\rm sph}\,\frac{n_{\rm PBH}}{s}\Big|_{T_{\rm evap}}, \tag{4.31}$$

where $\zeta$ accounts for any further entropy production after PBH evaporation. Here, we consider $\zeta = 1$. It is possible to analytically derive the mass range of RHNs emitted

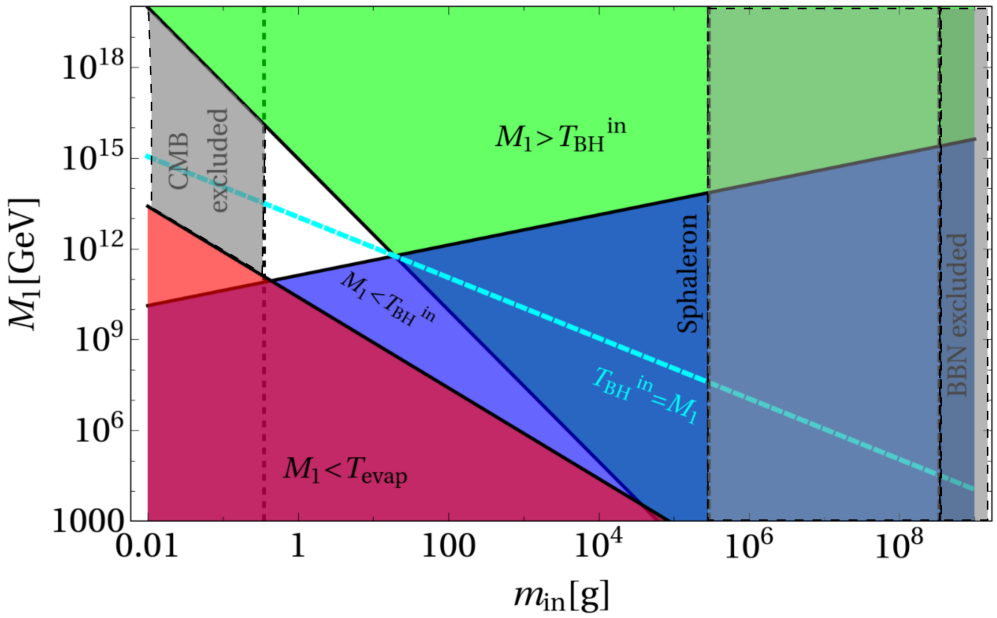


FIGURE 4.20: Bound on RHN mass from the requirement of obtaining observed baryon asymmetry from PBH evaporation. All the coloured regions are discarded from the bounds derived in Eqn. (4.32) and Eqn. (4.34). The vertical black dashed line corresponds to (from left to right) the bound from the scale of inflation (CMB), sphaleron transition and BBN. The white triangular region in the middle is the region that is allowed.

from PBH evaporation that can provide the required lepton asymmetry. In the Type-I seesaw mechanism, the quantity $\epsilon$ has an upper bound as given by Eqn. (1.45). On the other hand, the final asymmetry produced from PBH evaporation as computed from Eqn. (4.31), $Y_B = n_B/s\big|_{T_0} \simeq 8.7 \times 10^{-11}$ [47]. These together constrain the mass of the RHN produced from PBH evaporation both from above and from below

$$M_1 \begin{cases} > \frac{2\,g_{\star,H}}{a_{\rm sph}\,g_{N,H}}\,\frac{M_{\rm pl}^2\,v^2}{m_{\nu,\max}\,m_{\rm in}^2}\,\zeta\,\frac{Y_B(T_0)}{Y_{\rm PBH}(T_{\rm evap})} & \text{for } M_1 < T_{\rm BH}^{\rm in}\,; \\ < \frac{a_{\rm sph}\,g_{N,H}}{128\,\pi\,g_{\star,H}}\,\frac{M_{\rm pl}^2\,m_{\nu,\max}}{v^2}\,\frac{Y_{\rm PBH}(T_{\rm evap})}{\zeta Y_B(T_0)} & \text{for } M_1 > T_{\rm BH}^{\rm in}\,, \end{cases} \tag{4.32}$$

where $m_{\nu,\max}$ is the mass of the heaviest light neutrino and $Y_{PBH}(T_{\rm evap}) = \frac{n_{\rm PBH}}{s}\Big|_{T_{\rm evap}}$. We have used Eqn. (2.18) for the no. of RHNs produced from PBH and

$$n_{\rm PBH}\left(T_{\rm evap}\right) = \frac{1}{m_{\rm in}}\,\frac{\pi^2}{30}\,g_\star\left(T_{\rm evap}\right)\,T_{\rm evap}^4\,. \tag{4.33}$$

Another bound comes from the fact that if $M_1 < T_{\rm evap}$, then the RHNs produced from PBH evaporation are in thermal bath and then washout processes are in effect. Hence, to ensure non-thermal production of baryon asymmetry one must follow [96]

$$M_1 > T_{\rm evap} \implies M_1 \gtrsim 3\times 10^{-3}\left(\frac{\mathcal{G}^2\,g_\star\left(T_{\rm evap}\right)\,M_{\rm pl}^{10}}{m_{\rm in}^6}\right)^{1/4}. \tag{4.34}$$

We thus find that the observed baryon asymmetry is produced over a very tiny region for $10^{11} \lesssim M_1 \lesssim 10^{16}$ GeV and $0.5 \lesssim m_{\rm in} \lesssim 10$ g, depicted by the white triangular region in Fig. 4.20.

While the PBH evaporation cannot create baryon asymmetry directly in our minimal scenario, it can create DM directly, as discussed in different contexts [98, 102–105, 112, 245–253, 255, 258, 271–275]. However, as mentioned above, in asymmetric DM scenario, the final DM abundance is dictated by the dark sector asymmetry which is created only by the out-of-equilibrium decay of RHN where the latter is produced dominantly from PBH evaporation. Thus, in the present scenario asymmetric DM yield can be expressed as

$$Y_{\rm DM}\left(T_0\right) = \epsilon_{\Delta\chi}\,\mathcal{N}\,\frac{n_{\rm PBH}}{s}\left(T_{\rm evap}\right)\,, \tag{4.35}$$

that leads to DM abundance

$$\Omega_{\rm DM}\, h^2 = \frac{m_{\rm DM}\, s_0}{\rho_c}\, Y_{\rm DM}\,(T_0)\ , \tag{4.36}$$

where $\mathcal{N}$ is defined via Eqn. (2.18), which results in

$$\Omega_{\rm DM}\, h^2 = \frac{g_{N,H}}{g_{\star,H}}\,\frac{m_{\rm DM}\, s_0}{\rho_c}\,\epsilon_{\Delta\chi}\,\frac{n_{\rm PBH}}{s}\Big|_{T_{\rm evap}} \begin{cases} \frac{4\pi}{3}\,\left(m_{\rm in}/M_{\rm pl}\right)^2 & \text{for } T_{\rm BH}^{\rm in} > M_1\,; \\ \frac{1}{48\,\pi}\,\left(M_{\rm pl}/M_1\right)^2 & \text{for } T_{\rm BH}^{\rm in} < M_1\,. \end{cases} \tag{4.37}$$

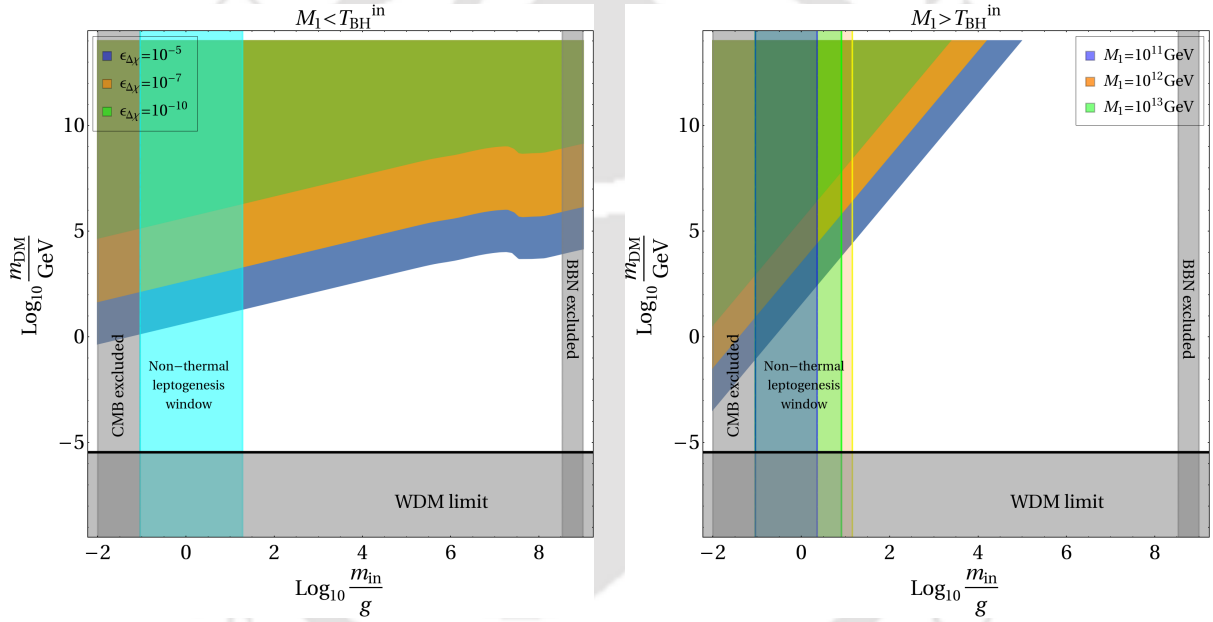


FIGURE 4.21: The dark green, orange and blue coloured regions are excluded from DM overproduction due to different choices of DM asymmetry (left panel) and RHN mass (right panel) shown by different colours. In the right panel we have chosen $\epsilon_{\Delta\chi} = 10^{-10}$. The gray shaded regions are disallowed from CMB, BBN and warm DM limit, while the cyan band (left) is where non-thermal leptogenesis from PBH is allowed for $M_1 \simeq 10^{12}$ GeV (see text).

Note that the final DM asymmetry depends on the mass of RHN as expected. To match the observed DM abundance $\Omega_{\rm DM}h^2 \simeq 0.12$, the DM yield has to be fixed so that $m_{\rm DM}\, Y_0 = \Omega_{\rm DM}h^2 \frac{1}{s_0}\frac{\rho_c}{h^2} \simeq 4.3 \times 10^{-10}$ GeV, where $\rho_c \simeq 1.1 \times 10^{-5} h^2$ GeV/cm$^3$ is the critical energy density and $s_0 \simeq 2.9 \times 10^3$ cm$^{-3}$ is the entropy density at present [151]. Fig. 4.21 depicts the allowed mass range for the DM obtained analytically using Eqn. (4.37). In the left

panel, different regions shown by the green, orange and blue colours correspond to different choices of DM asymmetry $\epsilon_{\Delta\chi}$, for the case where $T_{\rm BH}^{\rm in} > M_1$. All these regions correspond to DM overabundance and hence discarded. Here we see larger asymmetry imposes tighter constraint on the DM mass. This is expected since a larger asymmetry results in larger asymmetric DM abundance as per Eqn. (4.37). Hence slight increase in the DM mass results in overabundance. The slight distortion in the large DM mass region is due to the change in the number of light degrees of freedom around $T_{\rm evap} \simeq 150$ MeV, i.e., around the time of QCD phase transition. In the opposite limit $T_{\rm BH}^{\rm in} < M_1$, shown in the right panel, we see a lighter RHN imposes tighter bound since $\Omega_{\rm DM} \propto 1/M_1^2$ for a fixed CP asymmetry $\epsilon_{\Delta\chi} = 10^{-10}$.

If light DM is produced from PBH evaporation, it leads to a potential hot component in total DM abundance, tightly constrained by observations related to the CMB and baryon acoustic oscillation (BAO) leading to an upper bound on the fraction of this hot component with respect to the total DM, depending on the value of DM mass [259]. A conservative 10 % upper bound on such hot dark matter (HDM) component [103] can lead to similar constraints on DM mass along with PBH initial fraction. The requirement of producing right relic abundance, together with these lower limits on the DM mass put tight constraint on the DM mass emitted by the PBH. This is shown by the gray shaded regions in Fig. 4.21. We also show the window of PBH mass in cyan where successful non-thermal leptogenesis from RHN emitted by PBH is possible (Fig. 4.20) for $M_1 \simeq 10^{12}$ GeV. In the right panel we have chosen different masses for the RHN, corresponding to which the allowed mass window for non-thermal leptogenesis changes (maximum for $M_1 = 10^{12}$ GeV shown in orange) as denoted by different coloured vertical bands. The upshot of Fig. 4.21 is that, it is possible to generate observed asymmetry in visible sector, together with right relic abundance of asymmetric DM with ultralight PBH and for DM mass $\gtrsim 10^{-5}$ GeV. The upper bound on the DM mass depends on the size of the asymmetry generated within the dark sector, which depends also on the RHN mass scale.

### 4.3.4 Results and Discussions

In order to compute the asymmetries we will now perform a full numerical analysis considering a set of coupled Boltzmann equations accounting for the energy and number densities of different components. We focus on the production of the observed baryon asymmetry via non-thermal leptogenesis, together with the correct relic abundance for the asymmetric DM. Thus, we track the evolution of the comoving number densities of the RHN, PBH, lepton and DM asymmetries and the radiation energy density via their coupled BEQs. What is crucial here is the fact that since the PBHs are assumed to be produced during the radiation dominated era, hence thermal contribution to leptogenesis can not be overlooked. The evolution equation for PBH mass, energy densities and bath temperature[6] in presence of PBH is similar to that in section 4.2.2 (cf. Eqns. (4.7)-(4.10), (4.14)). The coupled Boltzmann equations for the evolution of the DM and lepton asymmetries, on the other hand, are given by [100, 276]

$$
\begin{aligned}
a\mathcal{H}\frac{d\widetilde{N}_{B-L}}{d\xi} &= \epsilon_{\Delta L}\left[\left(\widetilde{n}^{T}_{N_1}-\widetilde{n}^{\rm eq}_{N_1}\right)\Gamma^{T}_{N_1}+\widetilde{n}^{\rm BH}_{N_1}\Gamma^{\rm BH}_{N_1}\right]-{\rm Br}_{\rm SM}\,\mathcal{W}\,\widetilde{N}_{B-L}\,,\\
a\mathcal{H}\frac{dX}{d\xi} &= \epsilon_{\Delta\chi}\left[\left(\widetilde{n}^{T}_{N_1}-\widetilde{n}^{\rm eq}_{N_1}\right)\Gamma^{T}_{N_1}+\widetilde{n}^{\rm BH}_{N_1}\Gamma^{\rm BH}_{N_1}\right]-{\rm Br}_{\rm DM}\,\mathcal{W}\,X\,,
\end{aligned}
\tag{4.38}
$$

where Br stands for the branching ratio of RHN into leptons (denoted by subscript SM) and DM (denoted by subscript DM). $\widetilde{N}_{B-L}, X$ are comoving densities of $B-L$ and dark sector asymmetries respectively. $\xi = a/a_{\rm in}$ and we take $a_{\rm in} = 1$. Here we would like to mention that the RHNs produced from PBH evaporation never come into thermal equilibrium with the SM bath. In order to ensure that, we computed the thermally averaged cross-section for scattering of RHNs produced from the PBH evaporation against the bath particles, e.g., $N_1\ell \to N_1\ell$ following the prescription in [105] (the detailed derivation is given in Appendix D), and compared the corresponding rate with the Hubble rate. We found that for $T \simeq T_{\rm evap}$, the RHN interaction rate is several orders of magnitude less

[6] In principle, the Boltzmann equation for radiation should also contain the contribution from RHN decay into the thermal, but such contributions are negligible compared to the PBH contribution and can be ignored.

than the Hubble expansion rate, typically $n_{\rm eq}\langle\sigma v\rangle/\mathcal{H} \lesssim 10^{-7}$. This shows that the RHNs produced from PBH are genuinely non-thermal. The thermally averaged decay rate of $N_1$ is denoted by $\Gamma^T_{N_1}$ and $\widetilde{n}^{\rm eq}_{N_1}$ is the equilibrium number density. The Hubble parameter $\mathcal{H}$ entering in the Boltzmann equations is given by

$$\mathcal{H} = \sqrt{\frac{8\,\pi}{3\,M^2_{\rm pl}}\,\frac{\widetilde{\rho}_{\rm BH}\,a_{\rm in}\,\xi + \widetilde{\rho}_R}{a^4_{\rm in}\,\xi^4}}\,, \tag{4.39}$$

The generation of lepton asymmetry has thermal and non-thermal sources stemming from the plasma and PBH evanescence respectively. On the other hand, DM can be present in the thermal bath while its asymmetric component arises from RHN decay and eventually only the asymmetric component survives. From Fig. 4.20 we have already realized that non-thermal leptogenesis from PBH necessarily requires ultralight PBH with $M_1 \gtrsim 10^{12}$ GeV. On the other hand, it is clear from the right panel of Fig. 2.5, for very light PBHs to dominate the energy density, the initial energy fraction of PBH density should be much higher. Hence, a long period of PBH domination is preferred for purely non-thermal leptogenesis from PBH [101]. Otherwise, the asymmetry production will be dominated by thermally generated RHNs with PBH leading to subsequent entropy dilution only [100, 276]. For $N_2$ leptogenesis, one can as well get an enhancement of asymmetry in the presence of PBH compared to the usual thermal case [276]. However, we restrict ourselves to $N_1$ leptogenesis only and consider the production to be dominant from non-thermal RHNs produced from PBH evaporation. In the rest of the analysis we will thus restrict the RHN mass to be $M_1 = 10^{12}$ GeV unless otherwise specified. We will first look at the impact of having PBHs on the energy densities and the yield of the asymmetries in visible and dark sectors. For this we consider some benchmark masses of the PBH in 1-100 g range falling in the allowed region of Fig. 4.20. We also fix the $N_1-$DM Yukawa coupling $y_\chi = 0.1$ that determines the asymmetry in dark sector.

The top left panel of Fig. 4.22 shows the evolution of radiation (orange) and PBH (black) energy densities with scale factor for PBH mass of 1 g. Here we see with time the PBH energy density rises compared to that of radiation (as $\rho_{\rm BH} \sim a^{-3}$) and at around

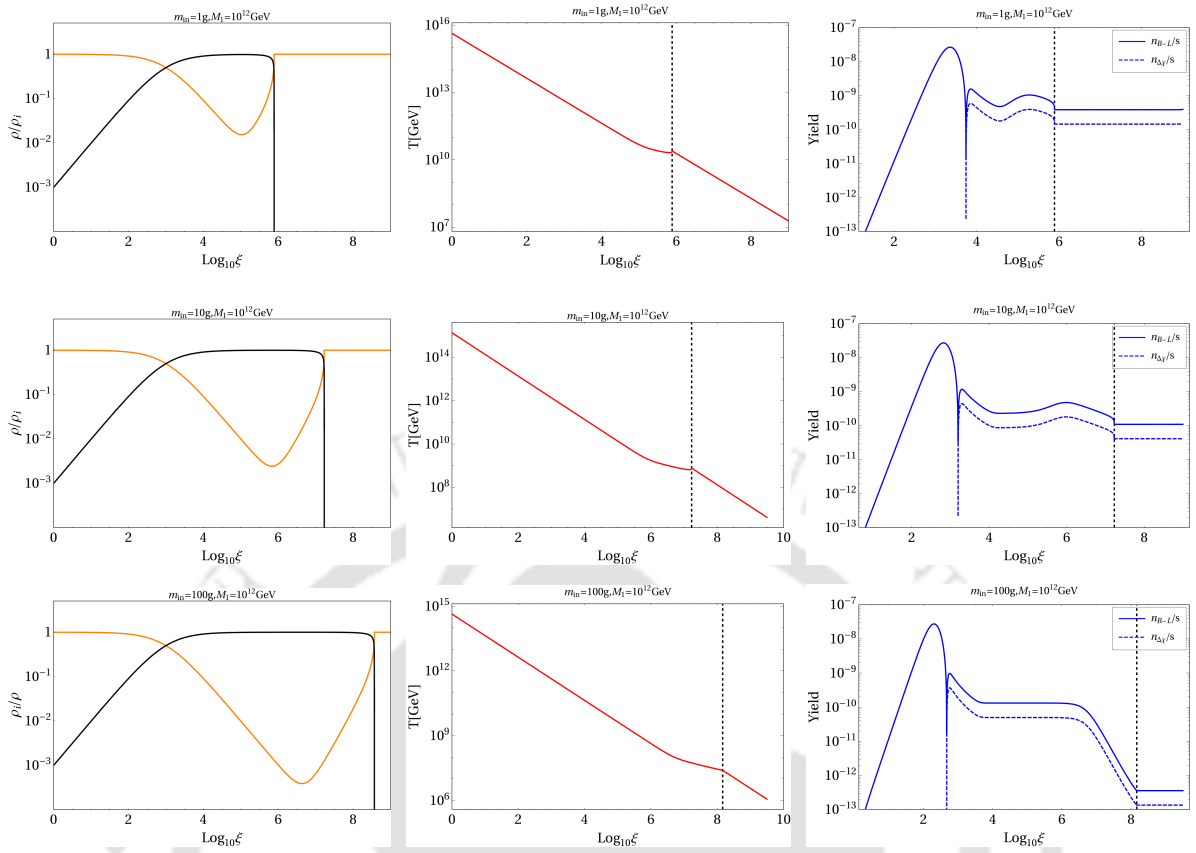


FIGURE 4.22: Energy density (left column), temperature of thermal bath (middle column) and yield of asymmetries (right column) as a function of scale factor for a three different choices of PBH mass and for a fixed RHN mass as mentioned in the plot label. In all cases we have considered PBH domination by considering $\beta = 10^{-3}$, $M_1 = 10^{12}$ GeV and $y_\chi = 10^{-1}$ . The black dashed vertical line in each case denotes the PBH evaporation time.

$\xi \sim 10^3$ the PBH energy density overtakes the radiation density. This corresponds to a bath temperature $T \sim 10^{12}$ GeV that can be read off from the adjacent panel on the right. Slightly beyond this point, the energy density in PBH shows a plateau. This plateau region gets broadened as the PBH mass increases (middle and bottom left panels) since a larger mass corresponds to a smaller evaporation temperature (Eqn. (2.12)). As a result, for ultralight masses, PBH domination era gets over earlier. The PBH dominated era ends at $\xi \sim 10^6$ for upper left panel plot where we see the black curve falls sharply. As the PBH evaporation dumps a huge amount of entropy into the thermal plasma, the plasma temperature shows a rise as one can notice from the kink in the red curve of upper middle panel plot. As the PBH mass increases, evaporation takes place at a later epoch, hence the kink in the red curve also shifts to a smaller temperatures as one can see from

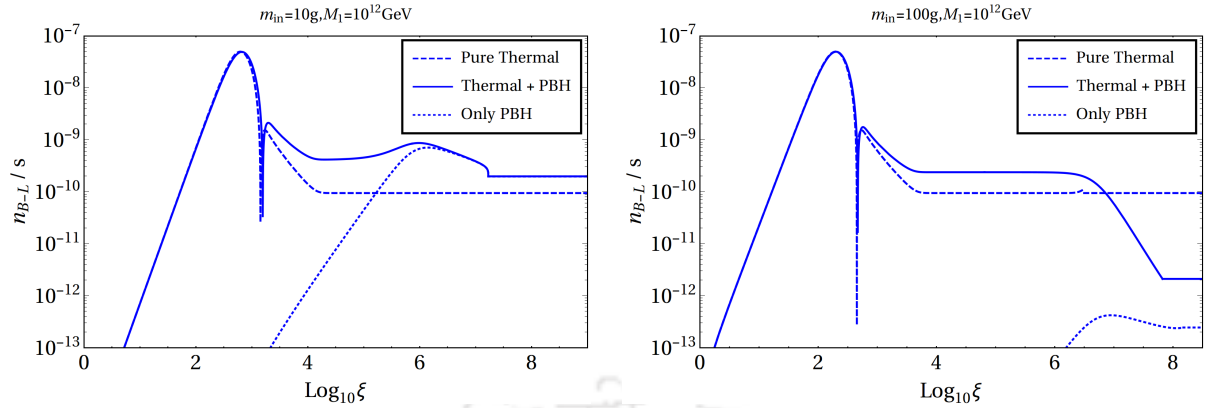


FIGURE 4.23: Evolution of the yield of asymmetries for three scenarios : (i) purely thermal, (ii) only non-thermal contribution from PBH and (iii) both thermal as well as non-thermal contributions. Here, $\beta = 10^{-3}$, $M_1 = 10^{12}$ GeV and $y_\chi = 10^{-1}$. The left panel represents a lighter PBH mass of 10 g, whereas the right panel shows the evolution for a higher PBH mass of 100 g.

the lower middle panel plots. Plots shown in extreme right columns of Fig. 4.22 depict the evolution of yield of the asymmetries. The asymmetries in both the sectors evolve identically because of the same source. The asymmetries first increase because of the thermal contribution, and then diminish for the washout effect due to the inverse decay of thermal RHNs. Afterwards, they remain unchanged till the time the production of non-thermal RHN from PBH overtakes the thermal contribution. Then during the period of PBH evaporation dilution effect becomes significant (depending on the PBH mass) because of entropy injection in the thermal bath. Finally, the asymmetries saturate once the PBH is completely evaporated. The effect of entropy injection becomes more prominent for comparatively massive PBH as the period of evaporation becomes longer. For better understanding of the asymmetry evolution, in Fig. 4.23, we compare three scenarios where the baryon asymmetry results from the decay of (i) only thermal RHN (dashed line) in the absence of PBH, (ii) only non-thermal RHN produced from PBH (dotted line) and (iii) both thermal as well as non-thermal RHN (solid line) for two different PBH masses. These plots clearly show the difference in the yield of baryon asymmetry for these three cases. For the lighter PBH mass as shown in the left panel of Fig. 4.23, one finds that even after the entropy injection due to the PBH evaporation, the final baryon asymmetry

remains larger than the one obtained in the scenario with no PBH[7]. On the other hand, for a heavier PBH as shown in the right panel of Fig. 4.23, one expects a relatively larger entropy injection resulting in a larger dilution of the final baryon asymmetry, making it lesser in comparison to the one produced in thermal leptogenesis. Since asymmetries in dark and visible sectors evolve similarly, one can also expect that for lighter PBH masses, the asymmetric DM production will be more compared to a purely thermal scenario discussed in earlier works.

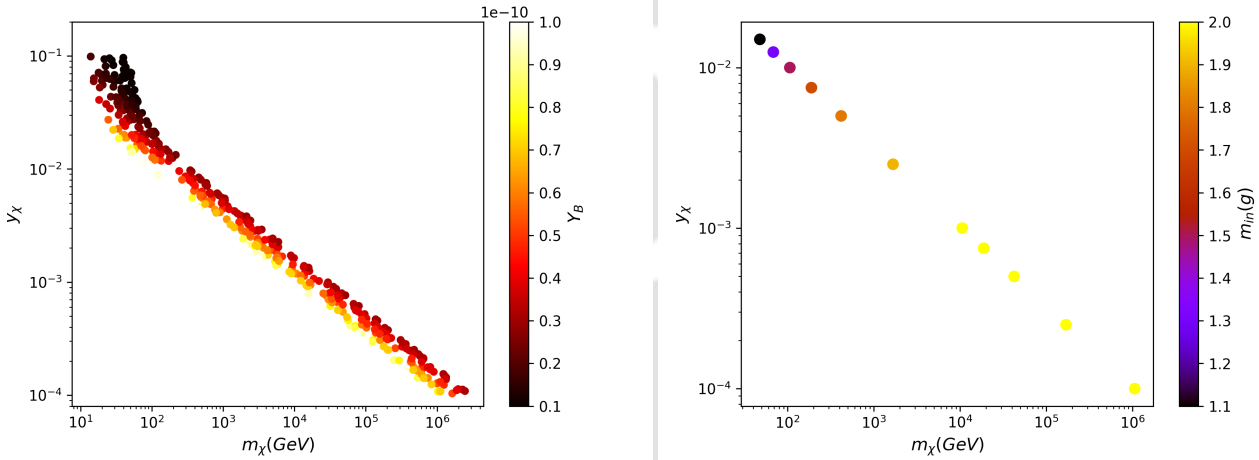


FIGURE 4.24: Left panel: Parameter space satisfying observed DM abundance in the bi-dimensional plane of $y_\chi - m_\chi$, where the colour coding is done with respect to $Y_B$. Right panel: Points satisfying both observed relic abundance and baryon asymmetry in $y_\chi - m_\chi$ plane, where the colour code shows variation of PBH mass. We have considered $\beta = 8 \times 10^{-3}$ to ensure PBH domination.

In Fig. 4.24 we have illustrated the viable parameter space where asymmetric DM relic abundance and observed baryon asymmetry can be produced entirely from RHNs emitted due to PBH evaporation by solving the set of BEQs numerically. We have performed a scan over the following parameters

$$m_\chi : \{1 - 10^5\}\ \text{GeV};\ m_{\text{in}} : \{1 - 12\}\ \text{g};\ y_\chi : \{10^{-4} - 10^{-1}\}\,, \tag{4.40}$$

[7]For comparatively lighter RHN, the effect of PBH on the final asymmetry is negligible [101], however to ensure non-thermal production we stick to $M_1 \gtrsim 10^{11}$ GeV following Fig. 4.20.

by keeping $M_1 = 10^{12} = M_2/50$ GeV and $\beta = 8 \times 10^{-3}$ to be fixed to ensure PBH domination as discussed before. The Dirac Yukawa coupling of neutrinos get fixed via Casas-Ibarra parametrisation mentioned earlier, after using the best-fit values of light neutrino parameters [72]. In the left panel of Fig. 4.24, we show the allowed parameter space giving correct ADM abundance in $y_\chi - m_\chi$ plane while the colour code denotes the baryon asymmetry generated. As can be seen from this plot, for heavier DM mass, one requires smaller Yukawa coupling $y_\chi$. This is because heavier DM requires smaller dark asymmetry $\epsilon_{\Delta\chi}$ and hence smaller $y_\chi$ to generate correct relic abundance, following Eqn. (4.37). The parameter space gets broadened as the PBH mass keeps varying. The right panel shows, to satisfy the right ADM relic along with observed baryon asymmetry via non-thermal leptogenesis, one has to necessarily rely on ultralight PBH which we have already realized from Fig. 4.20 and 4.21. The fact that heavier PBH mass requires heavier DM mass and hence smaller Yukawa $y_\chi$ to get smaller $\epsilon_{\Delta\chi}$, can also be understood from Fig. 4.21 based on approximate analysis. The results of complete numerical analysis also matches with this pattern as seen from the right panel plot of Fig. 4.24.

### 4.3.5 Conclusion

Asymmetric dark matter (DM) has been a well-studied framework motivated from explaining the baryon-DM coincidence problem dynamically. While the minimal frameworks to realise such possibility considers a heavy particle present in the thermal bath whose CP violating decays into visible and dark sectors generate the respective asymmetries, we consider the possibility of non-thermal origin of these asymmetries. In order to keep it minimal and also to connect to the origin of light neutrino masses, we consider the extension of Type-I seesaw model with dark sector particles [229] so that the lightest right handed neutrino can play the role of creating the dark and visible sector asymmetries. The DM is assumed to be a singlet Dirac fermion $\chi$ which couples to the right handed neutrinos (RHNs) through another scalar singlet $\mathcal{S}$. While the interaction of the RHNs with the SM Higgs and leptons is responsible for generating the neutrino mass via Type-I seesaw mechanism, its simultaneous decay to the visible and the dark sector generates

asymmetries in both the sectors. A fraction of lepton asymmetry is converted to baryon asymmetry via sphaleron transition, while the asymmetric component of $\chi$ survives and accounts for the observed DM relic. While thermal cogenesis has been discussed extensively in the literature, we consider the possibility of non-thermal RHNs by invoking the presence of additional sources.

We consider a framework where the RHNs are sourced from evaporating primordial black holes that are produced in the radiation dominated era with a monochromatic mass spectrum. While RHNs can be produced from the thermal bath as well, we show that the asymmetries produced from non-thermal RHNs dominate over the thermal one, specially for lighter PBH masses. Keeping the parameter space within such ballpark where non-thermal leptogenesis from PBH evaporation dominates over the thermal contribution in generating the $B - L$ asymmetry, we find that the observed baryon asymmetry is obtainable only for ultralight PBH of mass $\lesssim 15$ g and RHN mass $M_1 \gtrsim 10^{11}$ GeV. PBH mass in such a ballpark necessarily requires a prolonged period of PBH domination, typically requiring a large initial fraction $\beta > \beta_c$. Considering bounds from CMB, BBN and astrophysical constraints, we show that PBH evaporation is also capable of producing required asymmetry in the dark sector leading to correct relic abundance for asymmetric DM as massive as $\sim 10^5$ GeV, depending on the choice of the Yukawa coupling $y_\chi$. Several complementary prospects of detection for asymmetric DM can be realized depending on the UV completion of the dark sector, which we have not investigated in this minimal setup. In addition to the discovery potential for the particular particle physics framework, the ultra-light PBH leading to early matter domination can itself have observational consequences like emission of gravitational waves via Hawking radiation [147] or other ways [117, 149, 150] which can have interesting detection prospects at both high and low-frequency GW experiments [277].

# Chapter 5

# DM and Leptogenesis with both LLP and PBH domination

## 5.1 Introduction

In this chapter, we explore a scenario where multiple early matter-dominated eras emerge, in order to produce the observed DM abundance and baryon asymmetry of the Universe. The framework is motivated by the fact that all the observational evidences supporting the presence of DM in the Universe are based on purely gravitational interactions only, as discussed in chapter 1. Thus, it is appealing to consider the possibility of DM production in the early Universe via a mechanism relying on gravitational interactions only. The challenge is to find such a mechanism to produce dark matter in the early Universe only through gravitational interactions. Such *Purely Gravitational DM* scenarios have been studied for a long time in different contexts. Gravitational particle production was studied in Ref. [278] by Ford, where he considered scalar particle production of massless, non-conformally coupled fields as a result of the non-adiabatic evolution of the time-dependent dispersion relation during the transition from an inflationary accelerated expansion phase to a matter or radiation dominated decelerated phase. In Ref. [279, 280], this mechanism was used for the production of supermassive scalar DM. Such mechanisms have garnered interest in the recent years and have been used to study scalar, fermion as well as vector DM production [281–283]. Other possible gravitational production mechanisms include the 'Gravitational Misalignment Mechanism' [284–286] and

production through graviton mediated scatterings [287–289].

We consider another such alternative: production of gravitational DM from the evaporation of primordial black holes, assuming the latter to dominate the energy density of the Universe at some stage. Contrary to earlier works where either light or superheavy DM production from evaporating PBH was shown, here we show the possibility of a much wider range allowing the intermediate mass DM: from a few keV to PeV. This is achieved by considering the presence of three heavy right handed neutrinos (RHN) which also take part in typical Type-I seesaw mechanism [55, 56, 231, 232] of neutrino mass generation, as discussed in chapter 1 (cf. Eqn. (1.27)). DM with mass in the intermediate regime mentioned above usually gets overproduced from PBH evaporation and can be brought within Planck limits by late entropy injection after PBH evaporation, from one of the right-handed neutrinos, similar to the setups discussed in one of the preceding chapters. The other two RHNs can not only reproduce neutrino oscillation data via Type-I seesaw but also can produce the baryon asymmetry of the Universe via leptogenesis. Since DM is assumed to have only gravitational interactions, it only has a mass term, the exact form of which depends on the particle nature of DM particle. In our numerical analysis, for simplicity, we will consider a real singlet scalar $S$ of mass $m_{\rm DM}$, to be a potential DM candidate[1] which is produced purely from PBH evaporation. One of the RHNs, $N_3$ in the present scenario, is considered to be long lived such that its decay rate is suppressed compared to the other two RHNs. As a consequence, the Universe undergoes a $N_3$-dominated epoch even after PBH are completely evaporated. The other two RHNs, namely $N_{1,2}$ can undergo CP-violating out-of-equilibrium decay, producing lepton asymmetry which can then be converted into the baryon asymmetry of the Universe, thanks to the electroweak sphaleron transitions. In Fig. 5.1 we schematically show the components which dominate the energy density of the Universe at different epochs. As the time flows from the left to the right, hence, as expected, the Universe is radiation dominated (RD) at

[1]We assume the strength of the portal interaction $S^2\ |H|^2$ is absent by construction to ensure only gravitational production of DM. Considering DM with a different spin does not alter the main outcome of our analysis.

the end of reheating. Once the PBH formation happens, the PBH energy density can dominate, which ends as the PBH evanescence is complete. The Universe is then dominated by RHN produced from the PBH. Finally, as the RHN decays away, the usual radiation domination era again commences. Note that, in addition to DM, the diluter $N_3$ is also dominantly produced from PBH evaporation as its coupling with SM leptons is tiny due to the requirement of its long-lifetime.


FIGURE 5.1: Dominant component of the energy density of the Universe at different epoch (time runs from left to right).

This paper is organised as follows. In section 5.2, we provide some analytical estimates for PBH generated DM and leptogenesis from PBH generated RHN decay, including late-time entropy injection after PBH evaporation. In section 5.3, we discuss the details of our numerical analysis followed by a brief discussion on production of DM and RHN from gravity mediated scatterings in section 5.4. Finally, we conclude in section 5.5.

## 5.2 PBH and Cogenesis

We consider DM with *only* gravitational interaction such that it can be produced solely from PBH evaporation. Along with the DM, the PBH also emits right handed neutrinos $N_i$ with $i \in 1,2,3$. The number of any particle $X$ radiated during the evaporation of a single PBH is given by Eqn. (2.18). The DM yield produced by evaporation can be directly related to the BH abundance at evaporation, as shown in Eqn. (4.19). Then, the DM relic abundance $\Omega_{\rm DM}\,h^2 = \frac{m_{\rm DM}\,s_0}{\rho_c}\,Y_{\rm DM}\,(T_0)$ , in the present epoch reads

$$\Omega_{\rm DM}\,h^2 = \mathbb{C}(T_{\rm ev}) \begin{cases} \frac{1}{\pi^2}\sqrt{\frac{M_{\rm pl}}{m_{\rm in}}}\,m_{\rm DM} & \text{for } m_{\rm DM} < T^{\rm in}_{\rm BH}\,, \\ \frac{1}{64\,\pi^4}\left(\frac{M_{\rm pl}}{m_{\rm in}}\right)^{5/2}\frac{M^2_{\rm pl}}{m_{\rm DM}} & \text{for } m_{\rm DM} > T^{\rm in}_{\rm BH}\,, \end{cases} \tag{5.1}$$

with $\mathbb{C}(T_{\rm ev}) = \frac{s_0}{\rho_c}\frac{1}{\zeta}\frac{g_{X,H}}{g_{\star,H}}\frac{5}{g_{*s}(T_{\rm ev})}\left(\frac{\pi^3 g_\star(T_{\rm ev})}{5}\right)^{3/4}\sqrt{\frac{\mathcal{G}\, g_{\star,H}}{10640\,\pi}}$. Here $\zeta$ parametrizes a possible entropy production after PBH evaporation until now, i.e., $\zeta\,(sa^3)_{\rm evap} = (sa^3)_0$. Note that, for the heavy DM case relic abundance has an inverse dependence on the DM mass, implying heavy DM leads to under abundance. The over abundant region for DM with spin $s = 0$ produced from PBH evaporation is shown in the left panel of Fig. 5.2 for $\zeta = \xi = 1$, i.e., considering no entropy injection at any given epoch, where $\xi$ is defined in Appendix E and for our scenario $\xi = \zeta$ as there is no entropy dilution after matter-radiation equality epoch. Here we note that in the majority of the parameter space the DM is over abundant irrespective of their spins and only $m_{\rm DM} \gtrsim 10^{10}$ GeV can lead to right abundance for $m_{\rm in} \gtrsim 10^6$ g [96, 290]. Here we would like to mention that for DM with different spins this over abundant region only slightly changes.

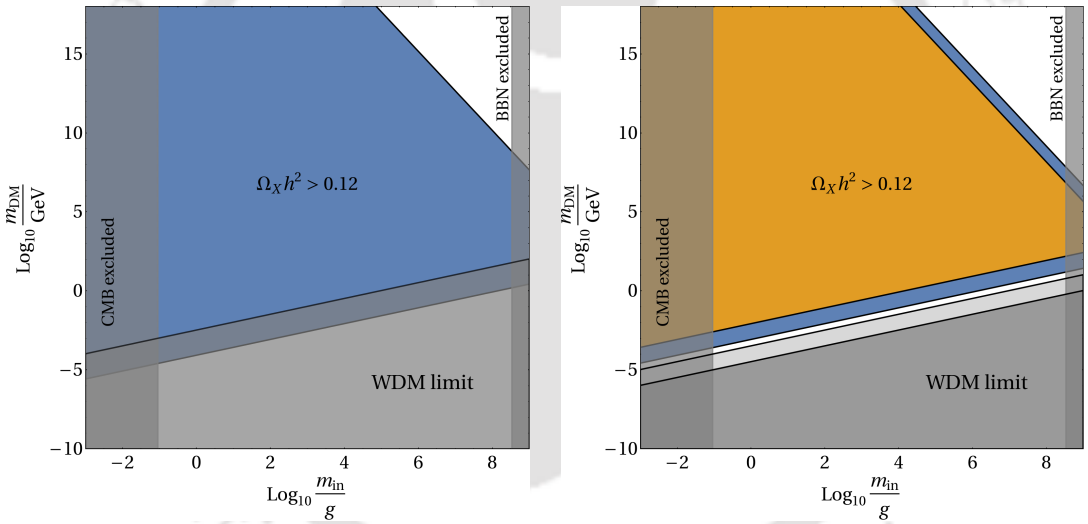


FIGURE 5.2: The DM is over-abundant in the blue shaded region, for $\zeta = \xi = 1$ (left) and in the blue (orange) shaded $\zeta = \xi = 10(100)$ (right) considering the DM to be scalar. The grey shaded regions are discarded due to limits on PBH mass from CMB (lower limit), BBN (upper limit) and Lyman-$\alpha$ (see text). Observed DM relic is achievable only in the white region in the top right corner (left), whereas non-zero values of $\xi$ opens up a window in the bottom (right).

Now, the lower bound on DM mass from Lyman-$\alpha$ can be found in Appendix E. Particularly, the low DM mass region is in conflict with the WDM limit, which is shown by the grey-shaded region in Fig. 5.2. An obvious way to overcome this tension is to consider

that the DM produced from PBH evaporation does not constitute the whole DM abundance. But since we are considering PBH is the *only* source of all of the DM, therefore this tension can be alleviated by considering entropy non-conservation [96, 112]. This is shown in the right panel of Fig. 5.2, where $\zeta = \xi = 10$ (in blue) and $\zeta = \xi = 100$ (in yellow) is assumed[2]. Here we see the low DM mass window can be resurrected simply because $\Omega_{\rm DM} \propto \zeta^{-1}\, m_{\rm DM}$[3].

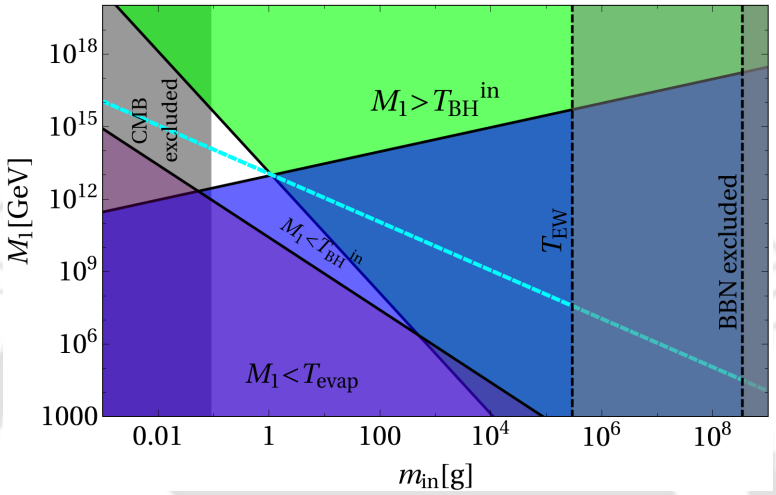


FIGURE 5.3: Constraints on RHN mass from the requirement of obtaining $Y_B^{\rm obs}$ considering $\zeta = 10$. All the coloured regions are discarded from the bounds derived in section 4.2.2. The white triangular region in the middle is the region that is allowed (see text). This region shrinks compared to that in Fig. 4.20, where $\zeta = 1$.

The RHNs emitted during PBH evaporation can undergo CP-violating decays, generating lepton asymmetry, which has been discussed in details in section 4.3.3. From Fig. 4.20, we concluded that the tiny triangular white part is the only window where $Y_B = Y_B^{\rm obs}$. This region typically corresponds to $0.1 \lesssim m_{\rm in} \lesssim 20$ g and $10^{12} \lesssim M_1 \lesssim 10^{17}$ GeV when entropy is assumed to be conserved, i.e., $\zeta = 1$. Note that, this region shrinks for larger $\xi = 10$, as shown in the right panel. This is expected since a larger $\zeta$ allows a larger entropy injection (from $T_{\rm evap}$ to $T_0$), diluting the asymmetry produced. Thus, while a larger $\zeta$ can provide breathing space for lighter DM (cf., Fig. 5.2), but in turn tightens the allowed parameter space for observed baryon asymmetry. It is therefore clear, satisfying both of them simultaneously needs a careful choice of $\zeta$, i.e., the entropy injection,

[2] Another way is to significantly increase $g_{\star,H}$ as mentioned in [112].
[3] For simplicity we consider $\zeta = \xi$, which is, of course not a mandate.

such that not only right DM abundance for lighter DM is obtained, but baryon asymmetry should also not get too much diluted. It is interesting to note that the heavy DM mass ($\gtrsim 10^{10}$ GeV) region although remains viable even in the absence of entropy injection, it is not possible to satisfy the observed asymmetry in those regions as they typically correspond to massive PBH ($\gtrsim 10^4$ g), leading to under production of asymmetry (cf. Fig. 4.20).

## 5.3 Numerical Analysis

To this end we have analytically established that in order to open up the low mass DM window (which is otherwise over abundant) it is necessary to have a substantial entropy injection ($\gtrsim \mathcal{O}(10)$). However, the same entropy injection reduces the viable parameter space for observed baryon asymmetry. Thus, it is rather difficult to satisfy both DM abundance and correct asymmetry together, and one has to stick to the region of comparatively lighter PBH mass to achieve both. In this section we will investigate the viability of the analytical results by solving a set of coupled Boltzmann equations numerically.

In order to compute the final lepton (baryon) and DM yield, we numerically solve the set of coupled Boltzmann equations, similar to that in chapters 3, 4. The additional equations for the diluter $N_3$ and DM are given by

$$a\mathcal{H}\frac{d\widetilde{n}^{\rm BH}_{N_3}}{da} = \Gamma_{\rm BH\to N_3}\frac{\widetilde{\rho}_{BH}}{m_{BH}} - \Gamma_3\widetilde{n}^{\rm BH}_{N_3} \tag{5.2}$$

$$a\mathcal{H}\frac{d\widetilde{n}^{\rm BH}_{DM}}{da} = \Gamma_{\rm BH\to DM}\frac{\widetilde{\rho}_{BH}}{m_{BH}}. \tag{5.3}$$

where $\Gamma_3$ denotes the decay width of $N_3$. Since $N_3$ plays the role of diluting the DM relic, it has to be long-lived. This results in suppressed Yukawas[4] and hence no thermal production. Also, note that we are considering a scenario of DM with only gravitational

[4]Here, we use the following choice of the $\mathbb{R}$ matrix in the Casas-Ibara parametrisation (cf. Eqn. (1.41))

$$\mathbb{R} = \begin{pmatrix} 0 & \cos z & \sin z \\ 0 & -\sin z & \cos z \\ 1 & 0 & 0 \end{pmatrix}, \tag{5.4}$$

$z$ being the complex angle.

interactions, hence it does not get produced from the thermal bath. The evolution of the comoving radiation energy density and temperature of the thermal bath (cf. Eqn. (4.8), (4.14)) has an additional term because of late time entropy injection from $N_3$, and are given by

$$\frac{d\widetilde{\rho}_R}{da} = -\frac{\epsilon_{\rm SM}(m_{\rm BH})}{\epsilon(m_{\rm BH})}\frac{a}{m_{\rm BH}}\frac{dm_{\rm BH}}{da}\widetilde{\rho}_{\rm BH} + \frac{a}{\mathcal{H}}\Gamma_3 M_3 \widetilde{n}^{\rm BH}_{N_3}\,, \tag{5.5}$$

$$\frac{dT}{da} = -\frac{T}{\Delta}\left[\frac{1}{a} + \frac{\epsilon_{\rm SM}(m_{\rm BH})}{\epsilon(m_{\rm BH})}\frac{1}{m_{\rm BH}}\frac{dm_{\rm BH}}{da}\frac{g_\star(T)}{g_{\star s}(T)}\,a\,\frac{\widetilde{\rho}_{BH}}{4\,\widetilde{\rho}_R} + \frac{\Gamma_3 M_3}{3\mathcal{H}\,s\,a^4}\widetilde{n}^{\rm BH}_{N_3}\right]. \tag{5.6}$$

Since we are interested in PBHs with mass $\lesssim \mathcal{O}(1)$ g (where leptogenesis from PBH dominates), with typical evaporation temperature $T_{\rm evap} \lesssim \mathcal{O}(10^{11})$ GeV, we do not include the $\Delta L = 2$ washout processes in the BEQ as such processes go out of equilibrium at temperatures $T \lesssim 6 \times 10^{12}$ GeV as shown in [291] and thus have no influence on final asymmetry[5]. We consider $\beta > \beta_c$, such that PBH dominate the energy density at some epoch and particle production takes place during PBH domination. The temperature of the thermal bath as a function of the scale factor is shown in the left panel of Fig. 5.4, where we can clearly see the effect of entropy dilution in two different epochs. The first one takes place at $a \sim 10^6$ when the PBH evaporation is completed, while the second one at a later epoch corresponding to $a \sim 10^{15}$ when the decay of $N_3$ is completed. Note that, prior to $N_3$ domination, the Universe is again dominated by radiation energy density for a brief period of time. This is clearly visible from the right panel plot where we have shown the energy density of radiation (red), PBH (blue) and $N_3$ (black) as functions of the scale factor $a$. The cyan-shaded regions indicate the two different epochs of early matter domination. Here one can see that the PBH energy density falls sharply at $a \sim 10^6$ denoting the end of PBH domination. Afterward the Universe goes through radiation domination, that is being overtaken by the $N_3$ energy density (second matter dominated era) at $a \sim 10^9$. Finally that ends at $a \sim 10^{15}$ with the complete decay of $N_3$ into radiation. It is important

[5]In the standard radiation dominated early Universe, if the lightest RHN mass exceeds $\sim 10^{15}$ GeV and heaviest active neutrino mass is greater than $\sim 0.1$ eV, $\Delta L = 2$ washout processes erase the lepton asymmetry.

to clarify that in these plots we have fixed the $N_3$ mass and adjusted its decay width accordingly such that it never achieves equilibrium with the SM bath (hence long-lived) by tuning the lightest active neutrino mass that we consider to be a free parameter.

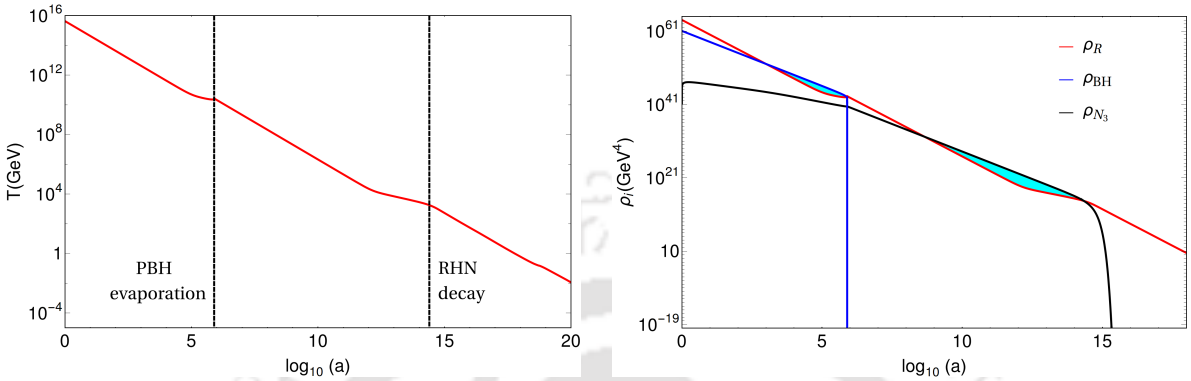


FIGURE 5.4: Evolution of temperature of the thermal bath $T$ as a function of the scale factor $a$ (left) and energy densities of radiation, PBH and $N_3$ as a function of the scale factor (right). We take $m_{in} = 1$ g, $M_1 = 10^{13}$ GeV, $M_3 = 10^{12}$ GeV, $m_{\rm DM} = 1$ GeV, with $N_3$ decay width adjusted to be $\Gamma_3 = 1.3 \times 10^{-11}$ GeV (see text).

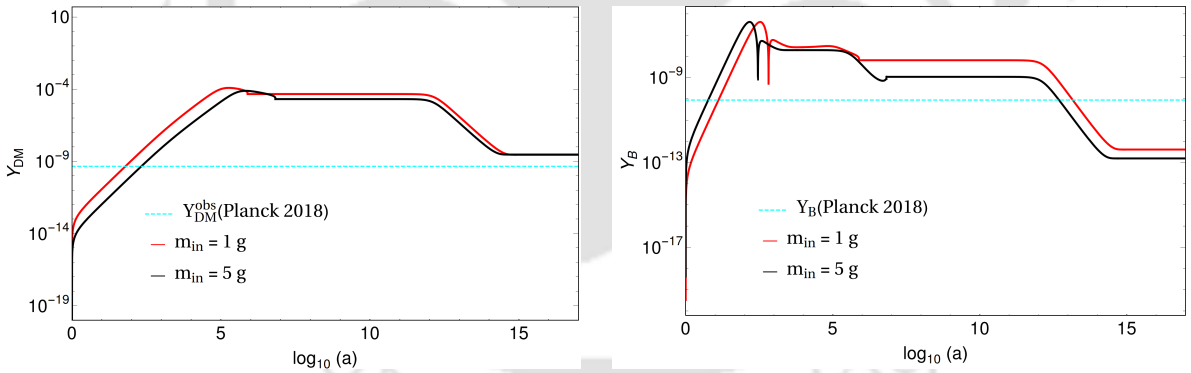


FIGURE 5.5: Evolution of DM (left) and baryon yield (right panel) for two different values of PBH masses shown in two different colours. We consider $m_{\rm DM} = 1$ GeV, $M_1 = 10^{13}$ GeV, $M_3 = 10^{12}$ GeV, while keeping $N_3$ decay $\Gamma_3 = 1.3 \times 10^{-11}$ GeV to be fixed.

As advocated in the last section, DM overproduced from PBH evaporation gets diluted to right abundance by introducing entropy injection at late epochs. In this case $N_3$ decay is responsible for adequate entropy dilution. The effect of entropy injection on the DM and baryon yield is demonstrated in Fig. 5.5, considering two different PBH masses. In the left panel we see DM is first overproduced at the end of PBH evaporation around

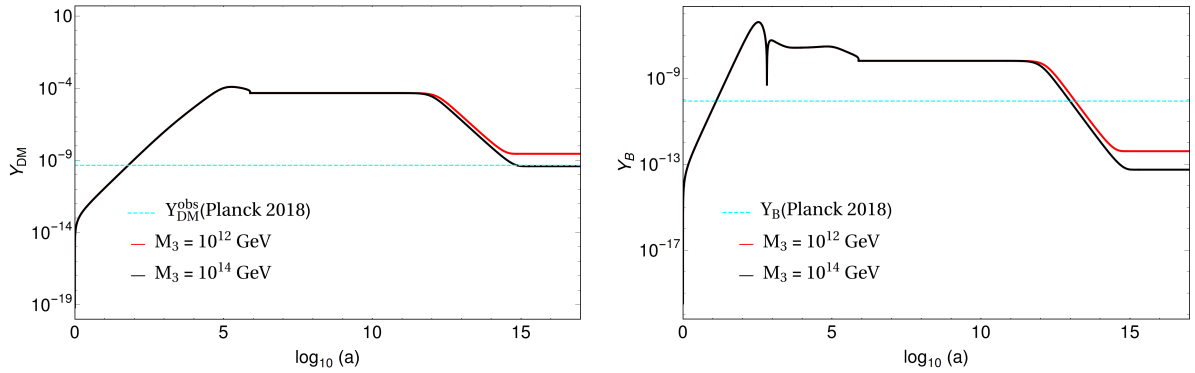


FIGURE 5.6: Evolution of DM (left) and baryon yield (right panel) for two different $M_3$ values, shown in two different colours. We consider $m_{\rm DM} = 1$ GeV, $m_{\rm in} = 1$ g, and the decay width $\Gamma_3 = 1.3 \times 10^{-11}$ GeV is kept fixed.

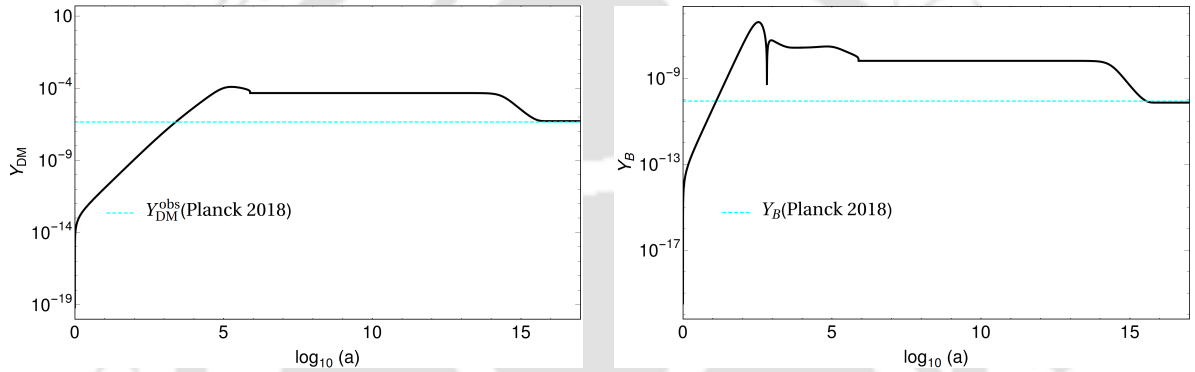


FIGURE 5.7: Evolution of DM yield (left panel) and baryon asymmetry yield (right panel) for choice of parameters which together satisfy observed DM relic and baryon asymmetry. We choose $m_{\rm DM} = 1$ MeV, $M_1 = 10^{13}$ GeV, $M_3 = 10^8$ GeV, $m_{in} = 1$g, and $\Gamma_3 = 4 \times 10^{-15}$ GeV.

$a \sim 10^6$. The DM yield then starts diminishing once $N_3$ starts decaying at later epoch near $a \sim 10^{12}$. Once $N_3$ decay is complete, the DM yield saturates close to the Planck 2018 limit for $m_{\rm DM} = 1$ GeV. As we already noticed in Fig. 5.3, entropy injection has a destructive effect on the baryon asymmetry since it dilutes the asymmetry generated from RHN decay as well. This is again established in the right panel, where we see the generated yield for asymmetry becomes under-abundant after the completion of $N_3$ decay for a fixed $M_3$. For a fixed PBH mass the effect of varying $M_3$ is shown in Fig. 5.6, where in the left panel we see that a heavier $M_3$ is capable of producing the right DM abundance for a fixed DM mass since a heavier $N_3$ results in larger entropy dilution. This affects $Y_B$ as well, as one can see from the right panel of Fig. 5.6. Therefore, one has to make a careful choice of PBH

and diluter mass in order to satisfy both DM abundance and right baryon asymmetry. In Fig. 5.7 we show a specific benchmark point which gives rise to right asymptotic yield for the DM and that of baryon asymmetry simultaneously, in agreement with observations. Here we choose a DM of mass $m_{\rm DM} = 1$ MeV, while $M_3 = 10^8$ GeV with a PBH of mass 1 g. The entropy released due to the decay of long-lived heavy $N_3$ can be expressed

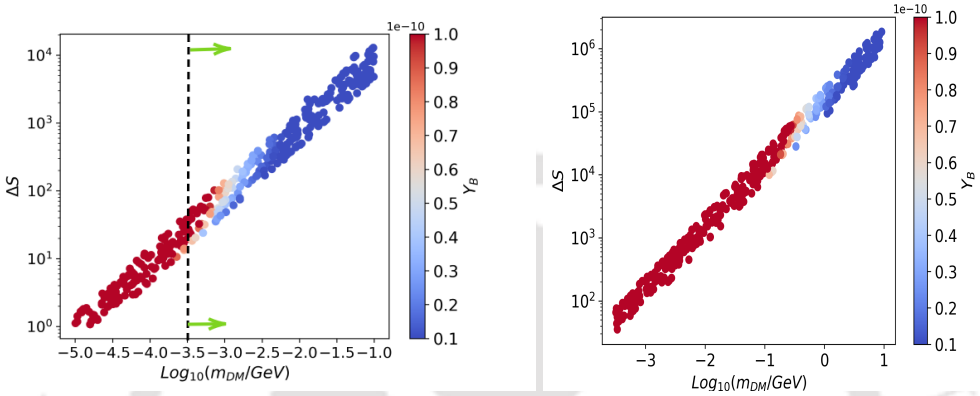


FIGURE 5.8: Left: Parameter space allowed by relic density in $\Delta S - m_{\rm DM}$ plane, where PBH mass is scanned over the range: {0.5-5} g. The colour code is with respect to $Y_B$, considering vanilla high scale leptogenesis. The black vertical dashed line corresponds to the conservative bound from WDM. The green arrows denote the net allowed parameter space. Right: Same as left, but considering resonant leptogenesis.

analytically, similar to Eqn. (3.30), as

$$\Delta S \simeq \left[1 + 2.95 \left(\frac{2\,\pi^2\, g_{*s}(T)}{45}\right)^{\frac{1}{3}} \left(\frac{Y_3^2\, M_3^2}{M_{\rm pl}\,\Gamma_3}\right)^{\frac{2}{3}}\right]^{\frac{3}{4}}, \tag{5.7}$$

where $Y_3 = n_{N_3}/s$ is the initial yield of $N_3$ before the onset of the second matter dominated era due to $N_3$ and $\Gamma_3$ is its decay width. Note that the amount of entropy injection is inversely proportional to $\Gamma_3$ as expected. Now, $\Gamma_3$ cannot be arbitrarily small as $N_3$ has to decay before BBN. This gives an upper bound on $\Delta\, S$, around $10^{11}$, which translates into an upper bound on the dark matter mass, $m_{\rm DM} \lesssim 10^6$ GeV. This is nevertheless a significant improvement as DM masses all the way till $m_{\rm DM} \sim 10^{10}$ GeV, if solely produced from PBH evaporation, remain disallowed in the usual scenario without late entropy injection, either due to overproduction or WDM limits, as shown in the left panel plot of Fig. 5.2. It is important to specify here that $\Delta S$ can be related to the lightest neutrino mass $m_\nu^1$,

since the value of the $N_3$ Yukawas are determined by $m_\nu^1$. For instance, we find that for $m_{\rm in} = 1$ g, and $M_3 < T_{\rm BH}^{\rm in}$, $1 \lesssim \Delta S \lesssim 10^6$ typically corresponds to lightest neutrino mass in the range $10^{-10}\,{\rm eV} \lesssim m_\nu^1 \lesssim 10^{-24}\,{\rm eV}$. Such tiny values of the lightest neutrino mass and hence tiny Dirac Yukawa couplings of $N_3$ are expected since $N_3$ has to be sufficiently long-lived. Now, in order to explore the viable parameter space we perform a numerical scan over the DM mass $m_{\rm DM}$ in keV-GeV range and on the PBH mass $m_{\rm in} : \{0.5 - 5\}$ g, fixing the leptogenesis scale $M_1$ at $10^{13}$ GeV. In the left panel of Fig. 5.8 we show the relic density allowed parameter space in $\Delta S - m_{\rm DM}$ plane. DM particles with large velocity, i.e., warm DM, are constrained by observations because their large free-streaming length prevents structure formation of the Universe. The formation of structures in WDM is suppressed for perturbations of comoving size $\lesssim \lambda_{\rm DM} \propto m_{\rm WDM}^{-4/3}$ [157, 292]. The signature of such WDM would thus be the suppression of the matter power spectrum (MPS) at scales below their free-streaming horizon. From cosmological data at large scales (CMB and galaxy surveys) we know that such a suppression should be sought at comoving scales well below a Mpc. The Lyman-$\alpha$ forest has been used for measuring the matter power spectrum at such scale [292, 293]. This lower bound on the mass of a thermal early decoupled WDM can be translated into a lower bound on the present velocity of a generic WDM. As already established earlier, light DM with mass below $\lesssim 3$ keV [294, 295] is disallowed from the Lyman-$\alpha$ bound on WDM[6], which are shown by the red points on the left side of black vertical dashed line. However, a substantial amount of entropy injection can improve this situation as already shown in the right panel plot of Fig. 5.2. Thus, DM mass $m_{\rm DM} \gtrsim \mathcal{O}(\text{MeV})$ is allowed for $\Delta S \gtrsim \mathcal{O}(10)$. The parameter space is also capable of explaining the observed baryon asymmetry in vanilla leptogenesis framework for $10 \lesssim \Delta S \lesssim 100$, which agrees with earlier observations in [96]. We project the most conservative WDM bound that disallows DM mass $m_{\rm DM} \lesssim 0.3$ MeV. Note that, as foretold, with the increase in $\Delta S$, the baryon asymmetry decreases (cf. Fig. 4.20). Thus, cogenesis of right DM abundance and baryon asymmetry is possible with an entropy production of the order of $\Delta S \lesssim \mathcal{O}(100)$.

[6] A more conservative bound on WDM mass has been derived in [296].

In order to overcome the large entropy dilution at late epochs, we also check if the lepton asymmetry can be significantly overproduced. Hence, we incorporate the resonant leptogenesis setup here, discusssed in chapter 1. Since a larger CP asymmetry results in larger baryon asymmetry, hence in this case one can allow larger entropy injection compared to the standard vanilla leptogenesis scenario. This in turn helps in relaxing the bound on DM mass, allowing heavier masses compared to the vanilla leptogenesis scenario. This is what we can see from the right panel of Fig. 5.8, where we find the allowed parameter space corresponds to $\Delta S \gtrsim \mathcal{O}(100)$. Note that for $\Delta S \gtrsim 100$, the WDM limit becomes relatively relaxed and thus the whole parameter space opens up for correct DM relic.

## 5.4 Production from Gravity Mediated Scattering

Apart from PBH, pure gravitational production of DM can also take place from the 2-to-2 scattering of the bath particles via $s$-channel mediation of massless graviton. The interaction rate density for such a process reads [297–302]

$$\gamma(T) = \alpha \frac{T^8}{M_{\rm pl}^4}\,, \tag{5.8}$$

with $\alpha \simeq 1.9 \times 10^{-4}$ (real scalar), $\alpha \simeq 1.1 \times 10^{-3}$ (Dirac fermion) or $\alpha \simeq 2.3 \times 10^{-3}$ (vector boson). This kind of production is unavoidable due to universal coupling between the gravity and the stress-energy tensor involving the matter particles. The BEQ governing the time evolution of DM number density is thus given by

$$\dot{n}_{\rm DM} + 3\,\mathcal{H}\,n_{\rm DM} = \gamma\,. \tag{5.9}$$

For temperatures much lower than the reheat temperature i.e., $T \ll T_{\rm rh}$, the DM yield can be analytically obtained by integrating Eqn. (5.9)

$$Y_0 = \frac{45\,\alpha}{2\,\pi^3\,g_{\star s}}\sqrt{\frac{10}{g_\star}}\left(\frac{T_{\rm rh}}{M_{\rm pl}}\right)^3\,, \tag{5.10}$$

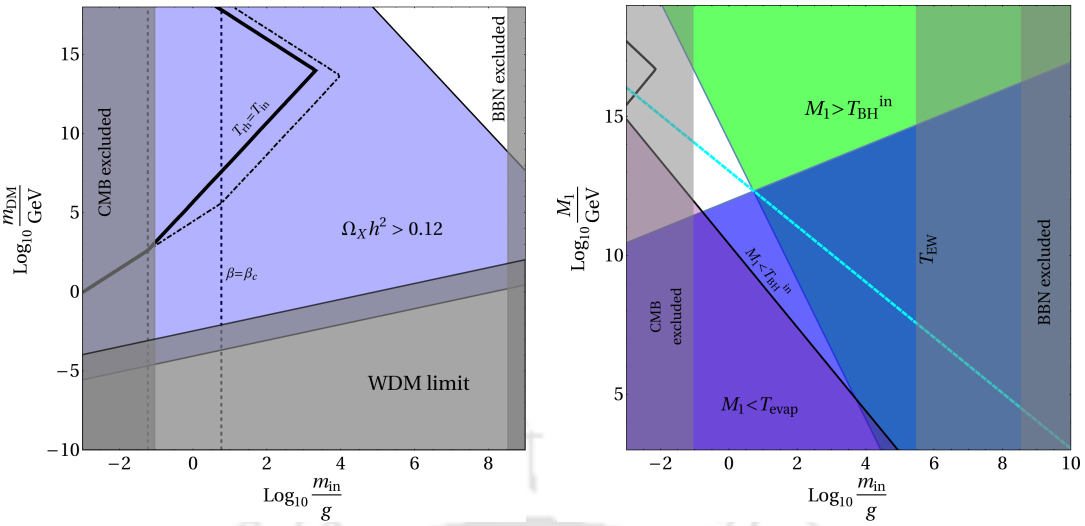


FIGURE 5.9: Left: The black thick line corresponds to right DM relic abundance via gravitational UV freeze-in. Along the contour we have $T_{\rm rh} = T_{\rm in}$. We consider no effect from entropy dilution (see text). Here the solid contour corresponds to $\beta = 10^{-4}$ and the dashed one for $\beta = 10^{-6}$. The straight vertical broken lines correspond to $\beta = \beta_c$. Right: The black solid and dashed contours correspond to observed baryon asymmetry for $\beta = 10^{-4}$ and $\beta = 10^{-6}$ respectively (the two contours overlap with each other and hence can not be distinguished). The coloured shaded regions are same as those in Fig. 4.20.

where we define the DM yield as $Y \equiv n_{\rm DM}/s$, with $s = \frac{2\,\pi^2}{45}\, g_{\star s}\, T^3$ and consider $m_{\rm DM} \ll T_{\rm rh}$. On the other hand, if the DM mass is such that $T_{\rm rh} \ll m_{\rm DM} \ll T_{\rm max}$, where $T_{\rm max}$ corresponds to the maximum temperature during reheating, then the DM can be produced during but not after the reheating. In the case the DM yield can be obtained by integrating Eqn. (5.9) for $T_{\rm max} \geq m_{\rm DM} \geq T_{\rm rh}$

$$Y_0 = \frac{45\,\alpha}{2\,\pi^3\,g_{\star s}}\sqrt{\frac{10}{g_\star}}\,\frac{T_{\rm rh}^7}{M_{\rm pl}^3\,m_{\rm DM}^4}\,. \tag{5.11}$$

Here we would like to mention that if the DM is produced during the transition from matter to radiation domination via an interaction rate that scales like $\gamma(T) \propto T^n$, for $n > 12$ the DM abundance is enhanced by a boost factor proportional to $(T_{\rm max}/T_{\rm rh})^{n-12}$ [303], whereas for $n \leq 12$ the results for the standard UV freeze-in calculation differ only by an $\mathcal{O}(1)$ factor from calculations taking into account of non-instantaneous reheating.

Now, the DM produced via gravitational UV freeze-in shall undergo dilution due to evaporation of the PBH, that can be quantified as [304, 305]

$$\frac{S(T_{\rm in})}{S(T_{\rm evap})} \simeq \frac{T_{\rm evap}}{T_{\rm peq}} \simeq 10^{-2} \left(\frac{M_{\rm pl}}{m_{\rm in}}\right)^{\frac{3}{2}} \frac{M_{\rm pl}}{\beta\, T_{\rm in}}\,, \tag{5.12}$$

for $\beta > \beta_c$, where we define $S = a^3\, s(T)$. The temperature $T_{\rm peq}$ is defined as the epoch of equality between SM radiation and the PBH energy densities $\rho_R(T_{\rm peq}) = \rho_{\rm BH}(T_{\rm peq})$, and is given by

$$T_{\rm peq} = \beta\, T_{\rm in} \left(\frac{g_{\star,s}(T_{\rm in})}{g_{\star,s}(T_{\rm in})}\right)^{\frac{1}{3}}. \tag{5.13}$$

The observed DM abundance can then be achieved

$$m_{\rm DM}\, Y_0\, \frac{S(T_{\rm in})}{S(T_{\rm evap})} = \Omega_{\rm DM}\, h^2\, \frac{1}{s_0}\, \frac{\rho_c}{h^2} \simeq 4.3 \times 10^{-10}\, {\rm GeV}\,, \tag{5.14}$$

with $\rho_c$ being the critical density of the Universe. In Fig. 5.9 the black thick contour in the left panel satisfies correct DM relic abundance via gravitational UV freeze-in, considering $T_{\rm rh} = T_{\rm in}$. To the left of the contour, DM is over produced due to gravitational UV freeze-in. From this plot, it is clear that in the region of DM mass we are interested in (see Fig. 5.8), the DM production from the gravitational UV freeze-in remains under-abundant.

Similar to the case of DM, it is also possible to have leptogenesis from the decay of the RHNs, that are gravitationally produced from the SM bath via massless gravtion mediated scatterings [306, 307]. Following the same methodology as above, in the right panel of Fig. 5.9 we show the contour corresponding to right baryon asymmetry, using the CP asymmetry parameter defined by Eqn. (1.45). We see that the gravitational leptogenesis can dominate the production from PBH only for very light PBH which are already excluded from CMB bounds.

## 5.5 Conclusions

We have proposed a scenario where gravitational dark matter is produced from evaporating primordial black holes. Except for the superheavy mass window $m_{\rm DM} \gtrsim 10^{10}$ GeV, DM production solely from PBH evaporation leads to overabundance if PBH dominates the energy density of the Universe at early epochs. While lighter mass window $m_{\rm DM} \lesssim \mathcal{O}(1)$ keV gives correct relic, it faces severe constraints from the requirement of structure formation. We particularly focus on this keV to $10^{10}$ GeV mass window of gravitational DM and incorporate it within a Type-I seesaw framework with three right handed neutrinos responsible for generating light neutrino masses. While DM in this mass window gets overproduced from PBH evaporation, late entropy injection from decay of one of the RHNs (acting as a diluter) can bring the DM abundance within observed limits. As the late entropy dilution must occur before the epoch of BBN in order not to disturb the successful prediction for light nuclei abundance, we impose the upper bound on diluter lifetime which gets translated into an upper bound on entropy injection, allowing DM mass upto $\sim 1$ PeV. Along with DM, the diluter also gets dominantly produced from PBH evaporation as its couplings to the SM particles remain suppressed from the requirement of long lifetime needed for sufficient entropy release due to its decay. This effectively leads to two different stages of early matter domination: first from PBH and then from the diluter. The other two RHNs can have sizeable couplings with SM leptons thereby generating the required neutrino mass and mixing. We consider the production of these RHNs both from the bath as well as PBH and show that their subsequent CP violating out-of-equilibrium decays can lead to successful leptogenesis as well. Since the lepton asymmetry is required to be overproduced initially in order to survive the subsequent entropy dilution, the DM parameter space gets squeezed from a few keV-PeV window to a smaller range around MeV-GeV ballpark from the requirement of producing both DM relic as well as the baryon asymmetry of the Universe, with PBH mass $m_{\rm BH} \lesssim 5$ g. The long-lived nature of $N_3$ necessarily pushes the lightest active neutrino mass $m_\nu^1$ to vanishingly small values ($\lesssim 10^{-10}$ eV). Thus, the effective neutrino mass will be very much out of reach from ongoing tritium beta decay experiments like KATRIN

[210], whereas any positive detection of $m_\nu^1$ in future experiments might be able to falsify our scenario. While gravitational DM has no scope of direct detection, the required PBH mass as well as multiple stages of early matter domination can have interesting observable consequences, especially in the context of gravitational wave observations [117, 118, 147, 149, 150, 277, 308–310]. Interestingly, if the seesaw scale is dynamically generated through a gauge symmetry breaking, such multiple matter domination can have interesting signatures in GW generated from cosmic strings, which we recently pursued in Ref. [311].

# Chapter 6

# DM and Baryogenesis with PBH domination

## 6.1 Introduction

This chapter explores a scenario of direct baryogenesis from PBH, without incorporating the leptogenesis route, along with superheavy gravitational dark matter produced from PBH. We consider a minimal particle physics setup to realize baryogenesis due to out-of-equilibrium CP violating decay of a coloured scalar. The baryon asymmetry can be generated at low scale, even below the sphaleron decoupling temperature due to non-thermal origin of the coloured scalar from PBH evaporation. Due to the possibility of low scale generation of baryon asymmetry, the allowed PBH mass range can be much bigger compared to the one in the PBH assisted leptogenesis works discussed in some of the preceding chapters. This also brings the GW spectrum created by PBH density fluctuations to the observable ballpark in mHz-kHz frequencies with peak amplitudes lying within reach of even LIGO/VIRGO as well as several planned experiments. Such non-thermal source of baryogenesis from PBH can escape the issues faced by thermal baryogenesis discussed in chapter 1. Particularly, the decaying heavy particle can be produced at a low scale from PBH depending on its initial mass, regardless of the temperature of the thermal bath. Also, since the asymmetry can be generated below the electroweak scale, they could avoid the washout because of sphaleron, especially for PBH with higher initial mass. In addition, the strong annihilations of the decaying particle can be avoided

at low scale, which could have otherwise led to a potential dilution of the asymmetry. Now, while such PBH dominated epoch in the early Universe typically leads to the over-production of DM except for superheavy regime, we find interesting correlations between DM mass and the coloured scalar mass responsible for creating BAU. Our analysis also differs from the recent work [312] where a second population of heavy stable PBH was considered which itself act as DM, in addition to the difference in GW production source and frequencies (MHz-GHz ballpark). While our GW signatures are similar to our recent work [152], there exist sharp differences in the cogenesis mechanism. In [152], high scale thermal leptogenesis leads to over-production of baryon asymmetry which gets diluted due to PBH evaporation at late epochs which also leads to the production of superheavy DM. On the other hand, we are studying direct baryogenesis (without taking the leptogenesis route) and DM production from PBH evaporation. The complementary detection prospects are more promising in the present setup due to the presence of additional coloured particles and baryon number violation. Depending upon the mass of the coloured scalar and its couplings, the model can also have complementary detection prospects at the LHC and experiments looking for baryon number violating processes like neutron-antineutron $(n - \bar{n})$ oscillations. Our aim here is to provide a testable scenario, based on existing particle physics model, that is capable of simultaneously explaining baryonic and dark matter abundance, thanks to the underlying gravitational production associated with PBH evaporation.

This chapter is organized as follows. In section 6.2 we briefly discuss the model and source of baryon asymmetry. In section 6.3, we discuss the role of PBH in baryogenesis, followed by discussion of the results related to BAU and superheavy DM from PBH in section 6.4. In section 6.5, we discuss the details of GW generation in our setup and finally conclude in section 6.6.

## 6.2 The Framework

### 6.2.1 Field content and interactions

In this section we describe the underlying particle physics model responsible for baryogenesis. To realise baryogenesis, we follow a simple particle physics setup similar to the earlier works [313–317]. We consider renormalisable baryon number (B) violating terms involving newly introduced particles as a source of BAU. In order to avoid $\Delta B = 1$ processes leading to proton decay, we consider $\Delta B = 2$ processes having other observable signatures like $n - \bar{n}$ oscillations [318–320]. We consider the presence of two iso-singlet scalars $S_i$, with $i = 1, 2$, that transform as $SU(3)_c$ triplets under the SM. The scalars also carry non-trivial $U(1)_Y$ charges that allow us to have a direct coupling term to right handed down type quarks as $S\, d^c\, d^c$. The presence of at least two $S$ is needed to produce a baryon asymmetry from the interference of tree and one-loop diagrams in a decay process governed by the $S\, d^c\, d^c$ interactions. However, although necessary, this is not sufficient. The reason being that the total asymmetry vanishes after summing over all flavors of $d^c$ in the final and intermediate states [321]. One therefore, requires additional baryon number violating interactions, and the simplest renormalisable term as such is $S\psi\, u^c$ where $\psi$ is a SM gauge singlet field. The newly added fields and their corresponding charges under the SM gauge symmetry are listed in Table 6.1. With this particle content at our disposal, we can now write the relevant part of the renormalisable Lagrangian as [316, 317, 322, 323]

$$-\mathcal{L} \supset \lambda\, S\, \psi\, u^c + \lambda'\, S^\star\, d^c\, d^c + \frac{1}{2}\, m_\psi\, \overline{\psi^c}\, \psi + \text{h.c.}\,, \tag{6.1}$$

where we have suppressed all the flavour indices. Clearly, the Majorana mass term of $\psi$ is the source of baryon number violation ($\Delta B = 2$) in this model.

The above particle content does not lead to a naturally stable DM candidate. For the interaction Lagrangian given in Eqn. (6.1), the neutral singlet fermion $\psi$ can be made kinematically stable by choosing its mass as $m_p - m_e \leq m_\psi \leq m_p + m_e$, forbidding both

| Fields | $SU(3)_c$ | $SU(2)_L$ | $U(1)_Y$ |
|---|---|---|---|
| $u^c$ | 3 | 1 | $-4/3$ |
| $d^c$ | 3 | 1 | $+2/3$ |
| $S_i\,(i \in 1,2)$ | 3 | 1 | $+4/3$ |
| $\psi$ | 1 | 1 | 0 |

TABLE 6.1: Relevant fields including the newly added ones and their corresponding charges under the SM gauge symmetry.

the possibilities of proton and $\psi$ decays. However, in the absence of additional symmetries, $\psi$ can couple to lepton and Higgs doublets of the SM opening up another decay channel. Even if additional symmetry is introduced to forbid such decay into leptons, a PBH dominated phase typically over-produces DM with mass $m_{\rm DM} \sim 1$ GeV, as we discuss below. Therefore, in our minimal setup, $\psi$ can not be a DM candidate. Therefore, $\psi$ can be much heavier in our setup while obeying the lower bound $m_p - m_e \leq m_\psi$ to forbid the corresponding proton decay mode $p \to \psi\, e^+\, \nu_e$. Interestingly, multiple generations of $\psi$ can also play a role in generating light neutrino mass via type-I seesaw mechanism [54, 56–58]. We consider DM to be purely gravitational such that it is produced dominantly from PBH evaporation. Since both DM and the coloured scalar S responsible for BAU originate non-thermally from PBH evaporation, this leads to a strong correlation among DM, coloured scalar as well as PBH initial masses. In addition, a purely gravitational DM is also motivated from the fact that all observational evidences of DM are based on its gravitational interactions only, with direct detection experiments continuing their null results.

### 6.2.2 Generation of baryon asymmetry

Baryon asymmetry is generated through the decay of the coloured scalars $S_i$, leading to CP asymmetries, via interference between a tree and loop-level diagrams as in Ref. [317]

$$\epsilon_\alpha = \frac{1}{8\,\pi}\,\frac{\sum_{i,j,k}\,{\rm Im}\,\left(\lambda^*_{\alpha k}\lambda_{\beta k}\lambda'^*_{\alpha ij}\lambda'_{\beta ij}\right)}{\sum_{i,j}\,|\lambda'_{\alpha ij}|^2 + \sum_i\,|\lambda_{\alpha i}|^2} \times \frac{\left(m^2_{S_\alpha} - m^2_{S_\beta}\right)\,m_{S_\alpha}\,m_{S_\beta}}{\left(m^2_{S_\alpha} - m^2_{S_\beta}\right)^2 + m^2_{S_\alpha}\,\Gamma^2_{S_\beta}}\,;\,{\rm with}\,\alpha\,,\beta = 1\,,2\,;\,\alpha \neq \beta\,, \tag{6.2}$$

such that the final baryon asymmetry, in the non-thermal ballpark (where washouts are negligible) can be estimated as

$$Y_B = \frac{n_B}{s} = \epsilon_1 \frac{n_{S_1}}{s} + \epsilon_2 \frac{n_{S_2}}{s}. \tag{6.3}$$

In Eqn. (6.2), the decay width of $S_\alpha$, at tree level, is estimated as

$$\Gamma_{S_\alpha} = \frac{m_{S_\alpha}}{16\pi} \left[ \sum_i |\lambda_{\alpha i}|^2 + \sum_{i,j} \left| \lambda'_{\alpha ij} \right|^2 \right]. \tag{6.4}$$

In order to compute the CP asymmetries from Eqn. (6.2), we parameterize the Yukawa matrices in Eqn. (6.1) as

$$\lambda = \begin{pmatrix} \lambda & \lambda & \lambda \\ \lambda e^{i\phi_1} & \lambda e^{i\phi_1} & \lambda e^{i\phi_1} \end{pmatrix}, \lambda'_1 = \begin{pmatrix} 0 & \lambda' & \lambda' \\ \lambda' & 0 & \lambda' \\ \lambda' & \lambda' & 0 \end{pmatrix}, \lambda'_2 = \begin{pmatrix} 0 & \lambda' e^{i\phi_2} & \lambda' e^{i\phi_2} \\ \lambda' e^{i\phi_2} & 0 & \lambda' e^{i\phi_2} \\ \lambda' e^{i\phi_2} & \lambda' e^{i\phi_2} & 0 \end{pmatrix}, \tag{6.5}$$

which provides us with two more free parameters, namely the arbitrary CP phases $\phi_{1,2}$. Also, the diagonal entries of $\lambda'_{1,2}$ are zero due to the requirement of colour anti-symmetry. Note that $\lambda'_{\alpha ij}$ denotes the components of the matrices $\lambda'_\alpha$ with $\alpha = 1, 2$. Utilizing this parametrisation, from Eqn. (6.2) we find $\epsilon_1 + \epsilon_2 = 0.1$ for $\lambda\,, \lambda' \simeq 10^{-3}$ with $m_{S_1} \approx m_{S_2}$. Typically, this corresponds to *resonant* baryogenesis scenario, where the mass difference between $S_{1,2}$ is of the same order as their decay width: $\Delta m \equiv |m_{S_1} - m_{S_2}| \sim \Gamma_{S_{1,2}}/2 \ll m_{S_{1,2}}$ [317], similar to the resonant leptogenesis framework [62]. Since $\Gamma_S \propto m_S$, hence the CP asymmetry in the resonance limit becomes independent of the scalar mass.

### 6.2.3 Constraints from the LHC and $n - \bar{n}$ Oscillations

While we do not perform a detailed collider study of our model here, we briefly mention the existing bounds on coloured scalars, which most part of our parameter space satisfy. The on-shell production of $S$ via $pp \to S \to d_i^c d_j^c$, can lead to dijet resonance that in turn can constraint the mass of $S$ and the couplings $\lambda\,, \lambda'$, as discussed in [317]. A search

for narrow resonances decaying to dijet final states put upper limits at 95% confidence level on the production cross section with masses above 0.6 TeV at $\sqrt{s} = 13$ TeV, with an integrated luminosity of 12.9 $\text{fb}^{-1}$ [324]. This excludes colour octet scalars below 3 TeV. This bound has been updated for an integrated luminosity of 137 $\text{fb}^{-1}$, that searches for a narrow (or broad) s-channel dijet resonance with mass above 1.8 TeV, constraining colour octet scalars below 3.7 TeV [325]. There is also a possible monojet signal of this model at the LHC from the on-shell production of $S$ and its subsequent decay through: $pp \to S \to \psi u^c$, that can be constrained from monojet plus missing energy searches from CMS [326] and ATLAS [327]. On the other hand, the colored scalars can also be pair-produced at a hadron collider: $pp \to SS^\star$, purely through QCD interactions, independent of the Yukawa couplings. The subsequent decay of $S \to d_i^c\, d_j^c$ will then lead to paired dijet resonance. As explained in [317], the baryon number violating term in the Lagrangian can induce a $B$-violating dimension-9 operator of the form $\left(m_\psi/m_S^6\right)\ (\lambda^{\frac{1}{2}}\,\lambda')^4\ (u^c\,u^c)\ (d^c\,b^c)\ (d^c\,b^c)$, corresponding to $\Delta B = 2$ transition, that can lead to $n - \bar{n}$ oscillation with the amplitude

$$\mathcal{M}_{n\bar{n}} \simeq \frac{\lambda^2\,(\lambda')^4\,m_\psi}{8\,\pi^2\,m_S^6}\,\ln\left[\frac{m_S}{m_\psi}\right], \tag{6.6}$$

at one loop level, which is constrained from current experimental lower bound [318–320, 328]: $\mathcal{M}_{n\bar{n}} \leq 10^{-28}\,\text{GeV}^{-5}$ or equivalently, an oscillation lifetime of $\tau_{n\bar{n}} \gtrsim 10^8$ s.

## 6.3 Baryogenesis from PBH

As advocated earlier, the present set-up allows us to have baryogenesis from the direct CP-violating decay of the coloured scalars $S_\alpha$. The final asymmetry, therefore, depends on the yield of $S$ from PBH evanescence. Then, from Eqn. (6.3), during PBH domination

we obtain[1]

$$
\begin{aligned}
Y_B(T_0) \equiv Y_B(T_{\rm evap}) &= (\epsilon_1+\epsilon_2)\,\frac{n_S}{s}\bigg|_{T_{\rm evap}} = (\epsilon_1+\epsilon_2)\,\mathcal{N}_X\,\frac{n_{\rm PBH}}{s}\bigg|_{T_{\rm evap}} \\
&= (\epsilon_1+\epsilon_2)\begin{cases}
\frac{g_{X,H}}{g_{\star,H}}\,\frac{5}{\pi^2\,g_{\star s}(T_{\rm evap})}\left(\frac{\pi^3\,g_\star(T_{\rm evap})}{5}\right)^{\frac{3}{4}}\sqrt{\frac{\mathcal{G}\,g_{\star,H}}{10640\,\pi}}\,\sqrt{\frac{M_{\rm Pl}}{m_{\rm in}}} & \text{for } m_S < T^{\rm in}_{\rm BH}\,, \\
\frac{g_{X,H}}{g_{\star,H}}\,\frac{5}{64\pi^4\,g_{\star s}(T_{\rm evap})}\left(\frac{\pi^3\,g_\star(T_{\rm evap})}{5}\right)^{\frac{3}{4}}\sqrt{\frac{\mathcal{G}\,g_{\star,H}}{10640\,\pi}}\left(\frac{M_{\rm Pl}^9}{m_{\rm in}^5\,m_S^4}\right)^{\frac{1}{2}} & \text{for } m_S > T^{\rm in}_{\rm BH}\,,
\end{cases}
\end{aligned}
\tag{6.7}
$$

where we consider $m_{S_1} \approx m_{S_2} \equiv m_S$, that leads to $n_{S_1} \approx n_{S_2} \equiv n_S$ [according to Eqn. (2.18)]. As evident from Eqn. (6.2), $\epsilon_{1,2}$ are functions of the two couplings $\lambda\,,\lambda'$ and the scalar mass $m_S$. In Fig. 6.1 we show the parameter space satisfying the observed baryon asymmetry in $m_S - m_{\rm in}$ plane assuming PBH domination ($\beta > \beta_{\rm crit}$), for different choices of $\epsilon_1+\epsilon_2$. The contours obeying observed baryon asymmetry are independent of $m_S$ when $m_S < T^{\rm in}_{\rm BH}$, while a larger $m_S$ requires lighter PBH to produce the desired asymmetry following Eqn. (6.7). The red shaded region corresponds to $\epsilon_1+\epsilon_2 > (\epsilon_1+\epsilon_2)_{\rm max}$, where the latter is $\simeq 0.4$ for our choice of parameters, as we shall discuss in later. The noteworthy point here is that a direct baryogenesis from PBH opens up a whole new PBH mass range compared to baryogenesis via leptogenesis (as seen in Fig. 4.20).

Here we would like to mention that, the condition $m_S < T_{\rm evap}$ is enough to ensure the non-thermal production of asymmetry, even though in this case the new scalar carries non-trivial colour charge. In order to verify that we first note, the dominant 2-to-2 interaction of the scalar with the thermal bath takes place through $SS \to \tilde{g}\tilde{g}$ at the end of PBH evaporation, where $\tilde{g}$ are the gluons. The corresponding cross-section reads

$$
\sigma(s)_{SS\to\tilde{g}\tilde{g}} = \frac{g_s^4}{576\,\pi\,s}\sqrt{\frac{s}{s-4\,m_S^2}}\,,
\tag{6.8}
$$

[1] As we will see, in most of our parameter space, the baryon asymmetry is created below the electroweak scale ($m_{\rm in} \gtrsim 10^5$ g). If the asymmetry is created above the electroweak scale, it can be washed out by sphalerons if $B-L$ number is conserved. But, since in our scenario we have $B-L$ violating interactions, such washouts would be absent. However, there exists a conversion factor because of sphaleron which is of $\mathcal{O}(1)$ [48].

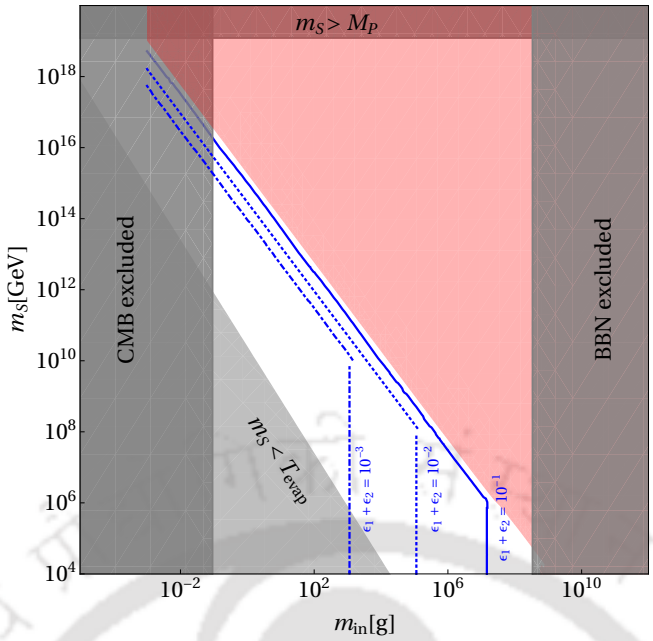


FIGURE 6.1: Contours satisfying $Y_B^{\rm obs}$ during PBH domination for different choices of the asymmetries, considering $\epsilon_1 + \epsilon_2$. The shaded vertical regions are ruled out. The shaded lower triangular region leads to thermal baryogenesis where our analysis based on non-thermal approximations is not applicable. The red shaded region is where the CP asymmetry exceeds the maximum value that is allowed by model parameters (see text).

where the presence of the strong coupling constant $g_s$ shows this is an irreducible process. The thermally averaged cross-section and decay rate of $S$ is given by

$$\begin{aligned}\langle\sigma v\rangle_{SS\to\tilde{g}\tilde{g}} &= \frac{1}{8\,m_S^4\,T_{\rm BH}\,K_2\left(m_S/T_{\rm BH}\right)^2}\int_{4\,m_S^2}^{\infty} ds\,\sigma(s)_{SS\to\tilde{g}\tilde{g}}\,\sqrt{s}\,K_1\left(\sqrt{s}/T_{\rm BH}\right)\\ \langle\Gamma_S\rangle &\approx \frac{K_1\left(m_S/T_{\rm BH}\right)}{K_2\left(m_S/T_{\rm BH}\right)}\,\Gamma_S\,,\end{aligned} \tag{6.9}$$

where $\Gamma_S$ is given by Eqn. (6.4). Note that, we have calculated the thermal average with respect to the PBH temperature and not the bath temperature. We find, for all PBH masses of our interest, the scattering rate $n_S \times \langle\sigma v\rangle$ stays below the decay rate at $T = T_{\rm evap}$, where

$$n_S = s(T_{\rm evap}) \times \begin{cases} \frac{g_{X,H}}{g_{\star,H}}\,\frac{5}{\pi^2\,g_{\star s}(T_{\rm evap})}\left(\frac{\pi^3\,g_\star(T_{\rm evap})}{5}\right)^{\frac{3}{4}}\sqrt{\frac{\mathcal{G}\,g_{\star,H}}{10640\,\pi}}\sqrt{\frac{M_{\rm Pl}}{m_{\rm in}}} & \text{for } m_S < T_{\rm BH}^{\rm in}\,,\\ \frac{g_{X,H}}{g_{\star,H}}\,\frac{5}{64\pi^4\,g_{\star s(T_{\rm evap})}}\left(\frac{\pi^3\,g_\star(T_{\rm evap})}{5}\right)^{\frac{3}{4}}\sqrt{\frac{\mathcal{G}\,g_{\star,H}}{10640\,\pi}}\left(\frac{M_{\rm Pl}^9}{m_{\rm in}^5\,m_S^4}\right)^{\frac{1}{2}} & \text{for } m_S > T_{\rm BH}^{\rm in}\,.\end{cases} \tag{6.10}$$

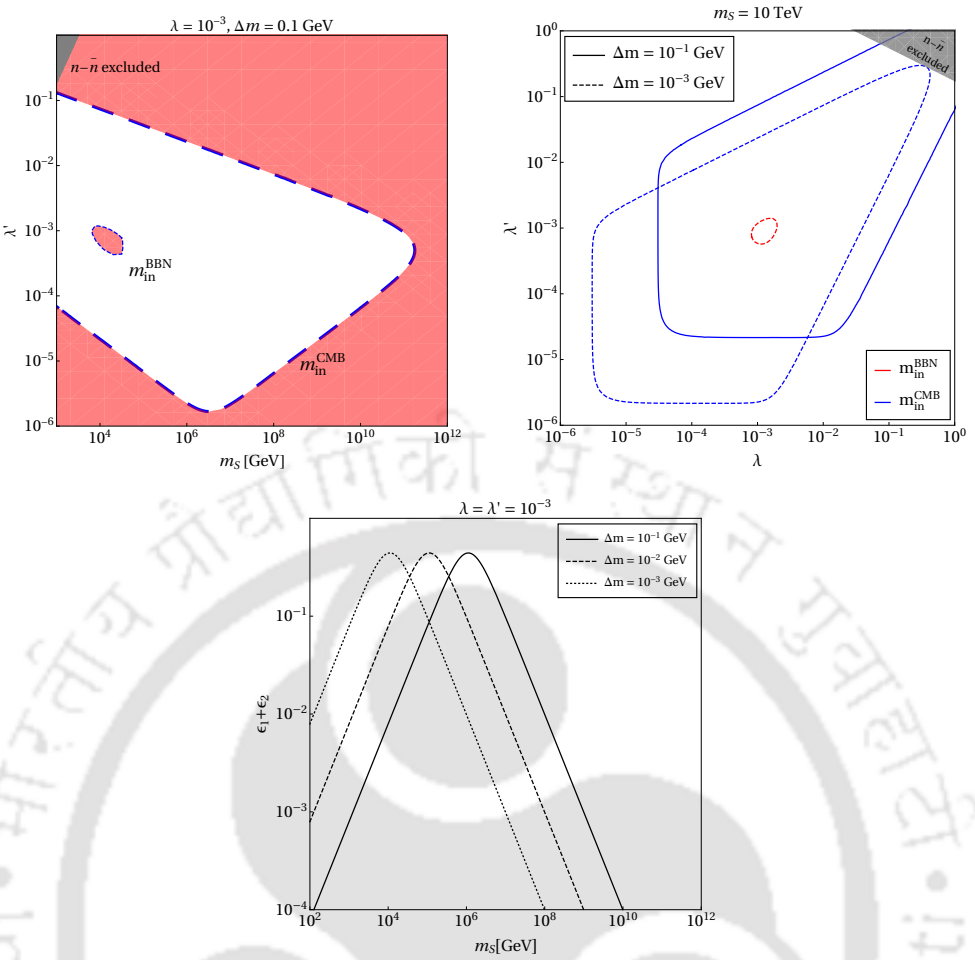


FIGURE 6.2: *Top Left:* Contours satisfying $Y_B^{\rm obs}$ in $\lambda' - m_S$ plane for $m_{\rm in} = m_{\rm in}^{\rm CMB}$ (blue) and $m_{\rm in} = m_{\rm in}^{\rm BBN}$ (red). bfThe shaded region is disallowed from BBN and CMB constraints on PBH mass (see text). *Top Right:* Contours of $Y_B^{\rm obs}$ in $\lambda' - \lambda$ plane for two different choices of $\Delta m$ shown in solid and dashed lines. The blue and red contours correspond to $m_{\rm in} = m_{\rm in}^{\rm CMB}$ and $m_{\rm in} = m_{\rm in}^{\rm BBN}$ respectively. *Bottom:* Variation of CP asymmetry as a function of $m_S$. In all cases we choose $m_\psi = 1$ GeV. The shaded regions are disfavoured from $n - \bar{n}$ oscillation limits [cf.Eqn. (6.6)].

This implies, the CP-violating decay rate of the scalar is much more efficient than its 2-to-2 scattering rate at $T = T_{\rm evap}$. Therefore, the asymmetry freezes in well before the thermalization takes place via the irreducible 2-to-2 process for $m_S > T_{\rm evap}$, making the non-thermal assumption viable[2]. This is typically because of the suppression from $m_S$ and $T_{\rm BH}$ in Eqn. (6.9).

Possible range of coupling values that can give rise to the observed BAU, are shown in Fig. 6.2. In the *top left* panel we plot contours of correct baryon asymmetry in $\lambda' - m_S$

[2]Following the prescription in [105] (also see Appendix D), we have also checked the scattering efficiency of a PBH generated $S$ scattering on a thermal $S$, and found that this rate is much below the Hubble rate for the range of PBH masses that produce right DM and baryon abundance.

plane for a fixed $\Delta m$, and choosing the minimum and maximum PBH masses that satisfy CMB and BBN bound respectively. The blue coloured contour corresponds to $m_{\rm in} = m_{\rm in}^{\rm CMB} \sim 0.1$ g, while the red coloured contour is for $m_{\rm in} = m_{\rm in}^{\rm BBN} \sim 10^8$ g. Thus, the region in between these two can produce $Y_B^{\rm obs}$ for gradually decreasing PBH mass, as we move from the red to the blue contour. The red shaded regions are disallowed as they require PBH lighter (heavier) than the one viable from CMB (BBN) bound. Note that, because of $\Delta m \ll m_S$, we do not discriminate between two scalar masses and refer to them as $m_S$. Note that, large Yukawa or lighter $m_S$ are forbidden (shown by the grey shaded region) as they give rise to $n - \bar{n}$ oscillations with small lifetime, in conflict with the bound on Eqn. (6.6). In the *top right* panel we project the allowed parameter space in $\lambda' - \lambda$ plane for a fixed $m_S = 10$ TeV, and for different choices of $\Delta m$, shown by blue coloured solid and dashed contours. The red and blue coloured contours are for PBH of masses allowed from BBN and from CMB bounds respectively. The region outside each blue contour is discarded, as they correspond to PBH masses lighter than the one allowed from CMB measurements, as shown by the red shaded region in the top left panel. However, as these contours overlap on each other, depending on the choice of $\Delta m$, we refrain from shading those regions. For each case we see that the correct asymmetry can be found twice as the CP-asymmetry shows a resonance behaviour, which becomes maximum when $\Delta m \sim \Gamma_S/2$, as shown in the *bottom* panel. This results in closed contours for right baryon asymmetry. Clearly, if we deviate from the resonance regime, the required CP asymmetry can be obtained by suitable choices of Yukawa couplings. We find, a maximum of CP asymmetry of $(\epsilon_1 + \epsilon_2)_{\rm max} = 0.43$ is possible for parameters of our interest. We thus discard values larger than $(\epsilon_1 + \epsilon_2)_{\rm max}$, as shown by the red shaded region in Fig. 6.1. As the *top right* panel figure shows, increasing the mass splitting $\Delta m$ corresponds to larger Yukawa couplings in order to obtain the desired asymmetry. Here we would like to remind the readers once again that the results so far apply for PBH dominated epoch, i.e., $\beta > \beta_c$.

As noted earlier, the simple estimate for baryon asymmetry adopted here holds in the non-thermal ballpark only. While PBH evaporation at late epoch ($T_{\rm evap} < m_S$) leads to

such non-thermal production of $S$, it is possible to have thermally generated $S$ too given the fact that prior to PBH domination, the Universe is assumed to be radiation dominated. However, being a coloured scalar, $S$ will be in equilibrium for a long epoch due to strong annihilations into gluons (independent of the Yukawas $\lambda\,, \lambda'$) leading to dilution in generated asymmetry. On the other hand, the out of equilibrium criteria of its decay will force the corresponding Yukawa couplings $(\lambda, \lambda')$ to be in smaller regime, reducing the CP-asymmetry [316, 317]. In other low scale baryogenesis scenarios like [329] and post-sphaleron baryogenesis [330], this is ensured by considering the decaying particle to be colour neutral whose baryon number violating decay into quarks create the asymmetry without requiring any non-thermal origin. Additionally, there will be washouts from inverse decay and scattering further reducing the baryon asymmetry produced from thermally generated $S$. Finally, PBH evaporation at late epoch is likely to cause entropy dilution to any baryon asymmetry generated at higher temperatures $(T > T_{\rm evap})$, as noticed in PBH-generated leptogenesis works earlier [100, 276]. Therefore, the thermally generated baryon asymmetry can be ignored in our setup validating the non-thermal estimates discussed above.

## 6.4 A common parameter space for baryogenesis and dark matter

DM of arbitrary intrinsic spin can be produced directly from PBH evaporation. Thus, the DM abundance can be expressed as

$$Y_{\rm DM}(T_0) \equiv \left.\frac{n_{\rm DM}}{s}\right|_{T_0} = \frac{3}{4}\frac{(T^{\rm in}_{\rm BH})}{} N_{\rm DM} \times \begin{cases} \beta \frac{T^{\rm in}_{\rm BH}}{m_{\rm in}}\,, \beta \leq \beta_c \\ \frac{\bar{T}_{\rm evap}}{m_{\rm in}}\,, \beta \geq \beta_c\,, \end{cases} \tag{6.11}$$

where $N_{\rm DM} \equiv \mathcal{N}_X$ as given in Eqn. (2.18). Thus, the DM relic abundance $\Omega_{\rm DM}\,h^2 = \frac{m_{\rm DM}\,s_0}{\rho_c}\,Y_{\rm DM}\,(T_0)$ , at the present epoch for PBH domination reads

$$\Omega_{\rm DM}\,h^2 = \mathbb{C}(T_{\rm ev}) \begin{cases} \frac{1}{\pi^2}\,\sqrt{\frac{M_P}{m_{\rm in}}}\,m_{\rm DM} & \text{for } m_{\rm DM} < T^{\rm in}_{\rm BH}\,, \\ \frac{1}{64\,\pi^4}\left(\frac{M_P}{m_{\rm in}}\right)^{5/2}\,\frac{M_P^2}{m_{\rm DM}} & \text{for } m_{\rm DM} > T^{\rm in}_{\rm BH}\,, \end{cases} \tag{6.12}$$

with $\mathbb{C}(T_{\rm ev}) = \frac{s_0}{\rho_c}\,\frac{1}{\zeta}\,\frac{g_{X,H}}{g_{\star,H}}\,\frac{5}{g_{\star s}(T_{\rm evap})}\,\left(\frac{\pi^3\,g_\star(T_{\rm evap})}{5}\right)^{3/4}\,\sqrt{\frac{\mathcal{G}\,g_{\star,H}}{10640\,\pi}}$. It is worth mentioning that if we assume a PBH dominated era, then for majority of the parameter space the DM gets over-produced from PBH evaporation irrespective of their spins and only $m_{\rm DM} \gtrsim 10^{10}$ GeV can lead to right abundance for $m_{\rm in} \gtrsim 10^6$ g [96, 290]. DM over-production can also be controlled by choosing sufficiently light DM mass, but it is likely to face constraints from structure formation. In order not to spoil the structure formation, a DM candidate which is part of the thermal bath or produced from the thermal bath should have mass above a few keV (depending upon the details of the production mechanism) in order to give required free-streaming length of DM as constrained from Lyman-$\alpha$ flux-power spectra [25, 331, 332]. Such light DM of keV scale leads to a warm dark matter (WDM) scenario having free-streaming length in the intermediate range relative to that of cold and hot DM. If such light DM is also produced from PBH evaporation, it leads to a potential hot component in total DM abundance, tightly constrained by observations related to the CMB and baryon acoustic oscillation (BAO) leading to an upper bound on the fraction of this hot component with respect to the total DM, depending on the value of DM mass [259]. The lower bound on DM mass from Lyman-$\alpha$ can be found in [96, 112, 333]. As for the heavy DM case relic abundance has an inverse dependence on the DM mass, hence heavy DM leads to under-abundance. This is shown in the left panel Fig. 6.3, considering the DM to be of spin zero. The white region in the top right corner is where the DM is under abundant, while along the black dashed line right relic abundance is obtained, without considering any extra source of entropy injection after PBH evaporation. Now, for the simultaneous realization of both the observed DM relic density and the baryon asymmetry, $m_S$ and $m_{\rm DM}$ become connected through Eqn. (6.7) and (6.12). In the

right panel of Fig. 6.3, we show the contour satisfying both DM relic density and baryon asymmetry, considering $\epsilon_1 + \epsilon_2 = 0.1$. The range of $m_{\rm in}$ which varies along this contour is shown with different colours. For $m_{\rm in} \lesssim 2.5 \times 10^4$ g, DM mass becomes super-Planckian. On the other hand, for $m_{\rm in} \gtrsim 3.4 \times 10^7$ g, $m_S$ becomes less than $T^{\rm in}_{\rm BH}$ and hence $Y_B$ becomes independent of $m_S$ (cf. Eqn. (6.7)). Note that,the parameter space features same characteristic as in Fig. 6.1 because of the requirement of simultaneously satisfying right relic abundance and baryon asymmetry.

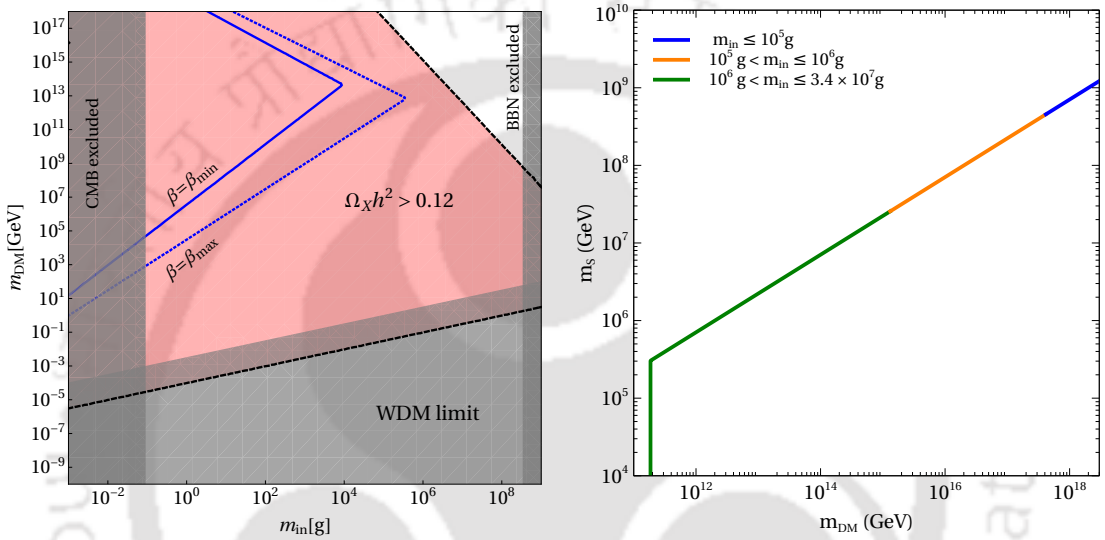


FIGURE 6.3: *Left:* The red coloured region of over-abundance for DM produced entirely from PBH evaporation. We also show the warm DM constraint, effective in the region of lower mass DM. Along the blue contours right relic abundance is produced considering gravitational UV freeze-in for lower (solid) and upper (broken) bound on $\beta$ [cf. Eqn. (2.15), (2.51) ]. Along the black dashed contour right abundance is obtained considering the entire DM is produced from PBH evaporation. *Right:* Viable parameter space satisfying relic density and baryon asymmetry in $m_{\rm DM} - m_S$ plane for a fixed $\epsilon_1 + \epsilon_2 = 0.1$ and scanned over a range of $m_{\rm in}$, shown with different colours.

Apart from PBH, pure gravitational production of DM can also take place from the 2-to-2 scattering of the bath particles via $s$-channel mediation of massless graviton, as discussed in section 5.4. Along the blue contours in the left panel of Fig. 6.3, correct DM abundance via gravitational UV freeze-in is obtained considering $T_{\rm rh} = T_{\rm in}$ and a spin-0 DM candidate. The two contours, shown via solid and dotted curves correspond to the lower and upper bound on $\beta$, following Eqn. (2.15), (2.51). To the left of each contours, DM is over-produced due to gravitational UV freeze-in. This shows, the region

of over-abundance corresponding to gravitational UV freeze-in overlaps with the region of over-abundance for DM production from PBH evaporation.

It should be noted that, we have considered a spin zero scalar to be the DM candidate in the above discussion and shown it to satisfy the correct relic abundance criteria, together with correct BAU produced from PBH evaporation, for superheavy DM masses. While the original model has a DM candidate $\psi$ provided its mass lies in the tiny window $m_p - m_e \leq m_\psi \leq m_p + m_e$ and its coupling to SM leptons and Higgs are forbidden by some additional symmetries. However, as the above discussion shows, such DM with mass around 1 GeV is likely to be over-produced for the PBH mass range and initial fraction ($\beta > \beta_{\rm crit}$) we are choosing to have desired baryogenesis and GW spectrum. In earlier works, for example [317], such light DM was found to be thermally over-produced requiring the non-thermal production from moduli decay. While non-thermal production of DM from a moduli dominated era can be controlled by suitable choice of couplings, this freedom no longer exists in a PBH dominated era due to democratic gravitational couplings to all particles. Therefore, we do not need to choose $\psi$ mass in the above-mentioned tiny window, it can be mass larger than proton mass and can also play some role in generating light neutrino masses via its coupling to SM leptons and Higgs, in a way similar to [322, 323].

## 6.5 Induced Gravitational Waves from PBH Density Fluctuations

There are several ways in which PBHs can be involved in the production of primordial gravitational waves, as discussed in chapter 2. We focus on the GW spectrum generated from PBH density fluctuations. Now, from the requirement of obtaining the observed baryon asymmetry $Y_B^{\rm obs}$, one can express $f_{\rm peak}$ and $\Omega_{\rm gw}^{\rm peak}$ (given by Eqn. (2.47) and (2.46)

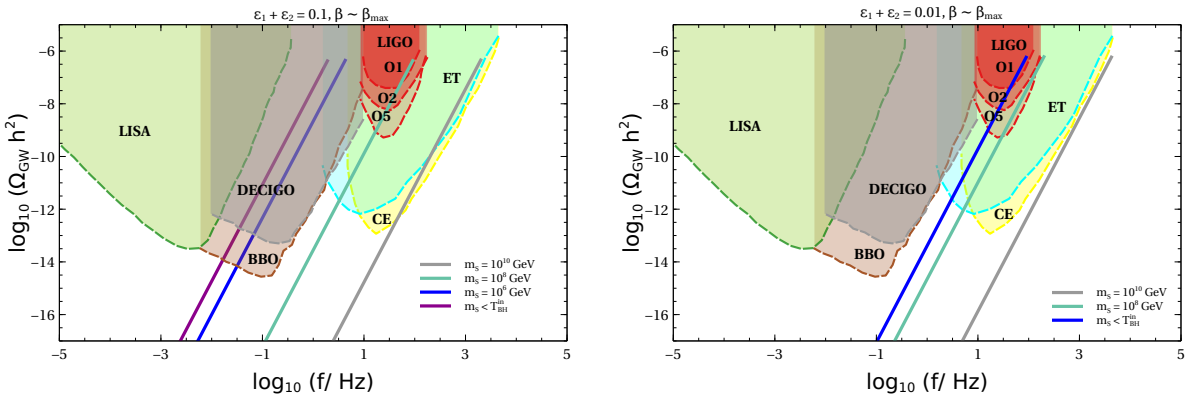


FIGURE 6.4: GW spectra induced from PBH density fluctuations, from the requirement of obtaining the observed baryon asymmetry $Y_B^{\rm obs}$, with $\epsilon_1 + \epsilon_2 = 0.1$ (left panel) and $\epsilon_1 + \epsilon_2 = 0.01$ (right panel). The experimental sensitivities of BBO [334–336], DECIGO [142, 143, 337], CE [139, 338], ET [144, 339–341], LISA [141] and aLIGO/VIRGO [139, 140, 342]. Here we use the sensitivity curves derived in Ref. [343] are shown as shaded regions of different colours.

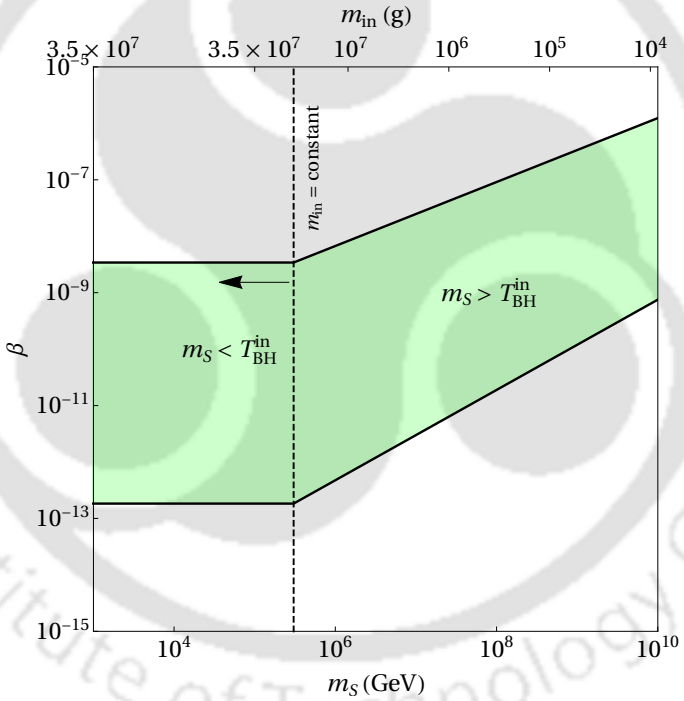


FIGURE 6.5: Bound on PBH initial fraction $\beta$ as a function of $m_S$, where $\epsilon_1 + \epsilon_2 = 0.1$. For each $m_S$ we also indicate the corresponding $m_{\rm in}$ in the upper horizontal axis that provides the right baryon asymmetry.

respectively) as a function of the baryogenesis scale $m_S$. Using Eqn. (6.7) for the PBH-dominated case, we arrive at

$$f^{\rm peak} \simeq \begin{cases} 4\times10^{-2}\,(\epsilon_1+\epsilon_2)^{-5/3}\ {\rm Hz} & \text{for } m_S < T^{\rm in}_{\rm BH}\,, \\ 2\times10^{-4}\,(\epsilon_1+\epsilon_2)^{-1/3}\left(\frac{m_S}{\rm GeV}\right)^{2/3}\ {\rm Hz} & \text{for } m_S > T^{\rm in}_{\rm BH}\,. \end{cases} \tag{6.13}$$

Similarly

$$\Omega_{\rm gw}^{\rm peak} \simeq \begin{cases} 7.8\times 10^{3}\left(\frac{\beta}{10^{-8}}\right)^{16/3}(\epsilon_1+\epsilon_2)^{68/9} & \text{for } m_S < T_{\rm BH}^{\rm in}\,, \\ 2.6\times 10^{14}\left(\frac{\beta}{10^{-8}}\right)^{16/3}(\epsilon_1+\epsilon_2)^{68/49}\left(\frac{m_S}{\rm GeV}\right)^{-136/45} & \text{for } m_S > T_{\rm BH}^{\rm in}\,. \end{cases} \tag{6.14}$$

From the above equations, it can be seen if the CP asymmetry parameters $\epsilon_1, \epsilon_2$ are fixed, the peak frequency $f_{\rm peak}$ is determined solely by the baryogenesis scale $m_S$. In addition, from the requirement of obtaining the observed DM relic, $m_S$ has one-to-one correspondence with the DM mass $m_{\rm DM}$ (as seen in Fig. 6.3). Now, for $m_S < T_{\rm BH}^{\rm in}$, the frequency is degenerate for all values of $m_S$. On the other hand, the peak amplitude depends also on the initial PBH fraction $\beta$, which remains a free parameter in our analysis.

In Fig. 6.4 , we show the GW spectra from PBH density fluctuations along with the current and future sensitivities of various GW experiments. In the left panel we fix $\epsilon_1 + \epsilon_2 = 0.1$ and as we keep on decreasing $m_S$, the peak frequency gets shifted to the left as expected (see Eqn. (6.13)). For $m_S < T_{\rm BH}^{\rm in}$, the spectrum becomes independent of $m_S$. Similar behavior is observed in the right panel for $\epsilon_1 + \epsilon_2 = 0.01$, with an overall shift towards higher frequency. This shift can be understood from Fig. 6.1, where the contours satisfying $Y_B^{\rm obs}$ for lower CP asymmetry values requires lower values of PBH mass, and hence corresponds to a higher peak frequency (cf. Eqn. (2.47)). We find that for $\epsilon_1 + \epsilon_2 \lesssim 0.001$, the peak frequency becomes out of reach of any planned GW experiments shown, even with $m_S < T_{\rm BH}^{\rm in}$. Note that in these plots we have chosen $\beta \sim \beta_{\rm max}$, where $\beta_{\rm max}$ corresponds to the upper bound given by Eqn. (2.51). While this maximal value of $\beta$ is consistent with dark radiation bound at the epoch of BBN, for some choice of parameters, the peak frequencies can fall within LIGO ballpark and hence can already be disfavoured by LIGO constraints [140].

The bounds on $\beta$ given by Eqn. (2.51), (2.15) can also be recast in terms of $m_S$, for fixed values of $\epsilon_1, \epsilon_2$. This is shown in Fig. 6.5, where we have fixed $\epsilon_1 + \epsilon_2 = 0.1$. Note that for $m_S < T_{\rm BH}^{\rm in}$, $m_{\rm in}$ is fixed from $Y_B^{\rm obs}$ (see Eqn. (6.7) and also Fig. 6.1) and hence the bounds on $\beta$ become independent of $m_S$. The shaded region in Fig. 6.5 represents the allowed range

| BP | $m_S$ (GeV) | $m_{\rm DM}$ (GeV) | $\epsilon_1+\epsilon_2$ | $m_{\rm in}(g)$ | $\log_{10}\beta$ | $\log_{10}\beta_c$ | GW experiment |
|---|---|---|---|---|---|---|---|
| BP1 | $10^6$ | $3\times10^{12}$ | 0.1 | $10^7$ | $-8.6$ | $-12.22$ | ET, DECIGO, BBO |
| BP2 | $10^7$ | $2.8\times10^{14}$ | 0.05 | $1.7\times10^6$ | $-8.2$ | $-11.45$ | CE, ET |
| BP3 | $3\times10^7$ | $2\times10^{17}$ | 0.01 | $10^5$ | $-7.3$ | $-10.22$ | LIGO O5, CE, ET |

TABLE 6.2: Some benchmark points (BP) of showing values of coloured scalar mass $m_S$, DM mass $m_{\rm DM}$, PBH mass fraction $\beta_c$, PBH mass $m_{\rm in}$ and the CP asymmetry parameter $\epsilon_1+\epsilon_2$, along with the GW experiments that can probe the peak of the induced GW spectrum.

of $\beta$ for different values of $m_S$. Similar pattern is observed for different values of $\epsilon_1$, $\epsilon_2$. By keeping $\beta$ within the allowed range, we provide some benchmark values in Table 6.2, along with the GW experiments which can probe the peak of the induced GW spectrum.

## 6.6 Conclusion

We have proposed a simple way of cogenesis of baryon and dark matter from PBH evaporation which can be tested via gravitational wave induced by PBH density fluctuations. Due to the presence of new heavy particles with baryon number violation, baryon asymmetry can be generated non-thermally due to out-of-equilibrium CP violating decay of a heavy coloured scalar, predominantly produced from PBH evaporation. The allowed parameter space in terms of PBH mass consistent with the non-thermal generation of the observed baryon asymmetry also leads to the production of superheavy DM with correct relic abundance. Assuming PBH to dominate the early Universe, we get one-to-one correspondence between DM mass and heavy coloured scalar mass responsible for baryogenesis. Since the induced GW spectrum also crucially depends upon PBH mass and initial fraction, we get very predictive GW spectrum at both ongoing and future experiments like LIGO, BBO, DECIGO, CE, ET etc. This is not possible in non-thermal leptogenesis from PBH scenarios where the requirement of PBH evaporation before sphaleron decoupling forces PBH mass to be much lighter leading to very high frequency induced GW out of reach from experiments. Since baryogenesis can occur at any temperature above the BBN epoch, contrary to the canonical baryogenesis via leptogenesis mechanism, one can have PBH as heavy as $\sim 10^6$ g, depending on the size of the CP-violation generated

from the decay of the new coloured scalars. We find, a common parameter space, satisfying both DM abundance and baryon asymmetry can be obtained entirely from PBH evaporation for PBHs within a mass range of $\sim 10^4 - 10^7$ g, where DM can be as heavy as $\sim 10^{12}$ GeV. Apart from such observable GW signatures of our cogenesis setup, the model can also have complementary signatures at collider as well as experiments searching for baryon number violation like neutron-antineutron oscillations.

# Chapter 7

# Conclusion and future outlook

To conclude, this thesis focuses on two currently unsolved problems: the origin of dark matter and the asymmetry between matter and antimatter in our Universe. While there have been many theoretical models to explain these two phenomena, a majority of which are based on standard mechanisms such as freeze-out, freeze-in, leptogenesis and so on, we build upon such mechanisms to explain these problems in the presence of non-standard cosmic epochs before BBN. This not only changes the parameter space of standard production regimes, but also leads to complementary indirect detection probes, mainly in the form of gravitational waves. Intriguingly, the thesis explores DM scenarios beyond the conventional WIMP paradigm, where the DM mass range and couplings are already tightly constrained from several DM search experiments. As a bonus, most of the setups we consider for our study can also accommodate tiny neutrino mass, which has been another long-standing puzzle in particle physics. Below, we briefly summarise the chapters of this thesis.

In chapter 3, we considered early matter domination because of a long-lived particle. Interestingly, in the kind of dark matter setups we consider, i.e. the keV scale warm dark matter and the Miracle-less WIMP dark matter, the need for such an early matter-dominated epoch naturally arises since DM is thermally overproduced in such scenarios. The DM relic abundance can be brought down by the decay of the long-lived matter field, which puts constraints on the model parameters such as DM mass and gauge couplings. In the case of Miracle-less WIMP, the presence of cosmic strings produces stochastic gravitational wave spectra with turning point frequencies having a one-to-one correspondence

with the DM mass, while being within the sensitivities of near-future GW experiments. The long-lived matter field, which is portrayed by one of the right-handed neutrinos present in the gauged $B - L$ setup for anomaly cancellation, predicts vanishingly small lightest neutrino mass. Hence, it provides a complementary detection prospect in neutrino experiments like KATRIN and neutrinoless double beta decays. In addition, leptogenesis can also be realised in such scenarios with the help of resonant enhancement. Chapter 4 focuses on early matter domination because of PBH, where the Hawking evaporation of PBH plays a role both in producing the dark matter/ baryon abundance and also diluting it. We considered the effect of PBH on the low-scale scotogenic model, and performed a detailed analysis considering both thermal and non-thermal productions of lepton asymmetry and dark matter. Solving the appropriate Boltzmann equations for the system, we found that with scalar inert doublet dark matter, which is constrained from collider searches, it is not possible to find a region of PBH parameters that can simultaneously affect DM genesis as well as leptogenesis. This is primarily because for PBH domination, DM production directly from PBH through Hawking evaporation leads to overabundance, unless DM is very light or superheavy leading to suppressed production. Hence, the only viable possibility considering PBH domination is that PBH evaporates earlier than the dark matter freeze-out epoch, such that the final relic is dictated solely by the thermal component. Interestingly, we see that this condition itself constrains the DM mass and the PBH parameters. To explore the possibility of cogenesis further, we have also considered the scenario where leptogenesis occurs due to $N_2$ decay while the lightest right-handed neutrino $N_1$ is the DM candidate. Here, the scale of leptogenesis is pushed higher, but the gauge singlet nature of $N_1$ allows us to consider it in the light mass window around few MeVs, evading the overabundance region. $N_1$ in this scenario can also be produced via freeze-in, and we have a scenario of mixed DM with both hot and warm/cold components which has constraints from astrophysical bounds. We then considered the generation of asymmetric DM from PBH, motivated from the cosmic coincidence problem. We found that for ultralight PBH of $\sim 0.1 - 10$ g, it is possible to produce the required asymmetry simultaneously in the visible and dark sectors, through

the decay of a heavy RHN produced from PBH, with the non-thermal production dominating over the thermal. While this requires a heavy RHN scale of $\mathcal{O}(10^{12})$ GeV, DM with a wide mass range from a few GeV upto $\sim 10^5$ GeV becomes possible, depending on the Yukawa couplings of RHN to DM.

Next, in chapter 5, we consider a scenario of purely gravitational DM from PBH, which is motivated by the fact that all the pieces of evidence of DM found so far are purely of gravitational origin. As also mentioned in the preceding chapters, DM produced directly from PBH in the light mass regime of keV-PeV gets overproduced. Hence, we naturally require another period of matter domination to bring down the DM abundance, which is provided by a long-lived particle, leading to multiple matter dominated eras in the early Universe. Satisfying the criteria of successful leptogenesis in the same setup further constrains the DM mass to the MeV-GeV ballpark, with PBH mass $\lesssim 5$ g. Finally, in chapter 6, we consider a framework of direct baryogenesis from PBH at a low scale, from the CP violating decay of a colored scalar produced from PBH. This has the immediate advantage that PBH with comparatively heavier mass ranges upto $\sim 10^7$ g, evaporating after the sphaleron scale now becomes allowed. Dark matter in the superheavy mass regime which is not overproduced from PBH evaporation, can also be realized in this setup. The DM mass and the baryogeneis scale becomes connected via the required PBH mass to produce the observed baryon asymmetry and dark matter relic abundance. Interestingly, here because of the higher PBH mass, the DM mass and baryogenesis scale can also be probed with the help of gravitational wave spectra from PBH density fluctuations, where the peak frequency and amplitude are under the sensitivity of near future gravitational wave experiments. In addition, because of the presence of the colored scalars, the model also has complementary signatures in collider experiments. Moreover, because of the presence of baryon number violation in the setup, experiments like neutron-antineutron oscillations can also probe or constrain this scenario.

This thesis paves the way for several problems to look upon in the future. While the only non-standard epochs considered here are due to early matter domination, it would

be interesting to pursue dark matter phenomenology and baryogenesis with other possible cosmic backgrounds such as that of kination, early dark energy etc., and its connection to particle physics setups and observational signatures. The impact of such scenarios on the stochastic gravitational wave spectrum from early Universe sources such as PBH, cosmic strings, inflation etc. is also worth pursuing. In addition, the source of early matter domination because of some other sources such as inflaton can also be looked upon. We have also remained agnostic about the formation mechanisms of PBH and considered a monochromatic PBH mass function. In a UV complete particle physics framework, formation of PBH with a realistic mass function and initial fraction can also be investigated together with its consequence for production of DM, baryon asymmetry and stochastic GW background. We leave such analysis considering other mass functions of PBH and formation mechanisms for future studies.

# Appendix A

# Conversion of lepton asymmetry to baryon asymmetry

Here, we derive the sphaleron conversion factor given by Eqn. (1.39) of chapter 1, and used throughout this thesis in the leptogenesis calculations. We closely follow Ref. [48]. At high temperatures before the electroweak scale, the asymmetries in the number densities of particles and antiparticles of a relativistic species 'i' can be written in terms of its chemical potential $\mu_i$ as

$$\frac{n_i - n_{\bar{i}}}{s} = \frac{15 g_i}{4\pi^2 g_{*s}} \frac{\mu_i}{T} \begin{cases} 2 & \text{for bosons,} \\ 1 & \text{for fermions.} \end{cases} \tag{A.1}$$

Let us consider the SM to have $N_f$ generations of fermions and $N_{\mathbf{H}}$ Higgs doublets. For a reaction in chemical equilibrium through the electroweak interactions, one can equate the chemical potentials of the particles in the initial and final states. The relevant relations

are

$$\mu_W = \mu_{\mathbf{H}^-} + \mu_{\mathbf{H}^0}\,, \text{ for } W^- \leftrightarrow \mathbf{H}^- + \mathbf{H}^0\,, \tag{A.2}$$

$$\mu_W = -\mu_{u_L} + \mu_{d_L}\,, \text{ for } W^- \leftrightarrow \overline{u}_L + d_L\,, \tag{A.3}$$

$$\mu_W = -\mu_j + \mu_{e_{j,L}}\,, \text{ for } W^- \leftrightarrow \overline{\nu}_{j,L} + e_{j,L}\,, \tag{A.4}$$

$$\mu_{\mathbf{H}^0} = -\mu_{u_L} + \mu_{u_R}\,, \text{ for } \mathbf{H}^0 \leftrightarrow \overline{u}_L + u_R\,, \tag{A.5}$$

$$\mu_{\mathbf{H}^0} = \mu_{d_L} - \mu_{d_R}\,, \text{ for } \mathbf{H}^0 \leftrightarrow d_L + \overline{d}_R\,, \tag{A.6}$$

$$\mu_{\mathbf{H}^0} = \mu_{e_{j,L}} - \mu_{e_{j,R}}\,, \text{ for } \mathbf{H}^0 \leftrightarrow e_{j,L} + \overline{e}_{j,R}\,. \tag{A.7}$$

Here, $j = 1$ to $N_f$ and for the SM neutrinos, and we write $\mu_{\nu_{j,L}} = \mu_j$. L(R) denotes left(right) handedness. $\mathbf{H}^0_k$, $\mathbf{H}^\pm_k$ denotes components of the Higgs doublets with $k = 1$ to $N_{\mathbf{H}}$. Now, sphaleron processes can create left-handed fermions from the vacuum, which gives us

$$N_f(\mu_{uL} + 2\mu_{dL}) + \sum_j \mu_j = 0. \tag{A.8}$$

Using Eqn. (A.1), the baryon, lepton and charge comoving number densities can be written in terms of the chemical potentials as

$$B \equiv \frac{N_f}{T}(\mu_{uL} + \mu_{uR} + \mu_{dL} + \mu_{dR})\,, \tag{A.9}$$

$$L \equiv \frac{1}{T}\sum_j(\mu_j + \mu_{jL} + \mu_{jR})\,, \tag{A.10}$$

$$Q \equiv 2\frac{N_f}{T}(\mu_{u_L} + \mu_{u_R}) - \frac{N_f}{T}(\mu_{dL} + \mu_{dR}) - \frac{1}{T}\sum_j(\mu_{jL} + \mu_{jR}) - 4\frac{\mu_W}{T} - 2\frac{N_{\mathbf{H}}}{T}\mu_{\mathbf{H}^-}\,. \tag{A.11}$$

The chemical potential of the gauge bosons vanishes before the electroweak symmetry breaking, and hence $\mu_W = 0$. In addition, we have $Q = 0$. Using Eqns. (A.2)-(A.11), we

arrive at

$$B \equiv 4N_f \frac{\mu_{u_L}}{T}\,, \tag{A.12}$$

$$L \equiv -\frac{14N_f^2 + 9N_f N_{\mathbf{H}}}{2N_f + N_{\mathbf{H}}} \frac{\mu_{u_L}}{T}\,. \tag{A.13}$$

From the above two equations, we get the relation

$$B = \frac{8N_f + 4N_{\mathbf{H}}}{22N_f + 13N_{\mathbf{H}}}(B - L)\,. \tag{A.14}$$

# Appendix B

# Inflationary predictions for the gauged $B-L$ model

Here we briefly discuss the dynamics of inflation in view of the most recent data from combination of Planck and BICEP/Keck [344], which is relevant for chapter 3 for the case of keV DM. For a detailed discussion of inflation in the minimal B-L model, we refer to Ref. [345, 346]. We identify the real part ($\phi$) of singlet scalar field $\Phi$ as the inflaton. Along with the renormalisable potential in Eqn. (3.4), we also assume the presence of non-minimal coupling of $\Phi$ to gravity. The potential that governs the inflation is given by

$$V_{\rm Inf}(\phi) = \frac{\lambda_2}{4}\phi^4 + \frac{\xi}{2}\phi^2 R, \tag{B.1}$$

where $R$ represents the Ricci scalar and $\xi$ is a dimensionless coupling of singlet scalar to gravity. We have neglected the contribution of $v_{BL}$ in Eqn. (B.1) by considering it to be much lower than the Planck mass scale $(M_P)$. With this form of potential, the action for $\phi$ in Jordan frame is expressed as,

$$S_J = \int d^4x\sqrt{-g}\left[-\frac{M_P^2}{2}\Omega(\phi)^2 R + \frac{1}{2}(D_\mu\phi)^\dagger(D^\mu\phi) - \frac{\lambda_2}{4}\phi^4\right], \tag{B.2}$$

where $\Omega(\phi)^2 = 1 + \frac{\xi\phi^2}{M_P^2}$, $g$ is the spacetime metric in the $(-,+,+,+)$ convention, $D_\mu\phi$ stands for the covariant derivative of $\phi$ containing couplings with the gauge bosons which reduces to the normal derivative $D_\mu \to \partial_\mu$ (since during inflation, the SM and BSM fields

except the inflaton are non-dynamical).

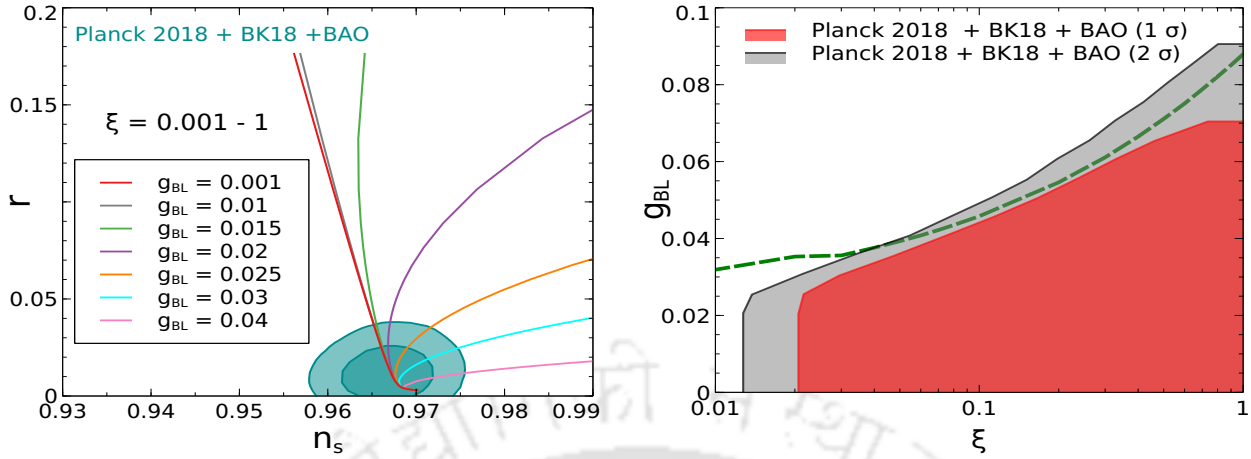


FIGURE B.1: *Left panel*: The predictions of the $B-L$ inflation in $n_s - r$ plane varying $\xi$ for different $g_{BL}$ values have been presented. The allowed $1\sigma$ and $2\sigma$ contours in the same plane from the most recent Planck 2018+BICEP/Keck analysis [344] are also included. *Right panel*: We show the favored region in $\xi - g_{BL}$ plane satisfying the $1\sigma$ and $2\sigma$ bounds as provided by Planck 2018+BICEP/Keck data. The green dashed line demonstrates the upper bound on $g_{BL}$ originating from appearance of local minimum along the inflationary trajectory.

Following the standard prescription, we use the following conformal transformation to write the action $S_J$ in the Einstein frame [347, 348] as

$$\hat{g}_{\mu\nu} = \Omega^2 g_{\mu\nu}, \quad \sqrt{-\hat{g}} = \Omega^4 \sqrt{-g}, \tag{B.3}$$

so that it resembles a regular field theory action of minimal gravity. In the above equation, $\hat{g}$ represents the metric in the Einstein frame. Furthermore, to make the kinetic term of the inflaton appear canonical, we transform the $\phi$ by

$$\frac{d\chi}{d\phi} = \sqrt{\frac{\Omega^2 + \frac{6\xi^2\phi^2}{M_P^2}}{\Omega^4}} = Z(\phi), \tag{B.4}$$

where $\chi$ is the canonical field. Using these inputs, the inflationary potential in the Einstein frame can be written as,

$$V_E(\phi(\chi)) = \frac{V_J(\phi(\chi))}{\left(\Omega(\phi(\chi))\right)^4} = \frac{1}{4}\frac{\lambda_2\phi^4}{\left(1+\frac{\xi\phi^2}{M_P^2}\right)^2}, \tag{B.5}$$

where $V_J(\phi)$ is identical to $V_{\rm Inf}(\phi)$ in Eqn. (B.1). We then make another redefinition: $\Phi = \frac{\phi}{\sqrt{1+\frac{\xi\phi^2}{M_P^2}}}$ and reach at a much simpler from of $V_E$ given by

$$V_E(\Phi) = \frac{1}{4}\lambda_2\Phi^4. \tag{B.6}$$

Note that for an accurate analysis, one should work with renormalisation group (RG) improved potential and in that case, $\lambda_2$ in Eqn. (B.6) will be function of $\Phi$ such that,

$$V_E(\Phi) = \frac{1}{4}\lambda_2(\Phi)\Phi^4. \tag{B.7}$$

One can notice that the inflaton field $\Phi$ $(= \phi/\sqrt{1+\frac{\xi\phi^2}{M_P^2}})$ in Eqn. (B.7) is non-canonical. Hence we redefine the slow roll parameters as functions of the non-canonical field $\Phi$ and arrive at [346] ,

$$\epsilon(\Phi) = \frac{M_P^2}{2Z(\Phi)^2}\left(\frac{V_E'(\Phi)A(\Phi)}{V_E(\Phi)}\right)^2, \tag{B.8}$$

$$\eta(\Phi) = \frac{M_P^2}{Z(\Phi)^2}\left(\frac{V_E''(\Phi)A(\Phi)^2}{V_E(\Phi)} + \frac{V_E'(\Phi)B(\Phi)}{V_E(\Phi)}\right), \tag{B.9}$$

where $'$ indicates the differentiation of the relevant quantity *w.r.t.* $\Phi$ and

$$A(\Phi) = \left(1-\frac{\xi\Phi^2}{M_P^2}\right)^{3/2}, \tag{B.10}$$

$$B(\Phi) = A(\Phi)A'(\Phi) - \frac{Z'(\Phi)A(\Phi)^2}{Z(\Phi)}. \tag{B.11}$$

The number of e-folds ($N_e$) is given by

$$N_e = \int_{\Phi_t}^{\Phi_{\rm end}} \frac{Z(\Phi)^2 V_E(\Phi)}{V_E'(\Phi)A(\Phi)^2}\frac{d\Phi}{M_{\rm P}} \tag{B.12}$$

where $\Phi_t$ and $\Phi_{\rm end}$ are the inflaton field values at horizon exit and end of inflation respectively.

Using these expressions, we obtain the predictions for the inflationary observables

namely the magnitude of spectral index ($n_s = 1 - 6\epsilon + 2\eta$) and tensor to scalar ratio ($r \sim 16\epsilon$). We also consider the number of e-folds ($N_e$) as 60.

The full set of one loop renormalisation group evolution (RGE) equations of the relevant parameters associated with the inflationary dynamics can be found in [346]. We consider a diagonal RH neutrino mass matrix with the hierarchy $M_{N_1}, M_{N_2} \ll M_{N_3}$ [1]. This implies $Y_{N_1}, Y_{N_2} \ll Y_{N_3}$ where $M_{N_i} = \frac{Y_{N_i} v_{BL}}{2}$. A simplified form for the RGE equation of $\lambda_2$ can be written by assuming $Y_{N_3}, g_{BL} \gg \lambda_2, \lambda_3$ leading to the following beta function,

$$\beta_{\lambda_2} \simeq 96 g_{BL}^4 - Y_{N_3}^4. \tag{B.13}$$

Below we provide the three important conditions to realise a successful RGE improved inflation in minimal gauged $B-L$ model.

• In general, for $\xi \lesssim 1$, the self-quartic coupling of inflaton must be very small in order to be in agreement with the experimental bounds on inflationary observables [349]. Since $\lambda_2$ is very small, any deviation of $\beta_{\lambda_2}$ from zero (due to larger $g_{BL}$ and $Y_{N_3}$), if sufficient, may cause sharp changes in $\lambda_2$ value from its initial magnitude during the RGE running. This may trigger unwanted instability to the inflationary potential [173, 346]. Therefore keeping the $\beta_{\lambda_2}$ in the vicinity of zero during inflation is a desired condition for successful inflation. To ensure $\beta_{\lambda_2} \sim 0$, the equality $\Delta = 96 g_{BL}^4 - Y_{N_3}^4 \sim 0$ needs to be maintained.

• In addition to the stability ($\beta_{\lambda_2} \sim 0$) confirmation, the inflationary potential should also be monotonically increasing function of the inflaton field value which implies $M_P \frac{d\beta_{\lambda_2}}{d\Phi} > 0$ during inflation. It is reported in [173, 346] that with the increase of $g_{BL}$, a local minimum appears (due to the violation of $M_P \frac{d\beta_{\lambda_2}}{d\Phi} > 0$) within the inflationary trajectory, which can stop the inflaton from rolling. This poses an upper bound on the size of $B-L$ gauge coupling.

• Finally, another constraint on $g_{BL}$ comes from the criteria that the inflationary predictions (*e.g.* spectral index and tensor to scalar ratio) stay within the $1-\sigma$ allowed range

[1] This choice is motivated from the fact that a heavier RH neutrino assists in obtaining larger amount of late entropy production and thus more effective in diluting the DM relic without violation the BBN bound.

as provided by Planck+BICEP experiment. This particular bound on $g_{BL}$ is stronger than the one arising due to appearance of a local minimum along the inflationary trajectory as we shall show in a while.

Next, we use the standard definitions of slow roll parameters ($\epsilon$ and $\eta$) [350] while calculating the magnitude of spectral index ($n_s = 1 - 6\epsilon + 2\eta$) and tensor to scalar ratio ($r \sim 16\epsilon$). We consider the number of e-folds ($N_e$) as 60. We also impose the condition $\Delta = 0$ at the scale of horizon exit of inflation while estimating the inflationary observables.

We perform a numerical scan over $g_{BL}$ and $\xi$ to estimate the inflationary observables $n_s$ and $r$ considering $\Delta = 0$. We have observed that the factor $\lambda_2$ does not alter the slow roll parameters, rather it is fixed by the measured value of scalar perturbation spectrum ($P_S = 2.4 \times 10^{-9}$) at horizontal exit of inflaton. It also turns out that the value of $r$ does not change much with the variation of $g_{BL}$ for a constant value of $\xi$ since $\beta_{\lambda_2}, \Delta \sim 0$ at inflationary energy scale. Contrary to this, value of $n_s$ is quite sensitive to $g_{BL}$ as it involves second order derivative of the inflationary potential. In the left panel of Fig. B.1, we show the $n_s - r$ predictions for different $g_{BL}$ lines (with varying $\xi$) and check its viability against the improved version of Planck+BICEP/Keck data [344] published in 2021. In the right panel of Fig. B.1, we constrain the $\xi - g_{BL}$ plane by using the criteria of yielding correct values for $n_s$ and $r$ allowed by the combined Planck+BICEP/Keck data [344]. The maximum permitted value (green dashed line) of $g_{BL}$ as function of $\xi$ is also depicted in the same figure which corresponds to non-appearance of any local minimum along the inflationary trajectory. The parameter $\lambda_2$ at inflationary energy scale can be fixed with the observed value of scalar perturbation spectrum as earlier mentioned. As an example, we find $\lambda_2^{\rm inf} \simeq \mathcal{O}(10^{-10})$ considering $\xi = 1$. We have used this particular reference point in our DM analysis.

# Appendix C

# Davidson-Ibarra bound in scotogenic model

Here, we briefly discuss about the Davidson-Ibara bound in the Scotogenic Model studied in chapter 4. From Eqn. (1.45) of chapter 1, one can see that we clearly do not have enough freedom to increase the CP asymmetry except by increasing the mass of the right-handed neutrino $N_1$. This bound is very strong and not weakened significantly even if one considers moderately hierarchical right handed neutrino spectrum [73]. For the correct order of baryon asymmetry to be generated, given the sphaleron conversion factor, one needs $\mid \epsilon_1 \mid > 10^{-6}$ which further implies $M_1 > 10^9$ GeV.

On the other hand, the Davidson-Ibarra bound for the scotogenic model can be found by using the simplified expression for corresponding CP asymmetry parameter (in hierarchical right handed neutrino limit) [239]

$$\mid \epsilon_1 \mid \lesssim \frac{3\pi}{4\lambda_5 v^2} \xi_3 M_1 (m_3 - m_1), \tag{C.1}$$

where

$$\xi_i = \left( \frac{1}{8} \frac{M_i^2}{m_{H_0}^2 - m_{A_0}^2} \left[ L(m_{H_0}^2) - L(m_{A_0}^2) \right] \right)^{-1}. \tag{C.2}$$

The values of $\xi_i$ are of the order of unity for most of the parameter space of interest. From equation (C.1), one can see that by choosing small values of $\lambda_5$ the required CP asymmetry can be generated even with small $M_1 \sim \mathcal{O}(10$ TeV). The reason for the appearance of the coupling $\lambda_5$ in the Davidson-Ibarra bound is because of the radiative mass generation of

the neutrinos through the quartic coupling of Higgs and inert doublet $\eta$. By choosing a small value of $\lambda_5$ one can have large values of the Yukawa couplings which satisfy the light neutrino data and also it makes the CP asymmetry parameter large. However, in the usual type I seesaw model smaller Yukawa is needed to satisfy the light neutrino data and therefore the asymmetry remains under-abundant unless $M_1 > 10^9$ GeV.

# Appendix D

# Thermally-Averaged cross-section with different temperatures

Here, we derive the thermally-averaged cross-section for two species with different temperatures, closely following Ref. [105]. This is relevant for the chapters on PBH (especially chapter 4) to ensure that the evaporation products from PBH carrying Hawking temperature do not thermalise with the SM bath. The thermally averaged cross-section is defined as

$$\langle \sigma v_{\rm mol} \rangle = \frac{\int \sigma \, v_{\rm mol} \, e^{-E_1/T_1} \, e^{-E_2/T_2} \, d^3p_1 \, d^3p_2}{\int \, e^{-E_1/T_1} \, e^{-E_2/T_2} \, d^3p_1 \, d^3p_2} \, . \tag{D.1}$$

The momentum-space volume element is given by [22]

$$d^3p_1 \, d^3p_2 = 4\,\pi \, p_1 \, dE_1 \, 4\,\pi \, p_2 \, dE_2 \, \frac{1}{2} \, d\cos\theta \, . \tag{D.2}$$

We consider mass of one of the particles to be negligible, and then perform the following variable transformation:

$$\begin{aligned}\zeta_+ &\equiv \frac{E_1}{T_1} + \frac{E_2}{T_2} \\ \zeta_- &\equiv \frac{E_1}{T_1} - \frac{E_2}{T_2} \\ s &\simeq M_1^2 + 2(E_1\,E_2 - p_1\,p_2\,\cos\theta)\,. \end{aligned} \tag{D.3}$$

Using the Jacobian transformation

$$\mathcal{J} = \frac{1}{2}\det\begin{pmatrix} T_1 & T_1 & 0 \\ T_2 & -T_2 & 0 \\ 0 & 0 & -\frac{1}{p_1\,p_2} \end{pmatrix} = \frac{T_1\,T_2}{4\,p_1\,p_2}\,, \tag{D.4}$$

the volume element turns out to be

$$d^3p_1\,d^3p_2 = \frac{1}{2}\,16\pi^2\,p_1\,p_2\,E_1\,E_2\,\mathcal{J}\,d\zeta_+\,d\zeta_-\,ds = 2\pi^2\,E_1\,E_2\,T_1\,T_2\,d\zeta_+\,d\zeta_-\,ds\,. \tag{D.5}$$

Now, the viable integration region: $E_1 \geq M_1\,, E_2 \geq M_1\,, |\cos\theta| \leq 1$ can be translated to the integration limits on the new variables as

$$\begin{aligned} |\cos\theta| &= \frac{M_1^2 + 2\,E_1\,E_2 - s}{2\,p_1\,p_2} = \frac{2s - 2M_1^2 + T_1\,T_2\,(\zeta_-^2 - \zeta_+^2)}{T_2\,(\zeta_- - \zeta_+)\sqrt{T_1^2\,(\zeta_+ + \zeta_-)^2 - 4\,M_1^2}} \\ \implies & \frac{M_1^2\,T_2^2\,\zeta_+ - \sqrt{T_2\,(s - M_1^2)^2\,\left[M_1^2\,(T_1 - T_2) + T_1\,(T_1\,T_2\,\zeta_+^2 - s)\right]}}{T_2\,\left[M_1^2\,(T_2 - T_1) + sT_1\right]} \leq \zeta_- \\ \leq & \frac{M_1^2\,T_2^2\,\zeta_+ + \sqrt{T_2\,(s - M_1^2)^2\,\left[M_1^2\,(T_1 - T_2) + T_1\,(T_1\,T_2\,\zeta_+^2 - s)\right]}}{T_2\,\left[M_1^2\,(T_2 - T_1) + sT_1\right]}\,, \end{aligned} \tag{D.6}$$

where by demanding the expression inside the square root in the above equation to be real, we obtain

$$|\zeta_+| \geq \sqrt{\frac{s\,T_1 + M_1^2\,(T_2 - T_1)}{T_1^2\,T_2}}\,. \tag{D.7}$$

Now, the numerator of Eqn. (D.1) reads

$$\begin{aligned}&\int \sigma v_{\rm mol}\, e^{-\zeta_+}\, 2\pi^2\, E_1\, E_2\, T_1\, T_2\, d\zeta_+\, d\zeta_-\, ds \\ &= 2\,\pi^2\, T_1\, T_2 \int_{M_1^2}^{\infty} ds \int_{\zeta_+^{\rm min}}^{\infty} d\zeta_+\, \sigma \left[\frac{s}{2}\sqrt{1-\frac{2\,M_1^2}{s}+\frac{M_1^4}{s^2}}\right] \mathcal{G}(s,\zeta_+ \ldots)\, e^{-\zeta_+}\,, \end{aligned} \tag{D.8}$$

where $\mathcal{G}(s,\zeta_+ \ldots) \equiv (\zeta_-^{\rm max} - \zeta_-^{\rm min})$ is obtained from Eqn. (D.6) and $\zeta_+^{\rm min}$ comes from Eqn. (D.7).

The denominator can similarly be written as

$$\int d^3p_1\, d^3p_2\, e^{-(E_1/T_1+E_2/T_2)} = 32\,\pi^2 M_1^2\, T_1\, T_2^3 K_2\left(\frac{M_1}{T_1}\right). \tag{D.9}$$

Therefore, the final expression turns out

$$\langle\sigma v\rangle = \frac{1}{16\,M_1^2\,T_2^2}\,\frac{1}{K_2(M_1/T_1)}\int_{M_1^2}^{\infty} ds \int_{\zeta_+^{\rm min}}^{\infty} d\zeta_+\, \sigma\left[\frac{s}{2}\sqrt{1-\frac{2\,M_1^2}{s}+\frac{M_1^4}{s^2}}\right](\zeta_-^{\rm max}-\zeta_-^{\rm min})\, e^{-\zeta_+}\,, \tag{D.10}$$

where $\zeta_+^{\rm min}$ can be obtained from Eqn. (D.7). We also verify that the above expression reproduces Eq.(B13) of Ref. [105] upon considering both the initial state particles to be massive with degenerate masses.

# Appendix E

# Lyman-$\alpha$ Constraint

Here, we derive the constraint from Lyman-$\alpha$ observations on gravitational DM produced from PBH, which has been used in chapters 5, 6. Due to their large initial momentum, DM particles could have a large free-streaming length leading to a suppression on the structure formation at small scales. In the present scenario where DM has no interactions with the SM or with itself, the DM momentum simply redshifts, and its value $p_0$ at present is [96]

$$p_0 = \frac{a_{\rm evap}}{a_0}\, p_{\rm evap} \simeq \frac{a_{\rm evap}}{a_{\rm eq}} \frac{\Omega_R}{\Omega_m} \langle E_{\rm evap} \rangle = \langle E_{\rm eq} \rangle \frac{\Omega_R}{\Omega_m}\,, \tag{E.1}$$

with

$$\langle E_{\rm eq} \rangle = \langle E_{\rm evap} \rangle \frac{a_{\rm evap}}{a_{\rm eq}} \approx \frac{T_{\rm BH}^{\rm in}}{\xi} \frac{T_{\rm eq}}{T_{\rm evap}} \left[\frac{g_{*s}(T_{\rm eq})}{g_{*s}(T_{\rm evap})}\right]^{\frac{1}{3}}\,, \tag{E.2}$$

where in the last line we have assumed entropy injection from PBH evaporation at $T = T_{\rm evap}$ to matter-radiation equality at $T = T_{\rm eq}$ as $\xi \left(sa^3\right)_{\rm evap} = \left(sa^3\right)_{\rm eq}$ [112]. Note that the average kinetic energy of the emitted particles depend on the Hawking temperature, and is given by $\langle E_{\rm evap} \rangle = 6\, T_{\rm BH}^{\rm in}$ [96]. However, a more refined calculation shows the factor 6 to be approximately 1.3 [112]. A lower bound on the DM mass can be obtained from the upper bound on a typical velocity of warm DM at the present time. Taking $v_{\rm DM} \lesssim 1.8 \times 10^{-8}$ [112] for $m_{\rm DM} \simeq 3.5$ keV [25], we obtain

$$m_{\rm DM} \gtrsim 10^4 \langle E_{\rm eq} \rangle \equiv 10^4 \frac{T_{\rm eq}}{\xi} \frac{T_{\rm BH}^{\rm in}}{T_{\rm evap}} \left[\frac{g_{*s}(T_{\rm eq})}{g_{*s}(T_{\rm evap})}\right]^{\frac{1}{3}} \simeq 2 \times 10^4 \frac{T_{\rm eq}}{\xi} \sqrt{\frac{m_{\rm BH}^{\rm in}}{M_{\rm pl}}} \left[\frac{g_{*s}(T_{\rm eq})}{g_{*s}(T_{\rm evap})}\right]^{\frac{1}{3}}\,, \tag{E.3}$$

where $a_{\rm eq} \equiv \frac{\Omega_R}{\Omega_m} \simeq 1.8 \times 10^{-4}$ and $T_{\rm eq} \simeq 0.75$ eV.

# Bibliography


1. Glashow, S. L. Partial Symmetries of Weak Interactions. *Nucl. Phys.* **22,** 579–588 (1961).

2. Weinberg, S. A Model of Leptons. *Phys. Rev. Lett.* **19,** 1264–1266 (1967).

3. Englert, F. & Brout, R. Broken Symmetry and the Mass of Gauge Vector Mesons. *Phys. Rev. Lett.* **13** (ed Taylor, J. C.) 321–323 (1964).

4. Higgs, P. W. Broken Symmetries and the Masses of Gauge Bosons. *Phys. Rev. Lett.* **13** (ed Taylor, J. C.) 508–509 (1964).

5. Guralnik, G. S., Hagen, C. R. & Kibble, T. W. B. Global Conservation Laws and Massless Particles. *Phys. Rev. Lett.* **13** (ed Taylor, J. C.) 585–587 (1964).

6. Zwicky, F. Die Rotverschiebung von extragalaktischen Nebeln. *Helv. Phys. Acta* **6,** 110–127 (1933).

7. Rubin, V. C. & Ford Jr., W. K. Rotation of the Andromeda Nebula from a Spectroscopic Survey of Emission Regions. *Astrophys. J.* **159,** 379–403 (1970).

8. Rubin, V. C., Thonnard, N. & Ford Jr., W. K. Rotational properties of 21 SC galaxies with a large range of luminosities and radii, from NGC 4605 /R = 4kpc/ to UGC 2885 /R = 122 kpc/. *Astrophys. J.* **238,** 471 (1980).

9. Markevitch, M. *et al.* Direct constraints on the dark matter self-interaction cross-section from the merging galaxy cluster 1E0657-56. *Astrophys. J.* **606,** 819–824. arXiv: astro-ph/0309303 (2004).

10. Clowe, D., Gonzalez, A. & Markevitch, M. Weak lensing mass reconstruction of the interacting cluster 1E0657-558: Direct evidence for the existence of dark matter. *Astrophys. J.* **604,** 596–603. arXiv: astro-ph/0312273 (2004).

11. Clowe, D. *et al.* A direct empirical proof of the existence of dark matter. *Astrophys. J. Lett.* **648,** L109–L113. arXiv: astro-ph/0608407 (2006).

12. Spergel, D. N. *et al.* Wilkinson Microwave Anisotropy Probe (WMAP) three year results: implications for cosmology. *Astrophys. J. Suppl.* **170,** 377. arXiv: astro-ph/0603449 (2007).

13. Aghanim, N. *et al.* Planck 2018 results. V. CMB power spectra and likelihoods. *Astron. Astrophys.* **641,** A5. arXiv: 1907.12875 [astro-ph.CO] (2020).

14. Aghanim, N. *et al.* Planck 2018 results. VI. Cosmological parameters. *Astron. Astrophys.* **641.** [Erratum: Astron.Astrophys. 652, C4 (2021)], A6. arXiv: 1807.06209 [astro-ph.CO] (2020).

15. Eisenstein, D. J. *et al.* Detection of the Baryon Acoustic Peak in the Large-Scale Correlation Function of SDSS Luminous Red Galaxies. *Astrophys. J.* **633,** 560–574. arXiv: astro-ph/0501171 (2005).

16. Abazajian, K. N. *et al.* The Seventh Data Release of the Sloan Digital Sky Survey. *Astrophys. J. Suppl.* **182,** 543–558. arXiv: 0812.0649 [astro-ph] (2009).

17. Jenkins, A. *et al.* Evolution of structure in cold dark matter universes. *Astrophys. J.* **499,** 20. arXiv: astro-ph/9709010 (1998).

18. Dodelson, S. *Modern Cosmology* ISBN: 978-0-12-219141-1 (Academic Press, Amsterdam, 2003).

19. Lin, T. Dark matter models and direct detection. *PoS* **333,** 009. arXiv: 1904.07915 [hep-ph] (2019).

20. Arcadi, G. *et al.* The waning of the WIMP? A review of models, searches, and constraints. *Eur. Phys. J. C* **78,** 203. arXiv: 1703.07364 [hep-ph] (2018).

21. Kolb, E. W. & Turner, M. S. *The Early Universe* ISBN: 978-0-201-62674-2 (1990).

22. Gondolo, P. & Gelmini, G. Cosmic abundances of stable particles: Improved analysis. *Nucl. Phys. B* **360,** 145–179 (1991).

23. Edsjo, J. & Gondolo, P. Neutralino relic density including coannihilations. *Phys. Rev. D* **56,** 1879–1894. arXiv: hep-ph/9704361 (1997).

24. Baumann, D. *Cosmology* ISBN: 978-1-108-93709-2, 978-1-108-83807-8 (Cambridge University Press, July 2022).

25. Iršič, V. *et al.* New Constraints on the free-streaming of warm dark matter from intermediate and small scale Lyman-$\alpha$ forest data. *Phys. Rev. D* **96,** 023522. arXiv: 1702.01764 [astro-ph.CO] (2017).

26. Yèche, C., Palanque-Delabrouille, N., Baur, J. & du Mas des Bourboux, H. Constraints on neutrino masses from Lyman-alpha forest power spectrum with BOSS and XQ-100. *JCAP* **06,** 047. arXiv: 1702.03314 [astro-ph.CO] (2017).

27. Murgia, R., Iršič, V. & Viel, M. Novel constraints on noncold, nonthermal dark matter from Lyman- $\alpha$ forest data. *Phys. Rev. D* **98,** 083540. arXiv: 1806.08371 [astro-ph.CO] (2018).

28. Hall, L. J., Jedamzik, K., March-Russell, J. & West, S. M. Freeze-In Production of FIMP Dark Matter. *JHEP* **03,** 080. arXiv: 0911.1120 [hep-ph] (2010).

29. Bernal, N., Heikinheimo, M., Tenkanen, T., Tuominen, K. & Vaskonen, V. The Dawn of FIMP Dark Matter: A Review of Models and Constraints. *Int. J. Mod. Phys. A* **32,** 1730023. arXiv: 1706.07442 [hep-ph] (2017).

30. Ellis, J. R. *et al.* Cosmic Ray Constraints on the Annihilations of Relic Particles in the Galactic Halo. *Phys. Lett. B* **214,** 403–412 (1988).

31. Steigman, G. Observational tests of antimatter cosmologies. *Ann. Rev. Astron. Astrophys.* **14,** 339–372 (1976).

32. Strumia, A. *Baryogenesis via leptogenesis* in *Les Houches Summer School on Theoretical Physics: Session 84: Particle Physics Beyond the Standard Model* (Aug. 2006), 655–680. arXiv: hep-ph/0608347.

33. Zyla, P. A. *et al.* Review of Particle Physics. *PTEP* **2020,** 083C01 (2020).

34. Guth, A. H. The Inflationary Universe: A Possible Solution to the Horizon and Flatness Problems. *Phys. Rev. D* **23** (eds Fang, L.-Z. & Ruffini, R.) 347–356 (1981).

35. Starobinsky, A. A. A New Type of Isotropic Cosmological Models Without Singularity. *Phys. Lett. B* **91** (eds Khalatnikov, I. M. & Mineev, V. P.) 99–102 (1980).

36. Linde, A. D. A New Inflationary Universe Scenario: A Possible Solution of the Horizon, Flatness, Homogeneity, Isotropy and Primordial Monopole Problems. *Phys. Lett. B* **108** (eds Fang, L.-Z. & Ruffini, R.) 389–393 (1982).

37. Sakharov, A. D. Violation of CP Invariance, C asymmetry, and baryon asymmetry of the universe. *Pisma Zh. Eksp. Teor. Fiz.* **5,** 32–35 (1967).

38. 't Hooft, G. Symmetry Breaking Through Bell-Jackiw Anomalies. *Phys. Rev. Lett.* **37** (ed Shifman, M. A.) 8–11 (1976).

39. Klinkhamer, F. R. & Manton, N. S. A Saddle Point Solution in the Weinberg-Salam Theory. *Phys. Rev. D* **30,** 2212 (1984).

40. Kajantie, K., Laine, M., Rummukainen, K. & Shaposhnikov, M. E. The Electroweak phase transition: A Nonperturbative analysis. *Nucl. Phys. B* **466,** 189–258. arXiv: hep-lat/9510020 (1996).

41. Rummukainen, K., Tsypin, M., Kajantie, K., Laine, M. & Shaposhnikov, M. E. The Universality class of the electroweak theory. *Nucl. Phys. B* **532,** 283–314. arXiv: hep-lat/9805013 (1998).

42. Grojean, C., Servant, G. & Wells, J. D. First-order electroweak phase transition in the standard model with a low cutoff. *Phys. Rev. D* **71,** 036001. arXiv: hep-ph/0407019 (2005).

43. Rosner, J. L. CKM matrix and standard model CP violation. *Nucl. Phys. B Proc. Suppl.* **59** (eds Kuno, Y. & Nojiri, M. M.) 1–16. arXiv: hep-ph/9612327 (1997).

44. Hocker, A. & Ligeti, Z. CP violation and the CKM matrix. *Ann. Rev. Nucl. Part. Sci.* **56,** 501–567. arXiv: hep-ph/0605217 (2006).

45. Georgi, H. & Glashow, S. L. Unity of All Elementary Particle Forces. *Phys. Rev. Lett.* **32,** 438–441 (1974).

46. Fritzsch, H. & Minkowski, P. Unified Interactions of Leptons and Hadrons. *Annals Phys.* **93,** 193–266 (1975).

47. Akrami, Y. *et al.* Planck 2018 results. X. Constraints on inflation. *Astron. Astrophys.* **641,** A10. arXiv: 1807.06211 [astro-ph.CO] (2020).

48. Harvey, J. A. & Turner, M. S. Cosmological baryon and lepton number in the presence of electroweak fermion number violation. *Phys. Rev. D* **42,** 3344–3349 (1990).

49. Menon, A. & Morrissey, D. E. Higgs Boson Signatures of MSSM Electroweak Baryogenesis. *Phys. Rev. D* **79,** 115020. arXiv: 0903.3038 [hep-ph] (2009).

50. Cohen, T., Morrissey, D. E. & Pierce, A. Electroweak Baryogenesis and Higgs Signatures. *Phys. Rev. D* **86,** 013009. arXiv: 1203.2924 [hep-ph] (2012).

51. Curtin, D., Jaiswal, P. & Meade, P. Excluding Electroweak Baryogenesis in the MSSM. *JHEP* **08,** 005. arXiv: 1203.2932 [hep-ph] (2012).

52. Affleck, I. & Dine, M. A New Mechanism for Baryogenesis. *Nucl. Phys. B* **249,** 361–380 (1985).

53. Fukugita, M. & Yanagida, T. Baryogenesis Without Grand Unification. *Phys. Lett. B* **174,** 45–47 (1986).

54. Minkowski, P. $\mu \to e\gamma$ at a Rate of One Out of $10^9$ Muon Decays? *Phys. Lett. B* **67,** 421–428 (1977).

55. Mohapatra, R. N. & Senjanovic, G. Neutrino Mass and Spontaneous Parity Nonconservation. *Phys. Rev. Lett.* **44,** 912 (1980).

56. Yanagida, T. Horizontal gauge symmetry and masses of neutrinos. *Conf. Proc. C* **7902131** (eds Sawada, O. & Sugamoto, A.) 95–99 (1979).

57. Gell-Mann, M., Ramond, P. & Slansky, R. Complex Spinors and Unified Theories. *Conf. Proc. C* **790927,** 315–321. arXiv: 1306.4669 [hep-th] (1979).

58. Mohapatra, R. N. & Senjanovic, G. Neutrino Masses and Mixings in Gauge Models with Spontaneous Parity Violation. *Phys. Rev. D* **23,** 165 (1981).

59. Luty, M. A. Baryogenesis via leptogenesis. *Phys. Rev. D* **45,** 455–465 (1992).

60. Flanz, M., Paschos, E. A. & Sarkar, U. Baryogenesis from a lepton asymmetric universe. *Phys. Lett. B* **345.** [Erratum: Phys.Lett.B 384, 487–487 (1996), Erratum: Phys.Lett.B 382, 447–447 (1996)], 248–252. arXiv: hep-ph/9411366 (1995).

61. Covi, L., Roulet, E. & Vissani, F. CP violating decays in leptogenesis scenarios. *Phys. Lett. B* **384,** 169–174. arXiv: hep-ph/9605319 (1996).

62. Pilaftsis, A. & Underwood, T. E. J. Resonant leptogenesis. *Nucl. Phys. B* **692,** 303–345. arXiv: hep-ph/0309342 (2004).

63. Chen, M.-C. *TASI 2006 Lectures on Leptogenesis* in *Theoretical Advanced Study Institute in Elementary Particle Physics: Exploring New Frontiers Using Colliders and Neutrinos* (Mar. 2007), 123–176. arXiv: hep-ph/0703087.

64. Xing, Z.-z. & Zhou, S. *Neutrinos in particle physics, astronomy and cosmology* ISBN: 978-3-642-17559-6, 978-7-308-08024-8 (2011).

65. Abada, A., Davidson, S., Josse-Michaux, F.-X., Losada, M. & Riotto, A. Flavor issues in leptogenesis. *JCAP* **04,** 004. arXiv: hep-ph/0601083 (2006).

66. Abada, A. *et al.* Flavour Matters in Leptogenesis. *JHEP* **09,** 010. arXiv: hep-ph/0605281 (2006).

67. Nardi, E., Nir, Y., Roulet, E. & Racker, J. The Importance of flavor in leptogenesis. *JHEP* **01,** 164. arXiv: hep-ph/0601084 (2006).

68. Blanchet, S. & Di Bari, P. Flavor effects on leptogenesis predictions. *JCAP* **03,** 018. arXiv: hep-ph/0607330 (2007).

69. Buchmuller, W., Di Bari, P. & Plumacher, M. Cosmic microwave background, matter - antimatter asymmetry and neutrino masses. *Nucl. Phys. B* **643.** [Erratum: Nucl.Phys.B 793, 362 (2008)], 367–390. arXiv: hep-ph/0205349 (2002).

70. Buchmuller, W., Di Bari, P. & Plumacher, M. Leptogenesis for pedestrians. *Annals Phys.* **315,** 305–351. arXiv: hep-ph/0401240 (2005).

71. Casas, J. A. & Ibarra, A. Oscillating neutrinos and $\mu \to e, \gamma$. *Nucl. Phys. B* **618,** 171–204. arXiv: hep-ph/0103065 (2001).

72. Zyla, P. A. *et al.* Review of Particle Physics. *PTEP* **2020,** 083C01 (2020).

73. Davidson, S. & Ibarra, A. A Lower bound on the right-handed neutrino mass from leptogenesis. *Phys. Lett. B* **535,** 25–32. arXiv: hep-ph/0202239 (2002).

74. Albrecht, A., Steinhardt, P. J., Turner, M. S. & Wilczek, F. Reheating an Inflationary Universe. *Phys. Rev. Lett.* **48,** 1437 (1982).

75. Kofman, L., Linde, A. D. & Starobinsky, A. A. Reheating after inflation. *Phys. Rev. Lett.* **73,** 3195–3198. arXiv: hep-th/9405187 (1994).

76. Jedamzik, K., Lemoine, M. & Martin, J. Collapse of Small-Scale Density Perturbations during Preheating in Single Field Inflation. *JCAP* **09,** 034. arXiv: 1002.3039 [astro-ph.CO] (2010).

77. Easther, R., Flauger, R. & Gilmore, J. B. Delayed Reheating and the Breakdown of Coherent Oscillations. *JCAP* **04,** 027. arXiv: 1003.3011 [astro-ph.CO] (2011).

78. Musoke, N., Hotchkiss, S. & Easther, R. Lighting the Dark: Evolution of the Postinflationary Universe. *Phys. Rev. Lett.* **124,** 061301. arXiv: 1909.11678 [astro-ph.CO] (2020).

79. Allahverdi, R. *et al.* The First Three Seconds: a Review of Possible Expansion Histories of the Early Universe. arXiv: 2006.16182 [astro-ph.CO] (June 2020).

80. Kane, G., Sinha, K. & Watson, S. Cosmological Moduli and the Post-Inflationary Universe: A Critical Review. *Int. J. Mod. Phys. D* **24,** 1530022. arXiv: 1502.07746 [hep-th] (2015).

81. Borah, D., Jyoti Das, S. & Saha, A. K. Thermal keV dark matter in a gauged B-L model with cosmic inflation. *Phys. Rev. D* **106,** 055010. arXiv: 2110.13927 [hep-ph] (2022).

82. Arias, P., Bernal, N., Herrera, A. & Maldonado, C. Reconstructing Non-standard Cosmologies with Dark Matter. *JCAP* **10,** 047. arXiv: 1906.04183 [hep-ph] (2019).

83. Hawking, S. Gravitationally collapsed objects of very low mass. *Mon. Not. Roy. Astron. Soc.* **152,** 75 (1971).

84. Carr, B. J. & Hawking, S. W. Black holes in the early Universe. *Mon. Not. Roy. Astron. Soc.* **168,** 399–415 (1974).

85. Drees, M. & Erfani, E. Running-Mass Inflation Model and Primordial Black Holes. *JCAP* **04,** 005. arXiv: 1102.2340 [hep-ph] (2011).

86. Bhaumik, N. & Jain, R. K. Primordial black holes dark matter from inflection point models of inflation and the effects of reheating. *JCAP* **01,** 037. arXiv: 1907.04125 [astro-ph.CO] (2020).

87. Hawking, S. W. Black Holes From Cosmic Strings. *Phys. Lett. B* **231,** 237–239 (1989).

88. Hawking, S. W., Moss, I. G. & Stewart, J. M. Bubble Collisions in the Very Early Universe. *Phys. Rev. D* **26,** 2681 (1982).

89. Escrivà, A. PBH Formation from Spherically Symmetric Hydrodynamical Perturbations: A Review. *Universe* **8,** 66. arXiv: 2111.12693 [gr-qc] (2022).

90. Carr, B., Kohri, K., Sendouda, Y. & Yokoyama, J. Constraints on primordial black holes. *Rept. Prog. Phys.* **84,** 116902. arXiv: 2002.12778 [astro-ph.CO] (2021).

91. Green, A. M. & Kavanagh, B. J. Primordial Black Holes as a dark matter candidate. *J. Phys. G* **48,** 043001. arXiv: 2007.10722 [astro-ph.CO] (2021).

92. Hawking, S. W. Black hole explosions. *Nature* **248,** 30–31 (1974).

93. Carr, B. J. Some cosmological consequences of primordial black-hole evaporations. *Astrophys. J.* **206,** 8–25 (1976).

94. Baumann, D., Steinhardt, P. J. & Turok, N. Primordial Black Hole Baryogenesis. arXiv: hep-th/0703250 (Mar. 2007).

95. Hook, A. Baryogenesis from Hawking Radiation. *Phys. Rev. D* **90,** 083535. arXiv: 1404.0113 [hep-ph] (2014).

96. Fujita, T., Kawasaki, M., Harigaya, K. & Matsuda, R. Baryon asymmetry, dark matter, and density perturbation from primordial black holes. *Phys. Rev. D* **89,** 103501. arXiv: 1401.1909 [astro-ph.CO] (2014).

97. Hamada, Y. & Iso, S. Baryon asymmetry from primordial black holes. *PTEP* **2017,** 033B02. arXiv: 1610.02586 [hep-ph] (2017).

98. Morrison, L., Profumo, S. & Yu, Y. Melanopogenesis: Dark Matter of (almost) any Mass and Baryonic Matter from the Evaporation of Primordial Black Holes weighing a Ton (or less). *JCAP* **05,** 005. arXiv: 1812.10606 [astro-ph.CO] (2019).

99. Hooper, D. & Krnjaic, G. GUT Baryogenesis With Primordial Black Holes. *Phys. Rev. D* **103,** 043504. arXiv: 2010.01134 [hep-ph] (2021).

100. Perez-Gonzalez, Y. F. & Turner, J. Assessing the tension between a black hole dominated early universe and leptogenesis. *Phys. Rev. D* **104,** 103021. arXiv: 2010.03565 [hep-ph] (2021).

101. Datta, S., Ghosal, A. & Samanta, R. Baryogenesis from ultralight primordial black holes and strong gravitational waves from cosmic strings. *JCAP* **08,** 021. arXiv: 2012.14981 [hep-ph] (2021).

102. Gondolo, P., Sandick, P. & Shams Es Haghi, B. Effects of primordial black holes on dark matter models. *Phys. Rev. D* **102,** 095018. arXiv: 2009.02424 [hep-ph] (2020).

103. Bernal, N. & Zapata, O. Dark Matter in the Time of Primordial Black Holes. *JCAP* **03,** 015. arXiv: 2011.12306 [astro-ph.CO] (2021).

104. Cheek, A., Heurtier, L., Perez-Gonzalez, Y. F. & Turner, J. Primordial black hole evaporation and dark matter production. I. Solely Hawking radiation. *Phys. Rev. D* **105,** 015022. arXiv: 2107.00013 [hep-ph] (2022).

105. Cheek, A., Heurtier, L., Perez-Gonzalez, Y. F. & Turner, J. Primordial black hole evaporation and dark matter production. II. Interplay with the freeze-in or freeze-out mechanism. *Phys. Rev. D* **105,** 015023. arXiv: 2107.00016 [hep-ph] (2022).

106. Hawking, S. W. Particle Creation by Black Holes. *Commun. Math. Phys.* **43** (eds Gibbons, G. W. & Hawking, S. W.) [Erratum: Commun.Math.Phys. 46, 206 (1976)], 199–220 (1975).

107. Page, D. N. Particle Emission Rates from a Black Hole: Massless Particles from an Uncharged, Nonrotating Hole. *Phys. Rev. D* **13,** 198–206 (1976).

108. Page, D. N. Particle Emission Rates from a Black Hole. 3. Charged Leptons from a Nonrotating Hole. *Phys. Rev. D* **16,** 2402–2411 (1977).

109. MacGibbon, J. H. & Webber, B. R. Quark and gluon jet emission from primordial black holes: The instantaneous spectra. *Phys. Rev. D* **41,** 3052–3079 (1990).

110. MacGibbon, J. H. Quark and gluon jet emission from primordial black holes. 2. The Lifetime emission. *Phys. Rev. D* **44,** 376–392 (1991).

111. Lunardini, C. & Perez-Gonzalez, Y. F. Dirac and Majorana neutrino signatures of primordial black holes. *JCAP* **08,** 014. arXiv: 1910.07864 [hep-ph] (2020).

112. Masina, I. Dark matter and dark radiation from evaporating primordial black holes. *Eur. Phys. J. Plus* **135,** 552. arXiv: 2004.04740 [hep-ph] (2020).

113. Barman, B., Borah, D., Das, S. J. & Roshan, R. Non-thermal origin of asymmetric dark matter from inflaton and primordial black holes. *JCAP* **03,** 031. arXiv: 2111.08034 [hep-ph] (2022).

114. Abbott, B. P. *et al.* A gravitational-wave standard siren measurement of the Hubble constant. *Nature* **551,** 85–88. arXiv: 1710.05835 [astro-ph.CO] (2017).

115. Caprini, C. & Figueroa, D. G. Cosmological Backgrounds of Gravitational Waves. *Class. Quant. Grav.* **35,** 163001. arXiv: 1801.04268 [astro-ph.CO] (2018).

116. Vilenkin, A. Cosmic Strings and Domain Walls. *Phys. Rept.* **121,** 263–315 (1985).

117. Papanikolaou, T., Vennin, V. & Langlois, D. Gravitational waves from a universe filled with primordial black holes. *JCAP* **03,** 053. arXiv: 2010.11573 [astro-ph.CO] (2021).

118. Domènech, G., Lin, C. & Sasaki, M. Gravitational wave constraints on the primordial black hole dominated early universe. *JCAP* **04.** [Erratum: JCAP 11, E01 (2021)], 062. arXiv: 2012.08151 [gr-qc] (2021).

119. Inomata, K., Kawasaki, M., Mukaida, K., Terada, T. & Yanagida, T. T. Gravitational Wave Production right after a Primordial Black Hole Evaporation. *Phys. Rev. D* **101,** 123533. arXiv: 2003.10455 [astro-ph.CO] (2020).

120. Kibble, T. W. B. Topology of Cosmic Domains and Strings. *J. Phys. A* **9,** 1387–1398 (1976).

121. Nielsen, H. B. & Olesen, P. Vortex Line Models for Dual Strings. *Nucl. Phys. B* **61** (ed Taylor, J. C.) 45–61 (1973).

122. Vilenkin, A. & Shellard, E. P. S. *Cosmic Strings and Other Topological Defects* ISBN: 978-0-521-65476-0 (Cambridge University Press, July 2000).

123. Ringeval, C., Sakellariadou, M. & Bouchet, F. Cosmological evolution of cosmic string loops. *JCAP* **02,** 023. arXiv: astro-ph/0511646 (2007).

124. Blanco-Pillado, J. J., Olum, K. D. & Shlaer, B. Large parallel cosmic string simulations: New results on loop production. *Phys. Rev. D* **83,** 083514. arXiv: 1101.5173 [astro-ph.CO] (2011).

125. Vilenkin, A. Gravitational radiation from cosmic strings. *Phys. Lett. B* **107,** 47–50 (1981).

126. Vachaspati, T. & Vilenkin, A. Gravitational Radiation from Cosmic Strings. *Phys. Rev. D* **31,** 3052 (1985).

127. Blanco-Pillado, J. J., Olum, K. D. & Shlaer, B. The number of cosmic string loops. *Phys. Rev. D* **89,** 023512. arXiv: 1309.6637 [astro-ph.CO] (2014).

128. Blanco-Pillado, J. J. & Olum, K. D. Stochastic gravitational wave background from smoothed cosmic string loops. *Phys. Rev. D* **96,** 104046. arXiv: 1709.02693 [astro-ph.CO] (2017).

129. Damour, T. & Vilenkin, A. Gravitational wave bursts from cusps and kinks on cosmic strings. *Phys. Rev. D* **64,** 064008. arXiv: gr-qc/0104026 (2001).

130. Gouttenoire, Y., Servant, G. & Simakachorn, P. Beyond the Standard Models with Cosmic Strings. *JCAP* **07,** 032. arXiv: 1912.02569 [hep-ph] (2020).

131. Martins, C. J. A. P. & Shellard, E. P. S. Quantitative string evolution. *Phys. Rev. D* **54,** 2535–2556. arXiv: hep-ph/9602271 (1996).

132. Martins, C. J. A. P. & Shellard, E. P. S. Extending the velocity dependent one scale string evolution model. *Phys. Rev. D* **65,** 043514. arXiv: hep-ph/0003298 (2002).

133. Auclair, P. *et al.* Probing the gravitational wave background from cosmic strings with LISA. *JCAP* **04,** 034. arXiv: 1909.00819 [astro-ph.CO] (2020).

134. Vilenkin, A. Cosmic string dynamics with friction. *Phys. Rev. D* **43,** 1060–1062 (1991).

135. Charnock, T., Avgoustidis, A., Copeland, E. J. & Moss, A. CMB constraints on cosmic strings and superstrings. *Phys. Rev. D* **93,** 123503. arXiv: 1603.01275 [astro-ph.CO] (2016).

136. Kramer, M. & Champion, D. J. The European Pulsar Timing Array and the Large European Array for Pulsars. *Class. Quant. Grav.* **30,** 224009 (2013).

137. Weltman, A. *et al.* Fundamental physics with the Square Kilometre Array. *Publ. Astron. Soc. Austral.* **37,** e002. arXiv: 1810.02680 [astro-ph.CO] (2020).

138. Aasi, J. *et al.* Advanced LIGO. *Class. Quant. Grav.* **32,** 074001. arXiv: 1411.4547 [gr-qc] (2015).

139. Abbott, B. P. *et al.* Exploring the Sensitivity of Next Generation Gravitational Wave Detectors. *Class. Quant. Grav.* **34,** 044001. arXiv: 1607.08697 [astro-ph.IM] (2017).

140. Abbott, B. P. *et al.* Upper Limits on the Stochastic Gravitational-Wave Background from Advanced LIGO's First Observing Run. *Phys. Rev. Lett.* **118.** [Erratum: Phys.Rev.Lett. 119, 029901 (2017)], 121101. arXiv: 1612.02029 [gr-qc] (2017).

141. Amaro-Seoane, P. *et al.* Laser Interferometer Space Antenna. arXiv: 1702.00786 [astro-ph.IM] (Feb. 2017).

142. Kawamura, S. *et al.* The Japanese space gravitational wave antenna DECIGO. *Class. Quant. Grav.* **23** (ed Mio, N.) S125–S132 (2006).

143. Yagi, K. & Seto, N. Detector configuration of DECIGO/BBO and identification of cosmological neutron-star binaries. *Phys. Rev. D* **83.** [Erratum: Phys.Rev.D 95, 109901 (2017)], 044011. arXiv: 1101.3940 [astro-ph.CO] (2011).

144. Maggiore, M. *et al.* Science Case for the Einstein Telescope. *JCAP* **03,** 050. arXiv: 1912.02622 [astro-ph.CO] (2020).

145. Cui, Y., Lewicki, M., Morrissey, D. E. & Wells, J. D. Probing the pre-BBN universe with gravitational waves from cosmic strings. *JHEP* **01,** 081. arXiv: 1808.08968 [hep-ph] (2019).

146. Cui, Y., Lewicki, M., Morrissey, D. E. & Wells, J. D. Cosmic Archaeology with Gravitational Waves from Cosmic Strings. *Phys. Rev. D* **97,** 123505. arXiv: 1711.03104 [hep-ph] (2018).

147. Anantua, R., Easther, R. & Giblin, J. T. GUT-Scale Primordial Black Holes: Consequences and Constraints. *Phys. Rev. Lett.* **103,** 111303. arXiv: 0812.0825 [astro-ph] (2009).

148. Zagorac, J. L., Easther, R. & Padmanabhan, N. GUT-Scale Primordial Black Holes: Mergers and Gravitational Waves. *JCAP* **06,** 052. arXiv: 1903.05053 [astro-ph.CO] (2019).

149. Hooper, D., Krnjaic, G., March-Russell, J., McDermott, S. D. & Petrossian-Byrne, R. Hot Gravitons and Gravitational Waves From Kerr Black Holes in the Early Universe. arXiv: 2004.00618 [astro-ph.CO] (Apr. 2020).

150. Saito, R. & Yokoyama, J. Gravitational wave background as a probe of the primordial black hole abundance. *Phys. Rev. Lett.* **102.** [Erratum: Phys.Rev.Lett. 107, 069901 (2011)], 161101. arXiv: 0812.4339 [astro-ph] (2009).

151. Aghanim, N. *et al.* Planck 2018 results. VI. Cosmological parameters. *Astron. Astrophys.* **641.** [Erratum: Astron.Astrophys. 652, C4 (2021)], A6. arXiv: 1807.06209 [astro-ph.CO] (2020).

152. Borah, D., Jyoti Das, S., Samanta, R. & Urban, F. R. PBH-infused seesaw origin of matter and unique gravitational waves. *JHEP* **03,** 127. arXiv: 2211.15726 [hep-ph] (2023).

153. Aprile, E. *et al.* The XENON1T Dark Matter Experiment. *Eur. Phys. J. C* **77,** 881. arXiv: 1708.07051 [astro-ph.IM] (2017).

154. Aalbers, J. *et al.* First Dark Matter Search Results from the LUX-ZEPLIN (LZ) Experiment. arXiv: 2207.03764 [hep-ex] (July 2022).

155. Boyarsky, A., Lesgourgues, J., Ruchayskiy, O. & Viel, M. Lyman-alpha constraints on warm and on warm-plus-cold dark matter models. *JCAP* **05,** 012. arXiv: 0812.0010 [astro-ph] (2009).

156. Merle, A., Niro, V. & Schmidt, D. New Production Mechanism for keV Sterile Neutrino Dark Matter by Decays of Frozen-In Scalars. *JCAP* **03,** 028. arXiv: 1306.3996 [hep-ph] (2014).

157. Drewes, M. *et al.* A White Paper on keV Sterile Neutrino Dark Matter. *JCAP* **01,** 025. arXiv: 1602.04816 [hep-ph] (2017).

158. Tremaine, S. & Gunn, J. E. Dynamical Role of Light Neutral Leptons in Cosmology. *Phys. Rev. Lett.* **42** (ed Srednicki, M. A.) 407–410 (1979).

159. Gorbunov, D., Khmelnitsky, A. & Rubakov, V. Constraining sterile neutrino dark matter by phase-space density observations. *JCAP* **10,** 041. arXiv: 0808.3910 [hep-ph] (2008).

160. Boyarsky, A., Ruchayskiy, O. & Iakubovskyi, D. A Lower bound on the mass of Dark Matter particles. *JCAP* **03,** 005. arXiv: 0808.3902 [hep-ph] (2009).

161. Seljak, U., Makarov, A., McDonald, P. & Trac, H. Can sterile neutrinos be the dark matter? *Phys. Rev. Lett.* **97,** 191303. arXiv: astro-ph/0602430 (2006).

162. Bulbul, E. *et al.* Detection of An Unidentified Emission Line in the Stacked X-ray spectrum of Galaxy Clusters. *Astrophys. J.* **789,** 13. arXiv: 1402.2301 [astro-ph.CO] (2014).

163. Boyarsky, A., Ruchayskiy, O., Iakubovskyi, D. & Franse, J. Unidentified Line in X-Ray Spectra of the Andromeda Galaxy and Perseus Galaxy Cluster. *Phys. Rev. Lett.* **113,** 251301. arXiv: 1402.4119 [astro-ph.CO] (2014).

164. Bullock, J. S. & Boylan-Kolchin, M. Small-Scale Challenges to the ΛCDM Paradigm. *Ann. Rev. Astron. Astrophys.* **55,** 343–387. arXiv: 1707.04256 [astro-ph.CO] (2017).

165. Lee, B. W. & Weinberg, S. Cosmological Lower Bound on Heavy Neutrino Masses. *Phys. Rev. Lett.* **39** (ed Srednicki, M. A.) 165–168 (1977).

166. Griest, K. & Kamionkowski, M. Unitarity Limits on the Mass and Radius of Dark Matter Particles. *Phys. Rev. Lett.* **64,** 615 (1990).

167. Davidson, A. *BL* as the fourth color within an $SU(2)_L \times U(1)_R \times U(1)$ model. *Phys. Rev. D* **20,** 776 (1979).

168. Mohapatra, R. N. & Marshak, R. E. Local B-L Symmetry of Electroweak Interactions, Majorana Neutrinos and Neutron Oscillations. *Phys. Rev. Lett.* **44.** [Erratum: Phys.Rev.Lett. 44, 1643 (1980)], 1316–1319 (1980).

169. Marshak, R. E. & Mohapatra, R. N. Quark - Lepton Symmetry and B-L as the U(1) Generator of the Electroweak Symmetry Group. *Phys. Lett. B* **91,** 222–224 (1980).

170. Masiero, A., Nieves, J. F. & Yanagida, T. $B^-$l Violating Proton Decay and Late Cosmological Baryon Production. *Phys. Lett. B* **116,** 11–15 (1982).

171. Mohapatra, R. N. & Senjanovic, G. Spontaneous Breaking of Global $B^-$l Symmetry and Matter - Antimatter Oscillations in Grand Unified Theories. *Phys. Rev. D* **27,** 254 (1983).

172. Buchmuller, W., Greub, C. & Minkowski, P. Neutrino masses, neutral vector bosons and the scale of B-L breaking. *Phys. Lett. B* **267,** 395–399 (1991).

173. Borah, D., Jyoti Das, S. & Saha, A. K. Cosmic inflation in minimal $U(1)_{B-L}$ model: implications for (non) thermal dark matter and leptogenesis. *Eur. Phys. J. C* **81,** 169. arXiv: 2005.11328 [hep-ph] (2021).

174. Carena, M., Daleo, A., Dobrescu, B. A. & Tait, T. M. P. $Z'$ gauge bosons at the Tevatron. *Phys. Rev. D* **70,** 093009. arXiv: hep-ph/0408098 (2004).

175. Cacciapaglia, G., Csaki, C., Marandella, G. & Strumia, A. The Minimal Set of Electroweak Precision Parameters. *Phys. Rev. D* **74,** 033011. arXiv: hep-ph/0604111 (2006).

176. Aaboud, M. *et al.* Search for new high-mass phenomena in the dilepton final state using 36 fb[1] of proton-proton collision data at $\sqrt{s} = 13$ TeV with the ATLAS detector. *JHEP* **10,** 182. arXiv: 1707.02424 [hep-ex] (2017).

177. Aad, G. *et al.* Search for high-mass dilepton resonances using 139 fb$^{-1}$ of $pp$ collision data collected at $\sqrt{s}$ =13 TeV with the ATLAS detector. *Phys. Lett. B* **796,** 68–87. arXiv: 1903.06248 [hep-ex] (2019).

178. Sirunyan, A. M. *et al.* Search for high-mass resonances in dilepton final states in proton-proton collisions at $\sqrt{s} = 13$ TeV. *JHEP* **06,** 120. arXiv: 1803.06292 [hep-ex] (2018).

179. Robens, T. & Stefaniak, T. Status of the Higgs Singlet Extension of the Standard Model after LHC Run 1. *Eur. Phys. J. C* **75,** 104. arXiv: 1501.02234 [hep-ph] (2015).

180. Chalons, G., Lopez-Val, D., Robens, T. & Stefaniak, T. The Higgs singlet extension at LHC Run 2. *PoS* **ICHEP2016,** 1180. arXiv: 1611.03007 [hep-ph] (2016).

181. López-Val, D. & Robens, T. $\Delta$r and the W-boson mass in the singlet extension of the standard model. *Phys. Rev. D* **90,** 114018. arXiv: 1406.1043 [hep-ph] (2014).

182. Khachatryan, V. *et al.* Search for a Higgs boson in the mass range from 145 to 1000 GeV decaying to a pair of W or Z bosons. *JHEP* **10,** 144. arXiv: 1504.00936 [hep-ex] (2015).

183. Strassler, M. J. & Zurek, K. M. Discovering the Higgs through highly-displaced vertices. *Phys. Lett. B* **661,** 263–267. arXiv: hep-ph/0605193 (2008).

184. Search for invisible Higgs boson decays with vector boson fusion signatures with the ATLAS detector using an integrated luminosity of 139 fb$^{-1}$ (Apr. 2020).

185. Biswas, A., Borah, D. & Nanda, D. keV Neutrino Dark Matter in a Fast Expanding Universe. *Phys. Lett. B* **786,** 364–372. arXiv: 1809.03519 [hep-ph] (2018).

186. Escudero, M. Neutrino decoupling beyond the Standard Model: CMB constraints on the Dark Matter mass with a fast and precise $N_{\rm eff}$ evaluation. *JCAP* **02,** 007. arXiv: 1812.05605 [hep-ph] (2019).

187. Ibarra, A. & Ross, G. G. Neutrino phenomenology: The Case of two right-handed neutrinos. *Phys. Lett. B* **591,** 285–296. arXiv: hep-ph/0312138 (2004).

188. Iso, S., Okada, N. & Orikasa, Y. Resonant Leptogenesis in the Minimal B-L Extended Standard Model at TeV. *Phys. Rev. D* **83,** 093011. arXiv: 1011.4769 [hep-ph] (2011).

189. Okada, N., Orikasa, Y. & Yamada, T. Minimal Flavor Violation in the Minimal $U(1)_{B-L}$ Model and Resonant Leptogenesis. *Phys. Rev. D* **86,** 076003. arXiv: 1207.1510 [hep-ph] (2012).

190. Newton, O. *et al.* Constraints on the properties of warm dark matter using the satellite galaxies of the Milky Way. *JCAP* **08,** 062. arXiv: 2011.08865 [astro-ph.CO] (2021).

191. Banik, N., Bovy, J., Bertone, G., Erkal, D. & de Boer, T. J. L. Novel constraints on the particle nature of dark matter from stellar streams. *JCAP* **10,** 043. arXiv: 1911.02663 [astro-ph.GA] (2021).

192. Scherrer, R. J. & Turner, M. S. Decaying Particles Do Not Heat Up the Universe. *Phys. Rev. D* **31,** 681 (1985).

193. Allahverdi, R. & Osiński, J. K. Early matter domination from long-lived particles in the visible sector. *Phys. Rev. D* **105,** 023502. arXiv: 2108.13136 [hep-ph] (2022).

194. Arzoumanian, Z. *et al.* The NANOGrav 12.5 yr Data Set: Search for an Isotropic Stochastic Gravitational-wave Background. *Astrophys. J. Lett.* **905,** L34. arXiv: 2009.04496 [astro-ph.HE] (2020).

195. Goncharov, B. *et al.* On the Evidence for a Common-spectrum Process in the Search for the Nanohertz Gravitational-wave Background with the Parkes Pulsar Timing Array. *Astrophys. J. Lett.* **917,** L19. arXiv: 2107.12112 [astro-ph.HE] (2021).

196. Ellis, J. & Lewicki, M. Cosmic String Interpretation of NANOGrav Pulsar Timing Data. *Phys. Rev. Lett.* **126,** 041304. arXiv: 2009.06555 [astro-ph.CO] (2021).

197. Blasi, S., Brdar, V. & Schmitz, K. Has NANOGrav found first evidence for cosmic strings? *Phys. Rev. Lett.* **126,** 041305. arXiv: 2009.06607 [astro-ph.CO] (2021).

198. Samanta, R. & Datta, S. Gravitational wave complementarity and impact of NANOGrav data on gravitational leptogenesis. *JHEP* **05,** 211. arXiv: 2009.13452 [hep-ph] (2021).

199. Buchmüller, W., Domcke, V., Kamada, K. & Schmitz, K. The Gravitational Wave Spectrum from Cosmological $B - L$ Breaking. *JCAP* **10,** 003. arXiv: 1305.3392 [hep-ph] (2013).

200. Dror, J. A., Hiramatsu, T., Kohri, K., Murayama, H. & White, G. Testing the Seesaw Mechanism and Leptogenesis with Gravitational Waves. *Phys. Rev. Lett.* **124,** 041804. arXiv: 1908.03227 [hep-ph] (2020).

201. Buchmuller, W., Domcke, V., Murayama, H. & Schmitz, K. Probing the scale of grand unification with gravitational waves. *Phys. Lett. B* **809,** 135764. arXiv: 1912.03695 [hep-ph] (2020).

202. King, S. F., Pascoli, S., Turner, J. & Zhou, Y.-L. Gravitational Waves and Proton Decay: Complementary Windows into Grand Unified Theories. *Phys. Rev. Lett.* **126,** 021802. arXiv: 2005.13549 [hep-ph] (2021).

203. Fornal, B. & Shams Es Haghi, B. Baryon and Lepton Number Violation from Gravitational Waves. *Phys. Rev. D* **102,** 115037. arXiv: 2008.05111 [hep-ph] (2020).

204. Buchmuller, W., Domcke, V. & Schmitz, K. Stochastic gravitational-wave background from metastable cosmic strings. *JCAP* **12,** 006. arXiv: 2107.04578 [hep-ph] (2021).

205. Masoud, M. A., Rehman, M. U. & Shafi, Q. Sneutrino tribrid inflation, metastable cosmic strings and gravitational waves. *JCAP* **11,** 022. arXiv: 2107.09689 [hep-ph] (2021).

206. Afzal, A., Ahmed, W., Rehman, M. U. & Shafi, Q. $\mu$-hybrid inflation, gravitino dark matter, and stochastic gravitational wave background from cosmic strings. *Phys. Rev. D* **105,** 103539. arXiv: 2202.07386 [hep-ph] (2022).

207. Blasi, S., Brdar, V. & Schmitz, K. Fingerprint of low-scale leptogenesis in the primordial gravitational-wave spectrum. *Phys. Rev. Res.* **2,** 043321. arXiv: 2004.02889 [hep-ph] (2020).

208. Gouttenoire, Y., Servant, G. & Simakachorn, P. BSM with Cosmic Strings: Heavy, up to EeV mass, Unstable Particles. *JCAP* **07,** 016. arXiv: 1912.03245 [hep-ph] (2020).

209. Auclair, P., Steer, D. A. & Vachaspati, T. Particle emission and gravitational radiation from cosmic strings: observational constraints. *Phys. Rev. D* **101,** 083511. arXiv: 1911.12066 [hep-ph] (2020).

210. Aker, M. *et al.* Improved Upper Limit on the Neutrino Mass from a Direct Kinematic Method by KATRIN. *Phys. Rev. Lett.* **123,** 221802. arXiv: 1909.06048 [hep-ex] (2019).

211. Dolinski, M. J., Poon, A. W. P. & Rodejohann, W. Neutrinoless Double-Beta Decay: Status and Prospects. *Ann. Rev. Nucl. Part. Sci.* **69,** 219–251. arXiv: 1902.04097 [nucl-ex] (2019).

212. Boucenna, S. M. & Morisi, S. Theories relating baryon asymmetry and dark matter: A mini review. *Front. in Phys.* **1,** 33. arXiv: 1310.1904 [hep-ph] (2014).

213. Nussinov, S. TECHNOCOSMOLOGY: COULD A TECHNIBARYON EXCESS PROVIDE A 'NATURAL' MISSING MASS CANDIDATE? *Phys. Lett. B* **165,** 55–58 (1985).

214. Davoudiasl, H. & Mohapatra, R. N. On Relating the Genesis of Cosmic Baryons and Dark Matter. *New J. Phys.* **14,** 095011. arXiv: 1203.1247 [hep-ph] (2012).

215. Petraki, K. & Volkas, R. R. Review of asymmetric dark matter. *Int. J. Mod. Phys. A* **28,** 1330028. arXiv: 1305.4939 [hep-ph] (2013).

216. Zurek, K. M. Asymmetric Dark Matter: Theories, Signatures, and Constraints. *Phys. Rept.* **537,** 91–121. arXiv: 1308.0338 [hep-ph] (2014).

217. Yoshimura, M. Unified Gauge Theories and the Baryon Number of the Universe. *Phys. Rev. Lett.* **41.** [Erratum: Phys.Rev.Lett. 42, 746 (1979)], 281–284 (1978).

218. Barr, S. M. Comments on Unitarity and the Possible Origins of the Baryon Asymmetry of the Universe. *Phys. Rev. D* **19,** 3803 (1979).

219. Baldes, I., Bell, N. F., Petraki, K. & Volkas, R. R. Particle-antiparticle asymmetries from annihilations. *Phys. Rev. Lett.* **113,** 181601. arXiv: 1407.4566 [hep-ph] (2014).

220. Cui, Y., Randall, L. & Shuve, B. A WIMPy Baryogenesis Miracle. *JHEP* **04,** 075. arXiv: 1112.2704 [hep-ph] (2012).

221. Bernal, N., Josse-Michaux, F.-X. & Ubaldi, L. Phenomenology of WIMPy baryogenesis models. *JCAP* **01,** 034. arXiv: 1210.0094 [hep-ph] (2013).

222. Bernal, N., Colucci, S., Josse-Michaux, F.-X., Racker, J. & Ubaldi, L. On baryogenesis from dark matter annihilation. *JCAP* **10,** 035. arXiv: 1307.6878 [hep-ph] (2013).

223. Kumar, J. & Stengel, P. WIMPy Leptogenesis With Absorptive Final State Interactions. *Phys. Rev. D* **89,** 055016. arXiv: 1309.1145 [hep-ph] (2014).

224. Racker, J. & Rius, N. Helicitogenesis: WIMPy baryogenesis with sterile neutrinos and other realizations. *JHEP* **11,** 163. arXiv: 1406.6105 [hep-ph] (2014).

225. Dasgupta, A., Hati, C., Patra, S. & Sarkar, U. A minimal model of TeV scale WIMPy leptogenesis. arXiv: 1605.01292 [hep-ph] (May 2016).

226. Borah, D., Dasgupta, A. & Kang, S. K. TeV Scale Leptogenesis via Dark Sector Scatterings. *Eur. Phys. J. C* **80,** 498. arXiv: 1806.04689 [hep-ph] (2020).

227. Borah, D., Dasgupta, A. & Kang, S. K. Two-component dark matter with cogenesis of the baryon asymmetry of the Universe. *Phys. Rev. D* **100,** 103502. arXiv: 1903.10516 [hep-ph] (2019).

228. Dasgupta, A., Bhupal Dev, P. S., Kang, S. K. & Zhang, Y. New mechanism for matter-antimatter asymmetry and connection with dark matter. *Phys. Rev. D* **102,** 055009. arXiv: 1911.03013 [hep-ph] (2020).

229. Falkowski, A., Ruderman, J. T. & Volansky, T. Asymmetric Dark Matter from Leptogenesis. *JHEP* **05,** 106. arXiv: 1101.4936 [hep-ph] (2011).

230. Dutta Banik, A., Roshan, R. & Sil, A. Neutrino mass and asymmetric dark matter: study with inert Higgs doublet and high scale validity. *JCAP* **03,** 037. arXiv: 2011.04371 [hep-ph] (2021).

231. Gell-Mann, M., Ramond, P. & Slansky, R. Complex Spinors and Unified Theories. *Conf. Proc. C* **790927,** 315–321. arXiv: 1306.4669 [hep-th] (1979).

232. Glashow, S. L. The Future of Elementary Particle Physics. *NATO Sci. Ser. B* **61,** 687 (1980).

233. Ma, E. Verifiable radiative seesaw mechanism of neutrino mass and dark matter. *Phys. Rev. D* **73,** 077301. arXiv: hep-ph/0601225 (2006).

234. Merle, A. & Platscher, M. Running of radiative neutrino masses: the scotogenic model — revisited. *JHEP* **11,** 148. arXiv: 1507.06314 [hep-ph] (2015).

235. Mahanta, D. & Borah, D. TeV Scale Leptogenesis with Dark Matter in Non-standard Cosmology. *JCAP* **04,** 032. arXiv: 1912.09726 [hep-ph] (2020).

236. Hambye, T., Ling, F. S., Lopez Honorez, L. & Rocher, J. Scalar Multiplet Dark Matter. *JHEP* **07.** [Erratum: JHEP 05, 066 (2010)], 090. arXiv: 0903.4010 [hep-ph] (2009).

237. Racker, J. Mass bounds for baryogenesis from particle decays and the inert doublet model. *JCAP* **03,** 025. arXiv: 1308.1840 [hep-ph] (2014).

238. Clarke, J. D., Foot, R. & Volkas, R. R. Natural leptogenesis and neutrino masses with two Higgs doublets. *Phys. Rev. D* **92,** 033006. arXiv: 1505.05744 [hep-ph] (2015).

239. Hugle, T., Platscher, M. & Schmitz, K. Low-Scale Leptogenesis in the Scotogenic Neutrino Mass Model. *Phys. Rev. D* **98,** 023020. arXiv: 1804.09660 [hep-ph] (2018).

240. Borah, D., Dev, P. S. B. & Kumar, A. TeV scale leptogenesis, inflaton dark matter and neutrino mass in a scotogenic model. *Phys. Rev. D* **99,** 055012. arXiv: 1810.03645 [hep-ph] (2019).

241. Mahanta, D. & Borah, D. Fermion dark matter with $N_2$ leptogenesis in minimal scotogenic model. *JCAP* **11,** 021. arXiv: 1906.03577 [hep-ph] (2019).

242. Sarma, L., Das, P. & Das, M. K. Scalar dark matter and leptogenesis in the minimal scotogenic model. *Nucl. Phys. B* **963,** 115300. arXiv: 2004.13762 [hep-ph] (2021).

243. Kashiwase, S. & Suematsu, D. Baryon number asymmetry and dark matter in the neutrino mass model with an inert doublet. *Phys. Rev. D* **86,** 053001. arXiv: 1207.2594 [hep-ph] (2012).

244. Kashiwase, S. & Suematsu, D. Leptogenesis and dark matter detection in a TeV scale neutrino mass model with inverted mass hierarchy. *Eur. Phys. J. C* **73,** 2484. arXiv: 1301.2087 [hep-ph] (2013).

245. Green, A. M. Supersymmetry and primordial black hole abundance constraints. *Phys. Rev. D* **60,** 063516. arXiv: astro-ph/9903484 (1999).

246. Khlopov, M. Y., Barrau, A. & Grain, J. Gravitino production by primordial black hole evaporation and constraints on the inhomogeneity of the early universe. *Class. Quant. Grav.* **23,** 1875–1882. arXiv: astro-ph/0406621 (2006).

247. Dai, D.-C., Freese, K. & Stojkovic, D. Constraints on dark matter particles charged under a hidden gauge group from primordial black holes. *JCAP* **06,** 023. arXiv: 0904.3331 [hep-ph] (2009).

248. Allahverdi, R., Dent, J. & Osinski, J. Nonthermal production of dark matter from primordial black holes. *Phys. Rev. D* **97,** 055013. arXiv: 1711.10511 [astro-ph.CO] (2018).

249. Lennon, O., March-Russell, J., Petrossian-Byrne, R. & Tillim, H. Black Hole Genesis of Dark Matter. *JCAP* **04,** 009. arXiv: 1712.07664 [hep-ph] (2018).

250. Hooper, D., Krnjaic, G. & McDermott, S. D. Dark Radiation and Superheavy Dark Matter from Black Hole Domination. *JHEP* **08,** 001. arXiv: 1905.01301 [hep-ph] (2019).

251. Chaudhuri, A. & Dolgov, A. PBH Evaporation, Baryon Asymmetry, and Dark Matter. *J. Exp. Theor. Phys.* **133,** 552–566. arXiv: 2001.11219 [astro-ph.CO] (2021).

252. Baldes, I., Decant, Q., Hooper, D. C. & Lopez-Honorez, L. Non-Cold Dark Matter from Primordial Black Hole Evaporation. *JCAP* **08,** 045. arXiv: 2004.14773 [astro-ph.CO] (2020).

253. Bernal, N. & Zapata, O. Gravitational dark matter production: primordial black holes and UV freeze-in. *Phys. Lett. B* **815,** 136129. arXiv: 2011.02510 [hep-ph] (2021).

254. Kitabayashi, T. Primordial black holes and scotogenic dark matter. *Int. J. Mod. Phys. A* **36,** 2150139. arXiv: 2101.01921 [hep-ph] (2021).

255. Masina, I. Dark Matter and Dark Radiation from Evaporating Kerr Primordial Black Holes. *Grav. Cosmol.* **27,** 315–330. arXiv: 2103.13825 [gr-qc] (2021).

256. Aaboud, M. *et al.* Combination of searches for invisible Higgs boson decays with the ATLAS experiment. *Phys. Rev. Lett.* **122,** 231801. arXiv: 1904.05105 [hep-ex] (2019).

257. Lundstrom, E., Gustafsson, M. & Edsjo, J. The Inert Doublet Model and LEP II Limits. *Phys. Rev. D* **79,** 035013. arXiv: 0810.3924 [hep-ph] (2009).

258. Bernal, N. & Zapata, O. Self-interacting Dark Matter from Primordial Black Holes. *JCAP* **03,** 007. arXiv: 2010.09725 [hep-ph] (2021).

259. Diamanti, R., Ando, S., Gariazzo, S., Mena, O. & Weniger, C. Cold dark matter plus not-so-clumpy dark relics. *JCAP* **06,** 008. arXiv: 1701.03128 [astro-ph.CO] (2017).

260. Ahriche, A., Jueid, A. & Nasri, S. Radiative neutrino mass and Majorana dark matter within an inert Higgs doublet model. *Phys. Rev. D* **97,** 095012. arXiv: 1710.03824 [hep-ph] (2018).

261. Belanger, G. *et al.* Dilepton constraints in the Inert Doublet Model from Run 1 of the LHC. *Phys. Rev. D* **91,** 115011. arXiv: 1503.07367 [hep-ph] (2015).

262. Belyaev, A., Cacciapaglia, G., Ivanov, I. P., Rojas-Abatte, F. & Thomas, M. Anatomy of the Inert Two Higgs Doublet Model in the light of the LHC and non-LHC Dark Matter Searches. *Phys. Rev. D* **97,** 035011. arXiv: 1612.00511 [hep-ph] (2018).

263. Belyaev, A. *et al.* Advancing LHC probes of dark matter from the inert two-Higgs-doublet model with the monojet signal. *Phys. Rev. D* **99,** 015011. arXiv: 1809.00933 [hep-ph] (2019).

264. Arhrib, A., Tsai, Y.-L. S., Yuan, Q. & Yuan, T.-C. An Updated Analysis of Inert Higgs Doublet Model in light of the Recent Results from LUX, PLANCK, AMS-02 and LHC. *JCAP* **06,** 030. arXiv: 1310.0358 [hep-ph] (2014).

265. Arvanitaki, A. & Geraci, A. A. Detecting high-frequency gravitational waves with optically-levitated sensors. *Phys. Rev. Lett.* **110,** 071105. arXiv: 1207.5320 [gr-qc] (2013).

266. Chou, A. S. *et al.* First Measurements of High Frequency Cross-Spectra from a Pair of Large Michelson Interferometers. *Phys. Rev. Lett.* **117,** 111102. arXiv: 1512.01216 [gr-qc] (2016).

267. Ito, A., Ikeda, T., Miuchi, K. & Soda, J. Probing GHz gravitational waves with graviton–magnon resonance. *Eur. Phys. J. C* **80,** 179. arXiv: 1903.04843 [gr-qc] (2020).

268. Ejlli, A., Ejlli, D., Cruise, A. M., Pisano, G. & Grote, H. Upper limits on the amplitude of ultra-high-frequency gravitational waves from graviton to photon conversion. *Eur. Phys. J. C* **79,** 1032. arXiv: 1908.00232 [gr-qc] (2019).

269. Aggarwal, N. *et al.* Challenges and opportunities of gravitational-wave searches at MHz to GHz frequencies. *Living Rev. Rel.* **24,** 4. arXiv: 2011.12414 [gr-qc] (2021).

270. Kusenko, A. Sterile neutrinos: The Dark side of the light fermions. *Phys. Rept.* **481,** 1–28. arXiv: 0906.2968 [hep-ph] (2009).

271. Lacki, B. C. & Beacom, J. F. Primordial Black Holes as Dark Matter: Almost All or Almost Nothing. *Astrophys. J. Lett.* **720,** L67–L71. arXiv: 1003.3466 [astro-ph.CO] (2010).

272. Boucenna, S. M., Kuhnel, F., Ohlsson, T. & Visinelli, L. Novel Constraints on Mixed Dark-Matter Scenarios of Primordial Black Holes and WIMPs. *JCAP* **07,** 003. arXiv: 1712.06383 [hep-ph] (2018).

273. Adamek, J., Byrnes, C. T., Gosenca, M. & Hotchkiss, S. WIMPs and stellar-mass primordial black holes are incompatible. *Phys. Rev. D* **100,** 023506. arXiv: 1901.08528 [astro-ph.CO] (2019).

274. Carr, B., Kuhnel, F. & Visinelli, L. Black holes and WIMPs: all or nothing or something else. *Mon. Not. Roy. Astron. Soc.* **506,** 3648–3661. arXiv: 2011.01930 [astro-ph.CO] (2021).

275. Sandick, P., Es Haghi, B. S. & Sinha, K. Asymmetric reheating by primordial black holes. *Phys. Rev. D* **104,** 083523. arXiv: 2108.08329 [astro-ph.CO] (2021).

276. Jyoti Das, S., Mahanta, D. & Borah, D. Low scale leptogenesis and dark matter in the presence of primordial black holes. *JCAP* **11,** 019. arXiv: 2104.14496 [hep-ph] (2021).

277. Kozaczuk, J., Lin, T. & Villarama, E. Signals of primordial black holes at gravitational wave interferometers. *Phys. Rev. D* **105,** 123023. arXiv: 2108.12475 [astro-ph.CO] (2022).

278. Ford, L. H. Gravitational Particle Creation and Inflation. *Phys. Rev. D* **35,** 2955 (1987).

279. Chung, D. J. H., Kolb, E. W. & Riotto, A. Superheavy dark matter. *Phys. Rev. D* **59,** 023501. arXiv: hep-ph/9802238 (1998).

280. Chung, D. J. H., Crotty, P., Kolb, E. W. & Riotto, A. On the Gravitational Production of Superheavy Dark Matter. *Phys. Rev. D* **64,** 043503. arXiv: hep-ph/0104100 (2001).

281. Ema, Y., Nakayama, K. & Tang, Y. Production of Purely Gravitational Dark Matter. *JHEP* **09,** 135. arXiv: 1804.07471 [hep-ph] (2018).

282. Kolb, E. W. & Long, A. J. Superheavy dark matter through Higgs portal operators. *Phys. Rev. D* **96,** 103540. arXiv: 1708.04293 [astro-ph.CO] (2017).

283. Babichev, E., Gorbunov, D., Ramazanov, S. & Reverberi, L. Gravitational reheating and superheavy Dark Matter creation after inflation with non-minimal coupling. *JCAP* **09,** 059. arXiv: 2006.02225 [hep-ph] (2020).

284. Babichev, E., Gorbunov, D. & Ramazanov, S. Gravitational misalignment mechanism of Dark Matter production. *JCAP* **08,** 047. arXiv: 2004.03410 [hep-ph] (2020).

285. Laulumaa, L., Markkanen, T. & Nurmi, S. Primordial dark matter from curvature induced symmetry breaking. *JCAP* **08,** 002. arXiv: 2005.04061 [astro-ph.CO] (2020).

286. Borah, D., Jyoti Das, S. & Saha, A. K. Gravitational origin of dark matter and Majorana neutrino mass with non-minimal quartic inflation. *Phys. Dark Univ.* **33,** 100858. arXiv: 2011.02489 [hep-ph] (2021).

287. Mambrini, Y. & Olive, K. A. Gravitational Production of Dark Matter during Reheating. *Phys. Rev. D* **103,** 115009. arXiv: 2102.06214 [hep-ph] (2021).

288. Clery, S., Mambrini, Y., Olive, K. A. & Verner, S. Gravitational portals in the early Universe. *Phys. Rev. D* **105,** 075005. arXiv: 2112.15214 [hep-ph] (2022).

289. Clery, S., Mambrini, Y., Olive, K. A., Shkerin, A. & Verner, S. Gravitational portals with nonminimal couplings. *Phys. Rev. D* **105,** 095042. arXiv: 2203.02004 [hep-ph] (2022).

290. Samanta, R. & Urban, F. R. Testing super heavy dark matter from primordial black holes with gravitational waves. *JCAP* **06,** 017. arXiv: 2112.04836 [hep-ph] (2022).

291. Bernal, N., Fong, C. S., Perez-Gonzalez, Y. F. & Turner, J. Rescuing high-scale leptogenesis using primordial black holes. *Phys. Rev. D* **106,** 035019. arXiv: 2203.08823 [hep-ph] (2022).

292. Garzilli, A., Boyarsky, A. & Ruchayskiy, O. *Cutoff in the Lyman-α forest power spectrum: Warm IGM or warm dark matter?* in *14th Marcel Grossmann Meeting on Recent Developments in Theoretical and Experimental General Relativity, Astrophysics, and Relativistic Field Theories* **3** (2017), 2447–2452.

293. Croft, R. A. C. *et al.* Towards a precise measurement of matter clustering: Lyman alpha forest data at redshifts 2-4. *Astrophys. J.* **581,** 20–52. arXiv: astro-ph/0012324 (2002).

294. Viel, M., Becker, G. D., Bolton, J. S. & Haehnelt, M. G. Warm dark matter as a solution to the small scale crisis: New constraints from high redshift Lyman-$\alpha$ forest data. *Phys. Rev. D* **88,** 043502. arXiv: 1306.2314 [astro-ph.CO] (2013).

295. Baur, J., Palanque-Delabrouille, N., Yèche, C., Magneville, C. & Viel, M. Lyman-alpha Forests cool Warm Dark Matter. *JCAP* **08,** 012. arXiv: 1512.01981 [astro-ph.CO] (2016).

296. Garzilli, A., Magalich, A., Ruchayskiy, O. & Boyarsky, A. How to constrain warm dark matter with the Lyman-$\alpha$ forest. *Mon. Not. Roy. Astron. Soc.* **502,** 2356–2363. arXiv: 1912.09397 [astro-ph.CO] (2021).

297. Garny, M., Sandora, M. & Sloth, M. S. Planckian Interacting Massive Particles as Dark Matter. *Phys. Rev. Lett.* **116,** 101302. arXiv: 1511.03278 [hep-ph] (2016).

298. Tang, Y. & Wu, Y.-L. On Thermal Gravitational Contribution to Particle Production and Dark Matter. *Phys. Lett. B* **774,** 676–681. arXiv: 1708.05138 [hep-ph] (2017).

299. Garny, M., Palessandro, A., Sandora, M. & Sloth, M. S. Theory and Phenomenology of Planckian Interacting Massive Particles as Dark Matter. *JCAP* **02,** 027. arXiv: 1709.09688 [hep-ph] (2018).

300. Bernal, N. *et al.* Spin-2 Portal Dark Matter. *Phys. Rev. D* **97,** 115020. arXiv: 1803.01866 [hep-ph] (2018).

301. Barman, B. & Bernal, N. Gravitational SIMPs. *JCAP* **06,** 011. arXiv: 2104.10699 [hep-ph] (2021).

302. Barman, B., Bernal, N., Das, A. & Roshan, R. Non-minimally coupled vector boson dark matter. *JCAP* **01,** 047. arXiv: 2108.13447 [hep-ph] (2022).

303. Garcia, M. A. G., Mambrini, Y., Olive, K. A. & Peloso, M. Enhancement of the Dark Matter Abundance Before Reheating: Applications to Gravitino Dark Matter. *Phys. Rev. D* **96,** 103510. arXiv: 1709.01549 [hep-ph] (2017).

304. Bernal, N., Hajkarim, F. & Xu, Y. Axion Dark Matter in the Time of Primordial Black Holes. *Phys. Rev. D* **104,** 075007. arXiv: 2107.13575 [hep-ph] (2021).

305. Bernal, N., Perez-Gonzalez, Y. F. & Xu, Y. Superradiant production of heavy dark matter from primordial black holes. *Phys. Rev. D* **106,** 015020. arXiv: 2205.11522 [hep-ph] (2022).

306. Bernal, N. & Fong, C. S. Dark matter and leptogenesis from gravitational production. *JCAP* **06,** 028. arXiv: 2103.06896 [hep-ph] (2021).

307. Co, R. T., Mambrini, Y. & Olive, K. A. Inflationary gravitational leptogenesis. *Phys. Rev. D* **106,** 075006. arXiv: 2205.01689 [hep-ph] (2022).

308. Bernal, N. & Hajkarim, F. Primordial Gravitational Waves in Nonstandard Cosmologies. *Phys. Rev. D* **100,** 063502. arXiv: 1905.10410 [astro-ph.CO] (2019).

309. Guo, H.-K., Sinha, K., Vagie, D. & White, G. Phase Transitions in an Expanding Universe: Stochastic Gravitational Waves in Standard and Non-Standard Histories. *JCAP* **01,** 001. arXiv: 2007.08537 [hep-ph] (2021).

310. Borah, D., Jyoti Das, S., Saha, A. K. & Samanta, R. Probing WIMP dark matter via gravitational waves' spectral shapes. *Phys. Rev. D* **106,** L011701. arXiv: 2202.10474 [hep-ph] (2022).

311. Borah, D., Jyoti Das, S. & Roshan, R. Probing high scale seesaw and PBH generated dark matter via gravitational waves with multiple tilts. arXiv: 2208.04965 [hep-ph] (Aug. 2022).

312. Gehrman, T. C., Shams Es Haghi, B., Sinha, K. & Xu, T. Baryogenesis, primordial black holes and MHz–GHz gravitational waves. *JCAP* **02,** 062. arXiv: 2211.08431 [hep-ph] (2023).

313. Allahverdi, R., Dutta, B. & Sinha, K. Baryogenesis and Late-Decaying Moduli. *Phys. Rev. D* **82,** 035004. arXiv: 1005.2804 [hep-ph] (2010).

314. Allahverdi, R., Dutta, B. & Sinha, K. Cladogenesis: Baryon-Dark Matter Coincidence from Branchings in Moduli Decay. *Phys. Rev. D* **83,** 083502. arXiv: 1011.1286 [hep-ph] (2011).

315. Allahverdi, R., Dutta, B., Mohapatra, R. N. & Sinha, K. A Supersymmetric Model for Dark Matter and Baryogenesis Motivated by the Recent CDMS Result. *Phys. Rev. Lett.* **111,** 051302. arXiv: 1305.0287 [hep-ph] (2013).

316. Allahverdi, R. & Dutta, B. Natural GeV Dark Matter and the Baryon-Dark Matter Coincidence Puzzle. *Phys. Rev. D* **88,** 023525. arXiv: 1304.0711 [hep-ph] (2013).

317. Allahverdi, R., Dev, P. S. B. & Dutta, B. A simple testable model of baryon number violation: Baryogenesis, dark matter, neutron–antineutron oscillation and collider signals. *Phys. Lett. B* **779,** 262–268. arXiv: 1712.02713 [hep-ph] (2018).

318. Baldo-Ceolin, M. *et al.* A New experimental limit on neutron - anti-neutron oscillations. *Z. Phys. C* **63,** 409–416 (1994).

319. Abe, K. *et al.* The Search for $n - \bar{n}$ oscillation in Super-Kamiokande I. *Phys. Rev. D* **91,** 072006. arXiv: 1109.4227 [hep-ex] (2015).

320. Aharmim, B. *et al.* Search for neutron-antineutron oscillations at the Sudbury Neutrino Observatory. *Phys. Rev. D* **96,** 092005. arXiv: 1705.00696 [hep-ex] (2017).

321. Kolb, E. W. & Wolfram, S. Baryon Number Generation in the Early Universe. *Nucl. Phys. B* **172.** [Erratum: Nucl.Phys.B 195, 542 (1982)], 224 (1980).

322. Dev, P. S. B. & Mohapatra, R. N. TeV scale model for baryon and lepton number violation and resonant baryogenesis. *Phys. Rev. D* **92,** 016007. arXiv: 1504.07196 [hep-ph] (2015).

323. Davoudiasl, H. & Zhang, Y. Baryon Number Violation via Majorana Neutrinos in the Early Universe, at the LHC, and Deep Underground. *Phys. Rev. D* **92,** 016005. arXiv: 1504.07244 [hep-ph] (2015).

324. Sirunyan, A. M. *et al.* Search for dijet resonances in proton–proton collisions at $\sqrt{s}$ = 13 TeV and constraints on dark matter and other models. *Phys. Lett. B* **769.** [Erratum: Phys.Lett.B 772, 882–883 (2017)], 520–542. arXiv: 1611.03568 [hep-ex] (2017).

325. A search for dijet resonances in proton-proton collisions at $\sqrt{s} = 13$ TeV with a new background prediction method (2019).

326. Tumasyan, A. *et al.* Search for new particles in events with energetic jets and large missing transverse momentum in proton-proton collisions at $\sqrt{s}$ = 13 TeV. *JHEP* **11,** 153. arXiv: 2107.13021 [hep-ex] (2021).

327. Aad, G. *et al.* Search for new phenomena in events with an energetic jet and missing transverse momentum in $pp$ collisions at $\sqrt{s}$ =13 TeV with the ATLAS detector. *Phys. Rev. D* **103,** 112006. arXiv: 2102.10874 [hep-ex] (2021).

328. Mohapatra, R. N. Neutron-Anti-Neutron Oscillation: Theory and Phenomenology. *J. Phys. G* **36,** 104006. arXiv: 0902.0834 [hep-ph] (2009).

329. Claudson, M., Hall, L. J. & Hinchliffe, I. COSMOLOGICAL BARYON GENERATION AT LOW TEMPERATURES. *Nucl. Phys. B* **241,** 309–332 (1984).

330. Babu, K. S., Mohapatra, R. N. & Nasri, S. Post-Sphaleron Baryogenesis. *Phys. Rev. Lett.* **97,** 131301. arXiv: hep-ph/0606144 (2006).

331. Ballesteros, G., Garcia, M. A. G. & Pierre, M. How warm are non-thermal relics? Lyman-$\alpha$ bounds on out-of-equilibrium dark matter. *JCAP* **03,** 101. arXiv: 2011.13458 [hep-ph] (2021).

332. D'Eramo, F. & Lenoci, A. Lower mass bounds on FIMP dark matter produced via freeze-in. *JCAP* **10,** 045. arXiv: 2012.01446 [hep-ph] (2021).

333. Barman, B., Borah, D., Das Jyoti, S. & Roshan, R. Cogenesis of Baryon asymmetry and gravitational dark matter from primordial black holes. *JCAP* **08,** 068. arXiv: 2204.10339 [hep-ph] (2022).

334. Crowder, J. & Cornish, N. J. Beyond LISA: Exploring future gravitational wave missions. *Phys. Rev. D* **72,** 083005. arXiv: gr-qc/0506015 (2005).

335. Corbin, V. & Cornish, N. J. Detecting the cosmic gravitational wave background with the big bang observer. *Class. Quant. Grav.* **23,** 2435–2446. arXiv: gr-qc/0512039 (2006).

336. Harry, G. M., Fritschel, P., Shaddock, D. A., Folkner, W. & Phinney, E. S. Laser interferometry for the big bang observer. *Class. Quant. Grav.* **23.** [Erratum: Class.Quant.Grav. 23, 7361 (2006)], 4887–4894 (2006).

337. Seto, N., Kawamura, S. & Nakamura, T. Possibility of direct measurement of the acceleration of the universe using 0.1-Hz band laser interferometer gravitational wave antenna in space. *Phys. Rev. Lett.* **87,** 221103. arXiv: astro-ph/0108011 (2001).

338. Reitze, D. *et al.* Cosmic Explorer: The U.S. Contribution to Gravitational-Wave Astronomy beyond LIGO. *Bull. Am. Astron. Soc.* **51,** 035. arXiv: 1907.04833 [astro-ph.IM] (2019).

339. Punturo, M. *et al.* The Einstein Telescope: A third-generation gravitational wave observatory. *Class. Quant. Grav.* **27** (ed Ricci, F.) 194002 (2010).

340. Hild, S. *et al.* Sensitivity Studies for Third-Generation Gravitational Wave Observatories. *Class. Quant. Grav.* **28,** 094013. arXiv: 1012.0908 [gr-qc] (2011).

341. Sathyaprakash, B. *et al.* Scientific Objectives of Einstein Telescope. *Class. Quant. Grav.* **29** (eds Hannam, M., Sutton, P., Hild, S. & van den Broeck, C.) [Erratum: Class.Quant.Grav. 30, 079501 (2013)], 124013. arXiv: 1206.0331 [gr-qc] (2012).

342. Aasi, J. *et al.* Characterization of the LIGO detectors during their sixth science run. *Class. Quant. Grav.* **32,** 115012. arXiv: 1410.7764 [gr-qc] (2015).

343. Schmitz, K. New Sensitivity Curves for Gravitational-Wave Signals from Cosmological Phase Transitions. *JHEP* **01,** 097. arXiv: 2002.04615 [hep-ph] (2021).

344. Ade, P. A. R. *et al.* Improved Constraints on Primordial Gravitational Waves using Planck, WMAP, and BICEP/Keck Observations through the 2018 Observing Season. *Phys. Rev. Lett.* **127,** 151301. arXiv: 2110.00483 [astro-ph.CO] (2021).

345. Okada, N., Rehman, M. U. & Shafi, Q. Non-Minimal B-L Inflation with Observable Gravity Waves. *Phys. Lett. B* **701,** 520–525. arXiv: 1102.4747 [hep-ph] (2011).

346. Okada, N. & Raut, D. Running non-minimal inflation with stabilized inflaton potential. *Eur. Phys. J. C* **77,** 247. arXiv: 1509.04439 [hep-ph] (2017).

347. Capozziello, S., de Ritis, R. & Marino, A. A. Some aspects of the cosmological conformal equivalence between 'Jordan frame' and 'Einstein frame'. *Class. Quant. Grav.* **14,** 3243–3258. arXiv: gr-qc/9612053 (1997).

348. Kaiser, D. I. Conformal Transformations with Multiple Scalar Fields. *Phys. Rev. D* **81,** 084044. arXiv: 1003.1159 [gr-qc] (2010).

349. Okada, N., Rehman, M. U. & Shafi, Q. Tensor to Scalar Ratio in Non-Minimal $\phi^4$ Inflation. *Phys. Rev. D* **82,** 043502. arXiv: 1005.5161 [hep-ph] (2010).

350. Linde, A. D. Inflationary Cosmology. *Lect. Notes Phys.* **738,** 1–54. arXiv: 0705.0164 [hep-th] (2008).